

# Self-standing three-dimensional flexible electrodes for energy conversion and biosensing applications

A Thesis Submitted

In the fulfillment for the degree of

*Doctor of Philosophy*

by

**Alankar Kafle**

2018CYZ0014



**Department of Chemistry  
Indian Institute of Technology Ropar  
India**

April 2023



# Declaration

*I hereby declare that this thesis entitled "Self-standing three-dimensional flexible electrodes for energy conversion and biosensing applications" is the outcome of original research work performed by me under the able guidance of Dr. Tharamani C. N., Associate Professor at the Department of Chemistry, Indian Institute of Technology Ropar. I solemnly declare that the contents of this thesis both in part or complete has not been submitted elsewhere for the award of any degree or diploma.*

*Kafle* / 17-07-23

**Alankar Kafle**

**(2018CYZ0014)**

**Department of Chemistry  
Indian Institute of Technology Ropar**





# Certificate

This is to certify that the thesis entitled "Self-standing three-dimensional flexible electrodes for energy conversion and biosensing applications" submitted by Mr. Alankar Kafle for the award of the degree of "Doctor of Philosophy" in Chemistry is based on the results of studies carried out by him under my guidance and supervision.

The thesis or any part thereof has not been previously submitted for the award of any other degree or diploma.



Dr. Tharamani C.N.

Associate Professor  
Department of Chemistry  
Indian Institute of Technology Ropar  
Rupnagar 140001  
Punjab, INDIA

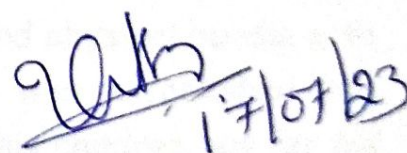




# Coursework Certificate

This is to certify that Mr. Alankar Kafle has undertaken the following coursework for the fulfillment of the degree of Doctor of Philosophy;

CY423	Solid State Chemistry
CY511	Instrumentation Analysis
CY613	Chemistry of Metal-Carbon bond
CY701	Molecular Spectroscopy
CY622	Applied Electrochemistry



**Dr. Tharamani C.N.**

**Associate Professor  
Department of Chemistry  
Indian Institute of Technology Ropar  
Rupnagar 140001  
Punjab, INDIA**



*Dedicated to my beloved father  
Late Pandit Netra Prasad Kafle*



A real educator who dedicated his whole life to teach needy people. A courageous fighter who defeated every social and physical hurdle with a single foot. A far-sighted father/teacher who established the foundation and set the future goal not only for his children but for his students also. Despite of his personal life struggles, he never got tired of teaching and always taught his students in a cheerful mood selflessly till his final breath and nurtured his students mind with courage and confidence. I am grateful to my father, though my words are not enough to appreciate all the hard work he had done for us, I feel so blessed and thankful to Almighty God to have him as a constant source of inspiration and motivation in my life.



# Acknowledgments

Completing this research, an output of more than four years, would have not been possible without the contribution of many notorious and ulterior individuals. It is a great opportunity for me to express my sincere gratitude to them for their unexcelled contributions. Foremost, my sincere thank goes to the Almighty God for providing shower of blessings and good health throughout my PhD tenure so that this research moved smoothly and successfully.

I want to express deep sense of gratitude to my research supervisor Dr. Tharamani C.N., Associate Professor, IIT Ropar, for providing me this platform to explore research career under her kind guidance. She was the only one who trusted me as a potential student in the crowd of young and energetic candidates and provided me the golden opportunity to work in her prestigious laboratory. It was a great pleasure to work under her guidance. I am whole heartedly thankful for her motivation, encouragements, advice, patience, continuous support and all that she has provided me. I found her, one of the most treasured persons who created my research foundation and shaped my future. She is one of the most proficient persons whom I have met in my life, bestowed with all the magnificent qualities who had more insight about me than myself. I remember how she motivated and showed me the correct path when I felt lost and confused during my research career. She has been an inspiration for me and I thank her for everything she offered me. I want to express my sincere gratitude to Dr. Vasanthkumar and Avish for cheerful and unforgettable moments that we spent together.

I am grateful to Dr. Debaprasad Mandal, Associate Professor, IIT Ropar, for providing all the valuable knowledge, cooperation and continuous support. I would like to extend my sincere gratitude to the doctoral committee: Dr. Dhilip Kumar, Dr. Avijit Goswami, and Dr. Ravi Mohan Prasad for their motivation, encouragement and valuable comments. I am very grateful to my respected teachers

who were involved directly or indirectly at various stages of my education, for their path finder guidance and thoughtful knowledge that always directed me toward academic excellence.

My research would not have been completed without association and cooperation of my intelligent and cheerful lab mates who always provided constructive and healthy laboratory environment. It's my fortune to gratefully acknowledge them for which I do not have sufficient words to express my appreciation for their contributions. I am very much thankful to my intimate friends Dr. Neha Thakur and Dr. Mukesh Kumar who always encouraged, guided and stood by me during the ups and downs of my research tenure both professionally and personally. Dr. Neha's working style, leadership quality, guidance, care and love always encouraged me to improve my research activity. Dr. Mukesh's in-depth knowledge, patience, hard-working nature, problem solving style, positive attitude and loving behavior always inspired me to concentrate on research. I am grateful to both of them, their association has made not only my research successful but also made my stay pleasurable and memorable. A special thanks to Daisy Mehta for her encouragement, love, care and continuous support. She was the one who introduced me to this research and local environment and made me stable at the beginning of this journey. I am thankful to her for all valuable supports and memorable moments during my stay. I would like to thank Man Singh from the bottom of my heart for his support, care and help which I got from him whenever needed. I extend my thanks to Akansha Chaturvedi for her sincere help, respect, and kindness. I express a very special gratitude to Sukhjot Kaur for her kindness, continuous support and sincere help with quick response whenever needed. My special thanks go to Shivangi Mehta and Kalpana Garg who always supported and helped with respect and kindness during my study. I am thankful to Devyani Dahare, Sukhdeep Singh and Sameer Kumar for their support in the laboratory. I express my sincere thanks to Naresh Bhatia sir for his motivation and inspiration. I am grateful to my senior Dr. Vikram Singh, for his guidance in understanding of fundamentals of research



area and laboratory culture. I am very much thankful to Dr. Subhasis Das Adhikary, Dr. Sinchan Maji, Dr. Anil Kumar Padhan, Dr. Gaje Singh, Diksha Sharma, Ganga Singh, Tino S. Thomas, Aayushi Sinha, and Rahul Kumar for their continuous support and cheerful memories at IIT Ropar. I express my special thanks to all staff members of IIT Ropar, especially Poonam Kataria, Gurparkash Kaur, Amit Kaushal, Sushil Kumar, Nagendera Singh, Samita Saini, Manish Kumar and Hanspreet Kaur, for their support and help.

I want to express a very special gratitude to my best friend, Divyani Gupta, with whom I started my PhD journey. My research work would not have gone straightforward and uninterrupted if she was not there with me. She was the only one with whom I could share all my professional and personal issues. We together had planned many research projects, but due to time constraint only few of them, we were able to execute. I have no words to express my appreciation to her. She always stood with me, trusted me, motivated me, scolded me and always helped me in taking right decision. She never allowed me to feel alone in either conditions, good or bad, both inside and outside the laboratory. Her fearlessness nature and dedication towards research always encouraged me to work hard optimum to my limits. I thank her for always being there and bearing me during my whole PhD time. A special thanks to Ms. Veenu Gupta for her support and beautiful memories.

Finally, I would like to express heartily gratitude to my family members for their love, and support, which was my strength. I am grateful to my mother Nakareshwari Kafle who always filled energy and courage inside me to make my father's dream true. My gratitude also goes to my sisters, Bani Kafle, Benu Kafle and Karuna Kafle, sister in laws Durga Guragain, Prof. Bhim Khatiwada and Om Prakash Wasti for their continuous motivation, love and care. I am deeply indebted to my brother Dr. Bhooshan Kafle, my hidden strength, who spent most of his time for the wellbeing of the family, borne the whole family responsibility and made me free for my career development. I am thankful to him for timely encouragement, unconditional trust, endless patience and everything what he provided to me. I also

thank for my sister-in-law Anita Baral Kafle and my nephews Manan, Parikshit, Aasara, Anugya, Awantika, Anupama, Aagam and Gargee for their heart-warming kindness. I would like to express my gratitude to my parents-in-law Nandalal Subedi and Sita Subedi for their love and encouragement.

Finally, but not the least, I wish to thank my wife, Sandhya Subedi Kafle who has stood by me throughout the whole journey. I am so appreciative for her constant love, motivation, understanding and encouraging, calmly handling my fits of pique and impatience, taking up the whole responsibilities of the kids and bearing the pressure of ups and downs during my studying period. I cannot forget my daughters Maitreyee and Vaidehee who maintained my working environment calm and smooth in home also even in their child age by saying “Baba has work, it is not good to disturb him”. They never ever demanded for extra activities, only counted the months and kept their all plans pending till my PhD work completion. I would like to thank them for their patience, kindness and making my mind relax during the hard times.

I am grateful to all individuals, whose name may have escaped here, who have helped me directly or indirectly throughout the journey.

Alankar Kafle

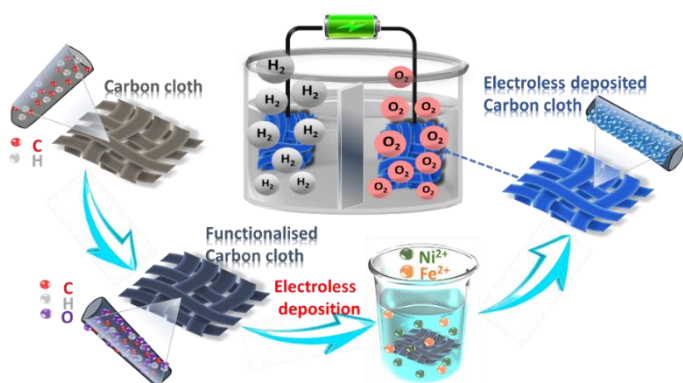
# Preface

Energy, the most fundamental fragment of the nature, is essential not only for the fulfilment of individual and community need, it is equally important for the nation's economic growth. However, the individual lifestyle is becoming luxuries with rapidly growing technological advancement, the current energy extraction pattern and future energy demand is pointing a dark image of the earth. Although, the planetary energy reserve contains high enough renewable energy sources than the finite source of energy but most of the current global energy extraction is dependent on fossil fuel only. The consumption of fossil fuel not only depletes its finite reserves but also creates serious environmental as well as health issues. Therefore, the production of green energy from clean and renewable sources is very urgent. Alternatively, energy extraction from the various renewable energy resources, has been explored but all these systems rely on continuous electricity generation that cannot be stored in current form for later use. But it can either be converted to value-added product or stored in an energy storage device. For this, hydrogen ( $H_2$ ) production from water electrolysis can be a good option as  $H_2$  itself is zero-emission energy as well as prime feeding gas for many industrial applications. Moreover, about 1% of current global energy consumption is involving in  $H_2$  production only. Similarly, the zinc-air battery can be an attractive choice for the energy storage device owing to its high energy density, involvement of air as a feedstock and more importantly it works with aqueous electrolytes with very low hazardous risk. But, the overall performance of these devices highly depends on electrode materials.

Besides the activity of the electrocatalyst, the electrode architecture is equally important for electrochemical performance. In general, the existing commercial electrolyser assembly contains a rigid electrode coated with electrocatalyst ink where the use of insulating binder during the catalyst ink preparation may provide

physical adhesion but it may limit the ion transport and hinder the release of bubbles resulting in catalyst peeling from the electrode surface and ultimately leading to a compromised electrochemical performance. Secondly, in the metal/carbon or any other conductive substrate based current collector, large mass densities of electrochemically inactive materials is not only issue for atom economy but also a challenge for the development of light weight devices. Additionally, the single side catalyst loaded electrode limits its actual output as well. Similarly, the waste management of the obsolete end-of-life product is also of environmental concern. Moreover, the emerging next-generation portable and wearable electronics is demanding customizable electrochemical energy storage device. Therefore, our research focused on the development of binder-free three-dimensional light-weight electrode decorated with highly active catalyst by a cost effective and straight forward approach which can demonstrate comparable activity with state of art materials.

Chapter 1 of this thesis briefly describes the energy extraction pattern and its

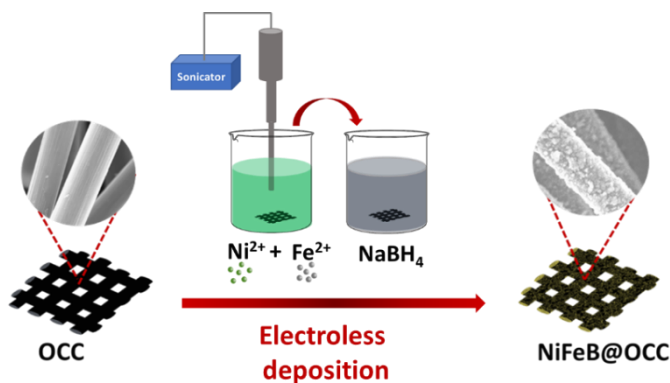


impacts along with probable alternatives followed by the importance of electrodes towards energy conversion/storage as well as healthcare applications. In the second

chapter we have described the details of the electrode preparation, characterization techniques, and basic terminology used in energy storage and biosensing applications.

In Chapter 3, we explored a novel strategy for the development of binder-free three-dimensional flexible electrode where Ni and Fe sulphide and phosphides decorated carbon cloth electrodes (NiFeS@OCC and NiFeP@OCC) were developed as promising bifunctional electrocatalysts towards overall water splitting. Herein,

activation free electroless deposition approach was explored for growing NiFeS and NiFeP over the highly flexible carbon cloth substrate. Conventionally, electroless deposition involves surface activation and sensitization using  $\text{SnCl}_2$  and  $\text{PdCl}_2$  followed by direct chemical reduction of the metal ion on the substrate. The present study eliminated the use of expensive  $\text{PdCl}_2$  and  $\text{SnCl}_2$  based activators/sensitizers to reduce the overall manufacturing cost by the introduction of functional groups on the carbon cloth which provides strong adsorption of metal ions and simultaneously enhance the conductivity along with mass transport kinetics. Thus developed NiFeS@OCC and NiFeP@OCC electrodes exhibited excellent OER



activity and stability as they required only 220 mV and 270 mV of overpotential respectively to achieve  $10 \text{ mA cm}^{-2}$ . These electrodes promise to be good bifunctional catalyst due to their ability to catalyse cathodic HER as well at 223 and 300 mV of overpotential for NiFeS@OCC and NiFeP@OCC respectively. An alkaline water electrolyser set up with these electrodes demonstrated good activity and stability for both catalysts and also showed good flexibility and electrochemical performance under various mechanical deformations.

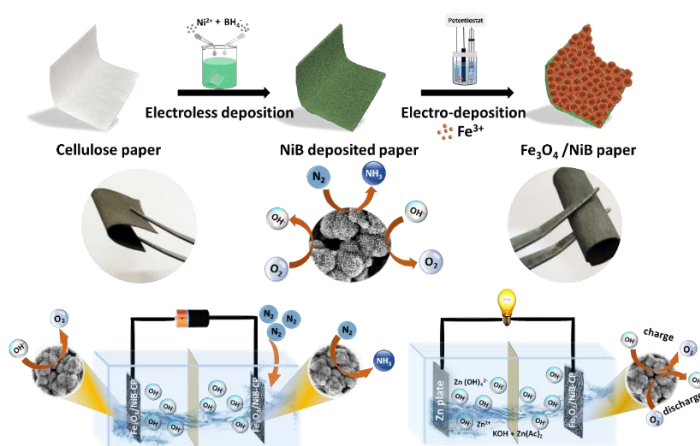
Despite being a clean and eco-friendly technology, the current commercial technologies for water electrolysis urge high-purity water which in turn hinders the broader implementation of the water electrolyzer. In this context, this thesis attempted to address the problem associated with shortage of freshwater for wide exploration of water electrolyzer by developing electrode material with good activity and high resistivity towards chloride ion corrosion for sustainable seawater splitting which is described in Chapter 4. In the first part of this chapter, a binder-free three-dimensional carbon cloth flexible electrode incorporated with active

electrocatalyst NiFeB over oxygen functionalized carbon cloth (NiFeB@OCC), was explored for sustainable seawater splitting which demonstrated a remarkable performance towards OER, HER and overall water splitting in 1 M KOH as well as in 1 M KOH + 0.5 M NaCl electrolyte system with excellent stability. The as fabricated NiFeB@OCC demonstrated the admirable OER performance with excellent durability even in corrosive environment in which it requires only 255 mV overpotential to achieve  $20 \text{ mA cm}^{-2}$  current density whereas it exhibits moderate HER activity demanding 241 mV overpotential. The two-electrode based alkaline water electrolyser further demonstrated good activity with excellent durability towards overall water splitting which even achieves comparable activity under harsh conditions also. In this way, this study can deliver a new insight to develop a cost-effective corrosion resistive flexible electrode for water splitting.

After exploring carbon cloth based flexible electrodes, our research was focused towards the search for biodegradable substrate-based three-dimensional electrodes. For this, cellulose paper (CP) has been chosen as a substrate. But the biggest hurdle for its exploration as an electrode material is the absence of a conductive pathway for the electric circuit which was overcome by modifying the surface of cellulose paper with conductive metal composites. Herein, a novel, cost-effective and straightforward electroless deposition approach has been explored to convert an insulating cellulose paper into a conductive substrate (designated as NiB-CP) over which active electrocatalyst was incorporated via electrodeposition method. In the second part of Chapter 4, NiP/NiB-CP electrode was developed via two-step electroless deposition followed by an electrodeposition approach. This NiP/NiB-CP electrode possesses excellent bifunctional activity and long-term durability in both alkaline pure water and seawater electrolytes which required 379 & 391 mV overpotential during OER and 178 & 196 mV during HER to drive  $100 \text{ mA cm}^{-2}$  in 1 M KOH and 1 M KOH+ 0.5M NaCl electrolyte whereas it demands 1.65 & 1.69 V potential to achieve  $20 \text{ mA cm}^{-2}$  current density during overall water and saline water splitting respectively. This work opened an area for the development

of cellulose paper based self-standing three-dimensional flexible electrodes for overall water/seawater splitting.

In addition to augmented energy demand, the incessantly increasing world's population also stresses high fertilizer production to provide the basis of nutrition. Therefore, the synthesis of  $\text{NH}_3$  is of huge significance, since it is a prime constituent of fertilizers. But the commercial production of ammonia highly relies on the Haber-Bosch process which involves harsh operating conditions, high energy consumption high  $\text{CO}_2$  emissions. Alternatively, electrochemical nitrogen reduction can be a good option for ammonia production with minimum energy consumption and reduced carbon footprint, by using water as the hydrogen source under ambient conditions but requires a power source. On the other hand, rechargeable metal-air batteries are emerging as a potential candidate for energy storage systems owing to their high energy density and straightforward fabrication procedure. In order to address these issues an eco-friendly cellulose paper based three-dimensional flexible electrode ( $\text{Fe}_3\text{O}_4/\text{NiB-CP}$ ) was developed via two step electroless deposition followed by electrodeposition approach and explored as an effective trifunctional (NRR/ORR/OER) electrode for the integrated Zn- $\text{O}_2$  battery powered dinitrogen reduction in the first part of Chapter 5. This electrode was able to demonstrate electrocatalytic dinitrogen reduction with good yield rate ( $245 \mu\text{g h}^{-1} \text{mg}_{\text{cat}}^{-1}$ ), promising Faradaic efficiency (4.32%) and a high TOF ( $0.83 \text{ h}^{-1}$ ) at a



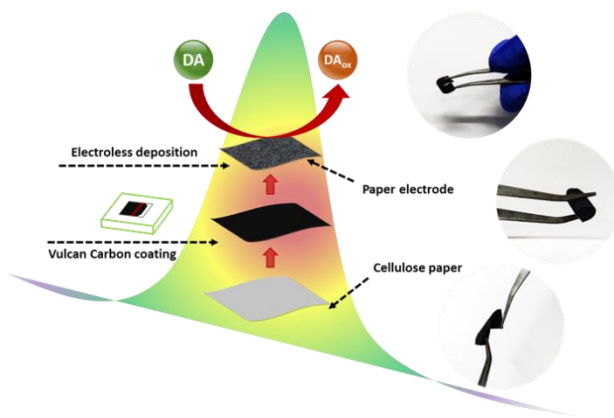
lower applied potential of  $-0.1 \text{ V vs. RHE}$ . Additionally, the designed electrode was also employed as an air-cathode for an aqueous Zn- $\text{O}_2$  battery which exhibited remarkable power density and fair

cyclic stability. Additionally, this Zn-O<sub>2</sub> battery was able to power an electrolyser to perform electrocatalytic dinitrogen reduction and achieved good NH<sub>3</sub> yield of 194.25  $\mu\text{g h}^{-1} \text{mg}_{\text{cat}}^{-1}$ .

Thereafter, the same strategy was applied in the second part of this chapter to develop eco-friendly cellulose paper based self-standing three-dimensional flexible electrodes (NiFeP/NiB-CP) exhibiting trifunctional activity towards ORR, OER and HER for self-powered water splitting. The fabricated NiFeP/NiB-CP electrode demonstrated excellent electrocatalytic activity towards OER ( $\eta_{100} = 310 \text{ mV}$ ), ORR (onset pot. = 0.85 V *vs.* RHE), and HER ( $\eta_{100} = 182 \text{ mV}$ ) with excellent durability. Further, the water electrolyser consisting of the designed electrode both as cathode and anode showed a good overall water splitting with a cell voltage of 1.62 V at 20  $\text{mA cm}^{-2}$ . Additionally, a rechargeable zinc–air battery was assembled by employing the NiFeP/NiB-CP air cathode which exhibited a power density of 145  $\text{mW cm}^{-2}$  at 1.95 V. Finally, a paper electrode-based Zn-O<sub>2</sub> battery powered water electrolyser was exhibited for overall water splitting. Therefore, this work can encourage researchers for the development of eco-friendly paper electrodes towards energy storage/conversion applications.

Besides these, the consumption of fossil fuels also caused environmental pollution which may result in serious health

issues. Polluted air may affect different body systems which can result in various hormonal imbalances, for instance, dopamine which is a major neurotransmitter has been reported to fluctuate with exposure to non-healthy living conditions. Therefore, identification of dopamine levels is important for clinical diagnosis and treatment purposes. In order to address this problem, in Chapter 6, cellulose paper based three-dimensional flexible electrodes (NiFeB/VC-CP and CuSnB/VC-CP)





were explored and directly employed as a three-dimensional flexible electrode towards electrochemical dopamine sensing. These NiFeB/VC-CP and CuSnB/VC-CP sensors established a good sensitivity of  $35.35 \mu\text{A } \mu\text{M}^{-1} \text{ cm}^{-2}$  and  $3.92 \mu\text{A } \mu\text{M}^{-1} \text{ cm}^{-2}$  with improved LOD of 2.1 nM and 0.5 nM respectively along with a wide detection range even in the presence of a high concentration of ascorbic acid, glucose and uric acid interferents. In this way, these works can be inspiring to the researchers for the development of wearable, foldable sensors for point of care sensing devices.

The overall thesis work was summerized in Chapter 7 and some probable future directions for the betterment in the related area has been proposed.



# Contents

<b>Chapter 1. Introduction</b>	<b>1</b>
1-1 Global energy resources	1
1-2 Energy extraction practices and their impacts	2
1-3 Renewable source of energy and their limitations	3
1-4 Hydrogen as a value-added product	5
1-5 Water electrolysis	7
1-6 Ammonia as a value-added product	8
1-7 Zn-O <sub>2</sub> battery as an energy storage device	11
1-8 Electrode architecture for energy conversion and storage device	14
1-9 Health impacts	16
1-10 Goals	18
1-11 References	21
 <b>Chapter 2. Material design and characterization techniques</b>	 <b>25</b>
2-1 Synthetic approach	26
2-1.1 Electroless deposition method	26
2-1.2 Electrodeposition method	26
2-2 Physical characterization	28
2-2.1 Electron microscopy	28
2-2.1.1 Scanning electron microscopy (SEM)	28
2-2.1.2 Field emission scanning electron microscopy (FE-SEM)	29
2-2.1.3 Transmission electron microscopy (TEM)	29
2-2.1.4 High-resolution transmission electron microscopy (HRTEM)	29

2-2.2	X-ray photoelectron spectroscopy (XPS)	30
2-2.3	Raman spectroscopy	30
2-2.4	Powder X-ray diffraction (PXRD)	31
2-2.5	UV-visible spectroscopy	31
2-2.5.1	Quantification of Ammonia	32
2-2.5.2	Quantification of hydrazine by Watt-Chrisp method	34
2-2.5.3	Nitrate ( $\text{NO}_3^-$ ) and nitrite ( $\text{NO}_2^-$ ) ion determination	34
2-3	Electrochemical measurements	34
2-3.1	Cyclic voltammetry (CV) and linear sweep voltammetry (LSV)	36
2-3.1	Differential pulse voltammetry (DPV)	37
2-3.4	Electrochemical surface area determination (ECSA)	37
2-3.2	Electrochemical Impedance spectroscopy	38
2-3.3	Chronopotentiometry and chronoamperometry techniques	38
2-5	Quantification of evolved gas	39
2-7	Zn-O <sub>2</sub> battery	39
2-6	Basic terminology used in biosensing	42
2-11	References	43

### **Chapter 3. The activation free electroless deposition of NiFe over carbon cloth as self-standing flexible electrode towards overall water splitting**

3-1	Introduction	46
3-2	Electrode fabrication	48
3-2.1	Pretreatment of carbon cloth	48
3-2.2	NiFeS deposition on carbon cloth (NiFeS@OCC)	48
3-2.3	NiFeP deposition on carbon cloth (NiFeP@OCC)	49
3-3	Results and discussion	49
3-3.1	Physical characterization	49
3-3.2	Catalytic activity towards OER and HER	52

3-3.3 Catalytic activity towards overall water splitting	60
3-3.4 Estimation of H <sub>2</sub> and O <sub>2</sub> evolved	61
3-4 Summary	62
3-5 References	62

## **Chapter 4. Development of corrosion resistive flexible electrodes towards alkaline saline water splitting**

### **4A. Facile fabrication of NiFeB deposited flexible carbon cloth electrode towards overall water splitting in alkaline and saline solutions**

4A-1 Introduction	68
4A-2 Electrode fabrication	71
4A-2.1 Pretreatment of carbon cloth	71
4A-2.2 NiFeB deposition on carbon cloth (NiFeB@OCC)	71
4A-3 Results and discussion	72
4A-3.1 Physical characterization	72
4A-3.2 Electrochemical study towards OER	74
4A-3.3 Electrochemical performance towards HER	79
4A-3.4 Full cell study for overall water/saline water splitting	82
4A-4 Summary	83
4A-5 References	84

### **4B. Development of cellulose paper based eco-friendly flexible electrode for overall water splitting in alkaline and saline solutions**

4B-1 Introduction	88
4B-2 Electrode fabrication	90
4B-2.1 Fabrication of NiB-CP	90
4B-2.2 Fabrication of NiP/NiB-CP	90
4B-3 Results and discussion	91
4B-3.1 Physical characterization	91

4B-3.2 Electrochemical studies	93
4B-4 Summary	99
4B-5 References	100

## **Chapter 5. Exploration of cellulose paper-based electrodes towards self powered nitrogen reduction and overall water splitting**

103

### **5A. Self-standing Fe<sub>3</sub>O<sub>4</sub> decorated paper electrode as binder-free trifunctional electrode for electrochemical ammonia synthesis and Zn-O<sub>2</sub> batteries**

105

5A-1 Introduction	106
5A-2 Electrode fabrication	109
5A-2.1 Fabrication of NiB-CP	109
5A-2.2 Fabrication of Fe <sub>3</sub> O <sub>4</sub> -T@NiB-CP	109
5A-3 Results and discussion	109
5A-3.1 Physical characterization	109
5A-3.2 Electrochemical N <sub>2</sub> reduction reaction	114
5A-3.3 Oxygen bifunctional activity	118
5A-3.4 Application in Zn-air battery	123
5A-3.5 Application as trifunctional flexible electrode	124
5A-4 Summary	125
5A-5 References	126

### **5B. NiFeP decorated cellulose paper based self-standing three-dimensional flexible electrode for self-powered alkaline water splitting**

129

5B-1 Introduction	130
5B-2 Electrode fabrication	133
5B-2.1 Fabrication of NiB-CP	133
5B-2.2 Fabrication of NiFeP/NiB-CP	133

5B-3 Results and discussion	133
5B-3.1 Physical characterization	133
5B-3.2 Electrochemical study	136
5B-4 Summary	144
5B-5 References	144

## **Chapter 6. Designing of the eco-friendly flexible paper electrodes for selective and sensitive detection of dopamine**

### **6A. Fabrication of NiFeB flexible electrode via electroless deposition towards selective and sensitive detection of dopamine**

6A-1 Introduction	150
6A-2 Electrode fabrication	152
6A-2.1 Fabrication of VC-CP	152
6A-2.2 Fabrication of NiFeB/VC-CP	152
6A-3 Results and discussion	153
6A-3.1 Physical characterization	153
6A-3.2 Electrochemical studies	155
6A-4 Summary	162
6A-5 References	162

### **6B. Modification of cellulose paper with CuSnB by electroless deposition for the selective and sensitive detection of dopamine**

6B-1 Introduction	166
6B-2 Electrode fabrication	169
6B-2.1 Fabrication of VC-CP	169
6B-2.2 Fabrication of CuSnB/VC-CP	169
6B-3 Results and discussion	169
6B-3.1 Physical characterization	169
6B-3.2 Electrochemical studies towards dopamine sensing	172

6B-4 Summary	179
6B-5 References	179
<b>Chapter 7. Summary and future perspective</b>	<b>181</b>
7-1 Summary	181
7-2 Future perspective	188
<b>Curriculum vitae</b>	<b>189</b>



# Chapter 1

## Introduction

### 1-1 Global energy resources

Energy is important for socio-economic growth as well as improved lifestyle.<sup>1</sup> It can be found in various forms *viz.* mechanical, chemical, electrical, thermal, gravitational, radiant, nuclear, sound etc. The available energy resources on the earth comprise of fossil fuel (coal, natural gas, petroleum etc.) and nuclear energy source (uranium, thorium, etc.) which are considered finite sources whereas alternative energies such as hydropower, solar, wind, geothermal, biomass etc. are renewable sources of energy. The availability of renewable energy around the globe per year is found to be in high excess in comparison to the total reserve of finite energy (Figure 1-1).<sup>2</sup> All these types of energy can be converted, amplified and stored according to the need of particular applications.<sup>3</sup>

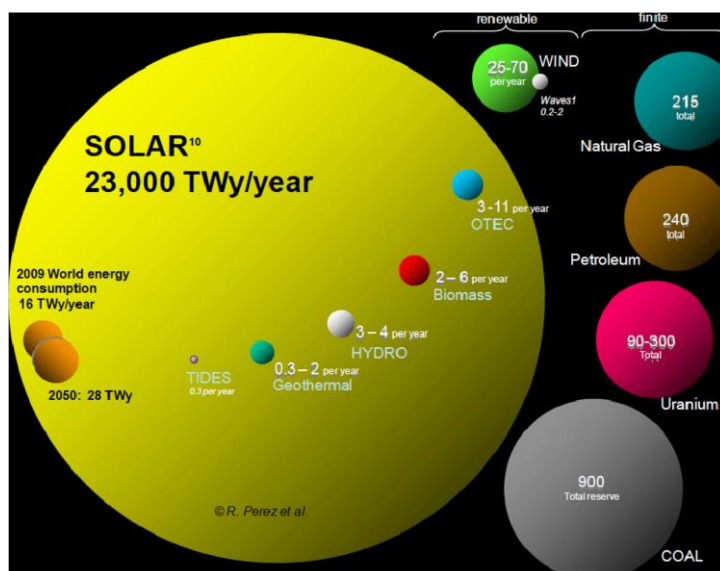


**Figure 1-1.** Comparison of finite and renewable planetary energy reserves measured in TW/year.<sup>2</sup>

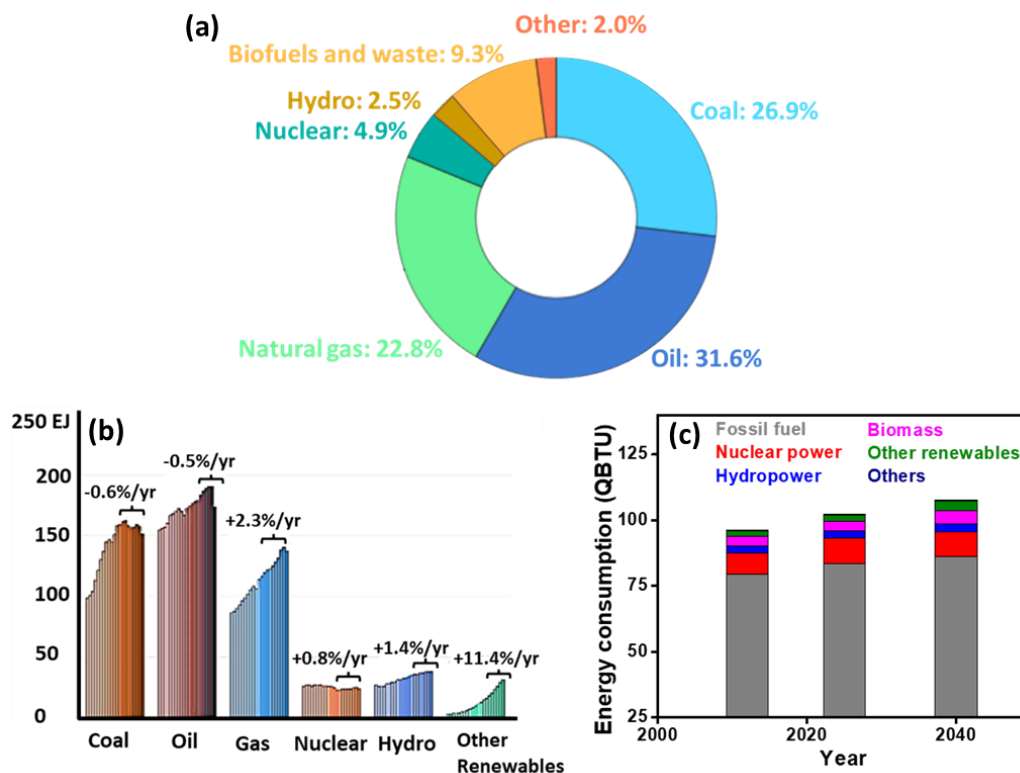


**Figure 1-2.** (a) Energy extraction pattern from different sources,<sup>4</sup> (b) energy consumption trend from 2015 to 2020<sup>5</sup> and (c) projection of energy consumption up to 2040.<sup>3</sup>

## 1-2 Energy extraction practices and their impacts

Although the planetary energy reserve contains more than ten times renewable energy than the finite source of energy but around 85% of current global energy production relies on finite sources of energy where the contribution of fossil fuel alone is around 80% [Figure 1-2(a-b)].<sup>4,5</sup> Furthermore, the global energy demand and resource consumption rate is projected to increase continuously over the coming several decades (Figure 1-2c).<sup>3</sup> This continuously increasing energy consumption trend with extreme dependency on fossil fuel is not only depleting their reserves but also resulting in air pollution which ultimately leads to severe environmental issues such as global warming, climate change, deforestation, water pollution etc. [Figure 1-3(a-c)]. According to recent reports, it has been projected that the global energy demand will increase by 30% and the CO<sub>2</sub> emission rate will

be  $35.7 \text{ Gt year}^{-1}$  in 2040.<sup>6</sup> In this scenario, India is the third largest  $\text{CO}_2$  emitter after China and the USA which produced 2.88 Gt of  $\text{CO}_2$  in 2021.<sup>7</sup> Besides environmental impacts, the polluted air may also affect the functioning of vital human organs such lungs, heart, brain, liver, stomach etc. leading to various fatal disorders and diseases (Figure 1-3d). Despite this, the increasing energy consumption rate is directly related to global economic growth and is a prime challenge to sustainability as well as a clean environment. Therefore, it is necessary to promote green energy production from clean and renewable sources to maintain the planet healthy and fit for living beings.

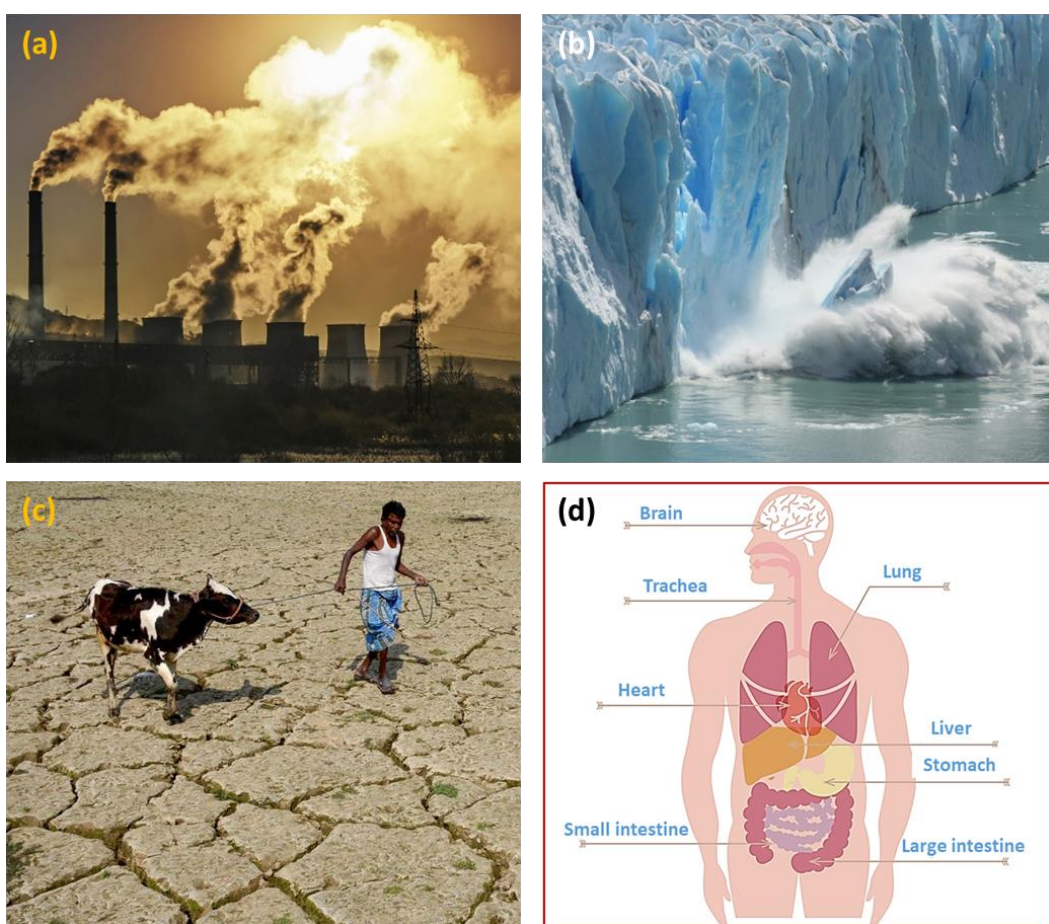


**Figure 1-3.** (a) Air pollution caused by fossil fuel<sup>8</sup> and their effect on (b) global warming,<sup>9</sup> (c) climate change<sup>10</sup> and (d) human health.<sup>11</sup>

### 1-3 Renewable sources of energy and their limitations

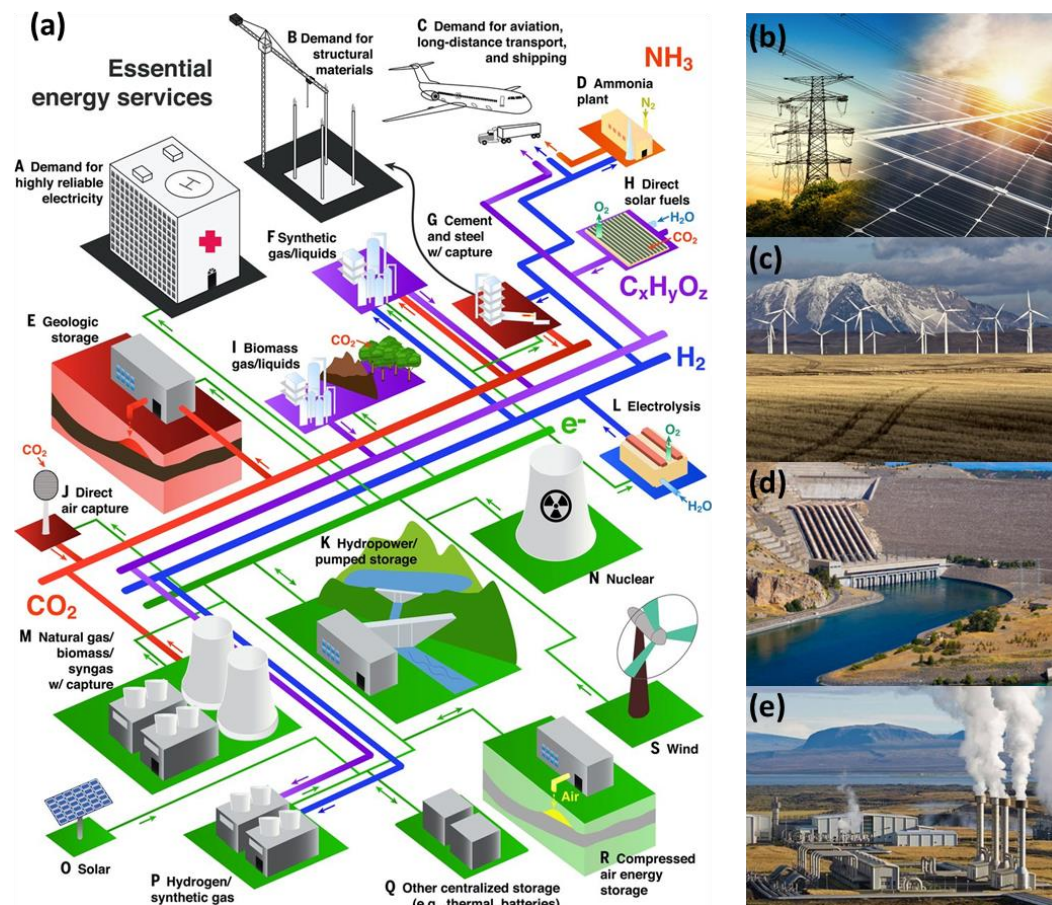


**Figure 1-4.** (a) Schematic representation of net zero emission mission<sup>16</sup> and renewable sources of energy (b) solar power,<sup>17</sup> (c) wind power,<sup>18</sup> (d) hydropower<sup>19</sup> and (e) geothermal power.<sup>20</sup>

In order to mitigate environmental impacts caused by current energy extraction practices, energy experts are extensively working on the challenges and opportunities for carbon emission-free energy systems to provide insight towards possible transformations of the energy-economy-land system.<sup>12</sup> For this, a net zero emission energy mission has been proposed (Figure 1-4a) but the consumption of finite energy resources in many processes may be an issue towards sustainability. Therefore, it is essential to harvest energy from renewable sources. Among the various renewable energy resources, solar power, hydropower, wind power and geothermal power are common [Figures 1-4(b-d)] but these renewables also have some major challenges. Firstly, there are location-constraints which need an

additional grid to supply the extracted energy.<sup>13</sup> Secondly, most of these are dependent on meteorological conditions due to which their output are intermittent in nature.<sup>14, 15</sup> Moreover, all these systems rely on continuous electricity generation which cannot be stored in current form for later use. either conversion of this electricity into some other value-added product or storing in some energy storage devices can be good options for maximum utilization of produced energy. Amongst various conversion options, hydrogen (H<sub>2</sub>) production through water electrolysis can be an attractive choice as H<sub>2</sub> is a carbon-free energy carrier. Similarly, the Zn-O<sub>2</sub> battery can be a potential energy storage device as it can be run with air feedstock.

#### **1-4 Hydrogen as a value-added product**

The development of the global economy has been largely dependent on carbon-rich fossil fuels. These fossil fuels are obtained from the conversion and storing of solar energy into chemical energy by living organisms over millions of years which is liberated back to energy during oxidation leaving CO<sub>2</sub> as the by-product.<sup>21, 22</sup> In this context, the earth does not have such hydrogen reserves but the available renewable energy resources such as solar, wind, hydropower, and geothermal can be utilized to generate H<sub>2</sub> or hydrogen-rich materials from which energy can be extracted by oxidation.<sup>22, 23</sup> Besides being a carbon-free energy carrier, it also has unique features such as (i) the most abundant element in the universe, (ii) the lightest element (molecular weight = 2.016) with highest known energy content (gravimetric energy density = 142 MJ Kg<sup>-1</sup>), (iii) non-toxic nature, (iv) environment friendly (water as oxidation product during energy conversion reactions) and (v) easy e recyclability .<sup>8, 26-29</sup> Additionally, H<sub>2</sub> is a prime feeding gas for various important products like ammonia, urea, methanol etc. (Figure 1-5a). But around 96% of global hydrogen has been extracted from fossil fuels mainly from hydrocarbon reforming and pyrolysis.<sup>30</sup> These hydrogens are classified into black, grey, blue and green hydrogen according to their contribution to carbon emission in the atmosphere (Figure 1-5b).<sup>25</sup> The black hydrogen is produced by direct coal



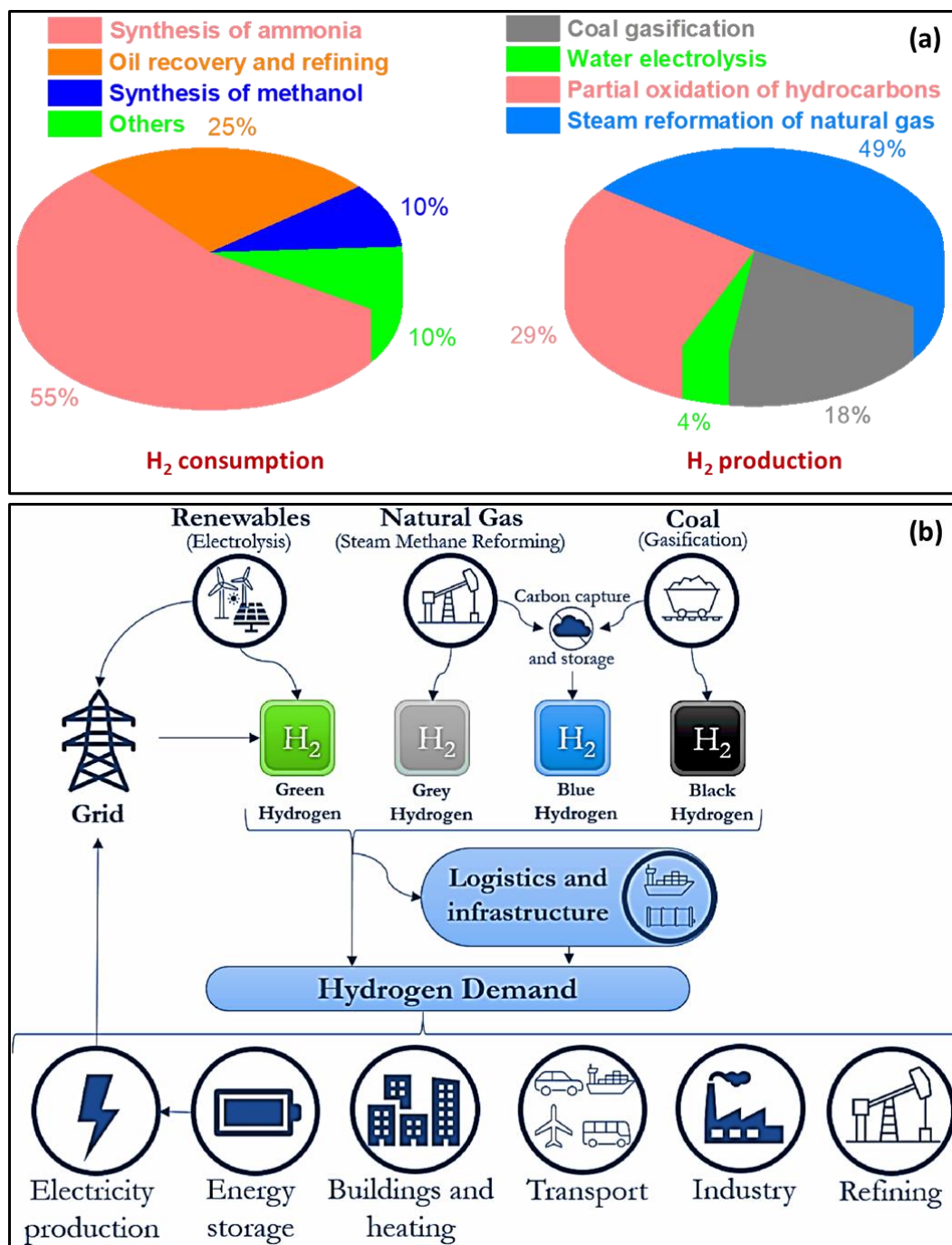


**Figure 1-5.** (a) Global hydrogen consumption and production pattern<sup>24</sup> and (b) schematic representation of the hydrogen economy.<sup>25</sup>

gasification whereas grey and blue hydrogen are obtained from natural gas steam methane reforming process without and with CO<sub>2</sub> capture respectively.<sup>31</sup> Similarly,

green hydrogen is produced via electrolysis by using renewable energy sources.<sup>31</sup> Moreover, about 1% of global energy consumption is involved in  $H_2$  production alone. Therefore, green hydrogen production through water electrolysis can be a good option for energy conversion to achieve value-added products.

## 1-5 Water electrolysis

In order to produce green hydrogen, the use of alternative approaches such as thermocatalytic, photocatalytic and electrocatalytic processes are appealing.<sup>32</sup> Among these, water electrolysis by using renewable energy sources is one of the promising approaches for the production of environment-friendly pure hydrogen at ambient conditions of temperature and pressure, uplifting the efficiency of the sustainable energy system.<sup>31</sup> Water electrolysis is the process of generation of  $H_2$  and  $O_2$  gas with the aid of electricity. When an electric current is passed through

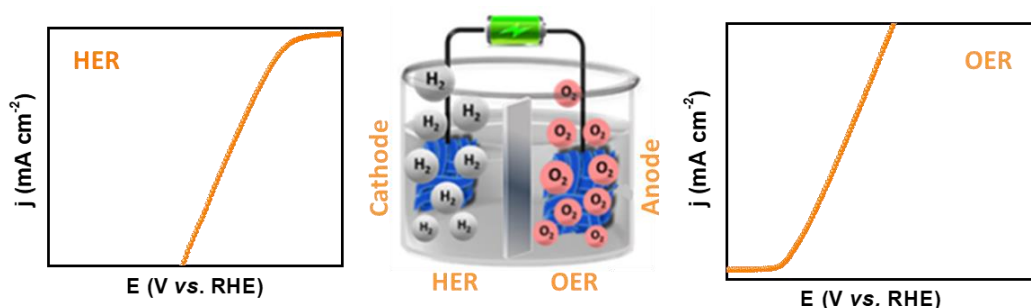


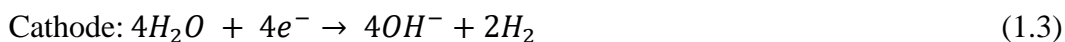
**Figure 1-6.** Representation of hydrogen evolution reaction and oxygen evolution reaction during electrocatalytic water splitting.

the electrodes into the water containing a suitable electrolyte, the water molecules get split into hydrogen and oxygen gases (Figure 1-6).<sup>33, 34</sup> The core of this technology involves two half-cell reactions shown in equations 1.1-1.4. At the cathode, the hydrogen evolution reaction (HER) takes place with an equilibrium potential of 0 V vs. RHE and at anode the oxygen evolution reaction (OER) occurs with an equilibrium potential of 1.23 V accompanied by a free energy change ( $\Delta G$ ) of  $237.2 \text{ kJ mol}^{-1}$ .<sup>35, 36</sup>

### Acidic media



### Alkaline media



### Overall reaction



Principally, HER involves two-electron transfer per mole of  $H_2$  formation whereas OER involves four-electron transfer for 1 mole of  $O_2$  formation which is responsible for its sluggish kinetics inducing large energy barriers and therefore, generally a large voltage ( $\sim 1.8$ - $2.0$  V) is required for the operation of a water electrolyser. At present, commercial/industrial water electrolysers employ Pt-based nanomaterials as state-of-art electrocatalysts for HER and Ru/Ir-based electrocatalysts as the benchmark for OER due to their high intrinsic activity and durability. But their scarcity and high cost hamper the large-scale development of these electrocatalysts. Therefore, there is a desperate need to look for alternate electrocatalysts whose production/fabrication statisfies the conditions such as cost-effectiveness, easyscalablility along with outstanding electrochemical activity towards HER and OER. Having said that, the current study is based on the designing of cost-effective non-noble metal-based electrocatalysts for this application.

## 1-6 Ammonia as a value-added product

Nitrogen is considered to be an essential primary plant nutrient whose unavailability or deficiency causes either the death of the plant or poor growth.



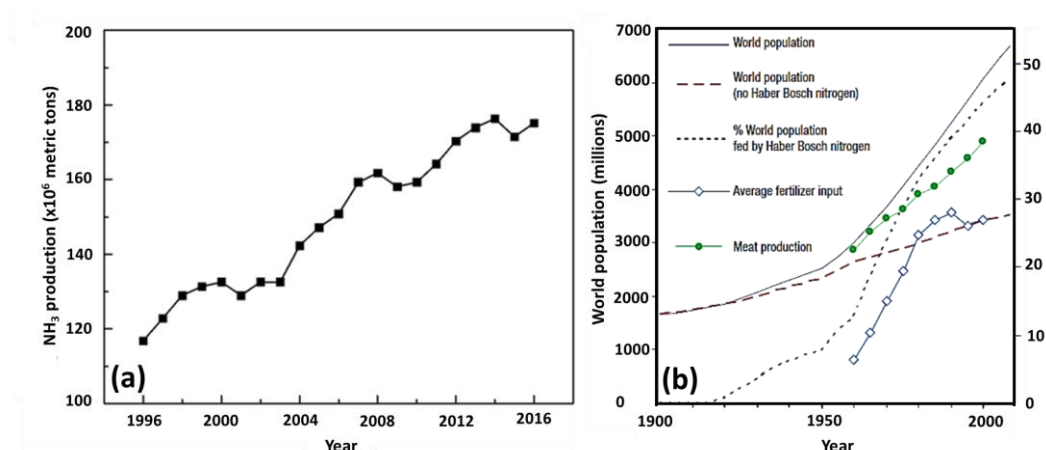


**Figure 1-7.** (a) Global ammonia production trend<sup>37</sup> and (b) comparison of human population and nitrogen utilization throughout the 20<sup>th</sup> century [second y-axis represents % world population, average fertilizer input ( $\text{Kg N ha}^{-1} \text{ yr}^{-1}$ ) and meat production ( $\text{Kg person}^{-1} \text{ yr}^{-1}$ )].<sup>38</sup>

<sup>39, 40</sup> Therefore, nitrogen-rich soil is mandatory for high agricultural productivity. The natural nitrogen fixation process makes soil nitrogen rich but it depletes very quickly with each harvest resulting in low crop yield so replenishment of nitrogen into the soil is necessary for high crop yield. Although a large amount of nitrogen exists in its gaseous form ( $\text{N}_2$ ) in the atmosphere (approximately 78% by volume) nevertheless its chemically inert nature made it inappropriate for consumption by most of the flora.<sup>41</sup> Ammonia has been widely used for fertilizer production and ammonia production is mostly dependent on the Haber-Bosch process. The global ammonia production rate is increasing annually and it has been found that 58 million metric tons more ammonia were produced globally in 2016 in comparison to that in 1996 (Figure 1-7a).<sup>37</sup> Also, the increasing food demand due to the rapidly increasing population has been fulfilled by industrial ammonia synthesis (Figure 1-7b).<sup>38</sup> Besides fertilizer production ammonia has been also widely explored as fuel, antimicrobial agent, refrigerant, chemical precursor, cleansing agent and fermentation agent as well (Figure 1-8).<sup>42, 43</sup> However, this Haber-Bosch process requires harsh conditions i.e., high temperature ( $400\text{--}500^\circ\text{C}$ ) and pressure (10-30 MPa) for the ammonia production. Furthermore, this process results in the

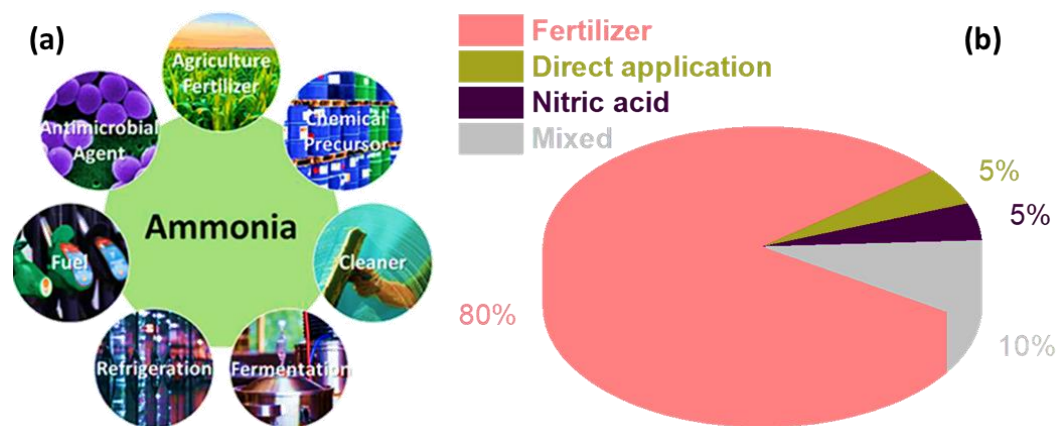


**Figure 1-8.** (a) Uses of ammonia for various practical applications<sup>42</sup> and (b) application of ammonia as a chemical precursor for different chemical productions.<sup>43</sup>

consumption of 1-2% of global energy consumption including half of the global hydrogen production. Additionally, this process alone is responsible for 1% of global energy-related CO<sub>2</sub> emissions.<sup>44-46</sup> Therefore, the development of high-performance, cost-effective and eco-friendly ammonia synthesis technology is very urgent not only for fertilizer production but also for advanced energy systems. Although, the replacement of a traditional steam reforming unit with electrochemical water splitting unit in the modern Haber-Bosch technology has been explored for green ammonia production, the direct ammonia synthesis via direct electrocatalytic dinitrogen reduction under ambient conditions with the use of water as a hydrogen source and renewable energy as a power source can be an optimal strategy (Figure 1-9).<sup>46, 47</sup> The electrochemical dinitrogen reduction to ammonia involves the transfer of six electrons and six protons. The half-cell reactions during nitrogen reduction occurs in acidic and alkaline media according to the equations 1.6 and 1.7 respectively:



A detailed discussion on ammonia synthesis via electrocatalytic dinitrogen reduction is given in Chapter 5.

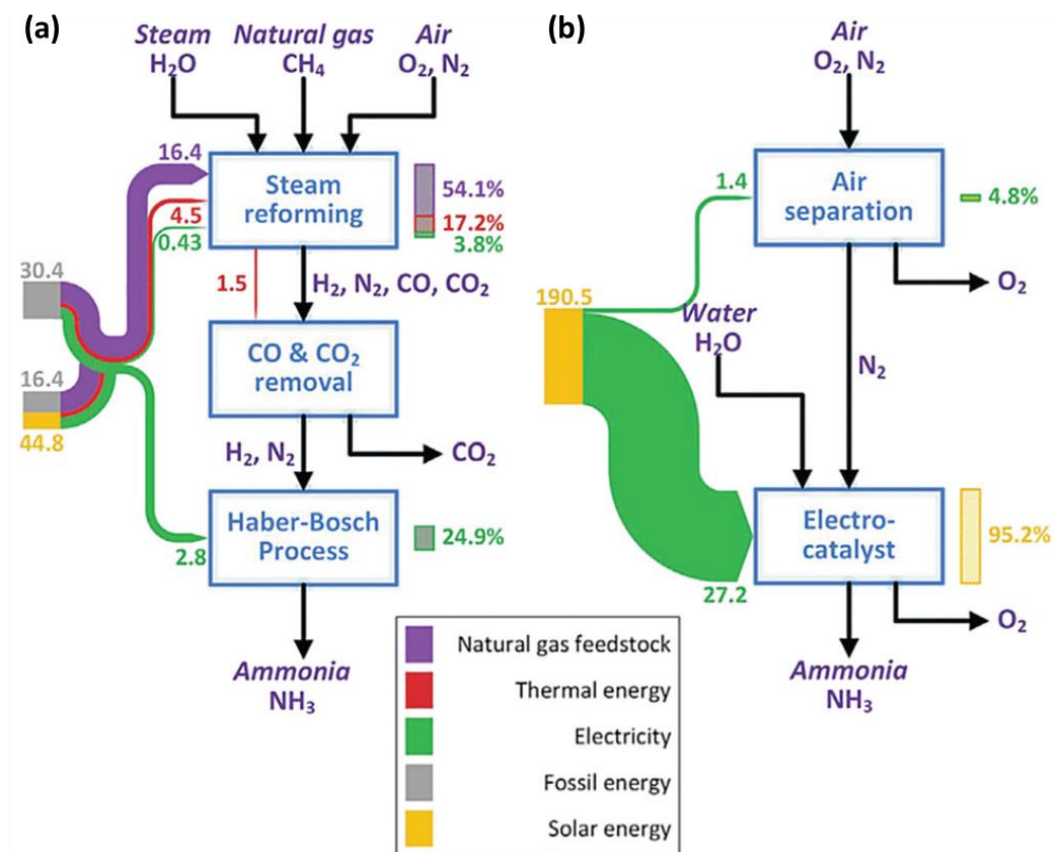


**Figure 1-9.** Comparison of energy efficiency for various ammonia synthesis strategies. (a) Conventional Haber–Bosch strategy and (b) electrocatalytic strategy.<sup>46</sup>

### 1-7 Zn- $\text{O}_2$ battery as an energy storage device

After the industrial revolution, energy consumption has increased tremendously. According to recent reports, energy demand is estimated to increase by 30 % at the end of the year 2040.<sup>6</sup> However, this demand doesn't remain constant throughout the day, therefore when the excess electrical energy over the demands is produced, it must be stored efficiently in energy storage devices. Energy storage devices can aid in managing issues brought on by intermittent renewable energy sources like wind and solar energy, reducing power supply imbalances, encouraging dispersed generation, and reducing grid congestion.<sup>48</sup> This energy can be stored in various modes and forms including mechanical, thermal, chemical, thermochemical,

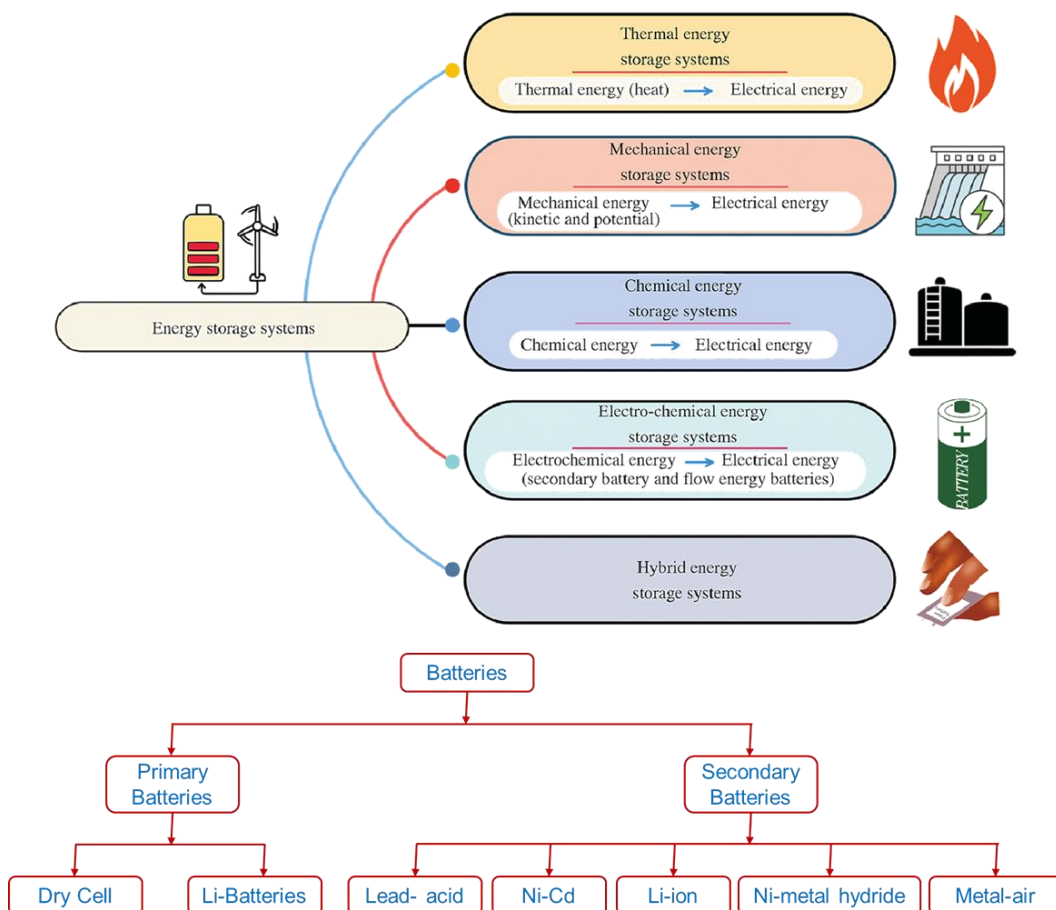


**Figure 1-10.** Classification of major energy storage systems.<sup>49</sup>

electrical and electrochemical (Figure 1-10). Among them, electrochemical energy storage devices show great potential in form of batteries, capacitors and supercapacitors. In this aspect, Li-ion batteries became the first rechargeable electrochemical devices to be commercialised and dominate the battery market. Recently, the development of electric vehicles has set the beginning of a new era. Although they show high energy densities, but limited Li resources, their cost and safety risks due to the use of flammable organic electrolytes cause them to be thermally less stable.<sup>50</sup> Moreover, the mining and extraction of transition metals used as electrode materials is a challenge. This has encouraged researchers to move towards the development of other battery systems which can deliver more specific capacity and energy density along with their cost-effective fabrication.

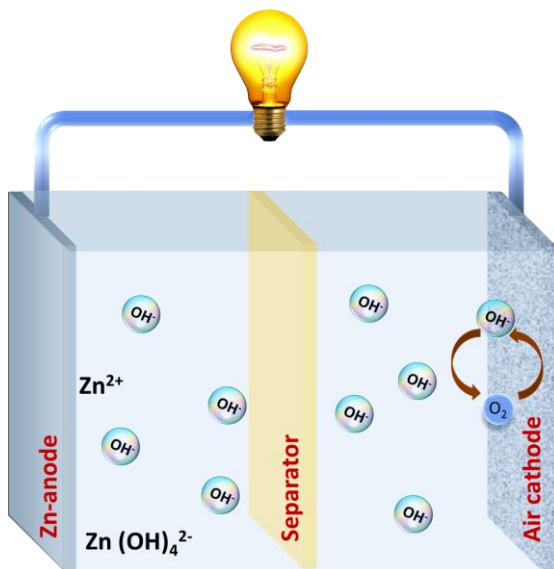


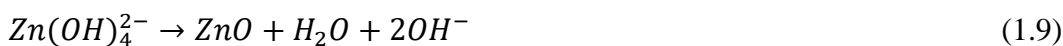
**Figure 1-11.** Schematic representation of a Zn-air battery displaying its components.

Alternatively, aqueous Zn-air batteries have shown potential due to their large theoretical energy density ( $1218 \text{ Wh kg}^{-1}$ ), low cost and safety features.<sup>51, 52</sup>

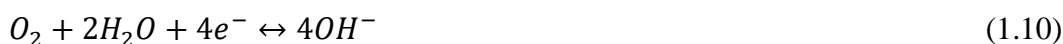
A Zn-air battery consists of a Zn-metal anode separated with a membrane separator from a porous cathode and immersed in a concentrated alkaline electrolyte (generally, 6 M KOH + 0.2 M Zn(Ac)<sub>2</sub>) (Figure 1-11). The Zn-metal anode can be in the form of fibres, nanoparticles, metal foams or plates and must show characteristics *viz.* low equivalent weight, high abundance, low cost and stability in aqueous alkaline media. The membrane separator must be chosen such that it shows low ionic resistance and high adsorption capacity for the electrolyte. Therefore, Celgard 5550 separators are generally used for this purpose. Further, the porous cathode contains a gas diffusion layer (GDL) for the oxygen to diffuse to the catalyst layer from the environment, the current collector (Ni foam/Cu foam/carbon paper) and the catalyst layer. The GDL consist of a carbon material (Vulcan carbon XC-72, Ketjen black etc.) and a non-conducting binder (PVDF, PTFE etc.) coated onto the current collector.. The mechanism of Zn-air battery during discharge involves oxidation of Zn metal to zincate ions ( $\text{Zn(OH)}_4^{2-}$ ) at the anode while oxygen reduction reaction (ORR) takes place at the cathode. The respective

electrode reactions get reversed during the charging of the battery. The individual reaction steps are believed to proceed as:<sup>51</sup>

**Anodic reactions:**



**Cathodic reactions:**



**Overall reaction:**



A detailed discussion on the mechanism of Zn-air batteries, their fabrication and applications in electrocatalytic activities is given in Chapter 2.

## 1-8 Electrode architecture for energy conversion and storage device

As it is well known that the electrode is an integral part electrochemical devices, the electrode morphology and its architecture play a crucial role in catalytic activity and overall device performance. The basic components of the electrode include an electrocatalyst and a current collector. In general, the existing commercial electrolyser assembly contains a rigid electrode coated with electrocatalyst ink (Figure 1-12) which is suffers from several problems. Firstly, the conventional electrode fabrication practice involves the use of an insulating binder during the catalyst ink preparation. Although the binder provides physical adhesion, it may limit the ion transport and hinder the release of bubbles resulting in catalyst peeling from the electrode surface and ultimately leading to compromised electrochemical performance.<sup>54-56</sup> Secondly, in the metal/carbon or any other conductive substrate-based current collector, large mass densities of electrochemically inactive materials is not only an issue for the atom economy but also a challenge for the development of lightweight devices.<sup>57, 58</sup> Similarly, surface passivation of the current collector

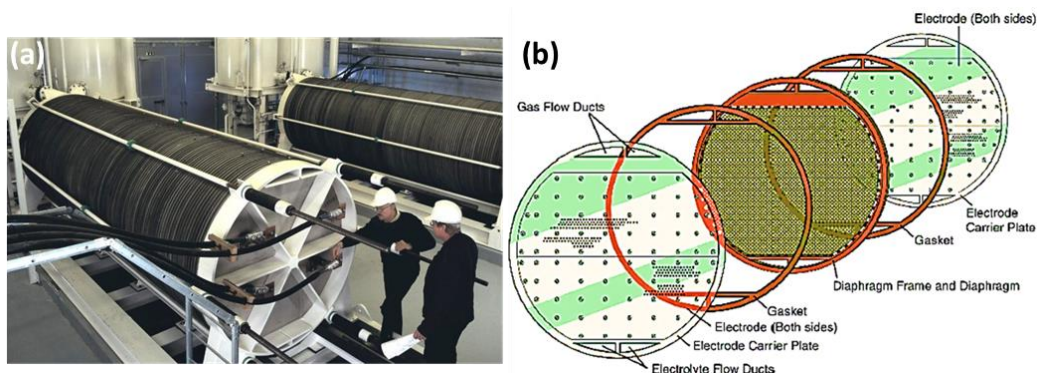


**Figure 1-12.** (a) Electrolyser plant and (b) electrode assembly of the water electrolyser for commercial production of hydrogen.<sup>53</sup>

due to oxidation of metallic substrate limits the activity and the single side catalyst loaded electrode limits its actual output as well.<sup>59</sup> Furthermore, the waste management of obsolete end-of-life product is also of environmental concern. Additionally, customizable electrochemical energy storage device is a need of the hour for the development of next-generation portable, foldable, wearable and bio-integrated electronics (Figure1-13).<sup>60</sup> Therefore, a three-dimensional lightweight

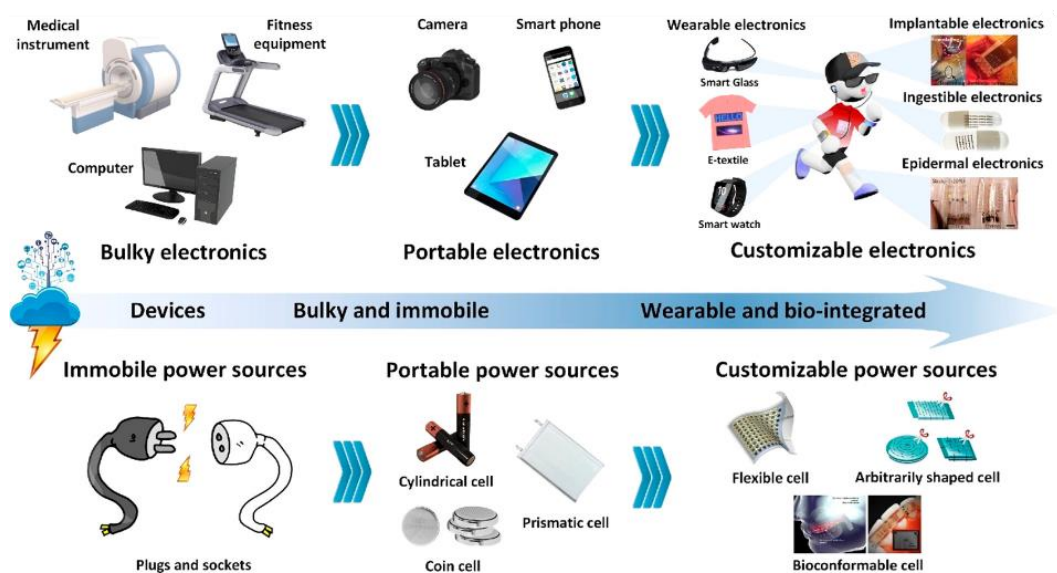


**Figure 1-13.** Progression of the customizable electronics with customizable electrochemical energy storage devices.<sup>60</sup>

electrode coated with binder-free active catalyst material can be a good strategy for the development of a highly efficient lightweight eco-friendly electrode. Regarding



this, electrode materials having extensive availability, lightweight, low cost, eco-friendly nature and mechanical flexibility can be beneficial to overcome the mentioned problems.<sup>61</sup> Interestingly, the three-dimensional flexible electrodes having good mechanical flexibility and electrocatalytic activity under various deformation conditions have fascinating applications as they can be applied as bendable and foldable electrodes as well as adjustable to various reactors without loss of active materials.<sup>62</sup> In this context, carbon cloth and cellulose paper can be better options for flexible energy storage and conversion applications, because of their improved mechanical strength, low cost and favourable fabrication procedure etc.<sup>63</sup> over the other conventional existing substrates (*e.g.*, metal foil/foam/wire, carbon paper etc.<sup>63-75</sup>) which involve high fabrication cost, structural fragility and loss of active catalyst during deformation.<sup>76, 77</sup> And so, we have fabricated and explored the flexible, binder free, self standing three dimensional electrodes based on carbon cloth and cellulose paper in the thesis.

### 1-9 Health impacts

Air pollution causes major health impacts by affecting our respiratory, cardiovascular and reproductive systems and is now also being considered as a risk factor for neurological diseases.<sup>78</sup> Among these, Parkinson's disease is the second-most prevailing neurodegenerative disease worldwide which is caused by the loss of nerve cells responsible for the production of dopamine.<sup>79</sup> Epidemiological studies have been reported considering the effect of long-term exposure to air pollution on neurological damage and resulting changes in dopamine levels (Figure 1-14). Dopamine is an important neurotransmitter which is responsible for the working of the cardiovascular, neurological and hormonal systems. Therefore, there is a need to develop biosensors which can detect dopamine for their rapid, efficient and accurate detection in the human body.<sup>80, 81</sup>

A biosensor is typically consisting of a bio-element, transducer, amplifier, processor, and computer software to demonstrate the results (Figure 1-15).<sup>82</sup> A bio-element or bio-molecule has the affinity to bind to the analyte (a molecule which



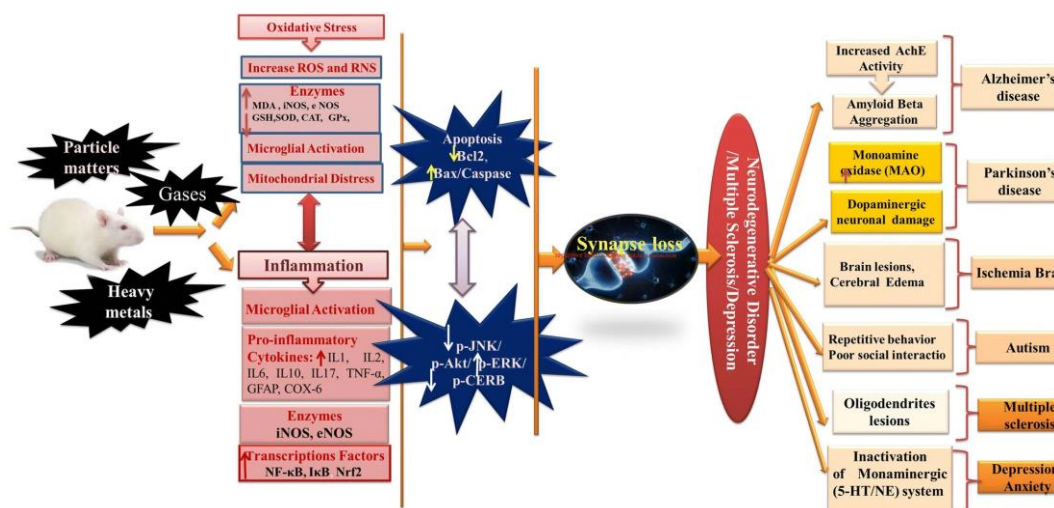


**Figure 1-14.** Summary of the neurotoxic effects resulted by the exposure to air pollutants.<sup>78</sup>

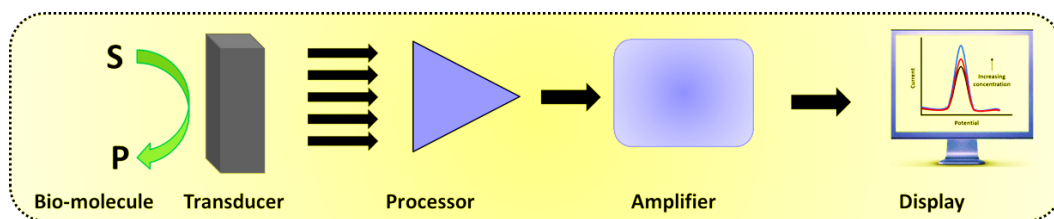
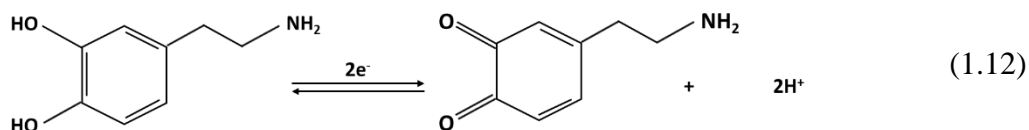


**Figure 1-15.** Schematic representation of components of a biosensor.

needs to be sensed). A signal is produced from the specific bonding/conversion of a substrate to a product and this signal is determined by the transducer. It is then amplified by a detector and then processed by software to display the output signal on the screen. For biosensing applications, the catalyst must be designed to be specific, sensitive and stable under biological conditions. The fabricated biosensor must be compact, portable, flexible and cost-effective.<sup>83</sup> Moreover, it must be free from transducer-induced noise and the analysis must be free of enzymes to reduce the pre-treatment time and cost. At present, various analytical techniques such as colorimetry, fluorimetry, high-performance liquid chromatography, and chemiluminescence are being used for sensing biomolecules. Nevertheless, their limited selectivity, sophisticated instruments and requirement of skilled operators are major drawbacks making it difficult to miniaturize the biosensors for portable applications. Alternatively, because of the electroactive nature of dopamine, its

electrooxidation is more viable (equation 1.10) consequently, the electrochemical technique for dopamine detection has gained tremendous attention.<sup>84</sup> In this aspect, electrochemical biosensors provide a better approach with rapid (faster response time) analysis, low detection limits (LOD), specificity, selectivity and wider



detection ranges. Therefore, for practical applications, electrochemical biosensors based on flexible, small size and highly active electrocatalysts are need of hour.<sup>85</sup>  
<sup>86</sup> Chapter 6 describes the mechanism involved in the biosensing of an important biological molecule, dopamine, the fabrication of electrodes and their activity for this application.

## 1-10 Goals

By considering the aforementioned importance, this thesis has focused to develop some eco-friendly three-dimensional flexible electrodes to address the demand of highly efficient reactor-friendly electrodes as well as customizable electronics with customizable energy storage devices. The highlights of this thesis include the designing of three-dimensional flexible bi- or tri-functional electrodes towards HER, ORR, OER and NRR as well as biosensing applications. In comparison to commercial state of art electrocatalysts (i.e., RuO<sub>2</sub> and IrO<sub>2</sub> for OER and 20% Pt/C for HER and ORR, the explored electrodes incorporating highly abundant transition metal-based (Ni, Fe) materials are found to be eco-friendly and cost-effective. The main target was to exploit a cost-effective approach for the development of the eco-friendly three-dimensional flexible electrode to achieve the desired activity.

Initially, Ni and Fe sulphide and phosphides coated carbon cloth electrodes were explored as promising bifunctional electrocatalysts towards overall water splitting. Because of their high flexibility, low cost, corrosion resistance properties and good biocompatibility as compared to metal foams or foils carbon fiber-based substrates are of great research interest for various applications. Herein, the electroless

deposition approach was explored for growing NiFeS and NiFeP over the highly flexible carbon cloth substrate. Therefore, the development of carbon cloth (CC) based flexible electrodes with the decoration of non-noble metal based electrocatalyst by just a simple activation-free electroless deposition method (eliminated the use of expensive PdCl<sub>2</sub> and SnCl<sub>2</sub> based activators/sensitizers) added up an initiation to develop a straightforward method towards flexible electrode fabrication. The fabricated electrode was used directly as a flexible electrode which demonstrated good bifunctional activity towards electrochemical water splitting in alkaline media and also showed good flexibility and electrochemical performance under various mechanical deformations (bending, twisting, folding etc.). Furthermore, this thesis attempted to address the problem associated with the shortage of freshwater for wide exploration of water electrolyzers by developing electrode material with good activity and high resistivity towards chloride ion corrosion for sustainable seawater splitting. Herein, a binder-free three-dimensional carbon cloth flexible electrode incorporated with active electrocatalyst NiFeB over oxygen-functionalized carbon cloth was explored for sustainable seawater splitting which demonstrated a remarkable performance towards OER, HER and overall water splitting in 1 M KOH as well as in 1 M KOH + 0.5 M NaCl electrolyte system with excellent stability.

Besides the carbon cloth-based flexible electrodes, our research was focused towards the development of biodegradable substrate-based (cellulose paper-based) three-dimensional electrodes. The biggest hurdle of the absence of a conductive pathway for the electric circuit in the insulating cellulose paper was addressed by the surface modification of cellulose paper with conductive metal composites via a cost-effective and straightforward electroless deposition approach and was employed as an eco-friendly substrate for flexible electrode development. Firstly, NiP/NiB-CP electrode was developed via two-step electroless deposition followed by an electrodeposition approach. This NiP/NiB-CP electrode possesses excellent bifunctional activity and long-term durability towards overall water splitting in both alkaline pure water and seawater electrolytes.

In addition to energy demand, this thesis also attempted to address the problem associated with the green synthesis of important chemicals of high demand such as  $\text{NH}_3$  via the electrochemical route by the development of trifunctional (NRR/ORR/OER) electrode  $\text{Fe}_3\text{O}_4/\text{NiB-CP}$  for the integrated  $\text{Zn-O}_2$  battery powered ammonia synthesis. The fabricated electrode demonstrated promising NRR as well as oxygen bifunctional activities along with long-term stability. Moreover, the integrated  $\text{Zn-O}_2$  battery-powered electrochemical nitrogen reduction resulted in promising activity for ammonia synthesis. This approach may act as a milestone in the development of cost-effective and eco-friendly flexible electrodes towards electrochemical energy conversion and storage applications.

Thereafter, the same strategy was employed to develop eco-friendly cellulose paper-based self-standing three-dimensional flexible electrodes exhibiting trifunctional activity towards ORR, OER and HER for self-powered water splitting. Herein,  $\text{NiFeP}/\text{NiB-CP}$  electrode was explored for the integrated  $\text{Zn-O}_2$  battery-powered electrochemical water splitting. The  $\text{NiFeP}/\text{NiB-CP}$  electrode demonstrated good trifunctional activity towards ORR, OER and HER. A  $\text{Zn-O}_2$  battery established with the designed electrode was able to power an alkaline water electrolyser to perform overall electrochemical water splitting.

Besides these, the consumption of fossil fuels also causes environmental pollution which may result in serious health issues. Polluted air may affect different body systems which can result in various hormonal imbalances, for instance, dopamine which is a major neurotransmitter has been reported to fluctuate with exposure to non-healthy living conditions. Therefore, the identification of dopamine levels is important for clinical diagnosis and treatment purposes. In order to address this problem, cellulose paper-based three-dimensional flexible electrodes ( $\text{NiFeB/VC-CP}$  and  $\text{CuSnB/VC-CP}$ ) were explored and directly employed as a three-dimensional flexible electrode towards electrochemical dopamine sensing without any additional step for preparing the sensor probe. As prepared electrodes

demonstrated good sensitivity along with a wide detection range even in the presence of a high concentration of ascorbic acid, glucose and uric acid interferents.

## 1-11 References

1. S. Bilgen, S. Keleş, A. Kaygusuz, A. Sarı and K. Kaygusuz, *Renew. Sustain. Energy Rev.*, 2008, **12**, 372-396.
2. O. Inganäs and V. Sundström, *Ambio*, 2016, **45**, 15-23.
3. S. Bilgen, *Renew. Sustain. Energy Rev.*, 2014, **38**, 890-902.
4. <https://www.iea.org/search?q=source%20of%20global%20energy>
5. R. Jackson, P. Friedlingstein, C. Le Quéré, S. Abernethy, R. Andrew, J. Canadell, P. Ciais, S. Davis, Z. Deng and Z. Liu, *Environ. Res. Lett.*, 2022, **17**, 031001.
6. G. Zhao, K. Rui, S. X. Dou and W. Sun, *Adv. Funct. Mater.*, 2018, **28**, 1803291.
7. B. Ozcan and R. Ulucak, *Nucl. Eng. Technol.*, 2021, **53**, 2056-2065.
8. <https://www.shutterstock.com/g/tatisol>
9. <https://www.newsecuritybeat.org/2021/02/tip-iceberg-polar-ice-loss-effects-planet/>
10. <https://www.dw.com/en/india-ipcc>
11. <https://lcf.org.in>
12. J. DeAngelo, I. Azevedo, J. Bistline, L. Clarke, G. Luderer, E. Byers and S. J. Davis, *Nat. Commun.*, 2021, **12**, 6096.
13. D. B. Richardson, *Renew. Sustain. Energy Rev.*, 2013, **19**, 247-254.
14. S. R. Sinsel, R. L. Riemke and V. H. Hoffmann, *Renew. Energy*, 2020, **145**, 2271-2285.
15. E. Pean, M. Pirouti and M. Qadrdan, *Renew. Energy*, 2016, **99**, 307-314.
16. S. J. Davis, N. S. Lewis, M. Shaner, S. Aggarwal, D. Arent, I. L. Azevedo, S. M. Benson, T. Bradley, J. Brouwer and Y.-M. Chiang, *Science*, 2018, **360**, eaas9793.
17. <https://www.buskowitz.com/electricity-vs-solar-energy/>
18. <https://www.thecanadianencyclopedia.ca/en/article/wind-energy>
19. <https://stock.adobe.com/search?k=penstock>
20. <https://indiaenergyportal.org/geothermal-energy/>
21. S. Dunn, *Int. J. Hydrog. Energy*, 2002, **27**, 235-264.
22. A. Sartbaeva, V. Kuznetsov, S. Wells and P. Edwards, *Energy Environ. Sci.*, 2008, **1**, 79-85.
23. R. Masel, *Nature*, 2006, **442**, 521-522.
24. G. Sdanghi, G. Maranzana, A. Celzard and V. Fierro, *Energies*, 2020, **13**, 3145.
25. K. Dillman and J. Heinonen, *Renew. Sustain. Energy Rev.*, 2022, **167**, 112648.
26. A. Midilli, M. Ay, I. Dincer and M. A. Rosen, *Renew. Sustain. Energy Rev.*, 2005, **9**, 255-271.
27. W. Ma, D. Li, L. Liao, H. Zhou, F. Zhang, X. Zhou, Y. Mo and F. Yu, *Small*, 2023, 2207082.
28. J. O. Abe, A. Popoola, E. Ajenifuja and O. M. Popoola, *Int. J. Hydrog. Energy*, 2019, **44**, 15072-15086.
29. K. Mazloomi and C. Gomes, *Renew. Sustain. Energy Rev.*, 2012, **16**, 3024-3033.
30. P. Nikolaidis and A. Poullikkas, *Renew. Sustain. Energy Rev.*, 2017, **67**, 597-611.
31. A. Ajanovic, M. Sayer and R. Haas, *Int. J. Hydrog. Energy*, 2022, **47**, 24136-24154.
32. H. Sun, X. Xu, H. Kim, W. Jung, W. Zhou and Z. Shao, *Energy Environ. Mater.*, 2022, e12441.
33. J. Zhu, L. Hu, P. Zhao, L. Y. S. Lee and K.-Y. Wong, *Chem. Rev.*, 2019, **120**, 851-918.
34. N.-T. Suen, S.-F. Hung, Q. Quan, N. Zhang, Y.-J. Xu and H. M. Chen, *Chem. Soc. Rev.*, 2017, **46**, 337-365.
35. M. Schalenbach, G. Tjarks, M. Carmo, W. Lueke, M. Mueller and D. Stolten, *J. Electrochem. Soc.*, 2016, **163**, F3197.

36. S. Jiao, X. Fu, S. Wang and Y. Zhao, *Energy Environ. Sci.*, 2021, **14**, 1722-1770.
37. K. Salazar and M. McNutt, *Reston*, VA, 2012.
38. J. W. Erisman, M. A. Sutton, J. Galloway, Z. Klimont and W. Winiwarter, *Nat. Geosci.*, 2008, **1**, 636-639.
39. M. Naeem, A. A. Ansari and S. S. Gill, *Essential plant nutrients: uptake, use efficiency, and management*, Springer, 2017.
40. E. A. Kirkby, in *Marschner's Mineral Nutrition of Plants*, Elsevier, 2023, pp. 3-9.
41. G. Qing, R. Ghazfar, S. T. Jackowski, F. Habibzadeh, M. M. Ashtiani, C.-P. Chen, M. R. Smith III and T. W. Hamann, *Chem. Rev.*, 2020, **120**, 5437-5516.
42. D. Zhou, R. Zhou, R. Zhou, B. Liu, T. Zhang, Y. Xian, P. J. Cullen, X. Lu and K. K. Ostrikov, *Chem. Eng. J.*, 2021, **421**, 129544.
43. G. Chehade and I. Dincer, *Fuel*, 2021, **299**, 120845.
44. H. Liu, *Ammonia synthesis catalysts: innovation and practice*, World Scientific, 2013.
45. C. Philibert, *Paris: International Energy Agency*, 2017, **65**.
46. C. Tang and S.-Z. Qiao, *Chem. Soc. Rev.*, 2019, **48**, 3166-3180.
47. L. Wang, M. Xia, H. Wang, K. Huang, C. Qian, C. T. Maravelias and G. A. Ozin, *Joule*, 2018, **2**, 1055-1074.
48. A. Z. Al Shaqsi, K. Sopian and A. Al-Hinai, *Energy Reports*, 2020, **6**, 288-306.
49. J. Mitali, S. Dhinakaran and A. Mohamad, *Energy Storage Saving*, 2022, **1**, 166-216.
50. J. Zhang, Q. Zhou, Y. Tang, L. Zhang and Y. Li, *Chem. Sci.*, 2019, **10**, 8924-8929.
51. Z. Zhao, X. Fan, J. Ding, W. Hu, C. Zhong and J. Lu, *ACS Energy Lett.*, 2019, **4**, 2259-2270.
52. Y. Zhang, Y.-P. Deng, J. Wang, Y. Jiang, G. Cui, L. Shui, A. Yu, X. Wang and Z. Chen, *Energy Storage Mater.*, 2021, **35**, 538-549.
53. <https://www.pv-magazine.com/2018/04/09/hydrogen-dont-give-up/>
54. R. Illathvalappil, P. S. Walko, F. Kanheerampockil, S. K. Bhat, R. N. Devi and S. Kurungot, *Chem. Eur. J.*, 2020, **26**, 7900-7911.
55. P. Wang and B. Wang, *ChemSusChem*, 2020, **13**, 4795-4811.
56. T. Jin, Q. Han and L. Jiao, *Adv. Mater.*, 2020, **32**, 1806304.
57. J. Zhang, L. Dong, C. Xu, J. Hao, F. Kang and J. Li, *J. Mater. Sci.*, 2017, **52**, 5788-5798.
58. L. Dong, C. Xu, Y. Li, Z.-H. Huang, F. Kang, Q.-H. Yang and X. Zhao, *J. Mater. Chem. A*, 2016, **4**, 4659-4685.
59. X. Chen, T. Zhang, M. Kan, D. Song, J. Jia, Y. Zhao and X. Qian, *Environ. Sci. Technol.*, 2020, **54**, 13344-13353.
60. Z. Lv, W. Li, L. Yang, X. J. Loh and X. Chen, *ACS Energy Lett.*, 2019, **4**, 606-614.
61. Z. Wang, Y. H. Lee, S. W. Kim, J. Y. Seo, S. Y. Lee and L. Nyholm, *Adv. Mater.*, 2021, **33**, 2000892.
62. Z. Yang, C. Zhao, Y. Qu, H. Zhou, F. Zhou, J. Wang, Y. Wu and Y. Li, *Adv. Mater.*, 2019, **31**, e1808043.
63. H. M. Shi, G. L. Wen, Y. Nie, G. H. Zhang and H. G. Duan, *Nanoscale*, 2020, **12**, 5261-5285.
64. D. Kong, Y. Gao, Z. Xiao, X. Xu, X. Li and L. Zhi, *Adv. Mater.*, 2019, **31**, e1804973.
65. M. I. Jamesh, Y. Kuang and X. Sun, *ChemCatChem*, 2019, **11**, 1550-1575.
66. G. Li, R. Li and W. Zhou, *Nanomicro Lett*, 2017, **9**, 46.
67. P. L. Zhai, Y. X. Zhang, Y. Z. Wu, J. F. Gao, B. Zhang, S. Y. Cao, Y. T. Zhang, Z. W. Li, L. C. Sun and J. G. Hou, *Nat. Commun.*, 2020, **11**, 1-12.
68. C. Zhao, X. T. Jia, K. W. Shu, C. C. Yu, G. G. Wallace and C. Y. Wang, *J. Mater. Chem. A*, 2020, **8**, 4677-4699.
69. Z. Lu, Y. Chao, Y. Ge, J. Foroughi, Y. Zhao, C. Wang, H. Long and G. G. Wallace, *Nanoscale*, 2017, **9**, 5063-5071.
70. M. H. Ye, Z. P. Zhang, Y. Zhao and L. T. Qu, *Joule*, 2018, **2**, 245-268.
71. K. Jayaramulu, D. P. Dubal, B. Nagar, V. Ranc, O. Tomanec, M. Petr, K. K. R. Datta, R. Zboril, P. Gomez-Romero and R. A. Fischer, *Adv. Mater.*, 2018, **30**, e1705789.

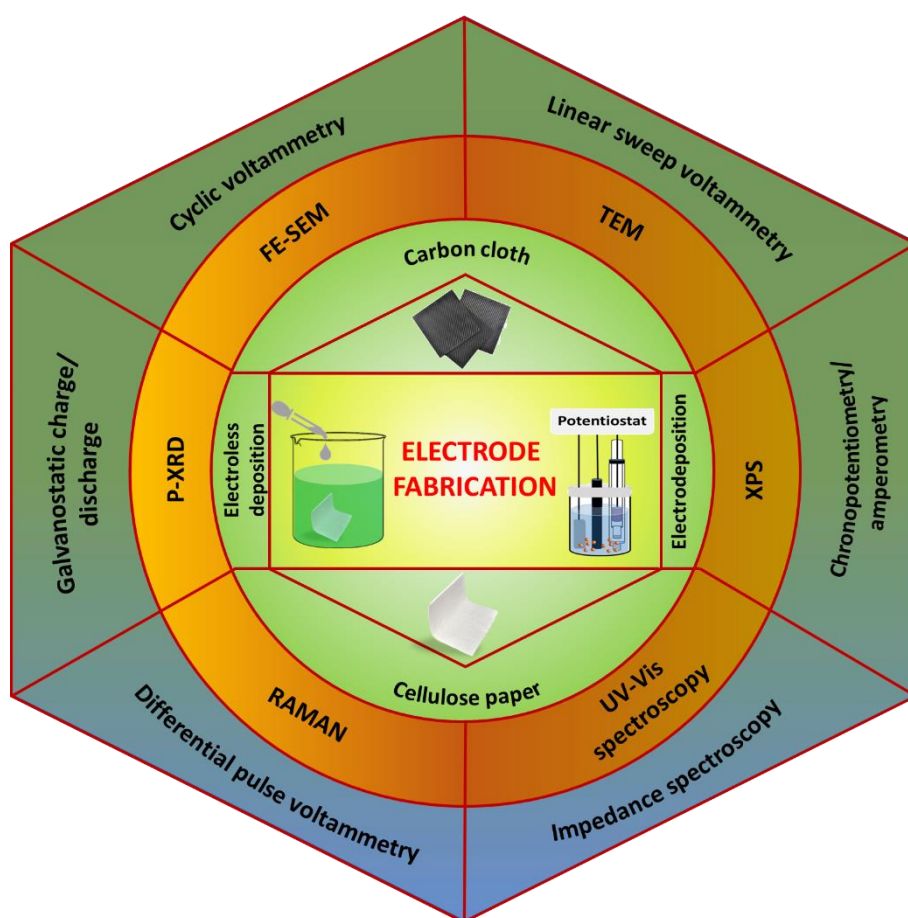
72. L. Liu, Y. X. Yin, J. Y. Li, S. H. Wang, Y. G. Guo and L. J. Wan, *Adv. Mater.*, 2018, **30**, 1706216.
73. H. Qiu, L. Zhao, M. Asif, X. Huang, T. Tang, W. Li, T. Zhang, T. Shen and Y. Hou, *Energy Environ. Sci.*, 2020, **13**, 571-578.
74. X. G. Li, B. Y. Guan, S. Y. Gao and X. W. Lou, *Energy Environ. Sci.*, 2019, **12**, 648-655.
75. A. Kafle, M. Kumar, D. Gupta and T. C. Nagaiah, *J. Mater. Chem. A*, 2021.
76. Q. Y. Jin, B. W. Ren, H. Cui and C. X. Wang, *Appl. Catal. B Environ.*, 2021, **283**, 119643.
77. A. Sahasrabudhe, H. Dixit, R. Majee and S. Bhattacharyya, *Nat. Commun.*, 2018, **9**, 1-14.
78. S. Shabani, *Environ. Sci. Pollut. Res.*, 2021, **28**, 6349-6373.
79. M. Jankowska-Kieltyka, A. Roman and I. Nalepa, *Front. Cell. Neurosci.*, 2021, **15**.
80. H. Lee, W. Myung, D. K. Kim, S. E. Kim, C. T. Kim and H. Kim, *Sci. Rep.*, 2017, **7**, 44741.
81. S. Yokota, S. Oshio, N. Moriya and K. Takeda, *PLoS One*, 2016, **11**, e0149737.
82. P. T. Kissinger, *Biosens. Bioelectron.*, 2005, **20**, 2512-2516.
83. A. Yang and F. Yan, *ACS Appl. Electron. Mater.*, 2021, **3**, 53-67.
84. Y. Ma, Z. Wei, Y. Wang, Y. Ding, L. Jiang, X. Fu, Y. Zhang, J. Sun, W. Zhu and J. Wang, *ACS Sustain. Chem. Eng.*, 2021.
85. N. Thakur, D. Gupta, D. Mandal and T. C. Nagaiah, *Chem. Commun.*, 2021, **57**, 13084-13113.
86. S. Lakard, I.-A. Pavel and B. Lakard, *Biosensors*, 2021, **11**, 179.





# Chapter 2

## Material design and characterization techniques



## 2-1 Synthetic approach

**2-1.1 Electroless deposition method:**<sup>1-7</sup> It is a chemical process of metal coating on various substrates by the chemical reduction of metal ions in a bath solution. As this method provides conformal metal coatings by surface-selective chemical reduction, it provides a route towards decoration of metal nanomaterials over a substrate via the wet-chemical approach, simply by immersing a substrate into the bath solution for a defined period of time. The method is flexible about the substrate irrespective of its nature (conductive/non-conductive), composition, and morphology. Although it is well established for metal finishing towards decorative as well as corrosion prevention applications, but its application towards nanomaterial synthesis is less common. This method is advantageous for coating nanomaterials of targeted composition over the substrate surface by controlling the reaction conditions. Additionally, nanomaterial deposition over the substrate surface within minutes is very beneficial especially in scenarios where the reactions cannot be terminated instantly. Therefore, this electroless deposition technique has led to a new generation of nanomaterials synthesis. Successful deposition of the materials of targeted composition depends on various factors including electroless bath composition, compatibility of the particles, bath reactivity, particle size distribution, and plating rate etc. Conventionally, electroless deposition involves surface activation and sensitization using  $\text{SnCl}_2$  and  $\text{PdCl}_2$  followed by direct chemical reduction of the metal ion on the substrate. The highlight of the present study is the elimination of expensive  $\text{PdCl}_2$  and  $\text{SnCl}_2$  based activators/sensitizers to reduce the overall manufacturing cost as represented in Figure 2-1. In this thesis, the activation free electroless deposition method has been employed for the preparation of  $\text{NiFeS@OCC}$ ,  $\text{NiFeP@OCC}$ ,  $\text{NiFeB@OCC}$ ,  $\text{NiB-CP}$ ,  $\text{NiFeB/VC-CP}$  and  $\text{CuSnB/VC-CP}$  electrodes, which are discussed in detail in chapters 3-6.

**2-1.2 Electrodeposition method:**<sup>4, 8-11</sup> Electrodeposition is the widely explored conventional process for the thin metallic layer coating on top of a conductive substrate for the modulation of the surface properties. In this process, the cations

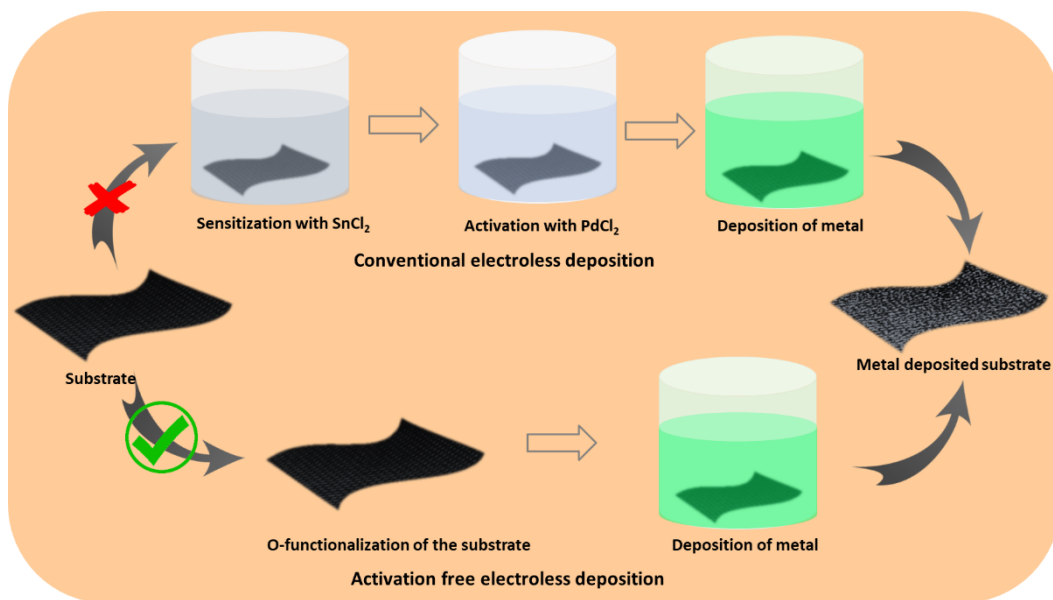


**Figure 2-1.** Schematic representation of electroless deposition method.

of the targeted material present in the electrolyte get reduced by means of electric current and consequently a thin film of those materials will be coated onto a conductive substrate surface. This is commonly practiced for decoration purposes and to achieve corrosion resistance, improve heat tolerance, reduce wear and friction. Therefore, this technique can be employed to explore new materials for a variety of applications by tailoring the surface properties of materials. In the course of electrodeposition, firstly, the metal ions in the electrolyte migrate towards the cathode under the influence of applied current and get neutralized and adsorbed as a result of electron transfer and diffuse to growth on the cathode surface. The thickness of the coated layer can be maintained by controlling the time duration of the deposition. The overall performance of electrodeposition depends on various factors including current density, current waveform, nature of the anions or cations in the solutions, bath composition and temperature, concentration of electrolyte solution, presence of impurities and physical and chemical nature of the substrate etc. Thus, the material of the desired composition over the substrate surface can be achieved by modulating the mentioned influencing factors. In the present study, the electrodeposition method has been explored for the preparation of NiP/NiB-CP,

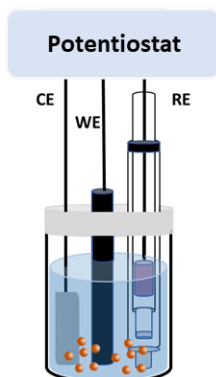


**Figure 2-2.** Schematic representation of electrodeposition method.

$\text{Fe}_3\text{O}_4/\text{NiB-CP}$  and  $\text{NiFeP}/\text{NiB-CP}$  electrodes, which are discussed in detail in chapters 4 and 5.

## 2-2 Physical characterization

**2-2.1 Electron microscopy:**<sup>12, 13</sup> It is a very important technique for the investigation of very small particles by the use of an accelerated beam of electrons as a source of illumination. Various types of electron microscopic techniques including scanning electron microscopy (SEM), field emission scanning electron microscopy (FE-SEM), transmission electron microscopy (TEM) and high-resolution transmission electron microscopy (HR-TEM) were employed in this thesis for the morphological characterization of the prepared electrodes.

**2-2.1.1 Scanning electron microscopy (SEM):**<sup>13-16</sup> It is one of the most widely used non-destructive techniques to analyze the morphology of the material by obtaining the high-resolution images of the materials as well as to show chemical composition by elemental mapping and spot chemical analysis. Briefly, a focused beam of high energy electrons is applied on the specimen surface, which dislocates the electrons from the specimen (secondary electrons) and generates a variety of signals which reveal information about the specimen including morphology, chemical composition and orientation of the material constituents of the sample. Energy-dispersive X-ray spectroscopy (EDX) equipped with an SEM instrument is useful for obtaining the chemical composition of the specimen. During the EDX

analysis, the X-ray resulting from the sample-electron beam interaction is utilized for the elemental distribution and chemical composition analysis. In this study, SEM measurements were carried out using JEOL, JSM-6610LV instrument with a thermionic gun as the electron source whereas EDS and elemental dot mapping were performed by using Oxford, INCAx-act, 51-ADD0013 instrument.

**2-2.1.2 Field emission scanning electron microscopy (FE-SEM):** This electron microscopy is an advanced version of SEM where a field emission electron gun is used instead of a thermionic one. As the electron beam diameter for the field emission electron gun is about 1000 times smaller than the thermionic gun, an improved and highly resolved image is achievable with FE-SEM. In this thesis, the FE-SEM measurements were performed using FESEM; SUPRA 55 VP- 4132 CARL ZEISS and FE-SEM, Hitachi, Japan, SU8010 instruments.

**2-2.1.3 Transmission electron microscopy (TEM):**<sup>17-20</sup> This electron microscopy involves the transmission of electrons through the specimen instead of scattering the electrons by the samples. During the TEM measurement, a very thin specimen is irradiated with the help of an electron gun which is focused through two or three condenser lenses and an image or diffraction pattern can be formed by the objective lens facilitated focused beam and can be viewed onto an imaging device like fluorescent screen or a layer of photographic film. The diffraction pattern resulted from the incident electrons, because of elastic scattering by the atoms of the specimen provides morphological, crystallographic and compositional information about the specimen. The TEM data were recorded during this study by using TEM, JEM 2100, JEOL instrument for the

characterization of the electrode material.

**2-2.1.4 High-resolution transmission electron microscopy (HRTEM):** It is a special mode of TEM which allows direct imaging of the atomic structure of the specimen. The HRTEM images can be employed for the analysis of properties of materials which can even resolve the lattice spacing of the sample up to 0.1 nm. A

phase contrast image obtained from the transmitted and scattered beams provides valuable information which is useful to analyze lattice imperfections as well as the crystal structure of the material. The HR-TEM data for this study were obtained from the FEI Tecnai (G2 F20) instrument operated at 200 keV.

**2-2.2 X-ray photoelectron spectroscopy (XPS):**<sup>21, 22</sup> It is a powerful spectroscopic technique for the investigation of the surface chemical composition and oxidation state of the materials. During the XPS measurement, the material under investigation is irradiated by applying a beam of X-rays (typically Al K $\alpha$  or Mg K $\alpha$ ) sources resulting in the escape of surface electrons from the specimen with certain kinetic energies. The XPS spectrum can be constructed employing the intensity of escaped electrons and binding energy (calculated from the kinetic energy), which provide the information about the elemental composition of element with an atomic number of three and above as well as the types of chemical bonds involved and oxidation state of the elements in the material surface both qualitatively and quantitatively. In this thesis, the XPS technique is well explored to analyze the surface chemical composition of the materials. The XPS data were obtained by using a PHI 5000 VersaProbe II spectrometer and Thermo scientific NEXSA with monochromatic Al K $\alpha$  radiation (1486.6 eV) under ultrahigh vacuum conditions (UHV;  $7 \times 10^{-10}$  mbar pressure). All the data were processed by calibrating with C 1s peak at 284.5 eV (precision of  $\pm 0.2$  eV).

**2-2.3 Raman spectroscopy:**<sup>23, 24</sup> It is a powerful tool for the determination of chemical states of the material. The underlying principal involves the measurement of vibrational energy modes by the interaction of scattered light with the chemical bonds within the material. The spectrum obtained can provide both chemical as well as structural information along with their characteristic Raman ‘fingerprint’. In this thesis, Raman analysis was performed to analyse the electrode materials by using LabRAM HR Evolution Raman spectrometer (Horiba Scientific) with a 532 nm laser.

**2-2.4 Powder X-ray diffraction (PXRD):**<sup>25, 26</sup> It is a primary characterization tool to examine crystalline materials by measuring diffraction patterns. During the PXRD measurement, crystalline material is irradiated by a monochromatic X-ray beam with a wavelength similar to the size of atomic grating where the constructive interference between scattered X-ray beams creates a diffraction pattern which is unique to the particular crystal structure. In this measurement diffracted beam intensity from crystal planes at different  $2\theta$  values is recorded which provides both qualitative and quantitative information regarding different phases present in the crystalline material along with crystallite size, crystal orientation and percentage crystallinity. During this study, PXRD information was obtained using PANalytical X'Pert Pro diffractometer in the  $2\theta$  range of  $10-80^\circ$  with a scan speed of  $2^\circ$  per minute using Cu-K $\alpha$  radiation ( $\lambda = 0.1542$  nm, 40 kV, 40 mA). The experimental PXRD data were analyzed by comparing them with reference patterns such as Inorganic Crystal Structure Database (ICSD) and Joint Committee on Powder Diffraction Standards (JCPDS).

**2-2.5 UV-Vis spectroscopy:**<sup>27, 28</sup> It is a simple analytical technique for the qualitative and quantitative assessment of solutions. During the measurement, a beam of UV-Visible radiation with a discrete wavelength is allowed to pass through the solution under investigation (Figure 2-3a). Because of the absorption of the radiation of the particular wavelength, the active molecule gets excited and promoted to a higher energy level. The amount of radiation that is adsorbed or transmitted through the sample solution as a function of wavelength will be recorded where the wavelength associated with the maximum absorbance ( $\lambda_{\max}$ ) is considered as a key point for the authentication of the particular molecule (Figure 2-3b). The amount of the particular compound can be determined quantitatively based on Beer-Lambert's law (equation 2.1);

$$A = \log \frac{I_0}{I} = \epsilon cl \quad (2.1)$$

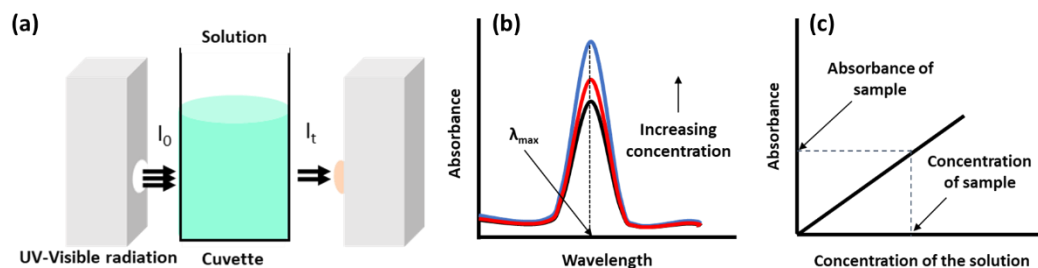


**Figure 2-3.** (a) Schematic representation of UV-Vis. spectroscopy, (b) UV-Vis. Spectrogram for various concentration solutions and (c) calibration curve prepared from the different known concentration solutions for determination of the unknown concentration of the solution.

where,

$A$  = measured absorbance,

$I_0$  = intensity of the incident radiation at a particular wavelength

$I$  = intensity of transmitted radiation

$l$  = the path length through the sample

$c$  = concentration of the absorbing species and

$\varepsilon$  = extinction coefficient

These measurements were carried out with the UV-Vis. spectrophotometer (SEC2000-DH light source) by taking a typical quartz cuvette (5 ml). In this thesis, the UV-Vis spectroscopic technique is widely explored in chapter 5A for the analysis of product as well as probable impurities during the course of electrolysis which is briefly described below.

### 2-2.5.1 Quantification of Ammonia<sup>29, 30</sup>

**A. Indophenol blue method:** The amount of ammonia formed during the electrochemical reduction of nitrogen was quantified spectrophotometrically in the UV-Visible region by the Indophenol blue method. For this, a fixed amount of electrolyte solution after the electrolysis was taken in which alkaline salicylic acid & sodium citrate solution, sodium hypochlorite solution and sodium nitroprusside solutions were added and left for two hours for complete color development (Figure 2-4a). Finally, the UV-Vis. absorption spectra were recorded at a wavelength of 655 nm (Figure 2-4b). The concentration–absorbance calibration curve was



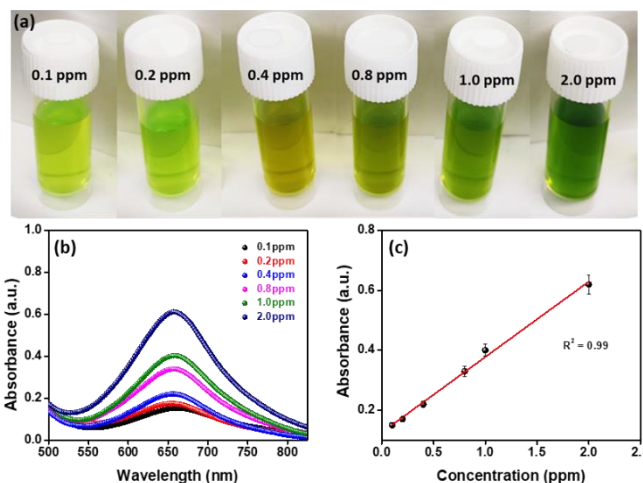


**Figure 2-4.** (a) Photographic images of analyte solution during color development, (b) UV-Vis spectrum of various known concentration standard  $\text{NH}_3$  solutions and (c) corresponding calibration curve for quantification of ammonia by Indophenol blue method.

generated with the help of a standard  $\text{NH}_4\text{Cl}$  solution with known  $\text{NH}_4^+$  concentrations from which the amount of ammonia was determined (Figure 2-4c).

The rate of ammonia formation was determined according to equation 2.2;

$$\text{Yield rate } (\mu\text{g cm}^{-2} \text{ h}^{-1}) = \frac{V \times C_{\text{NH}_3}}{t \times m_{\text{cat}}} \quad (2.2)$$

Here,  $C_{\text{NH}_3}$  is the measured  $\text{NH}_3$  concentration,  $V$  the volume of electrolyte,  $t$  the time of the reduction reaction and  $m_{\text{cat}}$  is the mass of the catalyst loaded onto the electrode.

Similarly, its Faradaic efficiency (F.E.) was calculated following equation 2.3 as;

$$\text{F. E. (\%)} = \frac{3 \times F \times V \times C_{\text{NH}_3}}{17 \times Q} \quad (2.3)$$

where  $F$  is the Faraday constant and  $Q$  is the total amount of charge passed through the electrodes during the electrolysis.

**B. Nessler's reagent method:** Nessler's reagent was prepared by mixing mercuric iodide and potassium iodide in the sodium hydroxide solution. A fixed amount of electrolyte was taken in which sodium potassium tartrate and Nessler's reagent were added for color development (Figure 2-5a). And finally, UV-Vis absorption

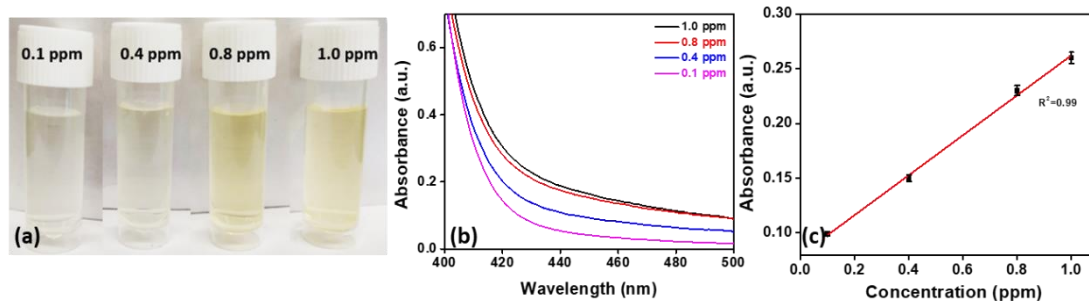


**Figure 2-5.** (a) Photographic images of analyte solution during color development, (b) UV-Vis spectrum of various known concentration standard  $\text{NH}_3$  solutions and (c) corresponding calibration curve for quantification of ammonia by Nessler's reagent method.

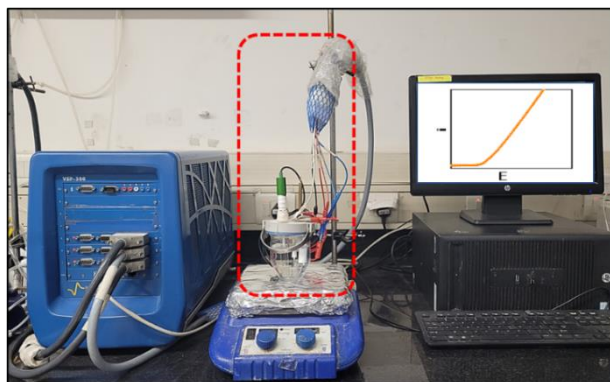
measurement was performed at  $\lambda = 420$  nm (Figure 2-5b). The calibration curve was developed by using standard  $\text{NH}_4\text{Cl}$  solutions with different known concentrations in the same way (Figure 2-5c).

**2-2.5.2 Quantification of hydrazine by Watt-Chrisp method:**<sup>31</sup> The hydrazine formed during the electrolysis was quantified by Watt and Chrisp method using UV-Vis. spectroscopy. In this method, the coloring solution composed of p-Dimethylaminobenzaldehyde ( $\text{p-C}_9\text{H}_{11}\text{NO}$ ) in HCl and ethanol. After electrolysis, a fixed volume of electrolyte was taken and mixed with the coloring solution and kept for 20 minutes at room temperature for color development. Finally, the  $\text{N}_2\text{H}_4$  was quantified spectrophotometrically with the help of a calibration curve generated by recording the absorbance at 455 nm by taking standard hydrazine solution of various known concentrations.

**2-2.5.3 Nitrate ( $\text{NO}_3^-$ ) and nitrite ( $\text{NO}_2^-$ ) ion determination:**<sup>32</sup> In order to determine the trace amount of  $\text{NO}_3^-$  present in the electrolyte, UV-Vis spectrophotometry was applied by considering the  $\lambda_{\text{max}}$  at 220 nm whereas the quantification of nitrites ( $\text{NO}_2^-$ ) was carried out through the formation of a reddish-purple azo dye product at pH 2-2.5 by coupling diazotized sulfanilamide with N-(1-naphthyl)-ethylenediamine dihydrogen chloride (NEDA). The photometric measurement of the colored dye is done at 540 nm.

## 2-3 Electrochemical measurements:<sup>27, 33</sup>

The electrochemical investigations were carried out in a single-compartment electrochemical cell during OER, ORR, HER and dopamine sensing experiments whereas the electrochemical characterizations for overall water splitting and electrochemical nitrogen reduction reaction were executed in a homemade two compartment H-cell, separated by a Nafion N117 membrane under ambient conditions of temperature and pressure. The cell setup consists of a working electrode (WE), counter electrode (CE) and reference electrode (RE) immersed in a suitable electrolyte solution (Figure 2-6). The prepared electrode is directly employed as a working electrode in which potential is applied with respect to a constant potential non-polarizable reference electrode such as Hg/HgO and



Ag/AgCl. A counter electrode (Pt wire or graphite rod) is taken to complete the

**Figure 2-6.** Photographic image of cell setup and electrochemical workstation employed during electrochemical analysis.

electric circuit which remains inert in the electrolytic environment under the applied potential window. During the electrochemical reaction, the current flows between WE and CE and the current response is recorded with respect to the applied potential to WE over the time duration. In the present study, potentiostat from Bio-Logic (VSP 300) was used for all the electrochemical measurements (Figure 2-6). In order to maintain uniformity in potential representation and compare with the reported literature the potentials measured against reference electrodes were converted to the reversible hydrogen electrode (RHE) according to equation (2.4);

$$E_{RHE} = E_{Ref} + E^{\circ}_{Ref} + 0.059 \text{ pH} \quad (2.4)$$

where,

$E_{RHE}$  = potential in RHE

$E_{Ref}$  = measured potential against the reference electrode and

$E^{\circ}_{Ref}$  = standard potential of the reference electrode

### 2-3.1 Cyclic voltammetry (CV) and linear sweep voltammetry (LSV):<sup>34, 35</sup>

Cyclic voltammetry (CV) is the most common voltammetric technique employed

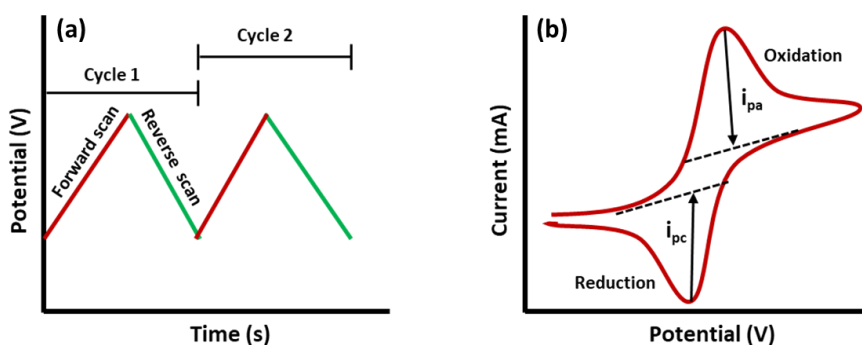


**Figure 2-7.** Cyclic voltammogram (a) potential vs. time plot and (b) current versus potential plot.

in almost all electrochemical measurements. In the course of CV measurement, the working electrode potential is ramped linearly with time between the initial potential ( $E_i$ ) and final potential ( $E_f$ ) at a specified scan rate ( $\text{mV s}^{-1}$ ) in a cyclic manner in which both oxidation and reduction behaviour of the working electrode is recorded. Whereas the linear sweep voltammetry (LSV) records either oxidation or reduction characteristics of the working electrode within the applied potential window  $E_i$  to  $E_f$ . The recorded current-potential curve during CV and LSV measurements are represented by voltammograms in which applied potential and current response are plotted on the x- and y-axis respectively (Figure 2-7). The electrochemical behavior can be analyzed on the basis of anodic and cathodic peak current obtained in the voltammogram by applying the Randles-Sevcik equation (2.5) which establishes the relation of peak current ( $i_p$ ) with scan rate ( $v$ ).

$$i_p = 2.69 \times 10^5 n^{3/2} v^{1/2} D^{1/2} A c \quad (2.5)$$

where,

$i_p$  = peak current

$n$  = number of electrons transferred in a redox reaction

$\nu$  = scan rate

$D$  = diffusion coefficient

$A$  = area of the electrode and

$C$  = concentration

**2-3.2 Differential pulse voltammetry (DPV):**<sup>36</sup> In this technique amplitude potential pulses are applied on a linear ramp potential, within the fixed potential window in the faradaic region (electron transfer to and from an electrode). During this measurement, the current is measured before the pulse application and at the end of the pulse the difference between them is recorded because of which the background current gets reduced consequently capacitive current-free response will be obtained. Therefore, the DPV can provide high sensitivity compared to the other voltammetric method as a result of low capacitive current. This method is often employed to detect analytes with similar oxidation potentials separately by achieving a sharp peak response due to small step sizes in DPV. The DPV with small pulses, are mainly important to study the very small amount of bounded reactant. Besides sensitivities, this technique have been widely employed to improve selectivity for different redox processes.

**2-3.3 Electrochemical surface area (ECSA):**<sup>37</sup> The electrocatalytic activity of the electrocatalyst depends on the number of exposed active sites of the catalyst, which can be investigated by determining the electrochemical active surface area (ECSA). The ECSA of the electrocatalysts were calculated by determining the double-layer pseudo-capacitance ( $C_{dl}$ ) of the catalyst. The cyclic voltammetry was recorded in the non-faradic potential zone at various scan rates and the double-layer pseudo-capacitance ( $C_{dl}$ ) was obtained as a slope of the graph of averaged current density  $[(j_a + j_c)]/2$ ; where,  $j_a$  and  $j_c$  are anodic and cathodic current densities at a particular potential *versus* the scan rate. The specific capacitance of  $40 \mu\text{F cm}^{-2}$  in 1 M KOH used during the determination of the electrochemically-active surface area was decided on the basis of reported capacitances for various metallic surfaces in

alkaline solutions. As the specific capacitances of Ni surfaces in alkaline solution have been ranging between 22 to 40  $\mu\text{F cm}^{-2}$  whereas after including the reported specific capacitances for carbon, Cu, Pt, Co, and Mo in alkaline solutions, the average specific capacitance changes to 43  $\mu\text{F cm}^{-2}$ . Therefore, on the basis of various reported literature a specific capacitance of 40  $\mu\text{F cm}^{-2}$  has been chosen for the measurement of ECSA in alkaline solution.

**2-3.4 Electrochemical impedance spectroscopy (EIS):**<sup>38, 39</sup> EIS is an important multifrequency AC electrochemical measurement technique to investigate the properties of materials and electrode reactions. This technique measures the electrical resistance (impedance) of the electrode/electrolyte interface over a wide range of frequencies and the obtained result provides the information for the solution resistance (high-frequency region), polarization resistance (low-frequency region), and capacitance of double layer. The charge transfer resistance ( $R_{ct}$ ) can be obtained by subtracting solution resistance ( $R_s$ ) from polarization resistance ( $R_p$ ). Besides solution resistance and charge transfer resistance the diffusion also can create an impedance called a Warburg impedance which is represented by slanting line at low frequency region. On a Nyquist Plot the Warburg impedance appears as a diagonal line with a slope of  $45^\circ$ .

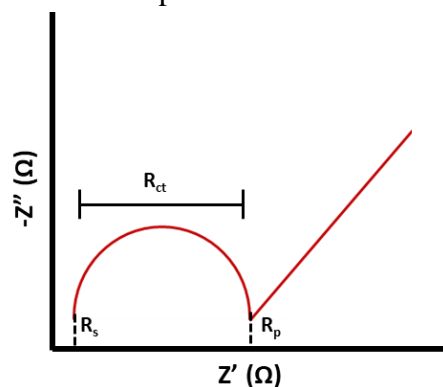


**Figure 2-8.** Nyquist plot showing solution resistance ( $R_s$ ), charge transfer resistance ( $R_{ct}$ ) and polarization resistance ( $R_p$ ).

**2-3.5 Chronopotentiometry and chronoamperometry techniques:** The durability of an electrocatalyst is very important for practical applications, which can be affected by the electrochemical conditions like the nature of the electrolyte,

electrode material, applied potential etc. In this study, the durability of the developed flexible electrodes was studied by employing chronopotentiometric and chronoamperometric techniques. A fixed current density value was applied and the corresponding potential response was recorded as a function of time. During the chronopotentiometric studies, fixed potential and current response were recorded as a function of time for a long duration, whereas chronoamperometry was performed at a fixed potential for a fixed time duration to examine the overall stability. Furthermore, the robustness of the electrode material with the variation of the potential was examined by carrying out chronopotentiometry sequentially at various current densities.

#### 2-4 Quantification of evolved gas:<sup>6, 40</sup>

The hydrogen and oxygen gas that evolved during electrolysis were estimated quantitatively by the eudiometric method. The experiment was performed with a three-electrode system in a homemade cell set up where an electrochemical cell was constructed by keeping the working electrode inside the inverted burette filled with the electrolyte. The developed flexible electrode operated as a working electrode along with a Pt wire counter electrode referenced against Hg/HgO/1 M NaOH reference electrode. Then the chronoamperometric experiment was performed at a fixed potential for a fixed time period. Thereafter, resulting gas volume was noted and the amount of H<sub>2</sub> and O<sub>2</sub> evolved was determined by using ideal gas approximation. The value of turn over number (TON) and turn over frequency (TOF) were calculated as

$$TON = \text{amount of product} / \text{amount of catalyst} \quad (2.6)$$

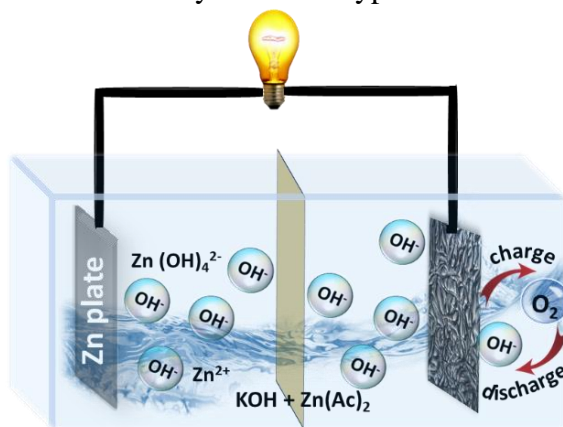
$$TOF = TON / \text{time} \quad (2.7)$$

$$\text{Faradaic efficiency} = V_{\text{measured}} / V_{\text{theoretical}} \quad (2.8)$$

#### 2-5 Zn-O<sub>2</sub> battery:<sup>41-43</sup>

A battery is an energy storage device that can store chemical energy and later convert it into electric energy by means of electrochemical reactions. It is

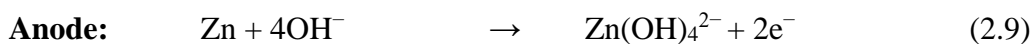
composed of an anode and cathode immersed in the electrolyte and separated by an insulating separator. Throughout discharge, the electrochemical reactions lead to the flow of electrons from the anode to the cathode through an external circuit and provide an electric current that can be utilized to power a device whereas, during charging, the battery is connected to an external electricity supply, which results in opposite electrode reaction to that during the discharging. In the field of battery technology, Li-ion batteries (LiBs) are leading the current market of energy storage device but their drawbacks like limited energy density, high cost, and safety hazards associated with flammable organic electrolyte limits wider applications towards next-generation electrical devices. In this respect aqueous Zn-air batteries are considered a promising candidate as it has high theoretical energy density (mention the value here), and the aqueous electrolyte is beneficial for assurance of safety, low cost and eco-friendly nature. A typical Zn-air battery consists of a Zn



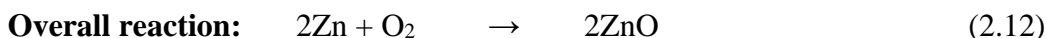
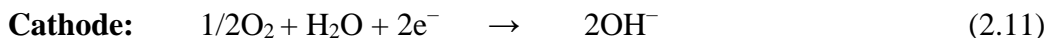
**Figure 2-9.** Schematic representation for the charge and discharge process in Zn-air battery.

anode and an air cathode separated by an insulating separator to avoid the short circuit and allow the transfer of ions across the cell with (6 M KOH + 0.2 M  $\text{Zn}(\text{ac})_2$ ) as an electrolyte (Figure 2-9). Briefly following reaction take place at respective the electrodes during discharging and charging of a Zn-air battery;

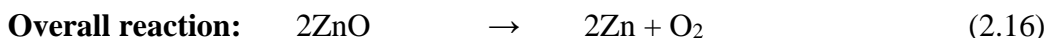
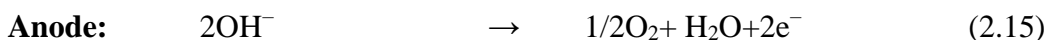
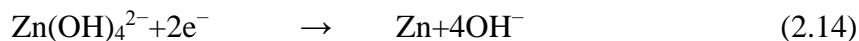
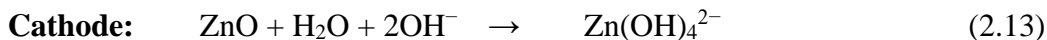
### Discharge







**Charge**



Generally, the overall performance of the battery is evaluated based on the following key parameters; which was employed in chapter 5A

**Specific capacity:** It is the measure of the quantity of energy that it can deliver in a single discharge. In general, the amount of electric charge that can be accumulated during the charging process, stored during the open circuit stay, and released during the discharge process is represented as battery capacity. The specific capacity can be calculated by using the formula given in equation (2.17)

$$\text{Specific capacity} = \frac{\text{current} \times \text{discharge time}}{\text{weight of zinc consumed}} \quad (2.17)$$

**Energy density:** It is the amount of charge that can be stored per gram or per litre of the compound which is expressed in terms of gravimetric ( $\text{Wh kg}^{-1}$ ) and volumetric energy density ( $\text{Wh L}^{-1}$ ). The energy density of a Zn – air battery can be calculated by using the formula given in equation (2.18)

$$\text{Energy density} = \frac{\text{current} \times \text{discharge time} \times \text{average discharge voltage}}{\text{weight of zinc consumed}} \quad (2.18)$$

**Power density:** The rate at which the stored energy can be released is known as power density which is expressed as  $\text{mW cm}^{-2}$ . A cell with high energy density is not always advantageous as this energy cannot be released to provide high power output, therefore cell with high power density is necessary to run high-power demanding devices. The power density can be determined from the product of the current density and the corresponding potential during the discharge of a battery.

**Cycle life:** The cycle life of a battery represents the total number of charge-discharge cycles which can be operated prior to the degradation of its performance

beyond its useful level.

**Battery assembly:** Zn-air battery performance was evaluated by constructing a homemade battery containing an air electrode, separator and zinc plate. The air electrode contained three layers i.e., gas diffusion layer (GDL), Ni-foam current collector and developed flexible paper air electrode separated by glass microfibre separator with the Zn-anode where 6 M KOH containing 0.2 M Zn (Ac)<sub>2</sub> was applied as electrolyte. The GDL containing Vulcan carbon with PVDF binder in a 1:1 ratio dispersed in NMP was applied in the Ni-foam and assembled the battery

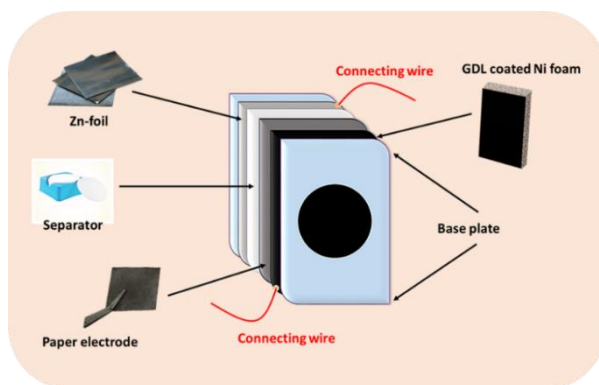


**Figure 2-10.** Schematic representation of the assembly of a homemade Zn-O<sub>2</sub> battery.

as shown in Figure 2-10. In order to compare the battery performance with state-of-the-art material a rechargeable battery was constructed by coating a slurry containing a 1:1 mass ratio of Pt/C (20 %) and RuO<sub>2</sub> (99.95 %) on NiB-CP by maintaining similar loading keeping the rest arrangement same and the measurements were performed under the ambient conditions. All the electrochemical experiments were carried out by using a Biologic BCS-810 battery cyclers.

## 2-6 Basic terminology used in biosensing:<sup>44-46</sup>

**Analyte:** It is a material (biomolecules) of interest which need to be detected. In this study, dopamine is termed as an ‘analyte’ in a biosensor developed to detect at a particular concentration.

**Limit of detection and sensitivity:** The minimum quantity of analyte which can be detected by a biosensor is designated as its limit of detection (LOD) which is

determined according to equation 2.19

$$LOD=3S/m \quad (2.19)$$

where,

$S$  = Standard deviation of the blank signal

$m$  = sensitivity which is obtained as a slope of the calibration curve between analyte concentrations and peak current density.

Smaller value of LOD and higher sensitivities are the ideal characteristics of a good biosensor.

**Selectivity:** It is the ability of the sensor to sense a particular analyte in a sample containing other interfering species. Generally, the body fluid contains various electroactive interfering species therefore the selectivity is considered a key parameter while constructing a biosensor.

**Recovery:** Generally, a recovery test is executed to evaluate the efficiency of a biosensor system in detecting a particular analyte. The recovery percentage is determined as;

$$\text{Recovery (\%)} = (\text{amount of analyte found}/\text{amount of analyte added}) \times 100 \quad (2.12)$$

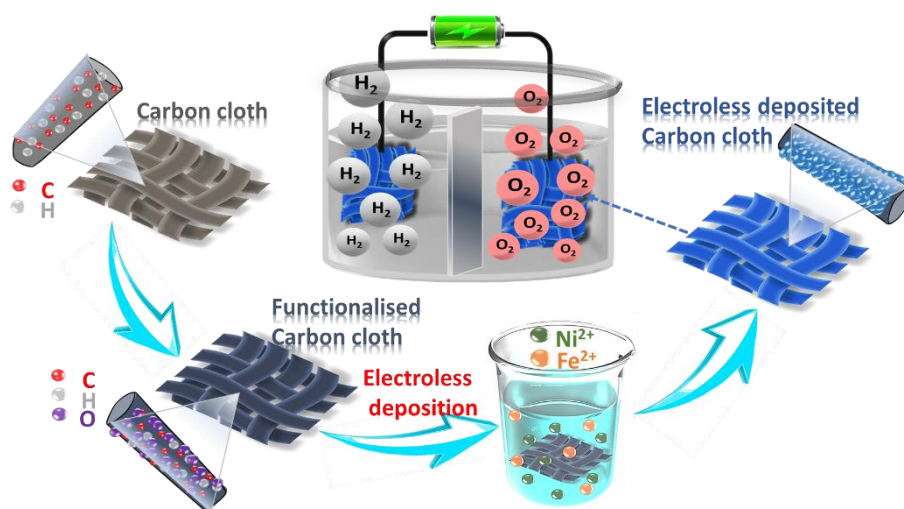
## 2-7 References

1. G. O. Mallory and J. B. Hajdu, *Electroless plating: fundamentals and applications*, William Andrew, 1990.
2. S. S. Djokić and P. L. Cavallotti, *Electrodeposition: Theory and Practice*, 2010, 251-289.
3. F. Muench, *ChemElectroChem*, 2021, **8**, 2993-3012.
4. M. Schlesinger and M. Paunovic, *Modern electroplating*, John Wiley & Sons, 2011.
5. A. Kafle, D. Gupta and T. C. Nagaiah, *Electrochim. Acta*, 2023, **441**, 141779.
6. A. Kafle, M. Kumar, D. Gupta and T. C. Nagaiah, *J. Mater. Chem. A*, 2021, **9**, 24299-24307.
7. A. Kafle, N. Thakur and T. C. Nagaiah, *J. Mater. Chem. B*, 2022, **10**, 3681-3686.
8. N. Kanani, *Electroplating: basic principles, processes and practice*, Elsevier, 2004.
9. F. Walsh and C. Ponce de Leon, *Transactions of the IMF*, 2014, **92**, 83-98.
10. Z. Shojaei, G. R. Khayati and E. Darezereshki, *Int. J. Miner. Metall. Mater.*, 2022, **29**, 1683-1696.
11. A. Kafle, D. Gupta, A. Bordoloi and T. C. Nagaiah, *Nanoscale*, 2022, **14**, 16590-16601.
12. W. Zhou and Z. L. Wang, *Scanning microscopy for nanotechnology: techniques and applications*, Springer science & business media, 2007.
13. L. Reimer, *Meas. Sci. Technol.*, 2000, **11**, 1826-1826.
14. S. J. B. Reed, *Electron microprobe analysis and scanning electron microscopy in geology*, Cambridge university press, 2005.
15. K. Smith and C. Oatley, *Br. J. Appl. Phys.*, 1955, **6**, 391.

16. R. J. Brook, *Concise encyclopedia of advanced ceramic materials*, Elsevier, 2012.
17. B. Fultz and J. M. Howe, *Transmission electron microscopy and diffractometry of materials*, Springer Science & Business Media, 2012.
18. D. B. Williams, C. B. Carter, D. B. Williams and C. B. Carter, *The transmission electron microscope*, Springer, 1996.
19. S. M. Bhagyaraj, O. S. Oluwafemi, N. Kalarikkal and S. Thomas, 2018.
20. N. Yao and Z. L. Wang, *Handbook of microscopy for nanotechnology*, Springer, 2005.
21. J. Chastain and R. C. King Jr, *Perkin-Elmer Corporation*, 1992, **40**, 221.
22. A. Proctor and P. M. Sherwood, *Anal. Chem.*, 1982, **54**, 13-19.
23. G. Socrates, *Infrared and Raman characteristic group frequencies: tables and charts*, John Wiley & Sons, 2004.
24. E. Smith and G. Dent, *Modern Raman spectroscopy: a practical approach*, John Wiley & Sons, 2019.
25. C. F. Holder and R. E. Schaak, Tutorial on powder X-ray diffraction for characterizing nanoscale materials, 2019, **13**, 7359-7365.
26. K. D. Harris, M. Tremayne and B. M. Kariuki, *Angew. Chem. Int. Ed.*, 2001, **40**, 1626-1651.
27. D. A. Skoog, F. J. Holler and S. R. Crouch, *Principles of instrumental analysis*, Cengage learning, 2017.
28. H.-H. Perkampus, *UV-VIS Spectroscopy and its Applications*, Springer Science & Business Media, 2013.
29. D. Gupta, A. Kafle, S. Kaur, P. P. Mohanty, T. Das, S. Chakraborty, R. Ahuja and T. C. Nagaiah, *J. Mater. Chem. A*, 2022, **10**, 20616-20625.
30. D. Gupta, A. Kafle, S. Kaur, T. S Thomas, D. Mandal and T. C. Nagaiah, *ACS Appl. Mater. Interfaces*, 2023, **15**, 4033-4043.
31. W. Liu, C. Li, Q. Xu, P. Yan, C. Niu, Y. Shen, P. Yuan and Y. Jia, *ChemCatChem*, 2019, **11**, 5412-5416.
32. H. Jin, L. Li, X. Liu, C. Tang, W. Xu, S. Chen, L. Song, Y. Zheng and S. Z. Qiao, *Adv. Mater.*, 2019, **31**, 1902709.
33. A. Bard and L. Faulkner, *Electrochemical Methods: Fundamentals and Applications*, Wiley, New York, 2001, 368.
34. N. Elgrishi, K. J. Rountree, B. D. McCarthy, E. S. Rountree, T. T. Eisenhart and J. L. Dempsey, *J. Chem. Educ.*, 2018, **95**, 197-206.
35. P. T. Kissinger and W. R. Heineman, *J. Chem. Educ.*, 1983, **60**, 702.
36. J. n. González, E. Laborda and A. n. Molina, *J. Chem. Educ.*, 2022.
37. A. Tiwari, V. Singh, D. Mandal and T. C. Nagaiah, *J. Mater. Chem. A*, 2017, **5**, 20014-20023.
38. B.-Y. Chang and S.-M. Park, *Annu. Rev. Anal. Chem.*, 2010, **3**, 207-229.
39. S. Wang, J. Zhang, O. Gharbi, V. Vivier, M. Gao and M. E. Orazem, *Nat. Rev. Methods Primers*, 2021, **1**, 41.
40. A. Sahasrabudhe, H. Dixit, R. Majee and S. Bhattacharyya, *Nat. Commun.*, 2018, **9**, 1-14.
41. J. Mei, T. Liao, J. Liang, Y. Qiao, S. X. Dou and Z. Sun, *Adv. Energy Mater.*, 2020, **10**, 1901997.
42. Y. Li and H. Dai, *Chem. Soc. Rev.*, 2014, **43**, 5257-5275.
43. J. Fu, Z. P. Cano, M. G. Park, A. Yu, M. Fowler and Z. Chen, *Adv. Mater.*, 2017, **29**, 1604685.
44. N. J. Ronkainen, H. B. Halsall and W. R. Heineman, *Chem. Soc. Rev.*, 2010, **39**, 1747-1763.
45. N. Thakur, D. Gupta, D. Mandal and T. C. Nagaiah, *Chem. Commun.*, 2021, **57**, 13084-13113.
46. M. Zhou, Y. Zhai and S. Dong, *Anal. Chem.*, 2009, **81**, 5603-5613.

## Chapter 3

### The activation free electroless deposition of NiFe over carbon cloth as electrode towards overall water splitting



### 3-1 Introduction

Environmental impact of fossil fuels and their sustainability has instigated the researchers towards the development of various forms of renewable energy production and storage system.<sup>1</sup> Hydrogen (H<sub>2</sub>) holds paramount significance in the quest of development of an environmentally benign, cleaner and ecological energy system.<sup>2-4</sup> Electrochemical water splitting provides a sustainable, cost-effective and greener approach for large-scale pure hydrogen production towards the vision of using H<sub>2</sub> as a future energy carrier without any carbon traits.<sup>5-7</sup> The overall water splitting includes an anodic oxygen evolution reaction (OER) and a cathodic hydrogen evolution reaction (HER) which are profoundly relying on the activity of the electrocatalyst as well as coherent design of electrode architecture.<sup>8-12</sup> Generally, the electrodes are prepared by casting the catalyst ink on a conductive substrate i.e., the current collectors *viz.*, carbon and metal foil/foam based substrate with the assistance of an insulating binder. Although the binder provides physical adhesion, it may flummox the ion transport and hinder the release of bubbles resulting in catalyst peeling from the electrode surface leading to a moderate electrochemical performance.<sup>13-15</sup> Besides the stability issues, the major disadvantages of these electrodes are the lengthy fabrication procedures, high cost, structural fragility of the substrate etc. In this regard, designing of three-dimensional binder free self-standing electrodes is an innovative approach which can possess increased density of active sites to realize faster mass transport, low contact resistance, low electrolyte penetration, reduced ohmic losses, and can provide excellent catalyst-substrate adhesion as compared to the binder assorted electrodes.<sup>16, 17</sup> Some of the common methods involved in the fabrication of three-dimensional self-standing electrodes are electrodeposition,<sup>18, 19</sup> electroless deposition<sup>20, 21</sup> chemical vapor deposition and so on.<sup>22, 23</sup> Among these, electroless deposition is getting tremendous attraction due to its unbeaten virtues like simplicity, cost effectiveness, rapidity, minimization of the mechanical damage to the substrate and providing secure uniform coating.<sup>24, 25</sup> In particular, it doesn't

require electricity and is applicable to even non-conductive substrate which can be scalable.

Although RuO<sub>2</sub> and Pt/C are considered as benchmark electrocatalysts for OER and HER respectively, but their low abundance, high cost and inadequate bifunctional activity somewhat restricts their practical application. Additionally, the benchmark OER catalyst is not suitable for HER and Pt/C is not stable under OER conditions.<sup>26</sup> More importantly pairing two different electrodes for OER and HER increase reaction complexity and overall manufacturing cost. Therefore, it is highly attractive to design and develop efficient and low-cost water splitting catalysts made of earth-abundant elements. Among non-precious metal based electrocatalysts, transition metal-based catalysts<sup>27, 28</sup> especially Ni and Fe-based bimetallic sulfide and phosphide are known to exhibit the most promising activity towards overall water splitting owing to their high electrical conductivity, earth abundance, high activity and excellent stability in alkaline media.<sup>29-31</sup> However, the synthesis of these catalysts is time-consuming which involves multistep process and expensive precursors.<sup>31, 32</sup>

The present study aims to explore the applicability of electroless deposition for growth of NiFeS and NiFeP electrocatalyst over the highly flexible carbon cloth substrate towards overall electrocatalytic water splitting. The carbon fiber-based substrates are of great research interest for various applications due to their high flexibility, low cost, corrosion resistance property and good biocompatibility as compared to metal foams or foils.<sup>33-35</sup> Therefore, the development of carbon cloth (CC) based flexible electrodes with deposition of non-noble metal based electrocatalyst by just simple dip-coating method adds up an initiation to overcome the above mentioned shortcomings. Conventionally, electroless deposition involves surface activation and sensitization using SnCl<sub>2</sub> and PdCl<sub>2</sub> followed by direct chemical reduction of the metal ion on the substrate.<sup>36</sup> The highlight of the present study is the elimination of expensive PdCl<sub>2</sub> and SnCl<sub>2</sub> based activators/sensitizers to reduce the overall manufacturing cost by the introduction

of functional groups on the carbon cloth which provides strong adsorption of metal ions and simultaneously enhance the conductivity along with mass transport kinetics. To the best of our knowledge this is the first report on elimination of preactivation procedure for electroless deposition of NiFe based sulphides and phosphides over carbon cloth. The fabricated electrode was used directly as a flexible electrode which demonstrated a good bifunctional activity towards electrochemical water splitting in alkaline media and also showed good flexibility and electrochemical performance at various mechanical deformation states.

### 3-2 Electrode fabrication

**3-2.1 Pretreatment of carbon cloth:** The commercially available carbon cloth was treated with concentrated nitric acid to functionalize it with hydrophilic oxygen groups by following a previously reported literature<sup>37</sup> and herein denoted as oxygen functionalized carbon cloth (OCC). The functionalized CC was then washed thoroughly with deionized water until it got neutralized, then dried in a hot air oven at 60 °C and used for further deposition.

**3-2.2 NiFeS deposition on carbon cloth (NiFeS@OCC):** The fabrication of flexible NiFeS deposited OCC (NiFeS@OCC) was carried out by electroless deposition method. For this, a piece of oxygen functionalized carbon cloth (OCC) of dimension 1 cm × 1 cm was taken as substrate and immersed in the bath solution consisting of 0.25M nickel nitrate ( $\text{NiNO}_3 \cdot 6\text{H}_2\text{O}$ ), 0.0825M ammonium ferrous sulphate ( $(\text{NH}_4)_2\text{SO}_4 \cdot \text{FeSO}_4 \cdot 6\text{H}_2\text{O}$ ), 2M thiourea ( $(\text{NH}_2)_2\text{CS}$ ) and 0.5M boric acid ( $\text{H}_3\text{BO}_3$ ). The pH of bath solution was maintained between 1-1.5 by adjusting with 2M  $\text{H}_2\text{SO}_4$  solution. The deposition on carbon cloth was carried out for 10 minutes at a bath temperature 60 °C and designated as NiFeS@OCC. The composition of the bath solution was optimized by varying the molar ratio of Ni and Fe from 1:1 to 4:1 by same procedure. In the similar fashion, deposition bath for NiS and FeS were carried out by keeping only respective metal salt in the same bath solution by keeping the rest of the procedure same.<sup>38</sup>



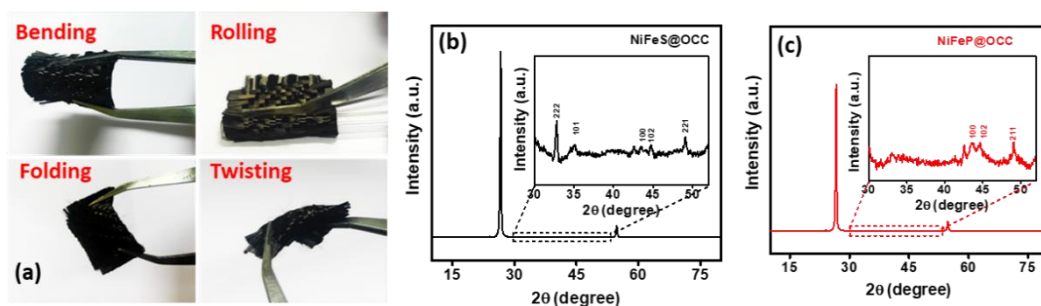


**Figure 3-1.** (a) Photographs of electroless-deposited flexible electrode under various deformations, P-XRD pattern of (b) NiFeS@OCC and (c) NiFeP@OCC electrodes.

**3-2.3 NiFeP deposition on carbon cloth (NiFeP@OCC):** The deposition of NiFeP over OCC was performed in the bath solution composed of  $\text{Ni}(\text{NO}_3)_2 \cdot 6\text{H}_2\text{O}$  (0.25M)  $\text{FeSO}_4 \cdot (\text{NH}_4)_2\text{SO}_4 \cdot 6\text{H}_2\text{O}$  (0.085M) triethanolamine (0.05M, 7 g/L)  $\text{H}_3\text{BO}_3$  (0.08M, 5 g/L),  $\text{NaH}_2\text{PO}_2$  (0.113M, 10 g/L) trisodium citrate (0.039M, 10 g/L),  $\text{NH}_3 \cdot \text{H}_2\text{O}$  (6 ml/L) and thereby mentioned as NiFeP@OCC. Similarly, bath for NiP and FeP were prepared by adding single metallic salt and keeping the rest of the procedure same.<sup>39</sup>

### 3-3 Results and discussion

**3-3.1 Physical characterization:** For the fabrication of the electrode, firstly, the commercially available carbon cloth was treated with nitric acid to introduce oxygen functional groups on the surface of carbon fiber (denoted as OCC) so as to facilitate the strong anchoring of metal ions during electroless deposition.<sup>40</sup> After the oxygen functionalization of the carbon cloth, the active NiFeS and NiFeP catalysts were decorated over it by a single step electroless deposition method. Thus fabricated electrodes exhibited good flexibility under various mechanical deformation states such as bending, rolling and twisting as shown in Figure 3-1a and was able to regain original shape after relaxing. The microstructure and morphology of these flexible electrodes were studied by P-XRD, SEM and Raman spectroscopic techniques. The observed peaks in the P-XRD patterns of

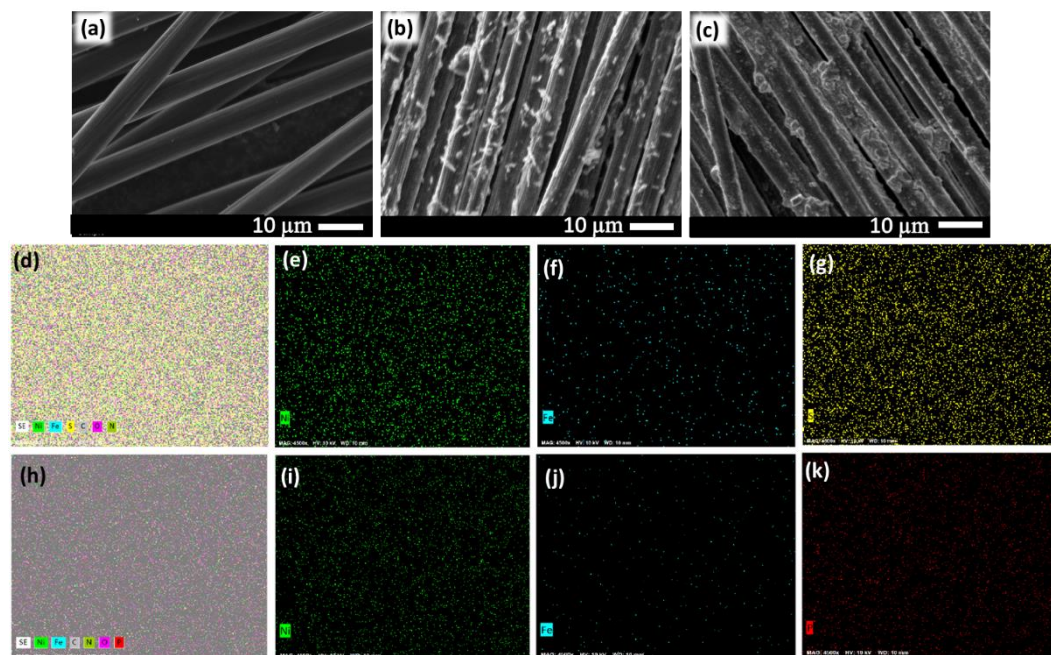


**Figure 3-2.** SEM images of (a) bare carbon cloth, (b) NiFeS@OCC and (c) NiFeP@OCC and elemental dot mapping images (d) for all elements, (e) Ni, (f) Fe, and (g) S elements of NiFeS@OCC electrode and (h) for all elements, (i) Ni, (j) Fe, (k) P of NiFeP@OCC electrode.

NiFeS@OCC (Figure 3-1b) at  $2\theta$  values of  $26.5^\circ$ ,  $43.5^\circ$  and  $54^\circ$  could be attributed to graphitic carbon and moderate peaks at  $32.7^\circ$ ,  $34.6^\circ$  and  $44.7^\circ$  could be ascribed to NiFeS (PDF no. 000120736) whereas peaks at  $49.1^\circ$  and  $53.1^\circ$  were assigned to NiS (PDF no. 01-075-0612)<sup>41</sup>. Similarly, NiFeP@OCC exhibited additional three peaks apart from graphitic carbon peaks i.e., one at  $44.6^\circ$  was assigned to  $\text{NiP}_2$ <sup>42</sup> and others at  $49.0^\circ$  and  $52.8^\circ$  corresponded to  $\text{Fe}_2\text{NiP}$  (Figure 3-1c).<sup>43</sup> The SEM images of the flexible NiFeP@OCC and NiFeS@OCC electrodes showed the sparse deposition of the NiFeP and NiFeS particles over carbon cloth when compared with that of the bare carbon cloth and the deposition was found to be denser in case of NiFeP@OCC (Figure 3-2a-c). Moreover, the uniform distribution of all the respective elements over the scanned area was observed in the elemental dot mapping images (Figure 3-2d-k) and revealed the successful deposition of NiFeP and NiFeS over the OCC. Additionally, the distinct characteristic peaks around  $1357$  and  $1612\text{ cm}^{-1}$  in the Raman spectra were assigned to the D and G

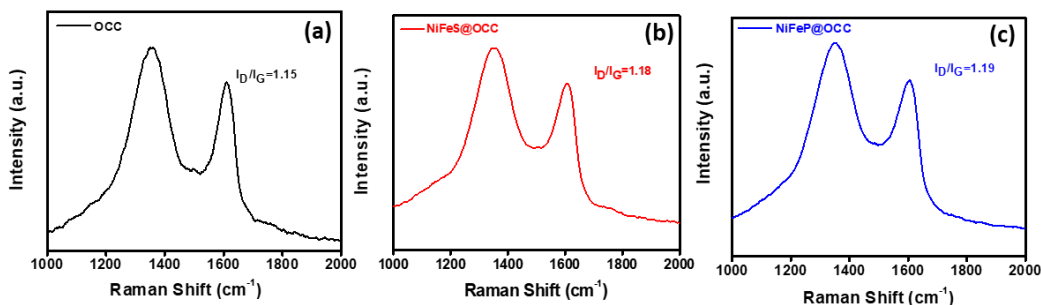


**Figure 3-3.** Raman spectra of (a) OCC, (b) NiFeS@OCC and (c) NiFeP@OCC electrode.

carbon band respectively where the intensity ratio of these bands ( $I_D/I_G$ ) was found to be high for NiFeS@OCC (1.18) and NiFeP@OCC (1.19) when compared to bare OCC (1.15) (Figure 3-3a-c), which could probably be due to the generation of higher number of defects as a consequence of the deposition of NiFeS and NiFeP particles over carbon cloth.<sup>18, 44</sup> Further, the surface properties of the NiFeS@OCC and NiFeP@OCC electrodes were examined by X-ray photoelectron spectroscopy. The XPS survey spectra of the NiFeS@OCC (Figure 3-4a) revealed the successful oxygen functionalization and deposition of materials on carbon cloth. The high resolution deconvoluted XP spectra of Ni 2p showed two peaks at 856.3 and 861.9 eV (Figure 3-4c) attributed to the presence of Ni in +2 oxidation state.<sup>41</sup> Similarly, peaks at 710.6 eV and 723.9 eV in the deconvoluted Fe 2p spectra (Figure 3-4d) evidenced the existence of Fe in +2 oxidation state. Additionally, the existence of peaks at 163.5 and 168.5 eV in the S 2p spectra revealed the presence of sulfide and sulphate respectively (Figure 3-4e), which further confirmed that the NiFeS@OCC electrode contains sulfides of nickel and iron. In the similar fashion, the deconvoluted Ni 2p XP spectra of the NiFeP@OCC electrode (Figure 3-4f-h), displayed a pair of peaks at 853.2 & 870.4 eV and 856.4 & 874.3 eV, which confirmed that Ni is present in 0 and +2 oxidation state. Furthermore, the high-resolution Fe 2p spectra demonstrated the spin orbit doublet peaks located at 711.8 and 724 eV corresponding to Fe in +2 oxidation state and the peaks at 130.2 eV and 133.2 eV in the P 2p spectrum confirmed the existence of M-P bonding and formation of phosphate (P-O) due to surface oxidation.

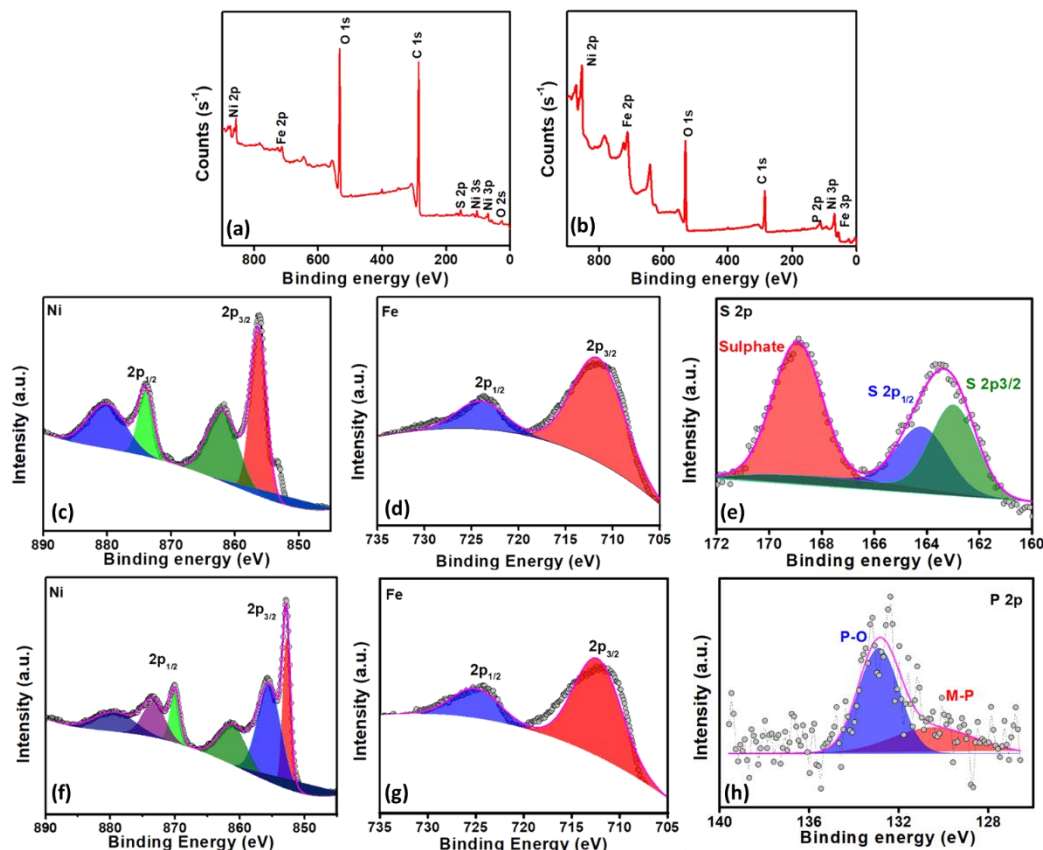


**Figure 3-4.** XPS survey spectra of (a) NiFeS@OCC and (b) NiFeP@OCC electrodes, deconvoluted XPS spectra of (c) Ni 2p, (d) Fe 2p and (e) S 2p of NiFeS@OCC electrode and (f) Ni 2p, (g) Fe 2p and (h) P 2p of NiFeP@OCC electrode.

**3-3.2 Catalytic activity towards OER and HER:** In order to evaluate the applicability of flexible NiFeS@OCC and NiFeP@OCC electrodes towards oxygen evolution reaction (OER), firstly, linear sweep voltammetry (LSV) was carried out in 1M KOH solution using conventional three-electrode configuration. Polarization curves were recorded by taking NiFeS@OCC and NiFeP@OCC electrodes directly as a working electrode (WE) where Pt wire and Hg/HgO/1M NaOH served as counter electrode (CE) and reference electrode (RE) respectively. Afterwards, the catalytic performance was compared with benchmark electrocatalyst RuO<sub>2</sub> and other control samples prepared under similar conditions. The LSV curve (Figure 3-5a) recorded at a scan rate of 5 mVs<sup>-1</sup> elucidate the

superior OER activity of NiFeS@OCC as validated by a sharp increase in oxidative current density with lower onset potential than bare OCC and other control electrodes where the evolution of oxygen at 1.43 V vs. RHE is clearly evident. Further sweeping on potential towards higher potential led to increase in anodic current density as a consequence of enhanced oxygen evolution. The flexible NiFeS@OCC electrode achieved 10 mA cm<sup>-2</sup> of current density at a low overpotential of 220 mV and attained a high current density of 138 mA cm<sup>-2</sup> at a potential of 1.80 V vs. RHE whereas, the monometallic FeS@OCC and NiS@OCC

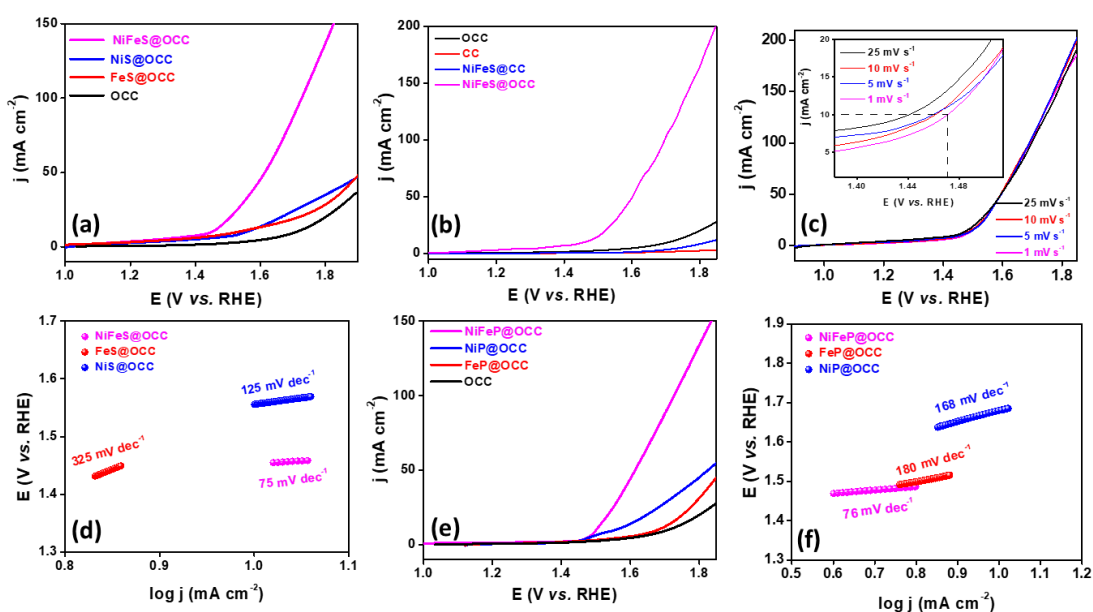


**Figure 3-5.** (a), (b) & (e) LSV curves of various electrodes at 5 mV s<sup>-1</sup> and (c) at various scan rates showing OER activity (d) & (f) corresponding Tafel slopes.

electrodes required 301 and 322 mV overpotential to reach the same 10 mA cm<sup>-2</sup> current density signifying that the synergetic effect between Ni and Fe boosts the electrochemical activity by tuning the electronic density on metals and hence accelerated the kinetics of sluggish OER. In order to identify the role of oxygen functionalization, NiFeS was deposited on carbon cloth without functionalization (CC) to obtain NiFeS@CC, which demonstrated a poor activity of 8 mA cm<sup>-2</sup> at 1.8 V vs. RHE (Figure 3-5b), emphasizing the importance of functionalization of

carbon cloth which led to the improved adsorption of reaction intermediates over the catalyst surface during OER. Similarly, the LSVs at various scan rates were recorded to check the effect of scan rate, where a negligible change in onset potential and current density was observed for NiFeS@OCC. The electrode exhibited similar behavior at different scan rates ranging from  $1 \text{ mV s}^{-1}$  to  $25 \text{ mV s}^{-1}$  representing its stability towards electrochemical OER (Figure 3-5c).<sup>45</sup> Moreover, Tafel slope is a powerful tool to evaluate the potential-dependent rate of electrochemical reaction since it is associated with surface coverage of adsorbed intermediate species. Herein, the lower Tafel slope of  $75 \text{ mV dec}^{-1}$  for NiFeS@OCC than other monometallic electrodes NiS@OCC ( $125 \text{ mV dec}^{-1}$ ) and FeS@OCC ( $325 \text{ mV dec}^{-1}$ ) signifies the enhanced adsorption/desorption and thus establishing superior kinetics of NiFeS@OCC (Figure 3-5d). In the similar fashion, as expected the NiFeP@OCC electrode showed higher OER activity than bare carbon cloth electrode and other monometallic phosphide electrodes (i.e., NiP@OCC and FeP@OCC) under similar conditions.

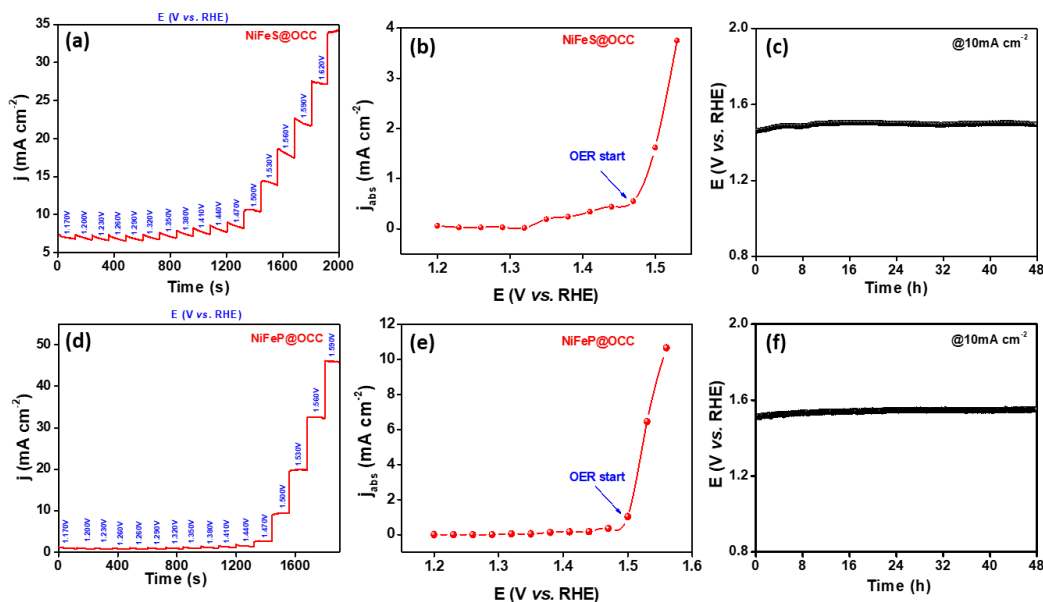


**Figure 3-6.** Stepwise chronoamperometry for (a) NiFeS@OCC & (d) NiFeP@OCC and their corresponding absolute current density curves for (b) NiFeS@OCC & (e) NiFeP@OCC and chronopotentiometric curves for (c) NiFeS@OCC & (f) NiFeP@OCC electrodes.



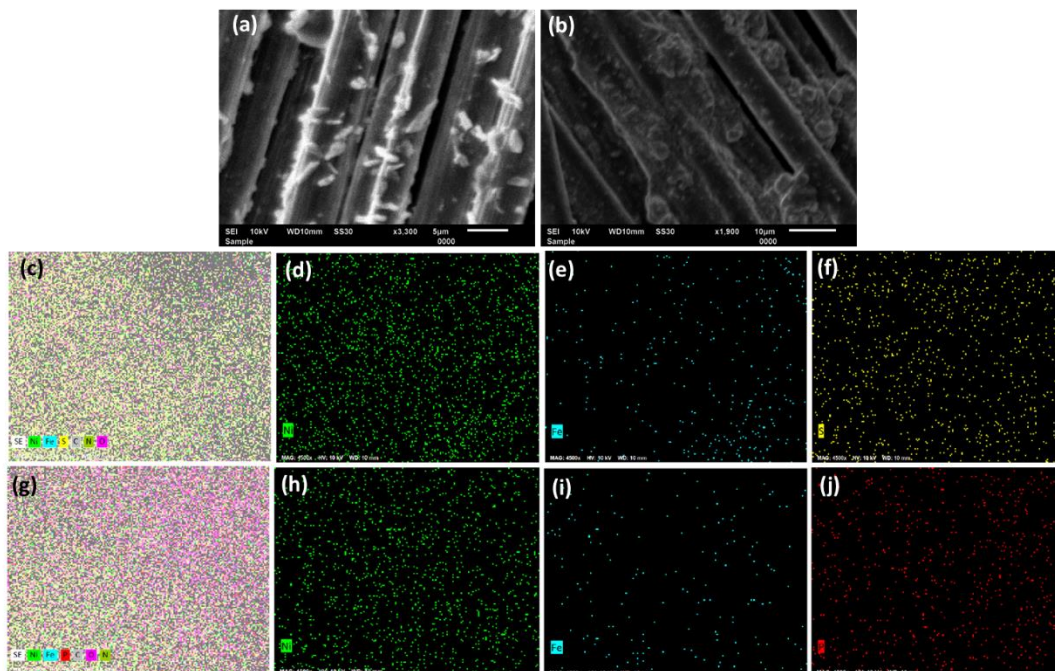


**Figure 3-7.** SEM images of (a) NiFeS@OCC, (b) NiFeP@OCC and elemental dot mapping images for (c) all elements, (d) Ni, (e) Fe, and (f) S elements of NiFeS@OCC electrode and (g) all elements, (h) Ni, (i) Fe, (j) P of NiFeP@OCC electrode after durability study.

Particularly, the NiFeP@OCC electrode required an overpotential of only 270 mV to achieve  $10 \text{ mA cm}^{-2}$  (Figure 3-5e) with a lower Tafel slope value of  $76 \text{ mVdec}^{-1}$  (Figure 3-5f) in comparison to 320 and 450 mV overpotential and Tafel slope of 168 and  $180 \text{ mV dec}^{-1}$  for monometallic NiP@OCC and FeP@OCC electrodes respectively, signifying the enhanced performance as a result of synergetic effect. Thereafter, the sequential chronoamperometric study was carried out for the further confirmation of the onset potential for OER. The recorded current response during stepwise increment of the working electrode potential for NiFeS@OCC and NiFeP@OCC electrodes (Figure 3-6) designated that onset potential determined from LSV curves are in agreement with the sequential chronoamperometric measurements. In addition to superior activity, long term operation stability of the electrode is also an imperative parameter to evaluate the performance of catalyst towards oxygen evolution. In addition, to evaluate the durability of the electrode under a highly alkaline environment, chronopotentiometry test was conducted at a

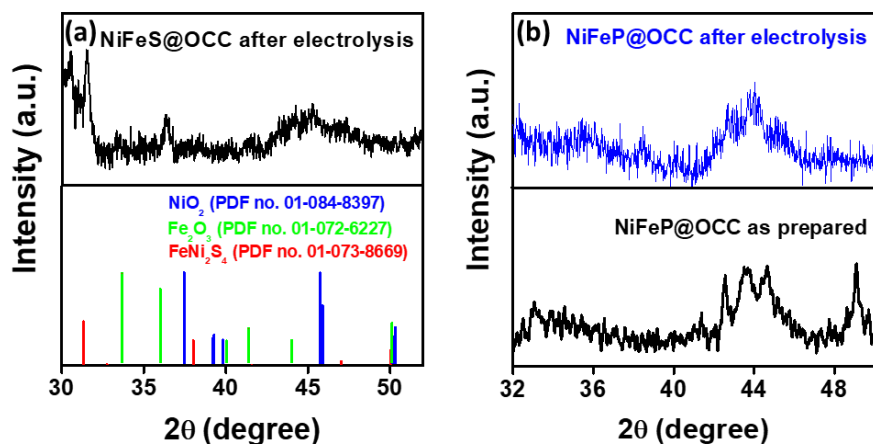


**Figure 3-8.** P-XRD pattern of (a) NiFeS@OCC and (b) NiFeP@OCC electrodes before and after durability study.

fixed current density of  $10 \text{ mA cm}^{-2}$  for 48 h for both NiFeS@OCC and NiFeP@OCC electrodes. As shown in Figure 3-6c & f, both the catalysts had maintained a stable potential response throughout the study without any significant deactivation. After the durability test, the electrode was subjected to P-XRD studies, SEM and EDS elemental dot mapping analysis wherein the SEM images after stability tests showed retention in deposition of the catalyst material over the carbon cloth (Figure 3-7a-b) and corresponding elemental dot mapping images (Figure 3-7c-j) displayed the presence of all the elements for NiFeS@OCC as well as NiFeP@OCC electrodes even after prolonged electrolysis over 48 h. Similarly, the retention of the P-XRD patterns for NiFeP@OCC after electrolysis validated the stability of catalyst whereas presence of  $\text{FeNi}_2\text{S}_4$  (PDF no. 01-073-8669),  $\text{Fe}_2\text{O}_3$  (PDF no. 00-039-0239) and  $\text{NiO}_2$  (PDF no. 01-089-8397) in P-XRD pattern of NiFeS@OCC after electrolysis indicated the partial surface oxidation of the catalyst (Figure 3-8). Furthermore, the stability for both the catalyst were examined by performing stepwise chronopotentiometry at multiple current densities from 10 to  $50 \text{ mA cm}^{-2}$ . Figure 3-9a-b clearly evidenced that the electrodes reveal excellent stability at multiple current densities and retain similar potential after switching back from higher to lower current densities, confirming excellent mass transport and mechanical robustness as well. It is noteworthy to mention that the



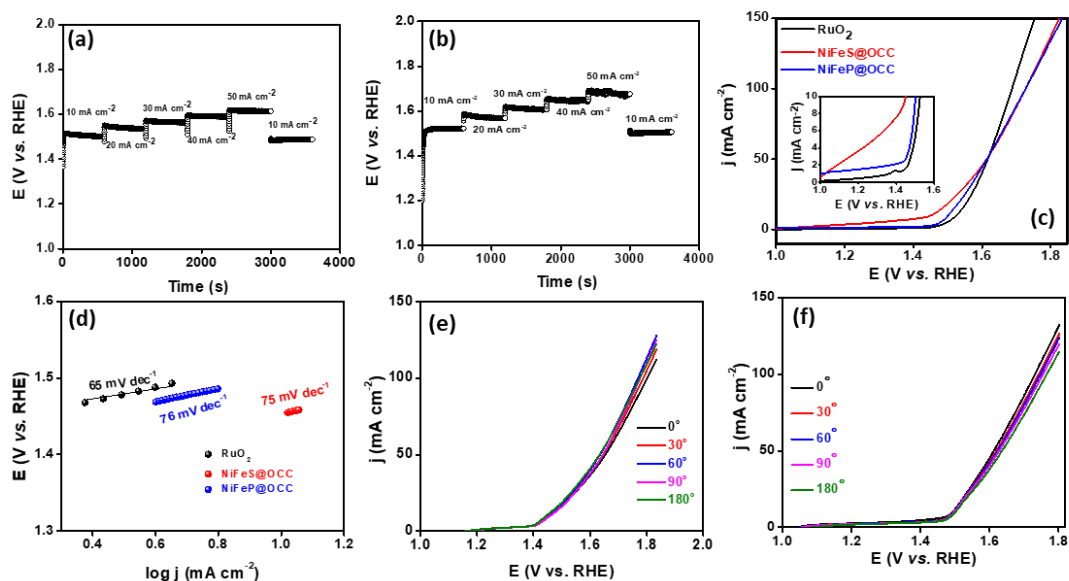


**Figure 3-9.** Stepwise chronopotentiometry for (a) NiFeS@OCC and (b) NiFeP@OCC electrodes, (c) LSV curve of various electrodes and (d) corresponding Tafel slopes. LSV curve at various bending angles for (e) NiFeS@OCC and (f) NiFeP@OCC electrodes during OER activity.

electrocatalytic activity of the as synthesized electrodes were found to be similar to that of the commercial benchmark RuO<sub>2</sub> catalyst in terms of Tafel slope (Figure 3-9c-d), but surpassed RuO<sub>2</sub> in terms of overpotential, as it required high overpotential of 290 mV to achieve 10 mA cm<sup>-2</sup> which was 70 and 20 mV greater than NiFeS@OCC and NiFeP@OCC respectively. More interestingly, thus developed self-standing three-dimensional electrode exhibited outstanding flexibility and maintained a similar electrochemical activity even after bending at various angles from 0°, 30°, 60°, 90° and 180° (Figure 3-9e-f) which demonstrated the applicability of these electrodes under extreme deformation conditions.

The excellent OER activity of these electrodes further captivated us to investigate HER activity under similar conditions. The oxygen functionalized carbon cloth (OCC) alone was found to be HER inactive even up to -0.6 V vs. RHE. Remarkably, NiFeS@OCC demonstrated a sharp increase in reductive current density and exhibited an overpotential of 223 mV at 10 mA cm<sup>-2</sup> in turn revealing

superior activity in comparison to control monometallic electrodes (Figure 3-10a). On the other hand, as indicated in Figure 3-10b, NiFeP@OCC achieved 10 mA cm<sup>-2</sup> current density at an overpotential of 300 mV, which was still a better activity than the other control samples. In this way, NiFeS@OCC showed a 77 mV lower overpotential than NiFeP@OCC to attain similar current density (Figure 3-10c). Also, the NiFeS@OCC showed a Tafel slope of 62.4 mV dec<sup>-1</sup> which was found to be significantly lower when compared to that of the NiFeP@OCC (Figure 3-10d) demonstrating a Volmer–Heyrovsky reaction mechanism where the rate-controlling step is electrochemical desorption of H<sub>2</sub>.<sup>46</sup> These results were found to be mediocre when compared with state of art catalyst Pt/C, which required only 60 mV of overpotential for hydrogen evolution with a lower Tafel slope of 59.2 mV dec<sup>-1</sup> (Figure 3-10d). In addition, the stability of NiFeS@OCC and NiFeP@OCC electrodes were examined by performing chronopotentiometric study at a fixed

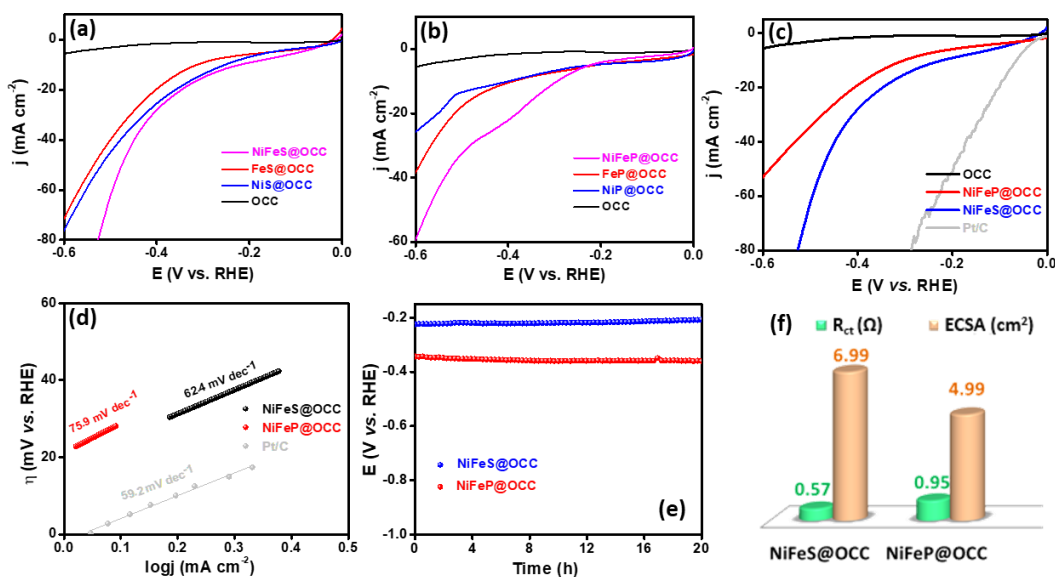


**Figure 3-10.** The LSVs for (a) NiFeS@OCC and (b) NiFeP@OCC with their control samples for the HER. (c) The HER activity compared with that of benchmark Pt/C under similar conditions. (d) Tafel slope, (e) chronopotentiometric measurements for NiFeS@OCC and NiFeP@OCC for 24 h, and (f) a bar diagram showing a comparison of ECSA and charge transfer resistance for NiFeP@OCC and NiFeS@OCC.

current density of  $10 \text{ mA cm}^{-2}$ . As witnessed from Figure 3-10e, both catalysts delivered a stable response over the stability window and such a high endurance perceived for 24 hrs of chronopotentiometry illustrate the suitability of the electrode for practical applications. In this way, intrinsically higher OER activity with sufficient HER activity of these electrodes make them a decent candidate for the bifunctional catalyst. The significant difference in the electrochemical activities of both the electrodes was revealed by the EIS study to understand the kinetics of interfacial charge transfer process at electrode-electrolyte interface (Table 3-1). The observed lower charge transfer resistance ( $R_{ct}$ ) i.e.,  $0.57 \Omega$  for NiFeS@OCC clearly evidenced the accelerated charge transfer dynamics at the electrode electrolyte interface which may be attributed to an adequate exposure of active sites for reactant species. On the other hand, NiFeP@OCC exhibited a relatively higher value of  $R_{ct}$  i.e.,  $0.95 \Omega$  designating the sluggish kinetics due to resistance at the electrode-electrolyte interface. This highlighted the fact that NiFeS@OCC exhibit faster kinetics as a consequence of facilitated electron transport at the catalyst surface which was further supported by higher electrochemical surface area (ECSA) of NiFeS@OCC ( $6.55 \text{ cm}^2$ ) in comparison to NiFeP@OCC ( $4.84 \text{ cm}^2$ ) which confirmed the presence of more exposed active sites resulting in a high catalytic performance (Table 3-2). For a better overview, we have compared the ECSA and  $R_{ct}$  of both catalysts in Figure 3-10f, signifying superior activity of NiFeS@OCC than that of NiFeP@OCC.

**Table 3-1: Electrochemical impedance analysis of various electrodes.**

S.No.	Electrode	$R_s (\Omega)$	$R_p (\Omega)$	$R_{ct} (\Omega)$
1.	NiFeS@OCC	2.12	2.69	0.57
2.	FeS@OCC	2.61	6.66	4.05
3.	NiS@OCC	2.23	5.98	3.75
4.	NiFeP@OCC	5.78	6.73	0.95
5.	FeP@OCC	6.45	9.73	3.28
6.	NiP@OCC	5.88	8.86	2.98

**Table 3-2: Electrochemical surface area (ECSA) of various electrodes.**

S.No.	Electrocatalyst	$C_{dl}^*$ ( $\mu\text{F}$ )	ECSA ( $\text{cm}^2$ )
1.	NiFeS@OCC	262	6.55
2.	NiFeP@OCC	193	4.82
3.	NiS@OCC	144	3.6
4.	NiP@OCC	140	3.5
5.	FeS@OCC	130	3.25
6.	FeP@OCC	136	3.4

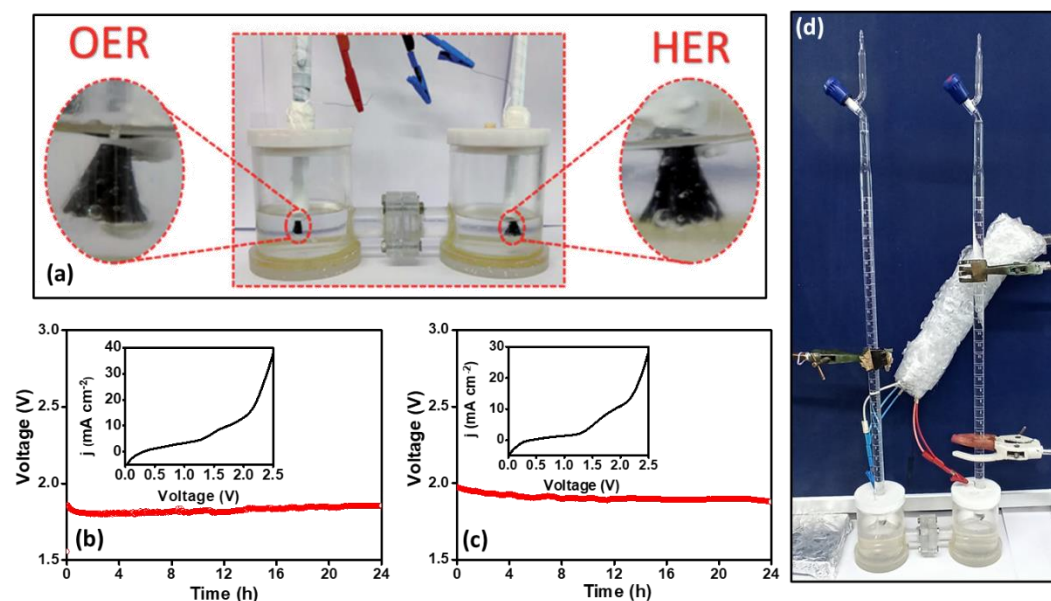


**Figure 3-11.** Photographs of full cell set up for overall water splitting showing hydrogen and oxygen evolution (a) demonstration of gaseous bubble formation on electrode (d) gaseous quantification eudiometrically. Chronopotentiometry curves at 10 mA cm<sup>-2</sup> with insets showing the LSVs of full cells assembled with (b) NiFeS@OCC and (c) NiFeP@OCC at both the anode and cathode for overall water splitting in 1M KOH.

**3-3.3 Catalytic activity towards overall water splitting:** Since these catalysts demonstrated a good bifunctional activity towards OER and HER, an alkaline water electrolyzer was developed by integrating NiFeS@OCC and NiFeP@OCC

as both anode and cathode separately in the two compartment cell setup containing 1M KOH electrolyte separated by a Nafion membrane. As shown in Figure 3-11a, abundant H<sub>2</sub> and O<sub>2</sub> bubbles on cathode and anode were observed during the full cell experiments for both NiFeS@OCC and NiFeP@OCC electrodes. The catalytic activity and durability towards overall water splitting was studied by performing LSV and chronopotentiometry. As observed in Figure 3-11b-c, NiFeS@OCC and NiFeP@OCC required only 1.75 V and 1.89 V respectively to reach 10 mA cm<sup>-2</sup>. Furthermore, durability of both the catalyst was evaluated by applying a constant current density of 10 mA cm<sup>-2</sup> and they exhibited good stability in the time scale of 24 hrs under total water splitting conditions without any significant potential alteration indicating the great performance of these electrodes to be a promising bifunctional catalyst along with high flexibility.

**3-3.4 Estimation of H<sub>2</sub> and O<sub>2</sub> evolved:** Finally, the amount of hydrogen and oxygen formed during the water electrolysis for NiFeS@OCC and NiFeP@OCC separately was estimated by eudiometric method.<sup>9</sup> A chronopotentiometric measurement at a current density of 10 mA cm<sup>-2</sup> was performed for one hour and the amount of gases evolved were collected in two different inverted burettes by the displacement of vertical water column (Figure 3-10d) and finally the molar mass of the gas was determined by applying ideal gas approximation. The ratio of the number of moles of H<sub>2</sub> and O<sub>2</sub> gas evolved during overall water splitting was found to be 1.7:1 for NiFeS@OCC and 1.65:1 for NiFeP@OCC respectively. Additionally, the amount of oxygen and hydrogen gas formed were quantified by performing chronoamperometry in a half-cell at an overpotential of 400 mV and 300 mV for OER and HER respectively followed by collecting O<sub>2</sub> and H<sub>2</sub> separately via eudiometric method. Turnover frequency (TOF) is a descriptor of kinetics of reaction i.e. higher TOF specifies the better conversion of the reactants into the products. The TOFs for NiFeP@OCC were found to be 0.018 and 0.013 s<sup>-1</sup> for OER and HER respectively, whereas NiFeS@OCC exhibited a TOF value of 0.019 s<sup>-1</sup> for the OER and 0.020 s<sup>-1</sup> for the HER. The observed trend for TOF

can be correlated with the Tafel slopes for the catalysts as both describe the reaction kinetics. Both the electrodes NiFeS@OCC and NiFeP@OCC demonstrated an analogous TOF during OER, whilst the difference is large during HER which is in accordance with the Tafel slope obtained for catalysts. Henceforth, this study highlights the potential of self-standing flexible NiFe deposited carbon cloth to be realized in practice for water electrolyzers.

### 3-4 Summary

In summary, we have developed a novel, cost-effective and straightforward single step electroless deposition approach for the fabrication of a highly flexible electrode by eliminating the use of conventional and highly expensive sensitizers and activators such as  $\text{SnCl}_2$  and  $\text{PdCl}_2$ . Thus developed NiFeS@OCC and NiFeP@OCC electrodes exhibited excellent OER activity and stability requiring only 220 mV and 270 mV of overpotential respectively to achieve  $10 \text{ mA cm}^{-2}$ . These electrode promise to be good bifunctional catalyst due to their ability to catalyze cathodic HER as well at 223 and 300 mV of overpotential for NiFeS@OCC and NiFeP@OCC respectively. An alkaline water electrolyzer set up with these electrodes demonstrated good activity and stability for both catalysts. The retention of electrocatalytic activity of these electrodes even under various deformation, along with the simple fabrication procedure, validated the application of these electrodes for the overall water splitting and will provide a new direction towards the development of cost-effective and stable flexible electrodes.

### 3-5 References

1. N.-T. Suen, S.-F. Hung, Q. Quan, N. Zhang, Y.-J. Xu and H. M. Chen, *Chem. Soc. Rev.*, 2017, **46**, 337-365.
2. L. Li, P. Wang, Q. Shao and X. Huang, *Chem. Soc. Rev.*, 2020, **49**, 3072-3106.
3. H. Zhang, A. W. Maijenburg, X. Li, S. L. Schweizer and R. B. Wehrspohn, *Adv. Funct. Mater.*, 2020, **30**, 2003261.
4. X. Ma, F. Gao, R. Dai, G. Liu, Y. Zhang, L. Lu and Y. Yu, *Anal. Methods*, 2020, **12**, 1845-1851.
5. Q. Yan, T. Wei, J. Wu, X. Yang, M. Zhu, K. Cheng, K. Ye, K. Zhu, J. Yan and D. Cao, *ACS Sustain. Chem. Eng.*, 2018, **6**, 9640-9648.

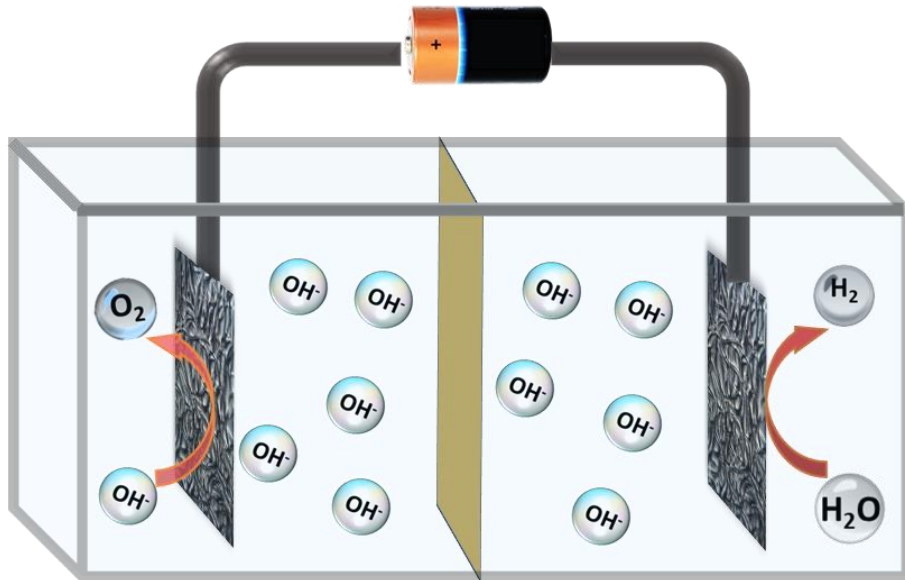
6. A. Wu, Y. Gu, B. Yang, H. Wu, H. Yan, Y. Jiao, D. Wang, C. Tian and H. Fu, *J. Mater. Chem. A*, 2020, **8**, 22938-22946.
7. Q. Liu, Z. Pan, E. Wang, L. An and G. Sun, *Energy Storage Mater.*, 2020, **27**, 478-505.
8. S. Chang, X. Huang, C. Y. A. Ong, L. Zhao, L. Li, X. Wang and J. Ding, *J. Mater. Chem. A*, 2019, **7**, 18338-18347.
9. A. Sahasrabudhe, H. Dixit, R. Majee and S. Bhattacharyya, *Nat. Commun.*, 2018, **9**, 2014.
10. S. D. Adhikary, A. Tiwari, T. C. Nagaiah and D. Mandal, *ACS Appl. Mater. Interfaces*, 2018, **10**, 38872-38879.
11. X. Du, H. Su and X. Zhang, *J. Catal.*, 2020, **383**, 103-116.
12. X. Du, H. Su and X. Zhang, *ACS Sustain. Chem. Eng.*, 2019, **7**, 16917-16926.
13. R. Illathvalappil, P. S. Walko, F. Kanheerampockil, S. K. Bhat, R. N. Devi and S. Kurungot, *Chem. Eur. J.*, 2020, **26**, 7900-7911.
14. P. Wang and B. Wang, *ChemSusChem*, 2020, **13**, 4795-4811.
15. T. Jin, Q. Han and L. Jiao, *Adv. Mater.*, 2020, **32**, 1806304.
16. L. An, L. Huang, P. Zhou, J. Yin, H. Liu and P. Xi, *Adv. Funct. Mater.*, 2015, **25**, 6814-6822.
17. H. Sun, Z. Yan, F. Liu, W. Xu, F. Cheng and J. Chen, *Adv. Mater.*, 2020, **32**, 1806326.
18. Y. Lv, A. Batool, Y. Wei, Q. Xin, R. Boddula, S. U. Jan, M. Z. Akram, L. Tian, B. Guo and J. R. Gong, *ChemElectroChem*, 2019, **6**, 2497-2502.
19. G. Barati Darband, M. Aliofkhazraei, S. Hyun and S. Shanmugam, *ACS Appl. Mater. Interfaces*, 2020, **12**, 53719-53730.
20. D. Zhu, M. Yan, R. Chen, Q. Liu, J. Liu, J. Yu, H. Zhang, M. Zhang, P. Liu and J. Li, *Chem. Eng. J.*, 2019, **371**, 348-355.
21. G. Zhou, A. Yang, G. Gao, X. Yu, J. Xu, C. Liu, Y. Ye, A. Pei, Y. Wu and Y. Peng, *Sci. Adv.*, 2020, **6**, eaay5098.
22. C. Young, J. Wang, J. Kim, Y. Sugahara, J. Henzie and Y. Yamauchi, *Chem. Mater.*, 2018, **30**, 3379-3386.
23. J. Zhou, Z. Wang, D. Yang, W. Zhang and Y. Chen, *Electrochim. Acta*, 2019, **317**, 408-415.
24. S. Abraham, B. Pal, K. Satyanarayana and V. Vaidyan, *J. Mater. Sci.*, 1990, **25**, 2839-2845.
25. M. P. Suryawanshi, U. V. Ghorpade, S. W. Shin, U. P. Suryawanshi, H. J. Shim, S. H. Kang and J. H. Kim, *Small*, 2018, **14**, 1801226.
26. Y. Tan, H. Wang, P. Liu, Y. Shen, C. Cheng, A. Hirata, T. Fujita, Z. Tang and M. Chen, *Energy Environ. Sci.*, 2016, **9**, 2257-2261.
27. T. Tian, H. Gao, X. Zhou, L. Zheng, J. Wu, K. Li and Y. Ding, *ACS Energy Lett.*, 2018, **3**, 2150-2158.
28. T. Tian, M. Zheng, J. Lin, X. Meng and Y. Ding, *Chem. Commun.*, 2019, **55**, 1044-1047.
29. F. Dionigi and P. Strasser, *Adv. Energy Mater.*, 2016, **6**, 1600621.
30. R.-Q. Li, B.-L. Wang, T. Gao, R. Zhang, C. Xu, X. Jiang, J. Zeng, Y. Bando, P. Hu and Y. Li, *Nano Energy*, 2019, **58**, 870-876.
31. Y. Guo, T. Park, J. W. Yi, J. Henzie, J. Kim, Z. Wang, B. Jiang, Y. Bando, Y. Sugahara and J. Tang, *Adv. Mater.*, 2019, **31**, 1807134.
32. C. G. Read, J. F. Callejas, C. F. Holder and R. E. Schaak, *ACS Appl. Mater. Interfaces*, 2016, **8**, 12798-12803.
33. L. Naderi, S. Shahrokhian and F. Soavi, *J. Mater. Chem. A*, 2020, **8**, 19588-19602.
34. H. Shi, G. Wen, Y. Nie, G. Zhang and H. Duan, *Nanoscale*, 2020, **12**, 5261-5285.

35. R. Koutavarapu, C. V. Reddy, B. Babu, K. R. Reddy, M. Cho and J. Shim, *Int. J. Hydrogen Energy*, 2020, **45**, 7716-7740.
36. Z.-F. Huang, J. Wang, Y. Peng, C.-Y. Jung, A. Fisher and X. Wang, *Adv. Energy Mater.*, 2017, **7**, 1700544.
37. C. Pittman Jr, G.-R. He, B. Wu and S. Gardner, *Carbon*, 1997, **35**, 317-331.
38. D. Tian, D. Y. Li, F. F. Wang, N. Xiao, R. Q. Liu, N. Li, Q. Li, W. Gao and G. Wu, *Surf. Coat. Technol.*, 2013, **228**, 27-33.
39. H. Zhou, J. Guo and J. Shang, *J. Electrochem. Soc.*, 2013, **160**, D233.
40. T. Yan, L. Li and L. Wang, *BioResources*, 2013, **8**, 340-349.
41. P. Ganesan, A. Sivanantham and S. Shanmugam, *J. Mater. Chem. A*, 2016, **4**, 16394-16402.
42. W.-K. Gao, J.-Q. Chi, Z.-B. Wang, J.-H. Lin, D.-P. Liu, J.-B. Zeng, J.-F. Yu, L. Wang, Y.-M. Chai and B. Dong, *J. Coll. Interface Sci.*, 2019, **537**, 11-19.
43. D. Zhang, L. Yuan, M. Lan, Y. Hu, J. Cai, W. Zhang and H. Li, *J. Magnetism Magnetic Mater.*, 2013, **346**, 48-52.
44. G. Jiang, N. Jiang, N. Zheng, X. Chen, J. Mao, G. Ding, Y. Li, F. Sun and Y. Li, *Energy Storage Mater.*, 2019, **23**, 181-189.
45. H. Jiang, J. Gu, X. Zheng, M. Liu, X. Qiu, L. Wang, W. Li, Z. Chen, X. Ji and J. Li, *Energy Environ. Sci.*, 2019, **12**, 322-333.
46. X. Lv, W. Tian, Y. Liu and Z.-Y. Yuan, *Mater. Chem. Front.*, 2019, **3**, 2428-2436.



## Chapter 4

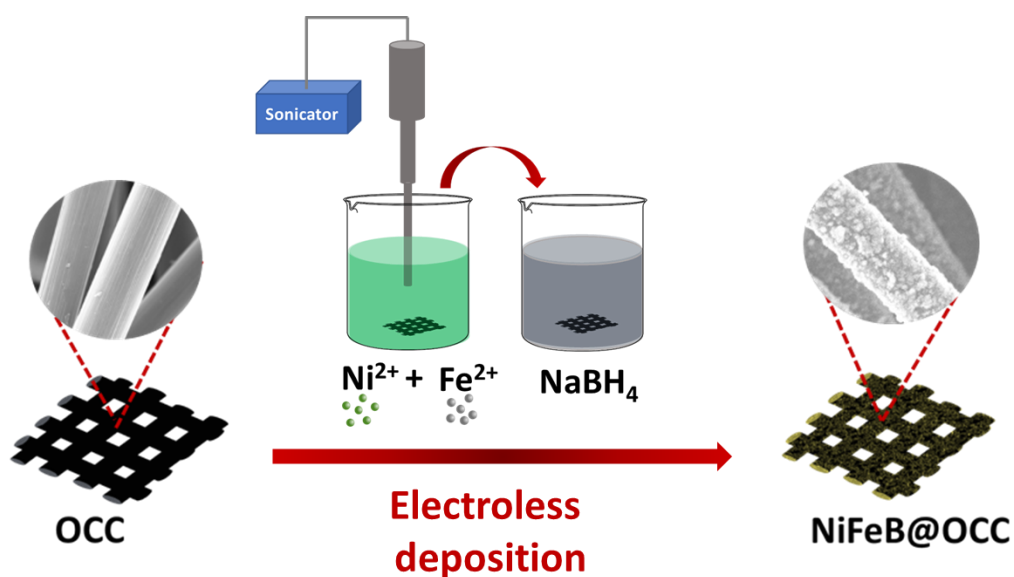
### Development of corrosion resistive flexible electrodes towards alkaline saline water splitting





# Chapter 4A

## Facile fabrication of NiFeB over carbon cloth electrode towards overall water splitting in alkaline and saline solutions



## 4A-1 Introduction

Hydrogen gas has emerged as a clean and sustainable energy carrier to overcome the global energy crisis. However, its major production is relying on natural gas reformation process which accounts for not only fossil fuel depletion but also carbon emission and thus creating serious environmental issues.<sup>1-3</sup> In this regard, electrochemical water splitting is one of the most striking methods for renewable hydrogen production to bring about energy conversion and storage.<sup>4-7</sup> In spite of being a clean and eco-friendly technology, the current commercial technologies for water electrolysis urge high purity water which in turn hinders the broader implementation of the water electrolyzers, especially in those area having shortage of freshwater even for drinking purpose.<sup>8</sup> The real scenario of the water distribution constitutes 96.5% of the total water on the earth is seawater whereas the availability of the non-frozen freshwater is less than 1% only.<sup>9</sup> Therefore the water purification system is compulsive either internally incorporated with electrolyser or external purification plant which raises the overall production cost.<sup>10</sup> In this aspect, the development of water electrolyser, in which low purity water or sea water can be directly employed as a feedstock can be a good alternative for cost effective and sustainable exploration of electrolyzers for green H<sub>2</sub> production.<sup>11</sup> Nevertheless, the direct seawater splitting has significant drawbacks such as presence of chloride ion in high concentration which reduces the faradaic efficiency due to competition with chloride oxidation reaction as well as lifetime of electrolyser can be reduced by impurities.<sup>12</sup> Furthermore, the high concentration of chloride ion in the seawater feedstock may also result into toxic chlorine gas evolution at anode (Equation 4.1) in competition to oxygen evolution reaction (OER).



The thermodynamic potential for chloride oxidation requires only 130 mV more than that for oxygen evolution reaction and also it is kinetically feasible since it involves two electrons in comparison to four electrons involved OER (Equation 4.2).



(Equation 4.2)

To overcome this problem, one can perform the sea water splitting in higher pH (alkaline) conditions so that the equilibrium potential of water oxidation is changed and simultaneously the thermodynamic window is extended. This is advantageous for avoiding the chloride oxidation reaction at lower potential values because in alkaline media, the hypochlorite ( $\text{ClO}^-$ ) formation (Equation 4.3) takes place at higher potentials which is too far from the thermodynamic potential for water oxidation.<sup>13</sup>



(Equation 4.3)

Thus, the development of alkaline water electrolyzer consisting of electrode material with good activity and high resistivity towards chloride ion corrosion could be a beneficial approach for the sustainable sea water splitting.<sup>14</sup> This advancement not only demands a good electrocatalyst but the coherent design of electrode architecture is equally important. Generally, the existing technologies are relying on application of catalyst slurry (prepared by mixing powder catalyst and insulating binder) on a rigid current collector which causes hindrance in ion transport and consequently suffer from loss of overall activity of the catalyst.<sup>15</sup> Therefore, the development of binder free, self-supported three-dimensional electrode is necessary. Interestingly, the three dimensional flexible electrodes having good mechanical flexibility and electrocatalytic activity under various deformation conditions has fascinated tremendously as they can be applied as bendable and foldable electrodes and can also be adjustable to various reactors without the loss of active materials.<sup>16</sup> In this context, carbon cloth is getting attraction for flexible energy storage and conversion applications, because of its improved mechanical strength, low cost and favorable fabrication procedure etc.<sup>17</sup> over the other conventional existing substrates (*e.g.*, metal foil/foam/wire, carbon

paper etc.<sup>6, 17-28</sup> which involve high fabrication cost, structural fragility and loss of active catalyst during deformation.<sup>15, 29</sup>

The flexible electrode fabrication with active electrocatalyst is another tedious task as generally practiced approaches have certain downsides, such as, chemical vapor deposition technique is expensive and requires harsh conditions, electrodeposition methods may result in non-uniform coating and hydrothermal process suffers from uncontrolled deposition over the substrate surface.,<sup>30, 31</sup> In this regard, electroless deposition can be a better approach for corrosion resistive self-standing flexible electrode fabrication as it can provide controlled uniform coating of the active material over the conductive or non-conductive substrate by a chemical reduction method in a simple and cost-effective manner.<sup>32-34</sup> The well-established state of art electrocatalysts for water splitting are noble metals (Pt, Ru, Ir, etc.) based materials and their high cost, low abundance and inadequate bifunctional activity prompt the researchers to search for highly abundant and low cost, non-noble metal-based catalysts.<sup>35-39</sup> Regarding this, NiFe based electrocatalysts mainly their oxides, oxyhydroxides, phosphides, chalcogenides, borides etc. have been explored as a promising electrocatalyst for overall water splitting which exhibit good catalytic activity with excellent stability.<sup>40-43</sup>

Herein, a facile and cost-effective fabrication strategy has been demonstrated for the fabrication of the binder free three-dimensional carbon cloth flexible electrode incorporated with active electrocatalyst NiFeB over oxygen functionalized carbon cloth, OCC (i.e., NiFeB@OCC) by a simple electroless deposition method. The prepared electrode provides the three-dimensional scaffold which could enable the effective mass transport, facilitate the adsorption of reactant species and also inhibit the gas bubble accumulation over the electrode surface. Moreover, the self-supported electrode avoids the hindrance of mass transport as well as the loss of conductivity caused by the use of insulating binder. This electrode demonstrated the remarkable performance towards OER and HER with an overpotential of 255 and 241 mV respectively to drive 20 mA cm<sup>-2</sup> in 1M KOH with excellent stability.

It also showed a promising electrocatalytic activity towards overall water splitting by achieving  $10 \text{ mA cm}^{-2}$  at a low cell potential of 1.69 V. The prepared NiFeB@OCC electrode performs alkaline saline water (1M KOH and 0.5M NaCl) splitting impressively with similar activity by maintaining long durability. Particularly, this auspicious electrocatalytic activity of such three dimensional flexible electrode can attract the researchers towards greener hydrogen production via saline water electrolysis.

## **4A-2 Electrode fabrication**

**4A-2.1 Pre-treatment of carbon cloth:** The commercial carbon cloth was treated with concentrated nitric acid prior to the coating of active electrocatalyst to generate oxygen groups on the surface of the carbon cloth by following a reported literature. The surface modified carbon cloth was washed with deionized water until it gets neutralized and finally dried in a hot air oven at 60 °C. The as-obtained carbon cloth was designated as OCC.

**4A-2.2 Fabrication of NiFeB@OCC:** The active electrocatalyst NiFeB was deposited over carbon cloth by electroless deposition method. First of all, a piece of OCC (1 cm x 1 cm) was immersed in an ice cold metal-bath solution composed of 3 mmole of ammonium ferrous sulfate ( $(\text{NH}_4)_2\text{SO}_4 \cdot \text{FeSO}_4 \cdot 6\text{H}_2\text{O}$ ) and 0.75 mmole of nickel nitrate ( $\text{NiNO}_3 \cdot 6\text{H}_2\text{O}$ ) in 30 mL water and sonicated for 1 minute. Then, the sonicated carbon cloth substrate was dipped into the ice-cold sodium borohydride solution (10 mmole in 50 mL water) under constant stirring till the seizing of effervescence. Thereafter, the NiFeB deposited carbon cloth was washed thoroughly with deionized water and finally with ethanol and kept for drying in hot air oven at 60 °C. Thus, fabricated carbon cloth electrode is designated as NiFeB@OCC. The bath composition for electroless deposition was optimized by varying the molar ratio of Ni and Fe from 1:1 to 4:1 and keeping rest of the procedure same. In the similar fashion, the control monometallic counterparts i.e. NiB and FeB were fabricated by taking only the corresponding metallic salt and

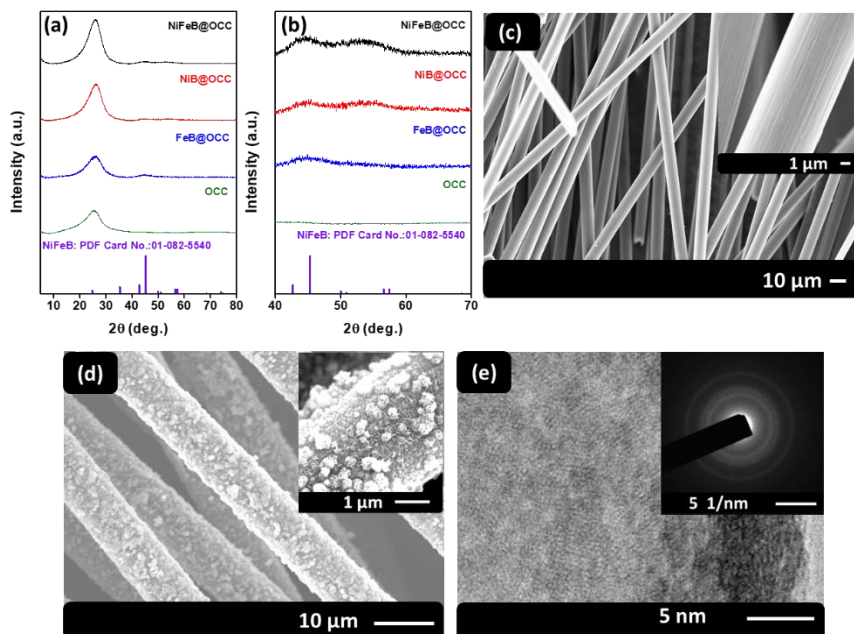


**Figure 4A-1** Powder X-ray diffraction pattern (a) comparison of OCC, FeB@OCC, NiB@OCC and NiFeB@OCC electrodes and (b) zoomed part of the particular range of the Figure 4A-1a, FE-SEM images of (c) bare OCC, (d) NiFeB@OCC, (e) HRTEM images of NiFeB@OCC (inset: SAED pattern).

keeping the rest of the procedure same.

### 4A-3 Results and discussion

**4A-3.1 Physical characterization:** The NiFeB@OCC flexible carbon cloth keeping the rest of the procedure same. electrode was fabricated by electroless deposition method. Initially the surface of commercially available carbon cloth was modified with oxygen functional groups by acidic treatment which in turn facilitate the anchoring of metal ions in the course of electroless deposition.<sup>44</sup> In order to incorporate the active electrocatalyst over the flexible substrate a piece (1 cm x 1 cm) of pretreated carbon cloth (OCC) was immersed in an ice cold metal-ion solution containing ammonium ferrous sulfate and nickel nitrate and continuously sonicated to adsorb the metallic ions on the surface of the OCC and finally dipped into the ice-cold sodium borohydride solution. Thereafter, the prepared electrodes were characterized by powder X-ray diffraction (PXRD), field



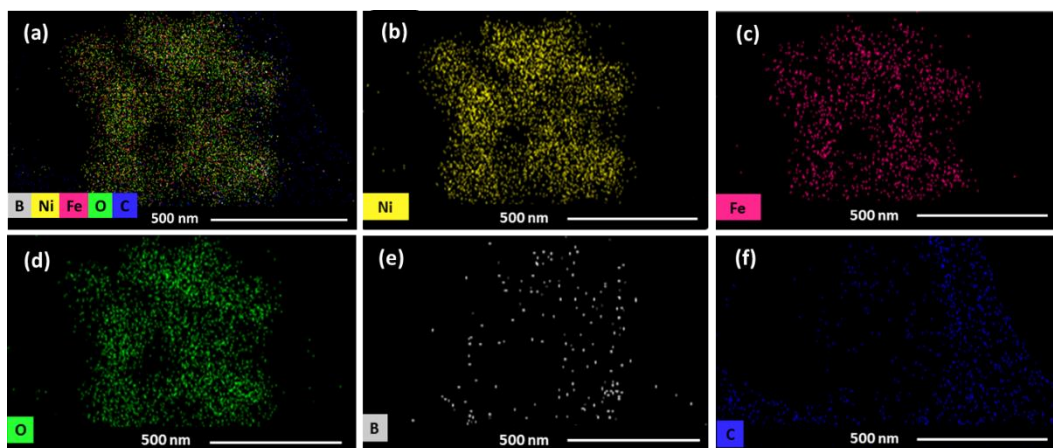


**Figure 4A-2.** Elemental dot mapping images of (a) all elements and separately for (b) Ni, (c) Fe, (d) O (e) B and (f) C of NiFeB@OCC electrode.

emission scanning electron microscopy (FESEM), transmission electron microscopy (TEM) and X-ray photoelectron microscopy (XPS) techniques. The microstructure of the prepared electrodes was analyzed by the PXRD patterns. As shown in Figures 4A-1(a-b) the OCC exhibits characteristic peaks at  $26.5^\circ$  corresponding to graphitic carbon whereas the additional broad peak from 42 to  $49^\circ$  corresponding to NiFeB (PDF No.. 01-082-5540) was observed for NiFeB@OCC and moreover the existence of all peaks associated with FeB@OCC and NiB@OCC in NiFeB@OCC further validates the formation of NiFeB. The FESEM image of bare OCC and NiFeB@OCC [Figures 4A-1(c-d)] demonstrated the uniform deposition of the NiFeB particles over carbon cloth. Additionally, the structural information was further analyzed with the help of TEM images and SAED pattern. As shown in Figure 4A-1e, the well dispersed NiFeB particles were found over the carbon cloth as visualized in the FESEM observations. Similarly, the corresponding SAED pattern confirmed the amorphous nature of deposited NiFeB particles (Figure 4A-1e, inset). Moreover, the elemental dot mapping images evidenced the uniform distribution of all the elements over the scanned area (Figure 4A-2) and confirmed the successful deposition of NiFeB over the oxygen functionalized carbon cloth. The chemical state and the composition of the NiFeB@OCC, were analyzed by (XPS). As shown in the XP survey spectra of the

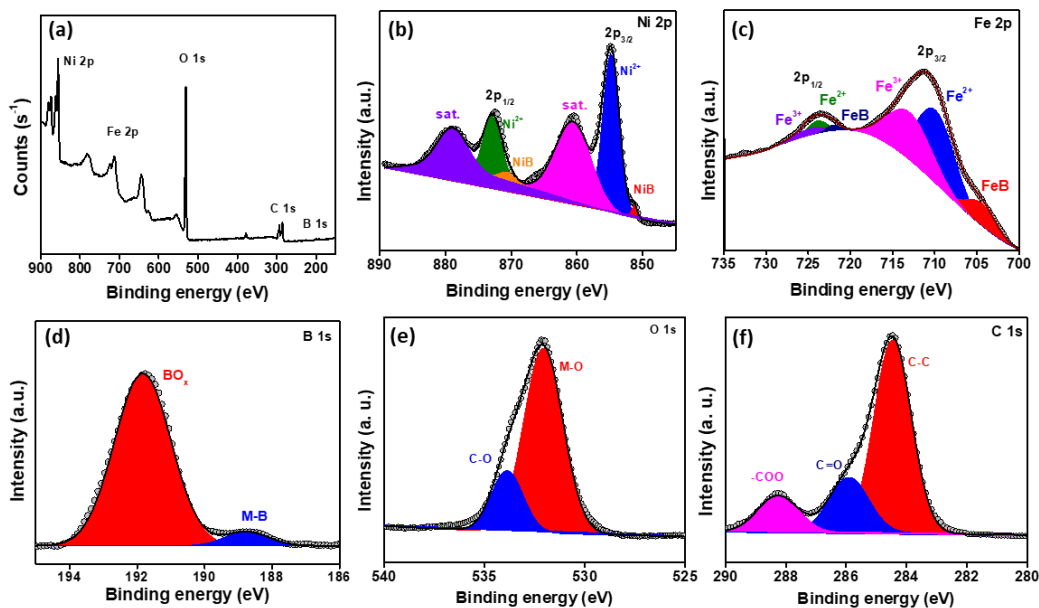


**Figure 4A-3.** (a) XPS survey spectra and deconvoluted XP spectra of (b) Ni 2p, (c) Fe 2p and (d) B 1s (e) O 1s and (f) C 1s for NiFeB@OCC electrode.

NiFeB@OCC (Figure 4A-3a), the peaks observed at binding energy of 856, 711, 532, 285 and 192 were ascribed to Ni 2p, Fe 2p, O1s, C1s, and B 1s respectively. The high-resolution Ni 2p XP spectra exhibited two major peaks at 855 and 873 eV corresponding to Ni 2p<sub>3/2</sub> and Ni 2p<sub>1/2</sub> respectively together with their satellite peaks (Figure 4A-3b), where the deconvoluted peaks at 852 eV and 870 eV confirmed the existence of NiB along with Ni<sup>2+</sup>. Similarly, the peaks at 710.5 & 714 eV and 722.5 & 727 eV in the deconvoluted high resolution Fe 2p XP spectra confirmed the presence of Fe in +2 & +3 oxidation states, whereas the peaks at 705 eV and 722 eV evidenced the existence of FeB species (Figure 4A-3c).<sup>45, 46</sup> Additionally, the deconvoluted high resolution B 1s XP spectra (Figure 4A-3d) demonstrated the peaks at 188.5 and 192 eV which confirmed the existence of M-B along with BO<sub>x</sub> whereas the presence of M-O & C-O peaks in deconvoluted O 1s spectra [Figures 4A-3(e-f)] further validated the presence of NiFeB in NiFeB@OCC.<sup>45, 47</sup>

#### 4A-3.2 Electrochemical study towards OER:

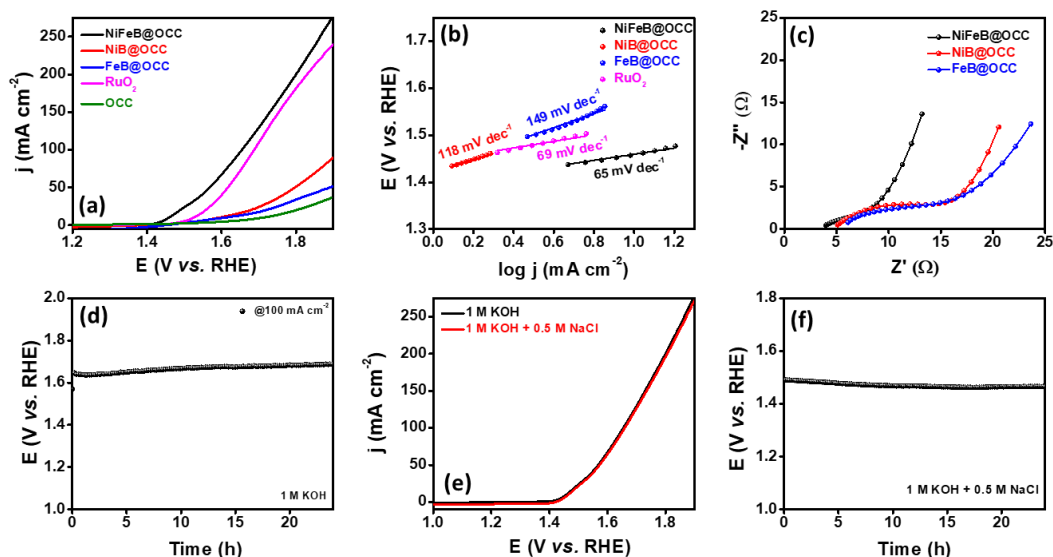


**Figure 4A-4.** (a) LSV curve for NiFeB@OCC with their control samples and state of art catalyst RuO<sub>2</sub> for OER, (b) corresponding Tafel slopes and (c) Nyquist plot for different electrodes and (d) chronopotentiometric curve recorded at 100 mA cm<sup>-2</sup> in 1 M KOH, (e) LSV curves in two different electrolyte system and (f) chronopotentiometric curve recorded at 100 mA cm<sup>-2</sup> in 1 M KOH + 0.5 M NaCl.

Initially, the applicability of the as prepared NiFeB@OCC electrode towards OER was studied by performing the linear sweep voltammetry (LSV) in 1 M KOH with a conventional three-electrode configuration. The as prepared NiFeB@OCC electrode directly employed as a working electrode (WE) without additional substrate and binder where Pt wire and graphite rod were used as a counter electrode (CE) during OER and HER study respectively with Hg/HgO/ 1M KOH as reference electrode (RE). The electrocatalytic activity of the NiFeB@OCC towards OER was compared with the control electrodes NiB@OCC, FeB@OCC and commercial benchmark RuO<sub>2</sub> catalyst by recording linear polarization curve at a scan rate of 1 mVs<sup>-1</sup>. The NiFeB@OCC exhibited the superior electrocatalytic activity as it requires only 255 mV overpotential to achieve 20 mA cm<sup>-2</sup>. The current density further increased on increasing the positive potential and attained a maximum current density of 275 mA cm<sup>-2</sup> at 1.90 V vs. RHE whereas the other control samples *viz.* NiB@OCC and FeB@OCC required 442 mV and 484 mV of

overpotential respectively and exhibit inferior current density at higher positive potential. Also, the commercial benchmark electrocatalyst  $\text{RuO}_2$  requires 320 mV for  $20 \text{ mA cm}^{-2}$  and achieves only  $239 \text{ mA cm}^{-2}$  at 1.90 V vs. RHE (Figure 4A-4a). The higher overpotential required to achieve the same current density by  $\text{NiB@OCC}$  and  $\text{FeB@OCC}$  than  $\text{NiFeB@OCC}$  designates that the synergetic effect resulted by the optimal combination of Ni:Fe ratio in  $\text{NiFeB@OCC}$  is responsible for tuning the electronic density, boosting the electrochemical activity and accelerating the kinetics of the oxygen evolution reaction.<sup>48</sup> The Tafel slope is a powerful indicator to evaluate the kinetics of the electrode reaction as it is associated with the surface coverage of the adsorbed intermediate species. The lower Tafel slope of  $65 \text{ mV dec}^{-1}$  for  $\text{NiFeB@OCC}$  than that for  $\text{NiB@OCC}$  and  $\text{FeB@OCC}$  118 and  $149 \text{ mV dec}^{-1}$  (Figure 4A-4b) respectively evidenced the boosted adsorption/desorption kinetics towards potential dependent electrocatalytic reaction. Moreover, it is noteworthy to mention that the as fabricated  $\text{NiFeB@OCC}$  electrode is able to show similar electrocatalytic activity to that of state of art  $\text{RuO}_2$  catalyst in terms of Tafel slope value but outperforms in terms of overpotential wherein  $\text{RuO}_2$  requires additional 65 mV to achieve  $20 \text{ mA cm}^{-2}$  of current density than  $\text{NiFeB@OCC}$ . The substantial difference in the electrocatalytic activity of the  $\text{NiFeB@OCC}$  electrode than  $\text{NiB@OCC}$  and  $\text{FeB@OCC}$  electrodes could be due to the varying interfacial charge transfer kinetics, which was revealed by conducting electrochemical impedance spectroscopy (EIS). As evident from Figure 4A-4c and Table 4a-1 the lower charge transfer resistance ( $R_{\text{ct}}$ ) of  $3.4 \Omega$  clearly indicates the accelerated charge transfer dynamics at the electrode and electrolyte interface which can be correlated to the adequate exposure of active sites for reactant species enhancing the electrochemical activity.<sup>49</sup> The higher electrocatalytic activity of the  $\text{NiFeB@OCC}$  was thereafter supported by the electrochemical surface area (ECSA). The higher ECSA of  $\text{NiFeB@OCC}$  in comparison to  $\text{NiB@OCC}$  and  $\text{FeB@OCC}$  (Table 4a-1) verifies the exposure of more active sites responsible for high electrocatalytic activity.

**Table 4A-1. Electrochemical Impedance and ECSA analysis for various electrodes.**

S.No.	Composites	$R_s (\Omega)$	$R_p (\Omega)$	$R_{ct} (\Omega)$	$C_{dl} (mF)$	ECSA ( $cm^2$ )
1	NiFeB@OCC	3.3	6.7	3.4	32.9	822
2	NiB@OCC	4.5	12.0	7.5	24.9	622
3	FeB@OCC	5.2	15.8	10.6	20.5	512

In addition to the superior electrocatalytic activity the durability of the electrode is also an imperious parameter for the evaluation of the performance of the electrocatalyst. In order to evaluate the long-term stability of the electrode under alkaline environment, chronopotentiometry study was performed at a fixed current density of  $100 \text{ mA cm}^{-2}$  for 24 hours (Figure 4A-4d) and it was found that the NiFeB@OCC electrode was able to maintain a constant potential response during the course of stability study without any notable deactivation.

Further, in order to examine the performance of the as fabricated electrode in the saline water environment, a simulated sea water electrolyte (0.5 M NaCl + 1 M KOH) was taken in which NiFeB@OCC demonstrated the similar activity as in 1 M KOH towards OER (Figure 4A-4e). The long-term durability of the electrode under the alkaline saline water was also evaluated by conducting the chronopotentiometric study. A negligible increment in the potential after 24 h (Figure 4A-4f) was obtained. The Faradic efficiency (FE) is another significant tool for the evaluation of the selectivity of the electrochemical reaction. Initially the amount of oxygen produced was quantified by eudiometric method and compared with the theoretical value. The estimated FE value (95-98%) in both the electrolyte solutions further confirmed the selective OER during electrolysis rather than competition with chloride oxidation (Figure 4A-5a). In order to evaluate the electrocatalytic activity under the harsh conditions, LSV was performed in 6 M KOH and 6 M KOH + 0.5 M NaCl electrolytes, where the NiFeB@OCC showed a promising activity even under harsh conditions (Figure 4A-5b).

Further, the effect of long-term electrolysis on electrode material was examined with the help of SEM and XPS techniques. The electrocatalyst coating was well

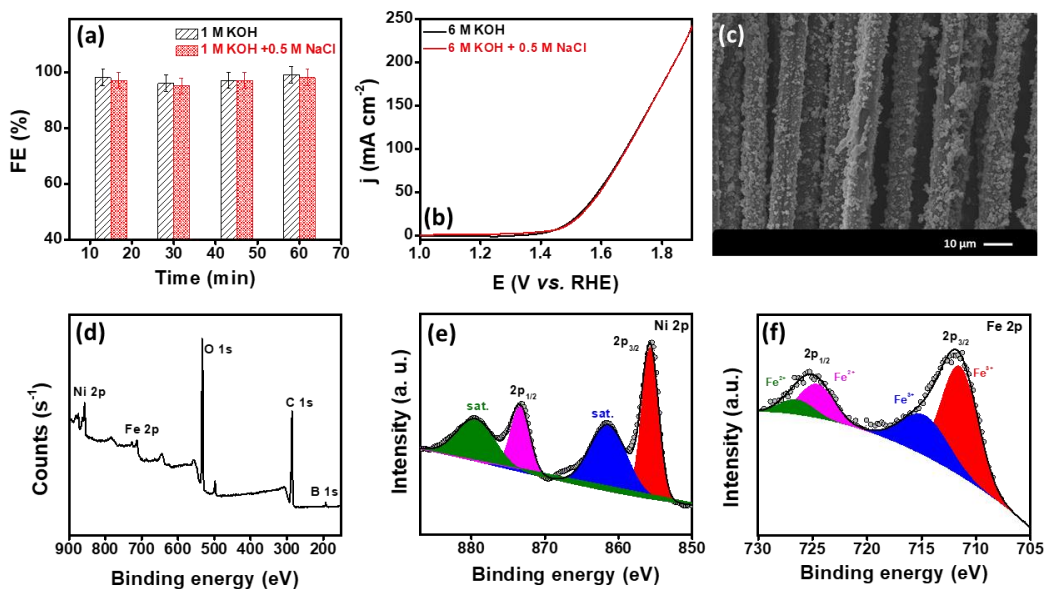


**Figure 4A-5.** (a) Faradic efficiency during OER in two different electrolyte systems (b) LSV curve for the NiFeB@OCC electrode during OER in 1 M KOH and 1 M KOH + 0.5 M NaCl electrolyte systems (c) SEM image of NiFeB@OCC electrode after stability study, (d) XPS survey spectra and deconvoluted XP spectra of (e) Ni 2p and (f) Fe 2p elements for NiFeB@OCC electrode after stability study.

retained over the substrate surface as observed in SEM image (Figure 4A-5c). Moreover, the existence of all the elements in XP spectra of the post operated electrode [Figures 4A-5(d-f)] further evidenced the stability of the electrode. Moreover, the XP spectra of the Ni 2p and Fe 2p for post OER electrode showed that there is a shift in binding energy for the Ni 2p<sub>3/2</sub> and Fe 2p<sub>3/2</sub> towards higher binding energy indicating the oxidation of metallic species to higher oxidation state during OER. Similarly, the increase in area of Fe<sup>3+</sup> and decrease in that of Fe<sup>2+</sup> further evidences the oxidation of the part of Fe<sup>2+</sup> to Fe<sup>3+</sup>. This also demonstrates the formation of nickel iron oxyhydroxide during the course of the OER. Thus, it can be concluded that the synergistic role of NiFe is responsible for the enhanced activity towards OER serving itself as active site.<sup>50, 51</sup> Besides the long-term durability test, the stability for the electrode was examined by performing chronopotentiometry at different current density ranging from 10 mA cm<sup>-2</sup> to 50 mA cm<sup>-2</sup> in both electrolytes. From Figures 4A-6(a-b), it was evident that the

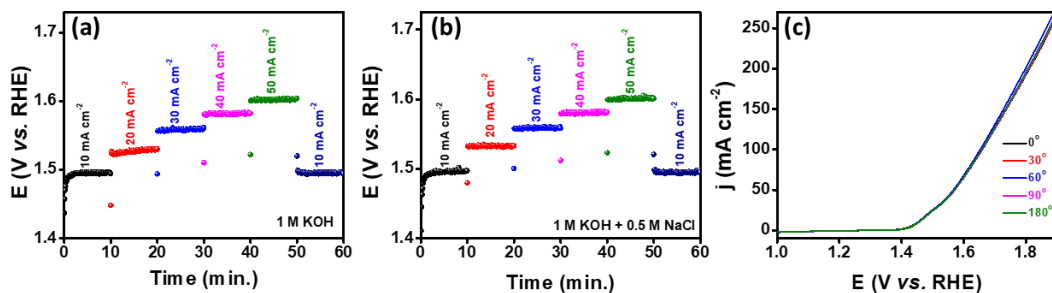


**Figure 4A-6.** Chronopotentiometry at various current densities for NiFeB@OCC in (a) 1 M KOH, (b) 1 M KOH + 0.5 M NaCl and (c) LSVs of NiFeB@OCC at various bending angles.

electrode revealed an outstanding stability at various current densities and moreover maintains similar potential even after switching back to lower potential from higher potential supporting the efficient mass transport as well as mechanical robustness of the electrode. Additionally, the flexibility of the electrode during the electrolysis was evaluated by performing the LSV in anodic sweep by bending the electrode at various angles from 0° to 180°. The as fabricated self-standing electrode displayed an excellent flexibility and similar electrocatalytic activity at various bending angles (Figure 4A-6c) which illustrates the applicability of three dimensional NiFeB@OCC electrode under various deformation conditions.

#### 4A-3.3 Electrochemical performance towards HER

The excellent OER activity further motivated us to investigate the HER activity under similar environment. Initially the LSV was recorded by sweeping the potential from 0 to -0.5V vs. RHE with a scan rate of 1 mVs<sup>-1</sup>. The NiFeB@OCC demonstrate a sharp increase in current density with an overpotential of 241 mV at 20 mA cm<sup>-2</sup> whereas the NiB@OCC and FeB@OCC requires 317 mV and 408 mV to achieve the same current density which in turn verifies the superior activity of the NiFeB@OCC over other control electrodes (Figure 4A-7a). The mechanism of the HER was further studied on the basis of Tafel slope (Figure 4A-7b). The calculated Tafel slope of 82 mV dec<sup>-1</sup> suggested the involvement of Volmer-Heyrovsky mechanism during HER where the desorption of H<sub>2</sub> is the rate controlling step.<sup>52</sup> The electrocatalytic activity of the as fabricated NiFeB@OCC

electrode is found to be mediocre in comparison to state of art catalyst Pt/C which required 102 mV overpotential for 20 mA cm<sup>-2</sup> current density and 61 mV dec<sup>-1</sup> Tafel slope towards HER. Furthermore, the stability of the electrode was evaluated by chronopotentiometric study at current density 20 mA cm<sup>-2</sup>. The NiFeB@OCC electrode delivered almost constant electrocatalytic activity for 24 hours (Figure 4A-7 c) revealing the high endurance. The electrode was further analyzed after the durability test for the identification of the active site. The high-resolution XP spectra [Figures 4A-7(d-e)] recorded after HER shows the shifting of the peaks

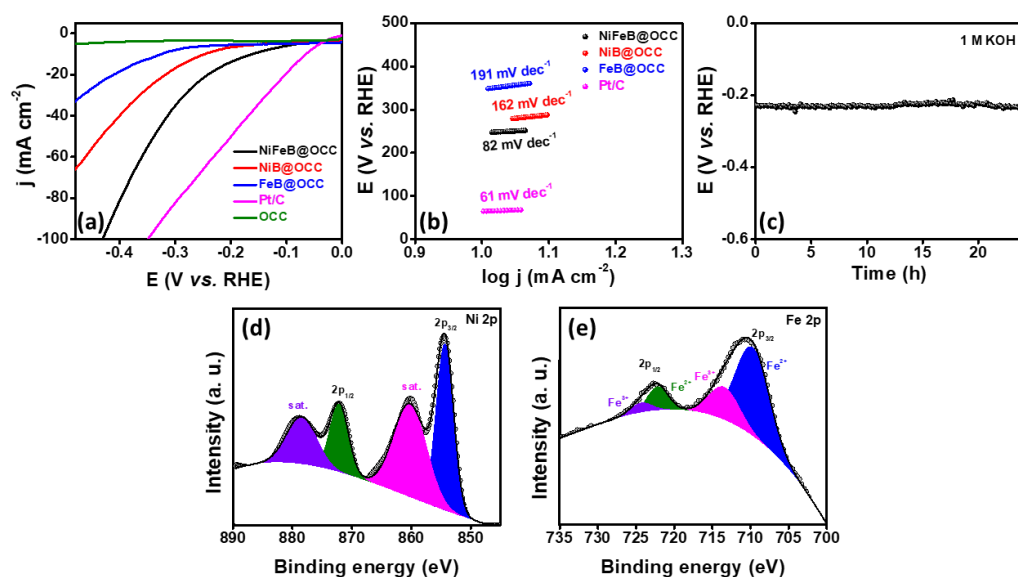


**Figure 4A-7.** (a) Linear sweep voltammogram for NiFeB@OCC with other control electrodes and state of art catalyst Pt/C for HER, (b) corresponding Tafel slopes and (c) chronopotentiometric curve recorded at 20 mA cm<sup>-2</sup> in 1 M KOH. Deconvoluted XP spectra for (d) Ni 2p and (e) Fe 2p after durability test during HER.

corresponding to Ni 2p<sub>3/2</sub> and Fe 2p<sub>3/2</sub> towards lower binding energy and evidences the reduction of the metallic species towards lower oxidation state which causes decrease in surface electron density during which results reduction in the adsorption free energy with H\* and finally promotes HER activity. Thus, the synergistic contribution of NiFe is responsible for the enhanced activity towards HER.<sup>50</sup> Moreover, the poor activity of the control electrodes NiB@OCC and FeB@OCC in comparison to NiFeB@OCC, as evidenced by current response



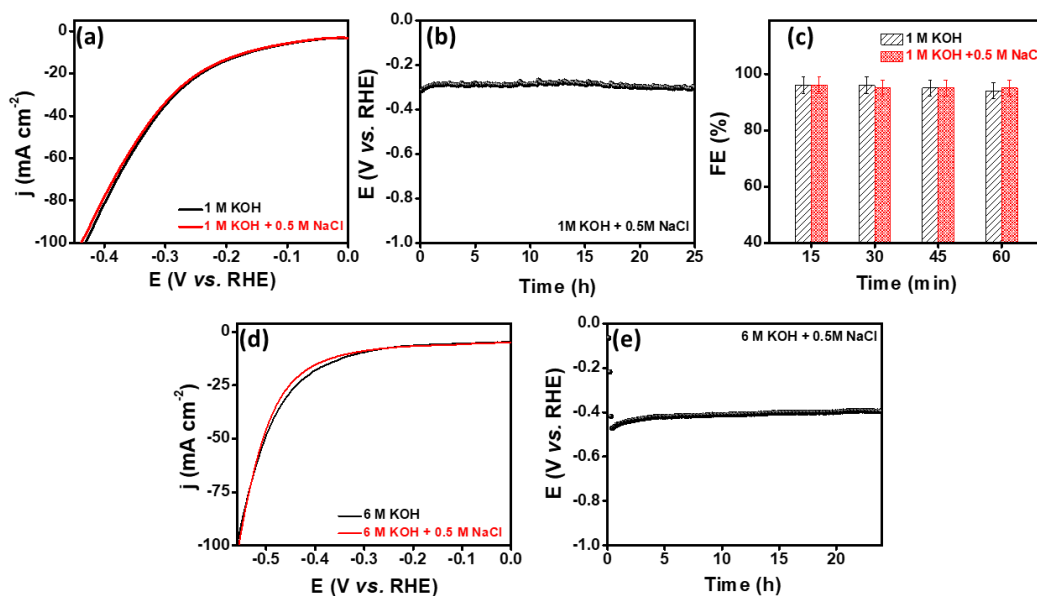


**Figure 4A-8.** (a) LSV curves at 1 M KOH and 1 M KOH + 0.5 M NaCl electrolyte system, (b) chronopotentiometric curve recorded in 1 M KOH + 0.5 M NaCl (c) Faradic efficiency in two different electrolyte system (d) LSV curves at 6 M KOH and 6 M KOH + 0.5 M NaCl electrolyte system and (e) chronopotentiometric curve in 6 M KOH + 0.5 M NaCl electrolyte system for NiFeB@OCC during HER.

during HER further supported the role of synergistic effect of NiFe. The activity and durability of the electrode against the probable chloride corrosion was studied by performing LSV and chronopotentiometry under the alkaline saline electrolyte. The achievement of similar electrocatalytic activity and long-term durability without voltage increment or obvious corrosion (Figures 4A-8(a-b)) evidenced its suitability towards saline water electrolysis. Additionally, the observed 95-98% Faradic efficiency for the hydrogen evolution reaction in both electrolyte system validated the low probability of chloride corrosion and suggests its high competence in different electrolyte solutions (Figure 4A-8c). Similarly, the electrocatalytic activity under the harsh conditions was studied to evaluate the feasibility for practical application by performing LSV and chronopotentiometry in 6 M KOH and 6 M KOH + 0.5 M NaCl electrolytes where the NiFeB@OCC demonstrated a quite inferior activity (Figure 4A-8d), but good durability (Figure

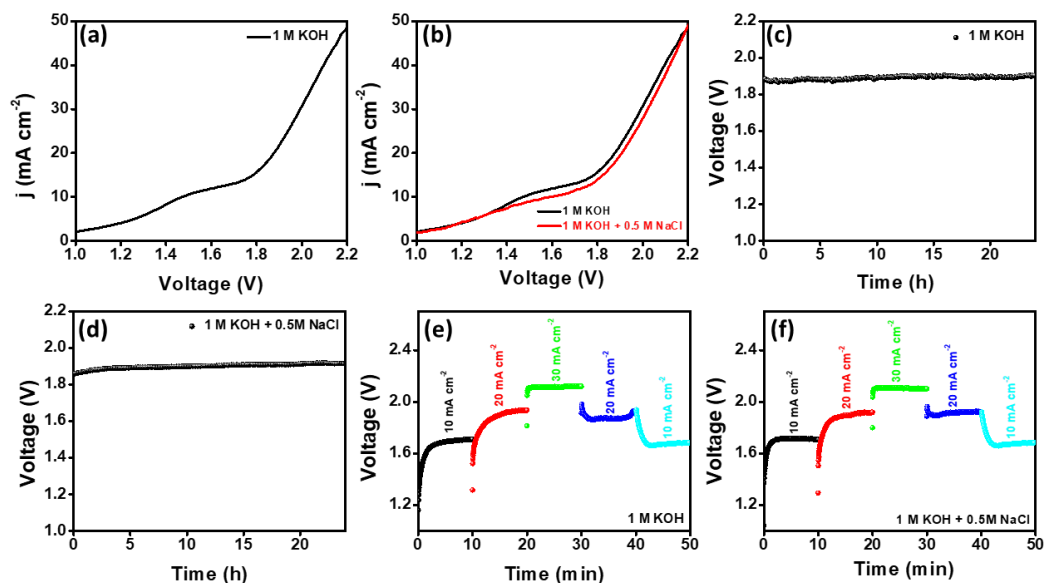


**Figure 4A-9.** LSV curve recorded for a full cell assembled with NiFeB@OCC at both anode and cathode in (a) 1 M KOH and (b) two different electrolytes. Chronopotentiometry curves at 20 mA cm<sup>-2</sup> in (c) 1 M KOH and (d) 1 M KOH + 0.5 M NaCl. Chronopotentiometry at various current densities in (e) 1 M KOH and (f) 1 M KOH + 0.5 M NaCl electrolyte systems for NiFeB@OCC during overall water splitting.

4A-8e) under the severe conditions also. The increased degree of alkalinity and viscosity of the electrolyte solution caused the high local alkalinity and viscosity and resulted significant decrease in activity.<sup>53</sup> Therefore, comparable electrocatalytic activity and long-term durability of the electrode in the saline alkaline electrolyte illustrated the suitability of the electrode towards practical applications. However, the electrocatalytic activity of the NiFeB@OCC was found to be comparable towards HER but the OER activity was superior in comparison to state of art catalysts. Consequently, the excellent OER activity with adequate HER activity proposes it as a promising electrode for the bifunctional electrocatalyst to carry out saline water splitting.

#### 4A-3.4 Full cell study for overall water/saline water splitting

By considering the promising bifunctional activity of the electrode, full cell study was carried out by constructing alkaline water electrolyzer integrated with

NiFeB@OCC as both anode and cathode in a two-compartment cell portioned by Nafion membrane. The LSV and chronopotentiometry were performed to evaluate the activity and durability of the catalyst towards overall water splitting in both 1M KOH and 0.5 M NaCl + 1 M KOH conditions separately. As observed from Figures 4A-9 (a-b) the NiFeB@OCC required only 1.69 V and 1.72 V to reach  $10 \text{ mA cm}^{-2}$  in 1M KOH and 1 M KOH + 0.5 M NaCl environments respectively. Similarly, the chronopotentiometric curve recorded for current density  $20 \text{ mA cm}^{-2}$  illustrated the good stability without significant increase in potential during the total water splitting for the time scale of 24 hours [Figures 4A-9(c-d)]. Additionally, the consistency in the chronopotentiometric response recorded for different current density ranging from  $10 \text{ mA cm}^{-2}$  to  $30 \text{ mA cm}^{-2}$  and back to the  $10 \text{ mA cm}^{-2}$  in both electrolytes [Figures 4A-9(e-f)] further supported the excellent mass transport as well as mechanical robustness of the electrode.

#### **4A-4 Summary**

In this study, we have successfully fabricated a self-standing and highly flexible NiFeB deposited binder free carbon cloth electrode by a cost-effective single step electroless deposition method, which reveal a promising corrosion resistive bifunctional activity towards overall saline water splitting. The as fabricated NiFeB@OCC demonstrated the admirable OER performance with excellent durability even in corrosive environment in which it requires only 255 mV overpotential to achieve  $20 \text{ mA cm}^{-2}$  current density whereas it exhibits moderate HER activity demanding 241 mV overpotential. The two-electrode based alkaline water electrolyzer further demonstrated good activity with excellent durability towards overall water splitting which even achieves comparable activity under harsh conditions also. Moreover, by maintaining the same electrocatalytic activity under various deformation conditions verifies that self-standing NiFeB@OCC bifunctional flexible electrode can be an effective corrosion resistive electrode for saline water splitting. Therefore, this study can deliver a new insight to develop a cost-effective corrosion resistive flexible electrode for water splitting.

## 4A-5 References

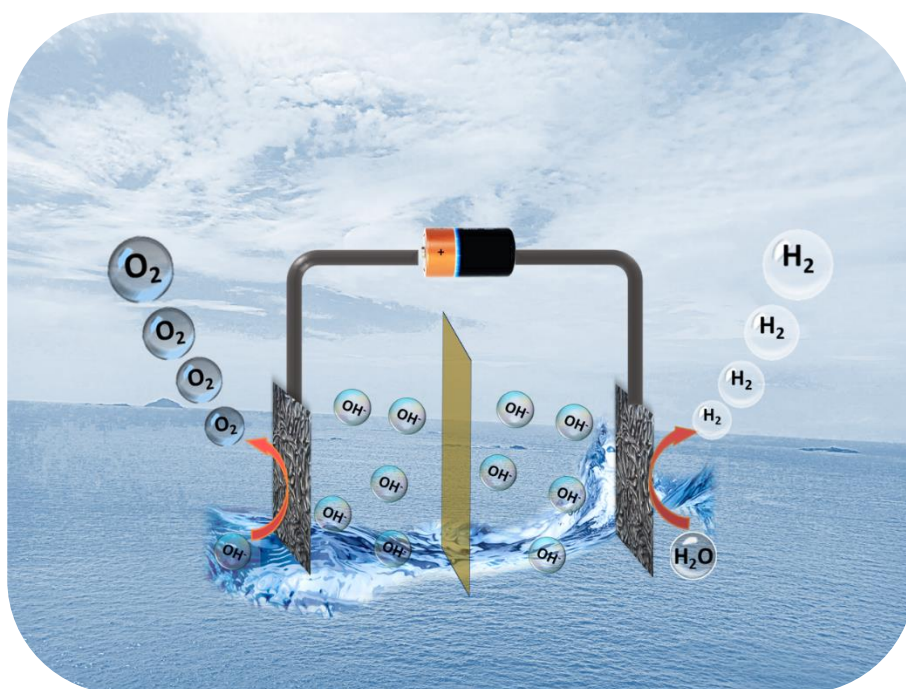
1. E. L. Hu, Y. F. Feng, J. W. Nai, D. Zhao, Y. Hu and X. W. Lou, *Energy Environ. Sci.*, 2018, **11**, 872-880.
2. Z. P. Ifkovits, J. M. Evans, M. C. Meier, K. M. Papadantonakis and N. S. Lewis, *Energy Environ. Sci.*, 2021, **14**, 4740-4759.
3. X. Li, L. Zhao, J. Yu, X. Liu, X. Zhang, H. Liu and W. Zhou, *Nanomicro Lett*, 2020, **12**, 131.
4. S. Gupta, M. K. Patel, A. Miotello and N. Patel, *Adv. Funct. Mater.*, 2020, **30**, 1906481.
5. H. Sun, X. Xu, Y. Song, W. Zhou and Z. Shao, *Adv. Funct. Mater.*, 2021, **31**, 2009779.
6. P. L. Zhai, Y. X. Zhang, Y. Z. Wu, J. F. Gao, B. Zhang, S. Y. Cao, Y. T. Zhang, Z. W. Li, L. C. Sun and J. G. Hou, *Nat. Commun.*, 2020, **11**, 1-12.
7. L. Liao, Y. Zhao, H. Zhou, D. Li, Y. Qi, Y. Zhang, Y. Sun, Q. Zhou and F. Yu, *Small*, 2022, **18**, 2203171.
8. S. Dresp, F. Dionigi, M. Klingenhof and P. Strasser, *ACS Energy Lett.*, 2019, **4**, 933-942.
9. S. Ahmadvand, B. Abbasi, B. Azarfar, M. Elhashimi, X. Zhang and B. Abbasi, *Water*, 2019, **11**, 696.
10. W. Tong, M. Forster, F. Dionigi, S. Dresp, R. Sadeghi Erami, P. Strasser, A. J. Cowan and P. Farràs, *Nat. Energy*, 2020, **5**, 367-377.
11. Q. Zhou, L. Liao, H. Zhou, D. Li, D. Tang and F. Yu, *Mater. Today Phys.*, 2022, 100727.
12. J. N. Hausmann, R. Schlögl, P. W. Menezes and M. Driess, *Energy Environ. Sci.*, 2021, **14**, 3679-3685.
13. Y. Kuang, M. J. Kenney, Y. T. Meng, W. H. Hung, Y. J. Liu, J. E. Huang, R. Prasanna, P. S. Li, Y. P. Li, L. Wang, M. C. Lin, M. D. McGehee, X. M. Sun and H. J. Dai, *Proc. Natl. Acad. Sci. U. S. A.*, 2019, **116**, 6624-6629.
14. S. Gupta, M. Forster, A. Yadav, A. J. Cowan, N. Patel and M. Patel, *ACS Appl. Energy Mater.*, 2020, **3**, 7619-7628.
15. Q. Y. Jin, B. W. Ren, H. Cui and C. X. Wang, *Applied Catalysis B-Environmental*, 2021, **283**, 119643.
16. Z. Yang, C. Zhao, Y. Qu, H. Zhou, F. Zhou, J. Wang, Y. Wu and Y. Li, *Adv. Mater.*, 2019, **31**, e1808043.
17. H. M. Shi, G. L. Wen, Y. Nie, G. H. Zhang and H. G. Duan, *Nanoscale*, 2020, **12**, 5261-5285.
18. D. Kong, Y. Gao, Z. Xiao, X. Xu, X. Li and L. Zhi, *Adv. Mater.*, 2019, **31**, e1804973.
19. M. I. Jamesh, Y. Kuang and X. Sun, *ChemCatChem*, 2019, **11**, 1550-1575.
20. G. Li, R. Li and W. Zhou, *Nanomicro Lett*, 2017, **9**, 46.
21. C. Zhao, X. T. Jia, K. W. Shu, C. C. Yu, G. G. Wallace and C. Y. Wang, *J. Mater. Chem. A*, 2020, **8**, 4677-4699.
22. Z. Lu, Y. Chao, Y. Ge, J. Foroughi, Y. Zhao, C. Wang, H. Long and G. G. Wallace, *Nanoscale*, 2017, **9**, 5063-5071.
23. M. H. Ye, Z. P. Zhang, Y. Zhao and L. T. Qu, *Joule*, 2018, **2**, 245-268.
24. K. Jayaramulu, D. P. Dubal, B. Nagar, V. Ranc, O. Tomanec, M. Petr, K. K. R. Datta, R. Zboril, P. Gomez-Romero and R. A. Fischer, *Adv. Mater.*, 2018, **30**, e1705789.
25. L. Liu, Y. X. Yin, J. Y. Li, S. H. Wang, Y. G. Guo and L. J. Wan, *Adv. Mater.*, 2018, **30**, 1706216.
26. H. Qiu, L. Zhao, M. Asif, X. Huang, T. Tang, W. Li, T. Zhang, T. Shen and Y. Hou, *Energy Environ. Sci.*, 2020, **13**, 571-578.
27. X. G. Li, B. Y. Guan, S. Y. Gao and X. W. Lou, *Energy Environ. Sci.*, 2019, **12**, 648-655.
28. A. Kafle, M. Kumar, D. Gupta and T. C. Nagaiah, *J. Mater. Chem. A*, 2021.
29. A. Sahasrabudhe, H. Dixit, R. Majee and S. Bhattacharyya, *Nat. Commun.*, 2018, **9**, 1-14.
30. K. L. Choy, *Prog. Mater. Sci.*, 2003, **48**, 57-170.
31. E. Kalinina and E. Pikalova, *Materials (Basel)*, 2021, **14**, 5584.

32. A. Kafle, M. Kumar, D. Gupta and T. C. Nagaiah, *J. Mater. Chem. A*, 2021, **9**, 24299-24307.
33. A. Kafle, N. Thakur and T. C. Nagaiah, *J. Mater. Chem. B*, 2022, **10**, 3681-3686.
34. F. Muench, *ChemElectroChem*, 2021, **8**, 2993-3012.
35. R. Gao and D. Yan, *Adv. Energy Mater.*, 2020, **10**, 1900954.
36. H. Li, P. Wen, Q. Li, C. Dun, J. Xing, C. Lu, S. Adhikari, L. Jiang, D. L. Carroll and S. M. Geyer, *Adv. Energy Mater.*, 2017, **7**, 1700513.
37. Y. Yan, B. Y. Xia, B. Zhao and X. Wang, *J. Mater. Chem. A*, 2016, **4**, 17587-17603.
38. J. Zhu, L. Hu, P. Zhao, L. Y. S. Lee and K.-Y. Wong, *Chem. Rev.*, 2019, **120**, 851-918.
39. L. Liao, C. Cheng, H. Zhou, Y. Qi, D. Li, F. Cai, B. Yu, R. Long and F. Yu, *Mater. Today Phys.*, 2022, **22**, 100589.
40. P. M. Bodhankar, P. B. Sarawade, G. Singh, A. Vinu and D. S. Dhawale, *J. Mater. Chem. A*, 2021, **9**, 3180-3208.
41. C. W. Liang, P. C. Zou, A. Nairan, Y. Q. Zhang, J. X. Liu, K. W. Liu, S. Y. Hu, F. Y. Kang, H. J. Fan and C. Yang, *Energy Environ. Sci.*, 2020, **13**, 86-95.
42. F. Cai, L. Liao, Y. Zhao, D. Li, J. Zeng, F. Yu and H. Zhou, *J. Mater. Chem. A*, 2021, **9**, 10199-10207.
43. H. Zhou, F. Yu, J. Sun, R. He, S. Chen, C.-W. Chu and Z. Ren, *Proceedings of the National Academy of Sciences*, 2017, **114**, 5607-5611.
44. T. G. Yan, L. H. Li and L. J. Wang, *Bioresources*, 2013, **8**, 340-349.
45. G. Liu, D. Y. He, R. Yao, Y. Zhao and J. P. Li, *Nano Res.*, 2018, **11**, 1664-1675.
46. Y. Zhao, F. Ma, Z. Wang, P. Wang, Y. Liu, H. Cheng, Y. Dai, Z. Zheng and B. Huang, *J. Alloys Compd.*, 2022, **903**, 163741.
47. Y.-W. Chen and N. Sasirekha, *Ind. Eng. Chem. Res.*, 2009, **48**, 6248-6255.
48. J. Zhu, M. Xiao, G. Li, S. Li, J. Zhang, G. Liu, L. Ma, T. Wu, J. Lu and A. Yu, *Adv. Energy Mater.*, 2020, **10**, 1903003.
49. T. C. Nagaiah, D. Gupta, S. Das Adhikary, A. Kafle and D. Mandal, *J. Mater. Chem. A*, 2021, **9**, 9228-9237.
50. H. Zhang, S. Geng, M. Ouyang, H. Yadegari, F. Xie and D. J. Riley, *Adv. Sci.*, 2022, 2200146.
51. Y. Duan, Z. Y. Yu, S. J. Hu, X. S. Zheng, C. T. Zhang, H. H. Ding, B. C. Hu, Q. Q. Fu, Z. L. Yu and X. Zheng, *Angew. Chem. Int. Ed.*, 2019, **58**, 15772-15777.
52. X. Lv, W. Tian, Y. Liu and Z.-Y. Yuan, *Mater. Chem. Front.*, 2019, **3**, 2428-2436.
53. A. Y. Faïd, F. Foroughi, S. Sunde and B. Pollet, *J. Appl. Electrochem.*, 2022, **52**, 1819-1826.



## Chapter 4B

### Development of cellulose paper based eco-friendly flexible electrode for overall water splitting in alkaline and saline solutions



## 4B-1 Introduction

The continuously rising energy demand and fossil fuel dependent energy extraction is leading to not only depletion of its reserves but also creating serious environmental issues, and therefore, development of renewable and clean energy as an alternative to traditional fossil fuels is of extreme need.<sup>1, 2</sup> Hydrogen ( $H_2$ ) is a potential energy carrier and has received tremendous attraction because of its unique features viz. high gravimetric energy density ( $142 \text{ MJ Kg}^{-1}$ ), it gives pure recyclable water as combustion product.<sup>3-5</sup> In this regard, production of hydrogen gas via electrochemical water splitting powered by renewable and clean energy sources can be a promising strategy.<sup>6</sup> Fundamentally, the overall electrochemical water splitting comprises of anodic oxygen evolution reaction (OER) and cathodic hydrogen evolution reaction (HER). So, the employment of electrocatalyst is beneficial to achieve energy efficient water electrolysis by catalysing the corresponding sluggish half-cell reactions.<sup>7, 8</sup> Although Ir/Ru- and Pt-based are well-established state of art electrocatalysts for OER and HER applications but the low abundance and high cost of these precious metals impede their wide application.<sup>9, 10</sup> Therefore, the development of nonprecious-metal based electrocatalysts is a straight forward and cost-effective approach. Additionally, an electrocatalyst with good bifunctional activity towards both OER and HER reactions are more beneficial for practical applications on account of the advantages of rationalising the devices as well as lowering the cost.<sup>11</sup> Besides the efficient electrocatalyst, the overall electrocatalytic efficiency also relies on the coherent design of the electrode (i.e., current collector with catalyst).<sup>12</sup> The conventional electrode fabrication techniques are involving with various pitfalls. Firstly, in the metal/carbon or any other conductive substrate based current collector, large mass densities of electrochemically inactive materials (as only outer layer is sufficient for conductive network) is not only issue for atom economy but also a challenge for the development of light weight devices.<sup>13, 14</sup> Secondly, surface passivation of the current collector due to oxidation of metallic substrate limits the



activity of the electrode.<sup>15</sup> Moreover, the waste management of the obsolete end-of-life product is also of environmental concern. Along with that the common practice of catalyst ink preparation (mixing catalyst material with insulative binders) results in hinderance of electrocatalytic activity due to blockage of active sites by insulating material.<sup>16</sup> Similarly, the single side catalyst loaded electrode also limits the its actual output. Therefore, three dimensional porous electrode filled with binder free active catalyst material can be a good strategy for the development of highly efficient light weight eco-friendly electrode. In this regard, cellulose papers are promising substrate for electrode materials owing to their extensive availability, light weight, low cost, bio-degradability, recyclability and mechanical flexibility.<sup>17</sup> Owing to the insulating nature of cellulose paper, direct growing of active electrocatalyst may not be an effective approach so the surface modification with conductive metal composites is neccesary to induce conductivity to the paper electrode followed by incorporation of the active electrocatalyst over it for cellulose paper based electrode development.<sup>18-22</sup>

Most importantly, the requirement of pure water for electrochemical water splitting technology is another inhibiting factor towards its flourishing as about 96.5% of the world's total water is available as sea water so it is necessary to develop the water electrolyzer proficient for saline water splitting.<sup>23-25</sup> But, the crucial challenges of sea water splitting are the OER competing chloride oxidation anodic reaction, caused due to chloride ions present in the sea water.<sup>26</sup> The competing chloride oxidation reaction can be managed by pH adjustment. At alkaline pH the hypochlorite formation reaction ( $\text{Cl}^- + 2\text{OH}^- = \text{ClO}^- + \text{H}_2\text{O} + 2\text{e}^-$ ) demands  $\approx 480$  mV more potential than that for anodic OER.<sup>27, 28</sup> Additionally, the chloride corrosion may poison the electrode material and deteriorate its durability.<sup>2, 5</sup> Thus, the development of alkaline water electrolyzer consisting of eco- friendly, three-dimensional flexible electrode having good bifunctional catalytic activity and high resistivity towards chloride corrosion is necessary to overcome the above-mentioned bottlenecks.

Although substantial efforts have been set forth for the development of transition metal based efficient electrocatalysts for overall water splitting in the pure water condition, however, applicability in the seawater are still underexplored. Based on several contemporary reports, the encouraging activity and stability, nickel phosphide is found to be promising bifunctional electrocatalysts towards overall seawater splitting.<sup>26, 29-33</sup> By considering all these points, cellulose paper based, three-dimensional, flexible NiP/NiB-CP electrode was developed via two step electroless deposition followed by electrodeposition approach. This NiP/NiB-CP electrode possesses excellent bifunctional activity and long-term durability in both alkaline pure water and seawater electrolytes. The fabricated NiP/NiB-CP electrode requires overpotentials of only 379 and 178 mV to achieve current density of 100 mA cm<sup>-2</sup> for OER and HER respectively. Similarly it requires 1.65 and 1.69 V potential for overall water/ seawater splitting, to drive current density of 20 mA cm<sup>-2</sup> in 1 M KOH and 1 M KOH + 0.5 M NaCl electrolytes respectively. In this context, this work presents a general and cost-effective approach toward the fabrication NiP decorated cellulose paper based self-standing three-dimensional flexible electrode for overall water/seawater splitting.

## 4B-2 Electrode fabrication

**4B-2.1 Fabrication of NiB-CP:** The conductive metal composite was introduced to convert cellulose paper to into conductive substrate by using electroless deposition.<sup>34</sup> Briefly, the Whatman filter paper of size 1cm x 1cm was dipped in a ice cold bath solution (6 mmol NiCl<sub>2</sub> + 13.5 mmol NH<sub>4</sub>Cl + 6 mmol trisodium citrate + 15 mL 1M NaOH solution) and ice cold NaBH<sub>4</sub> solution (12 mmol NaBH<sub>4</sub> dissolved in 10 mL of 1M NaOH), was poured slowly from the wall of the container and kept as such till the seizing of effervescence. The NiB coated paper was sonicated in water and ethanol water (1:1) solution then dried in hot air oven at 60°C.

**4B-2.2 Fabrication of NiP/NiB-CP:** The active electrocatalyst NiP was deposited over the NiB-CP surface by electrodeposition method. The as deposited NiB-CP

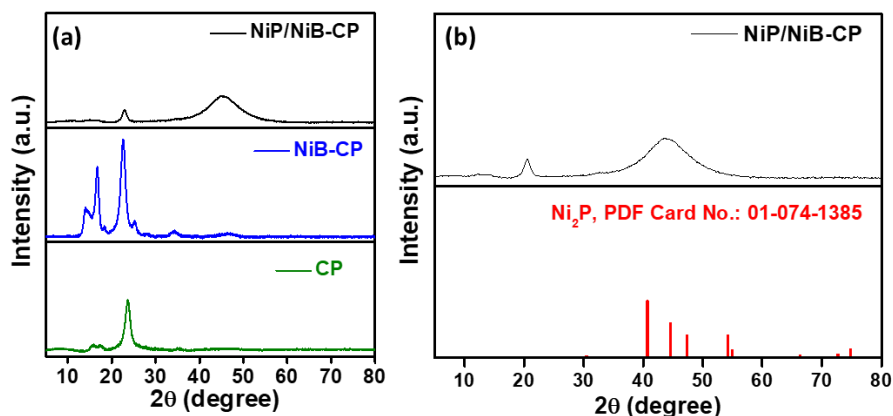


**Figure 4B-1.** P-XRD pattern showing the comparison of (a) bare CP, NiB-CP, and NiP/NiB-CP and (b) NiP/NiB-CP with PDF of Ni<sub>2</sub>P

was taken as working electrode whereas Ag/AgCl (3M KCl) and graphite rod were taken as reference and counter electrodes respectively. Then cyclic voltametric experiments were performed in a bath solution containing (NiSO<sub>4</sub> + Na(OAc) + NaH<sub>2</sub>PO<sub>2</sub> + 40 mL water) at -1.0 to -0.3 V vs. Ag/AgCl for fifteen cycles. After deposition the paper electrode was cleaned with deionized water and dried in hot air oven and designated as NiP/NiB-CP. In the similar fashion, the NiO/NiB-CP electrode was prepared by following the same procedure by eliminating NaH<sub>2</sub>PO<sub>2</sub> in the bath solution.

### 4B-3 Results and discussion

**4B-3.1 Physical characterization:** The structural and morphological attributes were confirmed by powdered X-ray diffraction (P-XRD) pattern and FE-SEM analysis. The P-XRD pattern of NiP/NiB-CP [Figures 4B-1(a-b)] show the crystalline cellulose peaks at 2θ value 16°, 17.5°, 23.7° and 35.3° corresponding to planes (110) (1 $\bar{1}$ 0), (200) and (004) respectively<sup>35</sup> which got diminished with the appearance of the broad diffraction peak between 40-50° which is attributed to the amorphous phase of the as-prepared electrode, that could be due to the coverage of the substrate surface by nickel phosphide (Ni<sub>2</sub>P, PDF no. 00-032-0463). The SEM images of Bare, NiB-CP and NiP/NiB-CP in Figures 4B-2(a-c) showed coating of NiB over the cellulose paper and deposition of the NiP over the NiB-CP

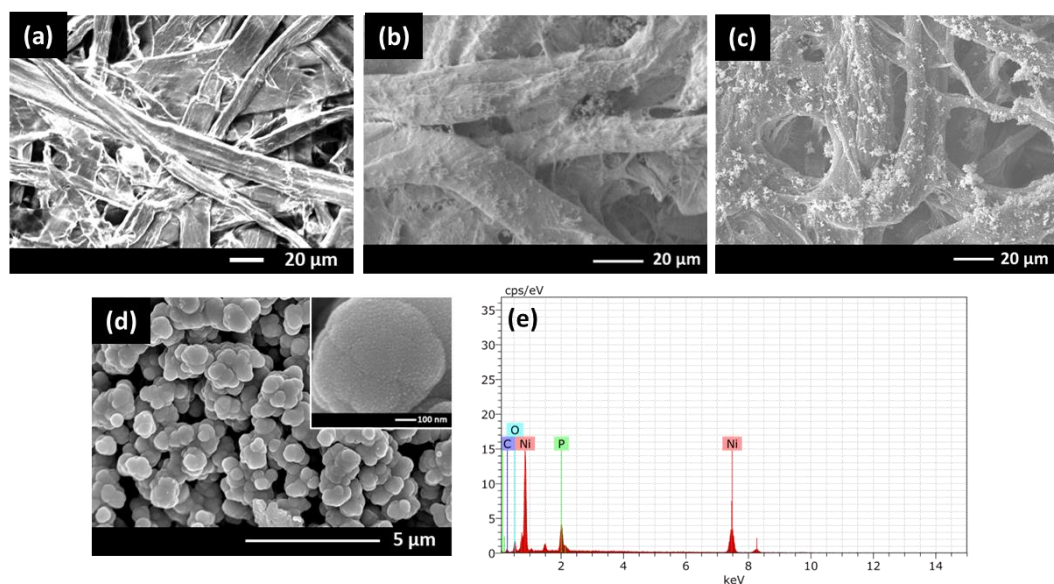


**Figure 4B-2.** SEM images of (a) bare cellulose paper (b) NiB-CP and (c) NiP/NiB-CP electrodes, (d) FE-SEM image and (e) EDX spectrum of NiP/NiB-CP electrode.

substrate. The sphere like morphology of deposited NiP over NiB/CP was confirmed from the FE-SEM image (Figure 4B-2d). The presence of Ni, P, and O elements was confirmed by the EDS spectra (Figure 4B-2e) where the elemental dot mapping images exhibited the uniform distribution of these elements (Figure 4B-3(a-e)).

The surface chemical composition and oxidation states of the NiP/NiB-CP were investigated by X-ray photoelectron spectroscopy (XPS) analysis. The characteristic peaks of elemental Ni, P, and B along with that of C and O were clearly observed in the XP survey spectra of NiP/NiB-CP (Figure 4B-4a). The high-resolution XP spectra of Ni 2p in NiP/NiB-CP (Figure 4B-4b) exhibited a pair of Ni 2p<sub>3/2</sub> and Ni 2p<sub>1/2</sub> peaks at binding energies at around 855.6 and 871.8 eV, respectively, along with two satellite peaks. The peaks of Ni 2p upon deconvolution showed set of peaks with binding energy at around 853.1, 869 eV and 856.1 & 871 eV corresponding to NiP/NiB and Ni<sup>2+</sup> respectively.<sup>32, 36</sup> Similarly, the high resolution XP spectra of P (Figure 4B-4c), exhibited two peaks at 134.5 eV and 129.5 eV, which are assigned to P-O and Ni-P bonds respectively.<sup>37, 38</sup> Furthermore,

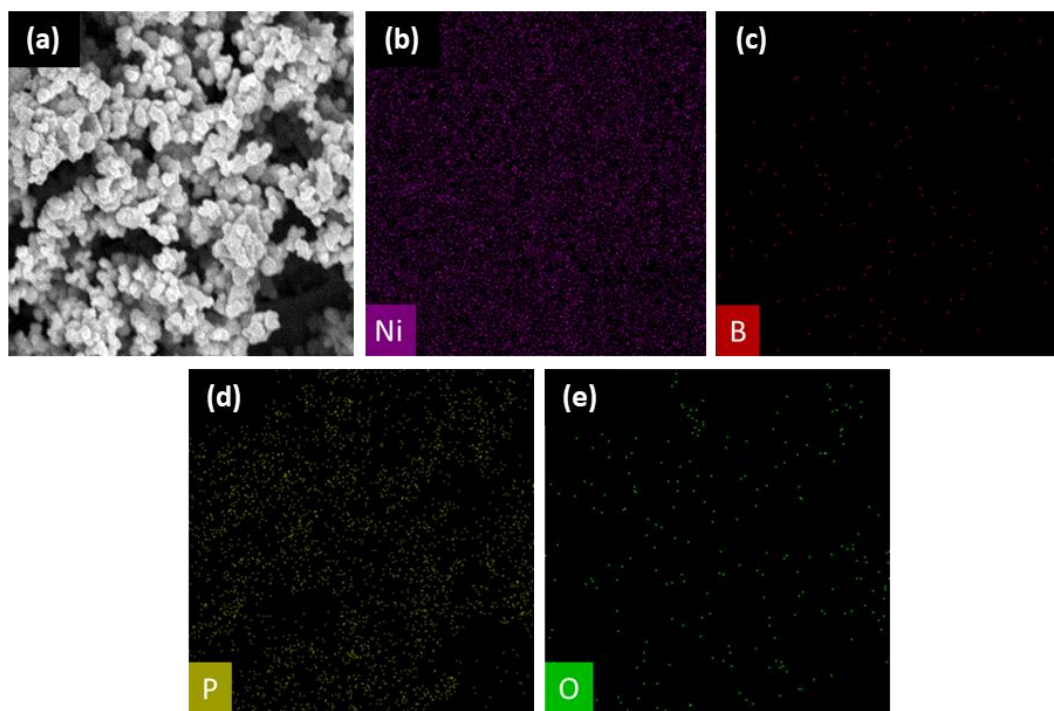


**Figure 4B-3.** (a) FE-SEM image of selected area for EDS analysis and elemental dot mapping images for (b) Ni, (c) B, (d) P, and (e) O elements for NiP/NiB-CP electrode.

the appearance of peaks at 187 and 191 eV corresponding to M- B and  $\text{BO}_x$  in the deconvoluted B 1s spectra (Figure 4B-4d) confirmed the presence of NiB<sup>39, 40</sup> whereas the existence of  $\text{OH}^-$  &  $\text{O}^{2-}$  peaks in the O 1s spectra (Figures 4B-4e) further evidenced the presence of nickel phosphide/phosphate moieties over the NiB-CP substrate.<sup>41</sup>

**4B-3.2 Electrochemical studies:** The electrocatalytic activities of the prepared electrodes were examined using a three-electrode configuration. Wherein, the prepared electrodes are employed as working electrode along with Hg/HgO (0.1M NaOH) as reference electrode where Pt-wire (during OER) and graphite (during HER) were used as counter electrodes. To examine the OER activity, firstly the linear sweep voltammetry (LSV) curves were recorded between the potential window 1.0 to 1.9 V vs. RHE with a scan rate of  $5 \text{ mV s}^{-1}$ . The LSV curves (Figure 4B-5a) revealed that the NiP/NiB-CP electrode exhibited superior OER activity compared to NiO/NiB-CP. The NiP/NiB-CP electrode required 379 mV

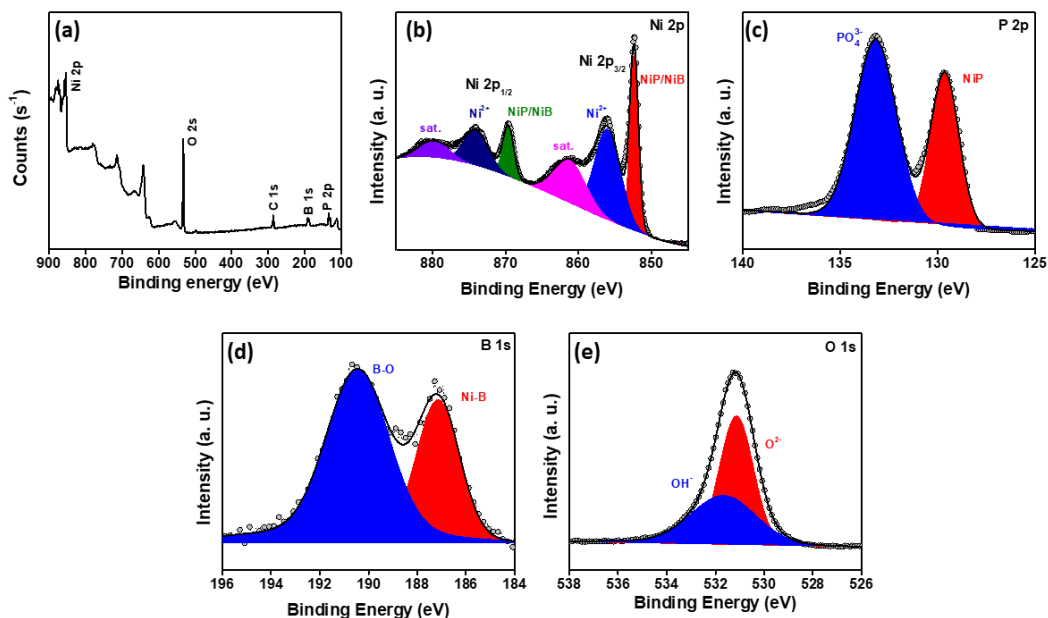


**Figure 4B-4.** The XPS spectra for NiP/NiB-CP electrode (a) full survey scan and deconvoluted spectra of (b) Ni 2p (c) Fe 2p (d) P 2p (e) B 1s and (e) O1s elements.

overpotentials to drive  $100 \text{ mA cm}^{-2}$  current density, which was smaller than the respective values for NiO/NiB-CP (419 mV), indicating a remarkable OER activity of the NiP/NiB-CP. Further assessment of the intrinsic catalytic activity of these electrodes were carried out by studying their OER catalytic kinetics with the corresponding Tafel plots extracted from Figure 4B-5b. As shown in Figure 4B-5B, the Tafel slope value of NiP/NiB-CP was found to be  $71 \text{ mV dec}^{-1}$ , which is much lower than that of NiP/NiB-CP ( $97 \text{ mV dec}^{-1}$ ) showing that the introduction of P resulted in enhanced electrochemical kinetic activity. Besides, the electrochemical impedance spectroscopy (EIS) analysis (Table 4B-1) further supported the improved kinetics of NiP/NiB-CP as it exhibited a low charge-transfer resistance ( $R_{ct}$ ) of  $\approx 0.31 \Omega$  which was much smaller than that of NiO/NiB-CP ( $\approx 4.75 \Omega$ ), that also confirmed the enhanced conductivity of NiP/NiB-CP.<sup>42, 43</sup> Electrochemically active surface area (ECSA) is another crucial parameter to evaluate the intrinsic surface-area activity of the electrocatalyst. The ECSA is proportional to the double-layer capacitance ( $C_{dl}$ ) i.e., higher the  $C_{dl}$  value higher

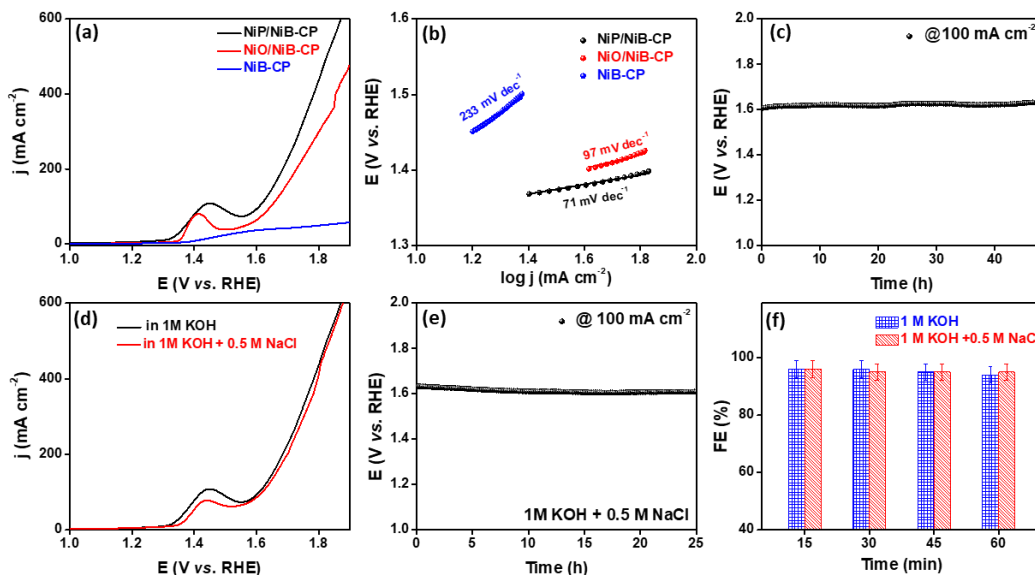


**Figure 4B-5.** (a) LSV curve for NiP/NiB-CP with their control samples for OER, (b) corresponding Tafel slopes and (c) chronopotentiometric curve recorded at  $100 \text{ mA cm}^{-2}$  in  $1 \text{ M KOH}$ . (d) Comparison of LSV curves in two different electrolyte systems, (e) chronopotentiometric curve recorded at  $100 \text{ mA cm}^{-2}$  in  $1 \text{ M KOH} + 0.5 \text{ M NaCl}$  and (f) Faradic efficiency in two different electrolyte systems for NiP/NiB-CP electrode during OER.

will be the ECSA and better will be the electrocatalytic activity. As shown in (Table 4B-1), the NiP/NiB-CP exhibited the largest  $C_{dl}$  ( $29.3 \text{ mF cm}^{-2}$ ) compared to other electrodes i.e., ( $23.7 \text{ mF cm}^{-2}$ ) and ( $20.5 \text{ mF cm}^{-2}$ ) for NiO/NiB-CP and NiB-CP respectively, implying that a larger electrochemically active area is created by NiP/NiB-CP electrode ( $732 \text{ cm}^2$ ) which further supported the enhanced activity of the NiP/NiB-CP electrode.

**Table 4B-1. Electrochemical Impedance and ECSA analysis for various electrodes.**

S.No.	Composites	$R_s (\Omega)$	$R_p (\Omega)$	$R_{ct} (\Omega)$	$C_{dl} (\text{mF})$	ECSA ( $\text{cm}^2$ )
1	NiP/NiB-CP	4.8	5.11	0.31	29.3	732
2	NiO/NiB-CP	4.70	9.45	4.75	23.7	592
3	NiB-CP	4.65	12.16	7.51	20.5	512

Besides the remarkable electrocatalytic activity the durability of the electrode is also equally important. In order to evaluate the durability of the NiP/NiB-CP

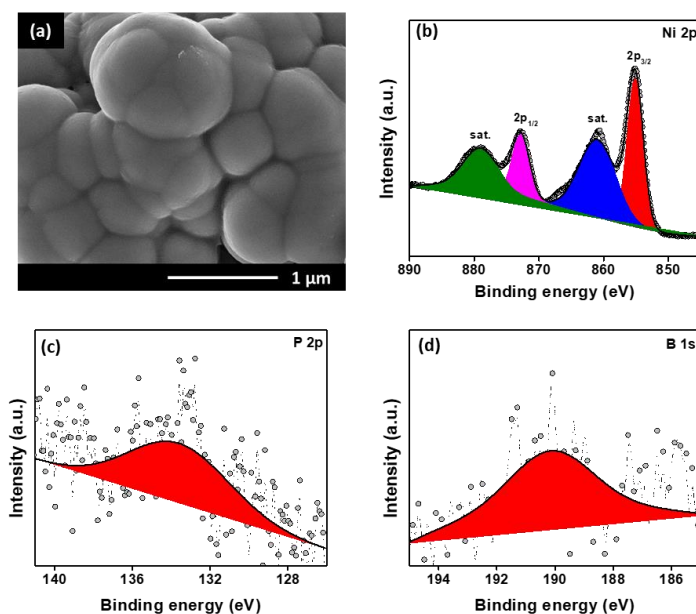


**Figure 4B-6.** (a) FE-SEM image, and deconvoluted XP spectra of (e) Ni 2p and (f) P 2p and (d) B 1s elements of NiP/NiB-CP electrode after stability study.

electrode in 1M KOH electrolyte, the chronopotentiometric study was carried out at  $100 \text{ mA cm}^{-2}$  for 24 h (Figure 4B-5c) which showed a negligible elevation in the potential during the course of the study indicating durability of the electrode. Further, the electrochemical performance of the electrodes were examined in the saline water environment, for which a simulated sea water ( $0.5 \text{ M NaCl} + 1 \text{ M KOH}$ ) was taken as an electrolyte and performed LSV and chronopotentiometry. The NiP/NiB-CP demonstrated the similar electrochemical activity i.e.  $\eta_{100} = 391 \text{ mV}$ , in saline electrolyte as that in 1 M KOH towards oxygen evolution reaction (Figure 4B-5d). The chronopotentiometric test of the electrodes under the alkaline saline electrolyte was also recorded for both the NiP/NiB-CP and NiO/NiB-CP electrodes. The NiP/NiB-CP showed a negligible increment in the potential for 24 hours (Figure 4B-5e) signifying the durability of the NiP/NiB-CP electrode. The selectivity of the OER in saline water is a crucial issue as chloride oxidation reaction is the competitive reaction. The selectivity of electrochemical reaction can be analyzed by determining Faradic efficiency (FE). The oxygen gas evolved during electrolysis was quantified eudiometrically and compared with the theoretical value. The FE was estimated within 94-97% in both electrolytic



solutions (Figure 4B-5f) and verified that oxygen evolution reaction is the only electrochemical reaction during electrolysis without any competition with chloride oxidation. Additionally, the effect of prolonged electrolysis on the electrode material was evaluated by analysing FE-SEM images and XP-spectra of the electrode recorded after stability study (Figures 4B-6(a-e)). The post electrolysis FE-SEM image of FeP/NiB-CP electrode demonstrated a well-maintained morphology whereas the disappearance of NiB/NiP peaks and increase in area of  $\text{Ni}^{2+}$  peak in Ni 2p spectra was resulted by the oxidation of the species into the  $\text{Ni}^{2+}$ . All these findings collectively confirmed the durability of the electrode during electrolysis.

The HER activity of the NiP/NiB-CP, NiO/NiB-CP and NiB-CP electrodes were studied by recording LSV curves between the potential window 0.0 to 0.5 V vs. RHE at scan rate of  $5 \text{ mV s}^{-1}$ . The LSV curves (Figure 4B-7a) demonstrated that the NiP/NiB-CP electrode exhibited superior HER activity and it required only 178 mV overpotential to drive  $100 \text{ mA cm}^{-2}$  current density, which was lower than the respective values for NiO/NiB-CP (216 mV), signifying a remarkable HER activity. The corresponding Tafel slope for NiP/NiB-CP electrode ( $69 \text{ mV dec}^{-1}$ , Figure 4B-7b) was also found to be smaller than that of NiO/NiB-CP electrode ( $109 \text{ mV dec}^{-1}$ ) indicating an enhanced electrocatalytic kinetics of NiP/NiB-CP towards HER. In addition, the superior durability of the NiP/NiB-CP electrode for HER was evidenced by the almost constant potential response for delivering  $100 \text{ mA cm}^{-2}$  current density (Figure 4B-7c) during chronopotentiometric measurement. The electrochemical activity and stability of the electrode under the probable chloride corrosion conditions was evaluated by carrying out LSV and chronopotentiometry study in  $1 \text{ M KOH} + 0.5 \text{ M NaCl}$  electrolyte. The realization of almost same electrocatalytic activity i.e.  $\eta_{100} = 196 \text{ mV}$  (Figure 4B-7d) evidenced the absence probable electrode corrosion. The long-term durability of the electrodes was studied by performing chronopotentiometry at  $100 \text{ mA cm}^{-2}$  in alkaline saline solution. The NiP/NiB-CP electrode demonstrated the constant voltage response during the course of electrolysis and validated the long-term durability without the

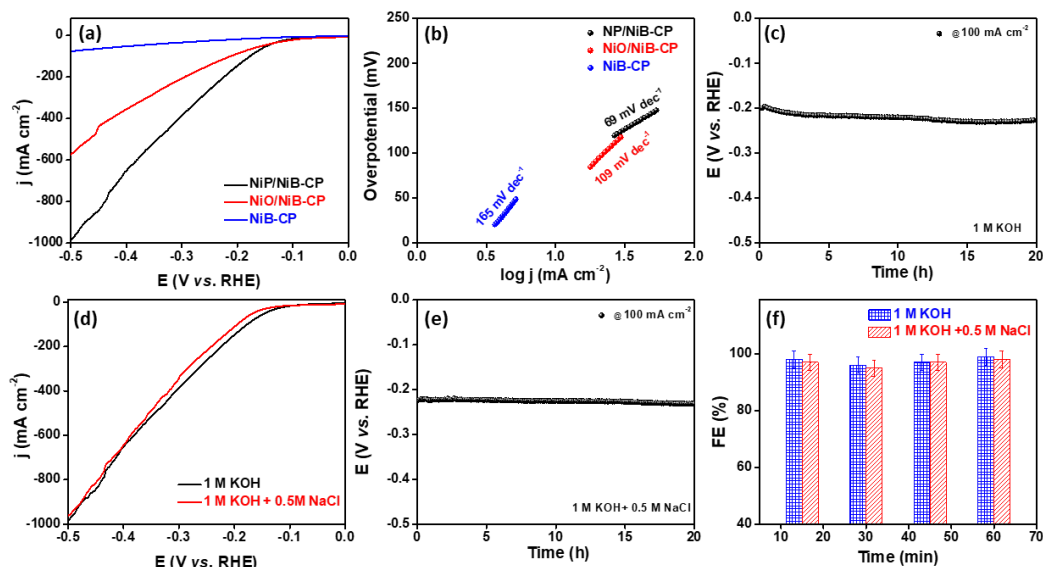


**Figure 4B-7.** (a) Linear sweep voltammogram for NiP/NiB-CP with other control electrodes for HER, (b) corresponding Tafel slopes and (c) chronopotentiometric curve recorded at 100 mA cm<sup>-2</sup> in 1 M KOH. (d) Comparison of LSV curves in two different electrolyte systems, (e) chronopotentiometric curve recorded at 100 mA cm<sup>-2</sup> in 1 M KOH + 0.5 M NaCl and (f) Faradic efficiency in two different electrolyte systems for NiP/NiB-CP electrode during HER.

obvious corrosion (Figure 4B-7e) and suggested the suitability of the NiP/NiB-CP electrode towards saline water electrolysis. Moreover, the electrode achieved the Faradic efficiency 95-98% for the hydrogen evolution reaction in both alkaline and saline alkaline electrolyte further confirmed that there are less chances of chloride corrosion suggesting its high competency in various electrolyte solutions (NiP/NiB-CP). The overall water/saline water splitting performance was studied by employing the prepared electrode both as cathode and anode for two-electrode cell assembly separated by Nafion membrane as water electrolyzer. The electrocatalytic activity and stability were evaluated by performing LSV and chronopotentiometry studies in both 1M KOH and 0.5 M NaCl + 1 M KOH electrolytes separately. The NiP/NiB-CP required only 1.65 V and 1.69 V to drive 20 mA cm<sup>-2</sup> in 1M KOH and 0.5 M NaCl + 1 M KOH electrolytes respectively (Figure 4B-8a). Additionally, the almost constant potential response for the time scale of 24 h during chronopotentiometric study recorded at 20 mA cm<sup>-2</sup> current density (Figure 4B-8b)

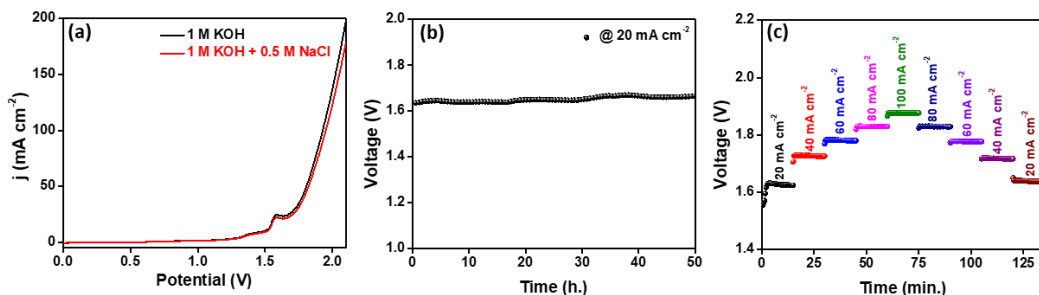


**Figure 4B-8.** (a) LSV curve recorded for a full cell assembled with NiP/NiB-CP at both anode and cathode in two different electrolytes. (b) Chronopotentiometry curve at 20 mA cm<sup>-2</sup> and (c) chronopotentiometry curves at various current densities for NiP/NiB-CP electrode in 1 M KOH during overall water splitting.

illustrated the good durability of the NiP/NiB-CP electrode during the overall water splitting. Furthermore, the consistency in the potential response during the chronopotentiometric study (Figures 4B-8c) for different current density (from 10 mA cm<sup>-2</sup> to 30 mA cm<sup>-2</sup> and back to the 10 mA cm<sup>-2</sup>) further evidenced the robustness of the electrode.

#### 4B-4 Summary

A novel and straight forward strategy was introduced to prepare the cellulose paper based three dimensional flexible NiP/NiB-CP as an efficient bifunctional electrode for alkaline overall water/saline water splitting which exhibited a remarkable electrocatalytic activity with high electronic kinetics and enhanced conductivity. Furthermore, its enhanced stability and corrosion resistance ability confirmed its suitability towards overall seawater splitting. The NiP/NiB-CP requires 379 & 391 mV overpotential during OER and 178 & 196 mV during HER to drive 100 mA cm<sup>-2</sup> in 1 M KOH and 1 M KOH+ 0.5M NaCl electrolyte whereas it demands 1.65 & 1.69 V potential to achieve 20 mA cm<sup>-2</sup> current density during overall water and saline water splitting respectively. Hence, this study opens a new avenue for the development of biodegradable cellulose paper based ecofriendly, flexible NiP/NiB-CP electrode as cost effective and straight forward approach for efficient hydrogen and stable production via water/saline water splitting.

## 4B-5 References

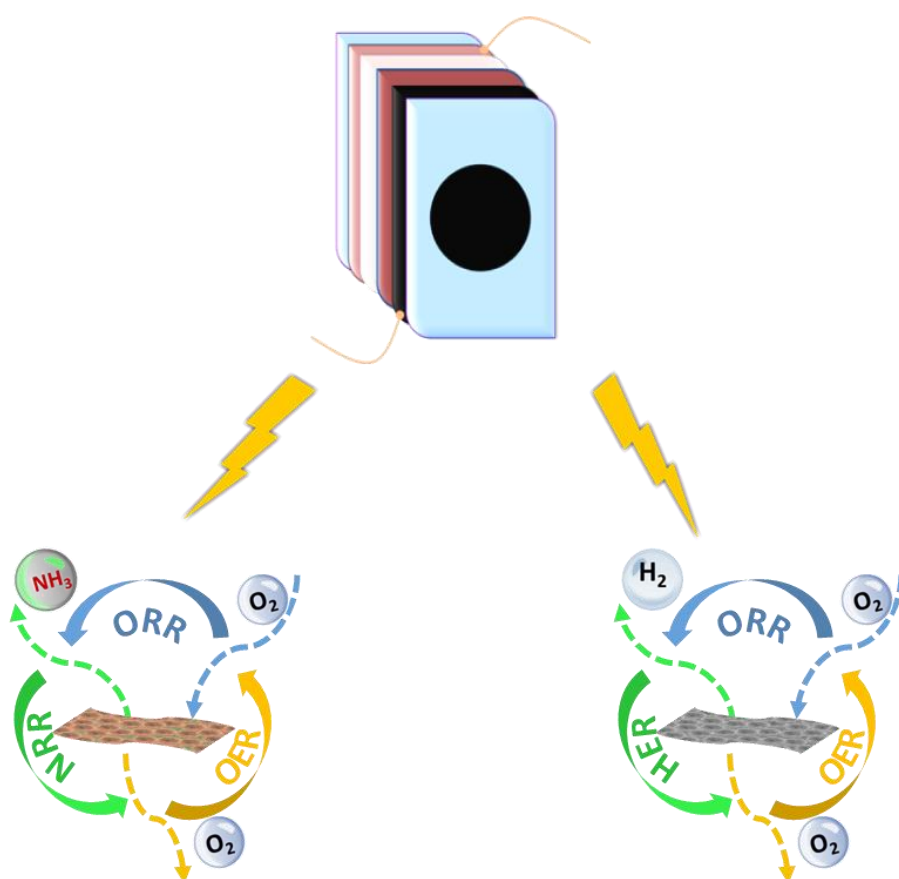
1. Z. W. Seh, J. Kibsgaard, C. F. Dickens, I. Chorkendorff, J. K. Nørskov and T. F. Jaramillo, *Science*, 2017, **355**, eaad4998.
2. J. Li, Y. Liu, H. Chen, Z. Zhang and X. Zou, *Adv. Funct. Mater.*, 2021, **31**, 2101820.
3. J. O. Abe, A. Popoola, E. Ajenifuja and O. M. Popoola, *Int. J. Hydrog. Energy*, 2019, **44**, 15072-15086.
4. A. Midilli, M. Ay, I. Dincer and M. A. Rosen, *Renew. Sustain. Energy Rev.*, 2005, **9**, 255-271.
5. W. Ma, D. Li, L. Liao, H. Zhou, F. Zhang, X. Zhou, Y. Mo and F. Yu, *Small*, 2023, 2207082.
6. S. Y. Tee, K. Y. Win, W. S. Teo, L. D. Koh, S. Liu, C. P. Teng and M. Y. Han, *Adv. Sci.*, 2017, **4**, 1600337.
7. Z. P. Ifkovits, J. M. Evans, M. C. Meier, K. M. Papadantonakis and N. S. Lewis, *Energy Environ. Sci.*, 2021, **14**, 4740-4759.
8. L. Li, P. Wang, Q. Shao and X. Huang, *Chem. Soc. Rev.*, 2020, **49**, 3072-3106.
9. F. Yu, H. Zhou, Y. Huang, J. Sun, F. Qin, J. Bao, W. A. Goddard III, S. Chen and Z. Ren, *Nat. Commun.*, 2018, **9**, 2551.
10. Z. Kou, K. Wang, Z. Liu, L. Zeng, Z. Li, B. Yang, L. Lei, C. Yuan and Y. Hou, *Small Struct.*, 2022, **3**, 2100153.
11. A. Kafle, M. Kumar, D. Gupta and T. C. Nagaiah, *J. Mater. Chem. A*, 2021, **9**, 24299-24307.
12. A. Sahasrabudhe, H. Dixit, R. Majee and S. Bhattacharyya, *Nat. Commun.*, 2018, **9**, 1-14.
13. J. Zhang, L. Dong, C. Xu, J. Hao, F. Kang and J. Li, *J. Mater. Sci.*, 2017, **52**, 5788-5798.
14. L. Dong, C. Xu, Y. Li, Z.-H. Huang, F. Kang, Q.-H. Yang and X. Zhao, *J. Mater. Chem. A*, 2016, **4**, 4659-4685.
15. X. Chen, T. Zhang, M. Kan, D. Song, J. Jia, Y. Zhao and X. Qian, *Environ. Sci. Technol.*, 2020, **54**, 13344-13353.
16. T. Jin, Q. Han and L. Jiao, *Adv. Mater.*, 2020, **32**, 1806304.
17. Z. Wang, Y. H. Lee, S. W. Kim, J. Y. Seo, S. Y. Lee and L. Nyholm, *Adv. Mater.*, 2021, **33**, 2000892.
18. Y. Yang, Q. Huang, G. F. Payne, R. Sun and X. Wang, *Nanoscale*, 2019, **11**, 725-732.
19. Y.-Y. Li, P. Kang, S.-Q. Wang, Z.-G. Liu, Y.-X. Li and Z. Guo, *Sens. Actuators B Chem.*, 2021, **327**, 128878.
20. D. Zhao, Y. Zhu, W. Cheng, W. Chen, Y. Wu and H. Yu, *Adv. Mater.*, 2021, **33**, 2000619.
21. S. Jiang, J. Li, J. Fang and X. Wang, *Small*, 2021, **17**, 1903760.
22. S. Zhou, L. Nyholm, M. Strømme and Z. Wang, *Acc. Chem. Res.*, 2019, **52**, 2232-2243.
23. W. Tong, M. Forster, F. Dionigi, S. Dresp, R. Sadeghi Erami, P. Strasser, A. J. Cowan and P. Farràs, *Nat. Energy*, 2020, **5**, 367-377.
24. S. r. Dresp, F. Dionigi, M. Klingenhof and P. Strasser, *ACS Energy Lett.*, 2019, **4**, 933-942.
25. J. N. Hausmann, R. Schlögl, P. W. Menezes and M. Driess, *Energy Environ. Sci.*, 2021, **14**, 3679-3685.
26. L. Wu, L. Yu, F. Zhang, B. McElhenny, D. Luo, A. Karim, S. Chen and Z. Ren, *Adv. Funct. Mater.*, 2021, **31**, 2006484.
27. A. Kafle, D. Gupta and T. C. Nagaiah, *Electrochim. Acta*, 2023, **441**, 141779.
28. S. Gupta, M. Forster, A. Yadav, A. J. Cowan, N. Patel and M. Patel, *ACS Appl. Energy Mater.*, 2020, **3**, 7619-7628.
29. H.-Y. Wang, J.-T. Ren, L. Wang, M.-L. Sun, H.-M. Yang, X.-W. Lv and Z.-Y. Yuan, *J. Energy Chem.*, 2022, **75**, 66-73.
30. T. Xu, D. Jiao, L. Zhang, H. Zhang, L. Zheng, D. J. Singh, J. Zhao, W. Zheng and X. Cui, *Appl. Catal. B Environ.*, 2022, **316**, 121686.

31. N. Wang, W. Wang, Q. Luo, J. Li, Y. Li, L. Li, X. Huo and X. Du, *Inorg. Chem. Front.*, 2023.
32. Z. Zhang, C. Li, H. Huang, J. Li, X. Zhang, Z. Li, H. Wei and H. Chu, *Electrochim. Acta*, 2020, **362**, 137172.
33. Y. Liu and Z. Xiang, *ACS Appl. Mater. Interfaces*, 2019, **11**, 41313-41320.
34. A. Kafle, D. Gupta, A. Bordoloi and T. C. Nagaiah, *Nanoscale*, 2022, **14**, 16590-16601.
35. M. Costa, B. Veigas, J. Jacob, D. Santos, J. Gomes, P. Baptista, R. Martins, J. Inácio and E. Fortunato, *Nanotechnology*, 2014, **25**, 094006.
36. L. Liao, C. Cheng, H. Zhou, Y. Qi, D. Li, F. Cai, B. Yu, R. Long and F. Yu, *Mater. Today Phys.*, 2022, **22**, 100589.
37. Z. Zhou, L. Wei, Y. Wang, H. E. Karahan, Z. Chen, Y. Lei, X. Chen, S. Zhai, X. Liao and Y. Chen, *J. Mater. Chem. A*, 2017, **5**, 20390-20397.
38. Y. Pan, Y. Liu, J. Zhao, K. Yang, J. Liang, D. Liu, W. Hu, D. Liu, Y. Liu and C. Liu, *J. Mater. Chem. A*, 2015, **3**, 1656-1665.
39. D. He, L. Zhang, D. He, G. Zhou, Y. Lin, Z. Deng, X. Hong, Y. Wu, C. Chen and Y. Li, *Nat. Commun.*, 2016, **7**, 1-8.
40. J. Schreifels, P. Maybury and W. Swartz Jr, *J. Catal.*, 1980, **65**, 195-206.
41. N. Thakur, M. Kumar, D. Mandal and T. C. Nagaiah, *ACS Appl. Mater. Interfaces*, 2021.
42. S. D. Adhikary, A. Tiwari, T. C. Nagaiah and D. Mandal, *ACS Appl. Mater. Interfaces*, 2018, **10**, 38872-38879.
43. T. C. Nagaiah, D. Gupta, S. D. Adhikary, A. Kafle and D. Mandal, *J. Mater. Chem. A*, 2021, **9**, 9228-9237.



# Chapter 5

## Exploration of cellulose paper-based electrodes towards self powered nitrogen reduction and overall water splitting

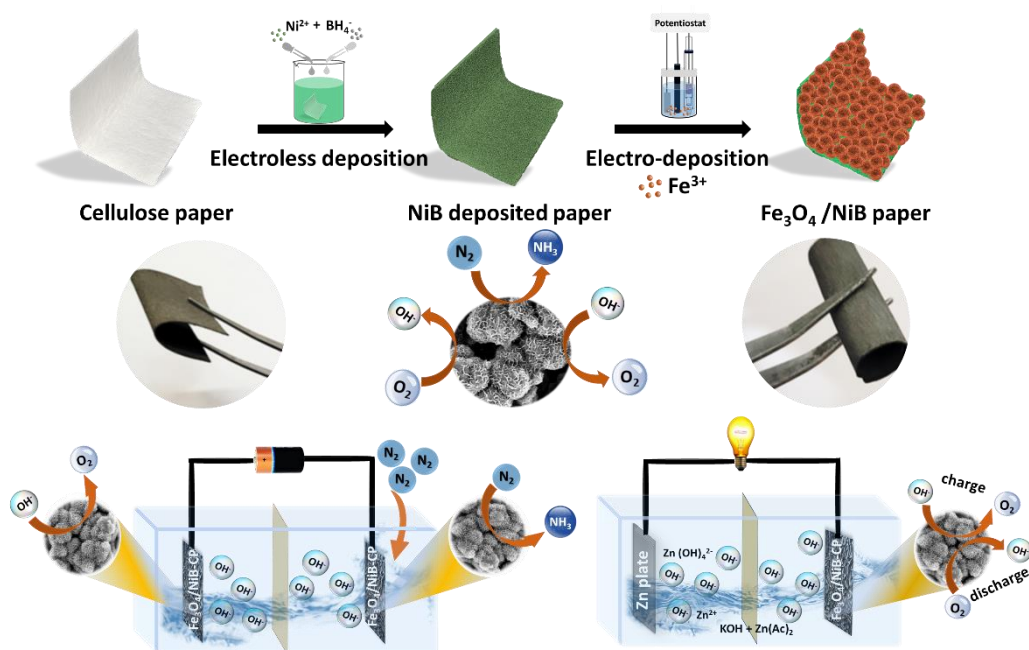






# Chapter 5A

## Self-standing $\text{Fe}_3\text{O}_4$ decorated paper electrode as binder-free trifunctional electrode for electrochemical ammonia synthesis and Zn- $\text{O}_2$ batteries



## 5A-1 Introduction

Fulfilling the world's energy demand by maintaining clean environment will be one of the arduous tasks for upcoming decades.<sup>1-3</sup> The electrochemical energy conversion and storage is booming attractively to meet the demand of sustainable energy and environment.<sup>4-7</sup> In addition to augmented energy demand, the incessantly increasing world's population also stresses for the high fertilizer production to provide the basis of nutrition. Therefore the synthesis of  $\text{NH}_3$  is of huge significance, since it is a prime constituent of fertilizers as well as a novel green  $\text{H}_2$  storage material.<sup>8</sup> But the commercial production of ammonia highly relies on Haber-Bosch process which has several disadvantages *viz.* requirement of harsh operating conditions, consumption of 2-3% of world's energy and responsible for the more than 2% of global  $\text{CO}_2$  emissions.<sup>9</sup> Among various existing technologies the electrochemical nitrogen reduction has received a tremendous attraction for ammonia production with minimum energy consumption and reduced carbon footprint, as the ammonia can be produced by using water as the hydrogen source under ambient conditions but requires a power source.<sup>10</sup> On the other hand, rechargeable metal air batteries are emerging as a potential candidate for energy storage systems owing to their high energy density and straightforward fabrication procedure.<sup>11, 12</sup> The potentiality of these above mentioned technologies relies upon three important electrochemical reactions with sluggish kinetics *i.e.* nitrogen reduction (NRR), oxygen evolution (OER) and oxygen reduction reaction (ORR) which determine the overall efficiency of the system. Therefore, the development of an electrode with trifunctional activity towards these electrochemical reactions is crucial.

Besides other factors, the activity of electrocatalyst also depends on the electrode architecture. Electrodes are commonly fabricated by coating the catalyst ink (prepared by mixing with insulating binders) over the current collector like glassy carbon or other conductive and rigid substrates which suffers with many drawbacks including the loss of electrocatalyst during electrochemical reactions, blockage of

active sites of the catalyst by insulating binder and so on, consequently the overall efficiency will be compromised.<sup>13, 14</sup> In this regard self-standing three dimensional flexible electrode with active catalyst grown over its surface can ensure the enhanced electrochemical activity with proper utilization of catalyst. Additionally, the flexible electrodes can demonstrate device friendly opportunity for any kind of reactor as well as portable and foldable electronics due to their stability under various mechanical deformations without alteration in the electrocatalytic activity.<sup>15-17</sup> Therefore, the development of durable, cost effective and eco-friendly flexible electrodes showing multifunctional activity is the need of the hour.

Although numerous conductive substrates like metallic wire,<sup>18, 19</sup> foam<sup>20</sup> and foils<sup>21</sup> (mainly nickel, titanium and iron), carbon cloth/paper<sup>22, 23</sup> etc. have been explored with satisfactory conductivity but they also have some limitations such as poor flexibility, high cost, heaviness and fragility.<sup>24, 25</sup> Besides, the non-biodegradability nature of these substrates may adversely affect the environment.<sup>26</sup> To overcome these issues bio-based materials such as cellulose paper (CP) can be a good alternative as a cost-effective and biodegradable substrate.<sup>27</sup> But the biggest hurdle for its exploration as an electrode material is the absence of conductive pathway for the electric circuit because of its insulating nature.<sup>28, 29</sup> In this regard, the surface modification of cellulose paper with conductive metal composites is an effective route to induce conductivity, where the hydroxyl groups of cellulose can act as anchoring sites for the metal ions.<sup>27, 30, 31</sup> Various techniques such as solvent free drawing,<sup>32</sup> bar coating,<sup>33</sup> screen printing,<sup>34</sup> flow directed filtration,<sup>35</sup> soak and drying,<sup>36</sup> sputtering techniques,<sup>37</sup> and the electroless plating method<sup>38</sup> are common for the conversion of insulating cellulose paper into conductive substrate. Amongst them, electroless deposition method stands out as the economical way to achieve uniform coating along its less hardous nature and time efficiency.<sup>39</sup> Recently Saharabuddhe *et al.*<sup>40</sup> reported the conversion of cellulose paper into conductive Ni-paper via. electroless deposition method by following sensitization-activation deposition route in which the use of the noble metal based PdCl<sub>2</sub> and SnCl<sub>2</sub> hikes the overall fabrication cost. In the similar fashion, Hao *et al.*<sup>41</sup> demonstrated an

alternate-dipping activation strategy to develop paper electrode, but the shortcomings such as involvement of expensive DMAB (dimethylamino borane) as a reducing agent, longer deposition time, single side deposition and high loading of material demands for a rapid and straight forward route to fabricate three dimensional (3D) paper electrode for practical applications.

The incorporation of well-structured electrocatalyst with distinct morphology over the conductive 3D-paper substrate can be a good strategy for designing the eco-friendly and efficient electrode. Therefore, the development of a précised process that can integrate both conductive material and active catalyst onto the flexible cellulose paper with optimal loading and controlled morphology is crucial for practical applications. Herein a cost effective and straightforward approach has been developed to convert an insulating cellulose paper into a conductive substrate via electroless deposition followed by incorporation of the active electrocatalyst over the same *via* electrodeposition method. A non-conductive cellulose paper was converted to nickel boride (NiB) coated conductive substrate by electroless deposition over which active catalyst  $\text{Fe}_3\text{O}_4$  was decorated by electrodeposition. It is noteworthy to mention that the  $\text{Fe}_3\text{O}_4$  was chosen as an active catalyst for the electrode fabrication because of the active nature of Fe and its oxides towards NRR.<sup>42, 43</sup> Furthermore, metal oxides having porous structure with controlled morphology is beneficial to facilitate the mass transport by exposure of maximum number of active sites and results improved activity. Thus, the fabricated electrode demonstrates promising NRR activity and long-term stability as well. Additionally, the oxygen bifunctional activity was also studied to assemble a Zn-O<sub>2</sub> battery equipped with the designed electrode as air-cathode. Remarkably, its practical applicability was confirmed by Zn-air battery and electrochemical nitrogen reduction performance using same battery as a power source. These exciting activities and the straightforward fabrication strategy may act as a milestone in the development of cost effective and eco-friendly flexible electrode towards electrochemical energy conversion and storage as well as other electrochemical applications.

## **5A-2 Electrode fabrication**

**5A-2.1 Fabrication of NiB-CP:** Laboratory Whatman filter paper was cleaned with acetone by sonicating it for five minutes then washed thoroughly with deionised water and dried in oven at 60° C. The clean cellulose paper (1cm x 1cm) was dipped in ice cold bath solution (prepared by dissolving 6 mmol NiCl<sub>2</sub>, 13.5 mmol NH<sub>4</sub>Cl and 6 mmol trisodium citrate in 15 mL 1M NaOH solution) and ice cooled NaBH<sub>4</sub> solution (12 mmol NaBH<sub>4</sub> dissolved in 10 mL 1M NaOH) was added dropwise from the wall of the container and kept as such till the seizing of effervescence. Then the Ni-B coated paper was sonicated in water followed by ethanol then dried in hot air oven at 60 °C.

**5A-2.2 Fabrication of Fe<sub>3</sub>O<sub>4</sub>-T@NiB-CP.** The as fabricated NiB-CP was taken as working electrode for the deposition of active material Fe<sub>3</sub>O<sub>4</sub> over it. The electrodeposition was carried out in a hot bath solution (prepared by dissolving 4.5 mmol ferric nitrate and 5 mmol triethanolamine in 50 mL of 2M NaOH) by performing chronoamperometry at -1.1 V vs. Ag/AgCl with graphite rod as a counter electrode. The bath temperature was optimized by performing the electrodeposition at 60-80 °C for the fabrication of Fe<sub>3</sub>O<sub>4</sub>-T/NiB-CP by keeping rest of the conditions as it is. Thus deposited Fe<sub>3</sub>O<sub>4</sub>-T/NiB-CP was washed with dilute KOH followed by deionized water and then finally dried in hot air oven at 60 °C.

## **5A-3 Results and discussion**

**5A-3.1 Physical characterization:** The Fe<sub>3</sub>O<sub>4</sub>-T/NiB-CP electrodes were prepared by a two-step fabrication approach. Firstly, the conductive NiB nanoparticles were coated over the non-conductive cellulose paper to make it conductive by a controlled electroless deposition method. The deposition of metallic species over cellulose paper became advantageous due to the presence of ample -OH functional sites which provided the anchoring of precursors during electroless deposition. The scanning electron microscopy (SEM) image of bare CP (Figure 5A-1a) showed a smooth surface with well-defined interconnected cellulose fibres of ~20 µm width

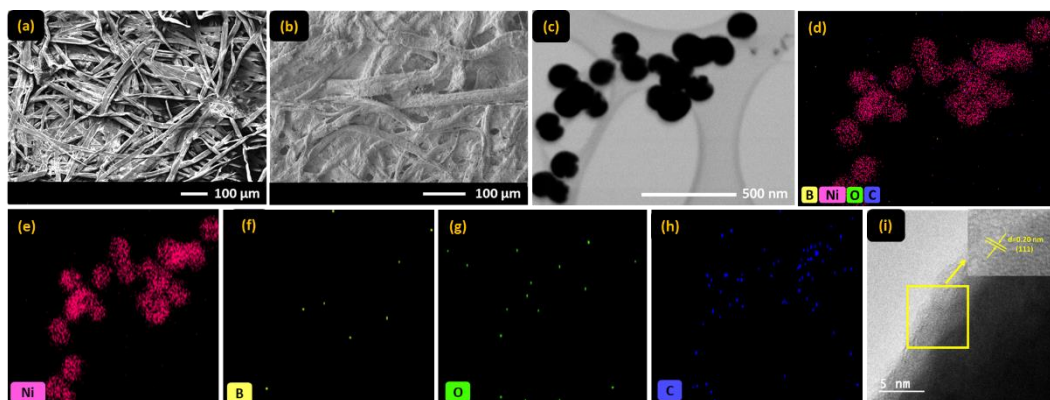


**Figure 5A-1.** SEM images of (a) bare cellulose paper, (b) NiB deposited cellulose paper and (c) TEM and TEM elemental dot mapping images for (d) all elements and separately for (e) Ni, (f) B, (g) O and (h) C elements of NiB-CP electrode and (i) HRTEM images of NiB deposited cellulose paper.

whereas a uniform coating of NiB nanoparticles over CP was observed after electroless deposition (Figure 5A-1b) which was further supported by the transmission electron microscopy (TEM) images (Figure 5A-1c) and the elemental dot mapping images [Figures 5A-1(d-h)]. The high-resolution transmission electron microscopy (HRTEM) images in (Figure 5A-1i) exhibited the d-spacing of 0.20 nm corresponding to (111) plane of Ni.<sup>44</sup>

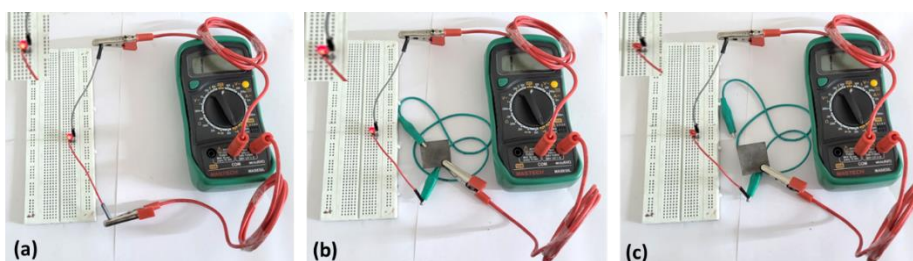


**Figure 5A-2.** Photograph of lighting LED (a) directly by multimeter, (b) through NiB-CP and (c) photograph of light off LED after disconnection. (Inset: zoomed part of the LED bulb).

Most importantly, the conductivity of the NiB-CP electrode is demonstrated by illuminating a light emitting diode (LED) of 2.0 V with the assistance of multimeter (Figure 5A-2). That further designated the competence of NiB-CP electrode to be applied for electrochemical applications. The electrical conductivity of NiB-

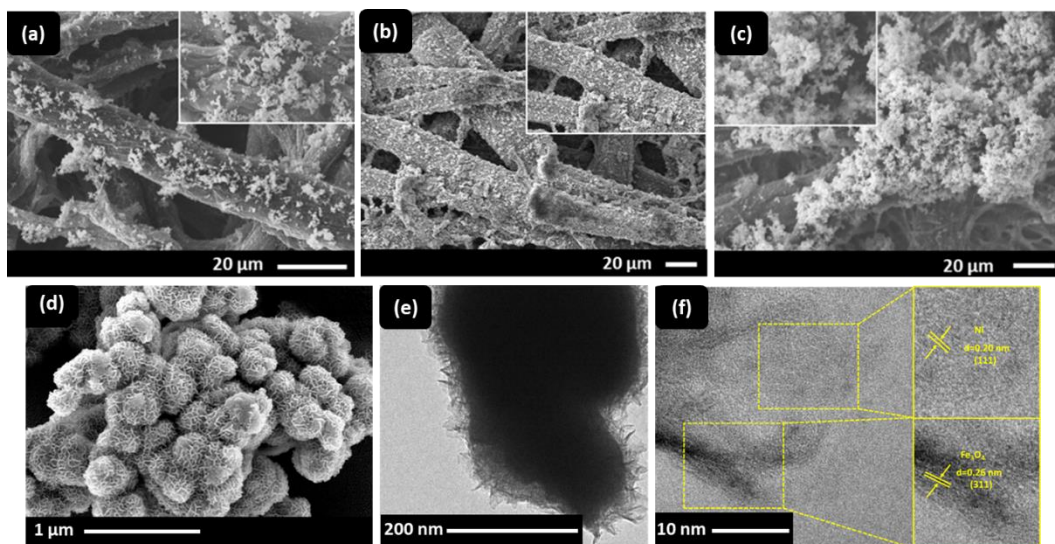


**Figure 5A-3.** SEM images of (a)  $\text{Fe}_3\text{O}_4$ -60/NiB-CP (b)  $\text{Fe}_3\text{O}_4$ -70/NiB-CP and (c)  $\text{Fe}_3\text{O}_4$ -80/NiB-CP electrodes, (d) FE-SEM, (e) TEM and (f) HRTEM images of  $\text{Fe}_3\text{O}_4$ -70/NiB-CP electrode.

CP electrode was measured by four-point probe method<sup>45</sup> and it was found to be  $4.15 \text{ S cm}^{-1}$  whereas the bare CP was non-conductive. Secondly, the NiB-CP was subjected to electrodeposition to decorate active catalyst  $\text{Fe}_3\text{O}_4$  over its surface to establish it as a trifunctional electrode. To achieve a high trifunctional activity the fabrication of  $\text{Fe}_3\text{O}_4$ -T/NiB-CP were optimized by varying the bath temperature between  $60\text{--}80^\circ\text{C}$  (T) during the electrodeposition of  $\text{Fe}_3\text{O}_4$  and keeping rest of the conditions as such. The SEM images of  $\text{Fe}_3\text{O}_4$ -60/70/80 deposited over NiB-CP are shown in Figures 5A-3(a-c). The less and uneven deposition of  $\text{Fe}_3\text{O}_4$  nanoparticles were found when bath temperature was kept at  $60^\circ\text{C}$  whereas agglomeration of the nanoparticles were observed when the bath temperature was changed to  $80^\circ\text{C}$ . On the other hand, optimal and uniform deposition was witnessed in  $\text{Fe}_3\text{O}_4$ -70/NiB-CP, which exhibited a uniform array of nanospheres composed of thin nanosheets, as evidenced by field-emission-scanning electron microscopy (FE-SEM) image in Figure 5A-3d. Particularly, the homogeneously distributed  $\text{Fe}_3\text{O}_4$  nanospheres at the surface demonstrated the presence of efficacious active sites for facile electron and mass transfer. This was further supported by the subsequent



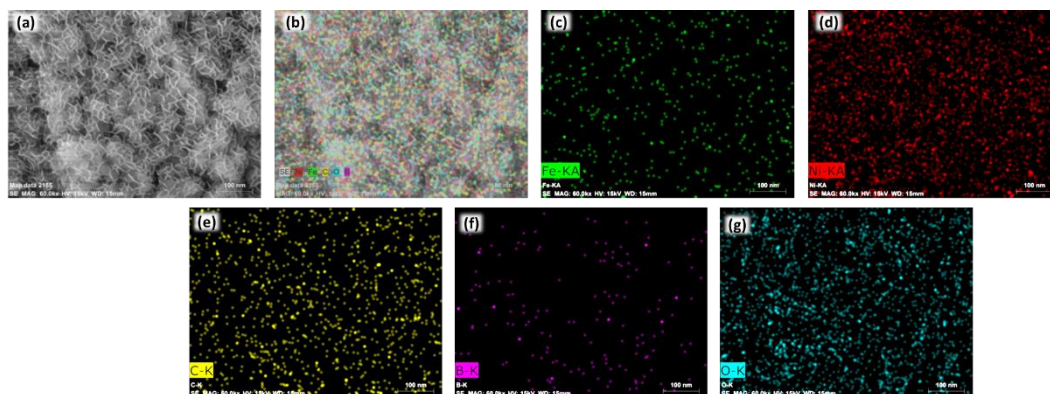


**Figure 5A-4.** (a) Scanned area for elemental dot mapping images of (b) all elements and separately for (c) Ni, (d) Fe (e) B, (f) C and (g) O of  $\text{Fe}_3\text{O}_4$ -70/NiB-CP electrode.

TEM images and well resolved lattice fringes [Figures 5A-3(e-f)] exhibiting the presence of  $\text{Fe}_3\text{O}_4$  having d-spacing of 0.26 nm corresponding to (311) plane<sup>46</sup> along with NiB. In order to identify the composition and distribution of Ni, Fe, C, and O elements in the  $\text{Fe}_3\text{O}_4$ -70/NiB-CP electrode, energy dispersive X-ray (EDX) analysis was acquired, which evidenced the presence of Ni, Fe, C and O with an atomic percentage of 46.5, 3.38, 20.29 and 19.89 respectively, which was in close agreement with the MP-AES analysis results (Table 5A-1). Further, the elemental dot mapping added to the confirmation of the homogeneous distribution of these elements over the scanned area (Figure 5A-4).

**Table 5A-1. Elemental analysis of  $\text{Fe}_3\text{O}_4$ -70/NiB-CP electrode.**

S.No.	Elements	EDS Analysis (mass %)	MP-AES Analysis (mass %)
1.	Nickel	46.5	45.64
2.	Iron	3.38	5.27
3.	Carbon	20.29	-
4.	Oxygen	19.89	-

The chemical composition and oxidation states of each element present in  $\text{Fe}_3\text{O}_4$ -70/NiB-CP electrode were executed by X-ray photoelectron spectroscopy (XPS) and powder X-ray diffraction (P-XRD) analysis. The XPS survey spectra demonstrated the successful deposition of the desired metals over the substrate surface (Figure 5A-5a). The Ni 2p high resolution XP spectrum demonstrated two



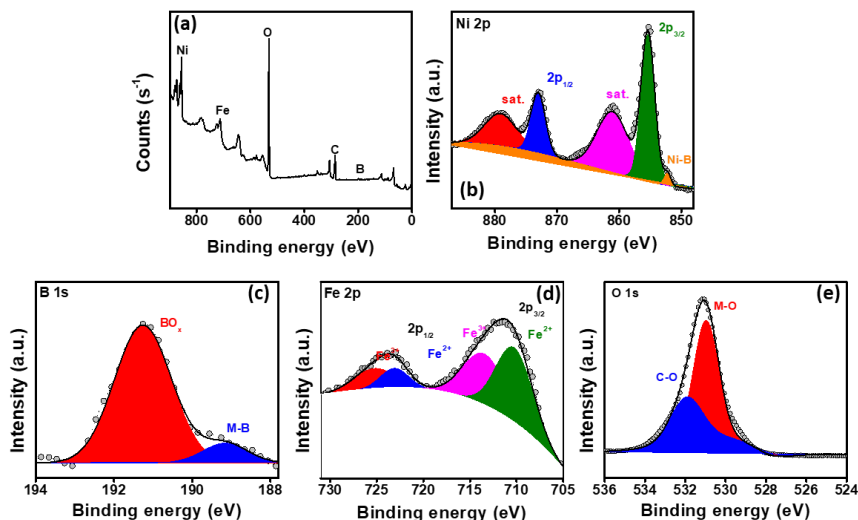


**Figure 5A-5.** The XP spectra of  $\text{Fe}_3\text{O}_4$ -70/NiB-CP (a) full survey scan and deconvoluted spectra of (b) Ni 2p (c) B s (d) Fe 2p and (e) O1s.

main peaks at 855.4 and 872.9 eV which were assigned to Ni  $2p_{3/2}$  and Ni  $2p_{1/2}$  spin-orbit states in addition to the corresponding satellite peaks at 861.4 and 879.1 eV. The deconvoluted XP spectra of Ni  $2p_{3/2}$  exhibited two peaks at 852.2 eV and 855.4 eV which were attributed to the NiB<sup>47</sup> and Ni<sup>+2</sup> respectively<sup>41, 48</sup> (Figure 5A-5b). The existence of corresponding M- B and BO<sub>x</sub> peaks at 189 and 192 eV in the deconvoluted B 1s spectra (Figure 5A-5c) further supported the presence of NiB.<sup>49, 50</sup> Similarly the high-resolution Fe 2p spectra (Figure 5A-5d), exhibited two major peaks at 711.2 and 723.4 eV corresponding to Fe  $2p_{3/2}$  and Fe  $2p_{1/2}$  respectively which upon deconvolution exhibited peaks at 710.3 eV, 713.6 eV, 723.1 eV and 724.8 eV which were ascribed to +2 and +3 oxidation states of Fe confirming the presence of  $\text{Fe}_3\text{O}_4$ <sup>51</sup> and this was further supported by the observed peaks at 532 eV and 530.9 eV corresponding to C-O and Fe-O respectively in the deconvoluted O 1s spectrum (Figure 5A-5e). The characteristic powder X-ray diffraction (P-XRD) pattern of bare cellulose paper (CP), NiB-CP and  $\text{Fe}_3\text{O}_4$ -T/NiB-CP are displayed in Figure 5A-6. The deposition of NiB nanoparticles over bare CP surface was validated by the presence of additional broad diffraction peak at  $2\theta = 45^\circ$  matching well with amorphous NiB phase (JCPDS card no.: 01-074-

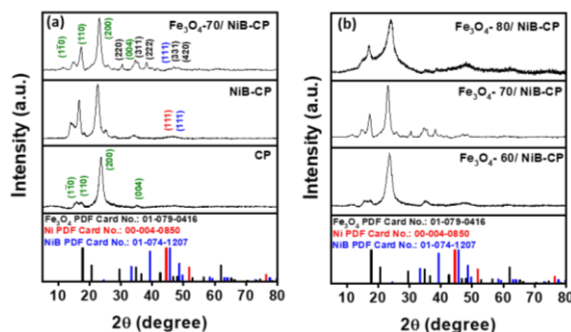


**Figure 5A-6.** The P-XRD pattern of (a) bare CP, NiB-CP, and Fe<sub>3</sub>O<sub>4</sub>-70/NiB-CP and (b) Fe<sub>3</sub>O<sub>4</sub>-60/NiB-CP, Fe<sub>3</sub>O<sub>4</sub>-70/NiB-CP and Fe<sub>3</sub>O<sub>4</sub>-80/NiB-CP electrodes.

1207). Additionally, the increment in the intensity of peaks at  $14^\circ$ ,  $23^\circ$  and  $16.5^\circ$  in NiB-CP corresponded to  $\alpha$ -Ni(OH)<sub>2</sub> and  $\beta$ -Ni(OH)<sub>2</sub> phase respectively, which could be due to the partial surface oxidation.<sup>40</sup> The appearance of the peaks at  $30.3^\circ$ ,  $35.7^\circ$ ,  $37.9^\circ$ ,  $46.8^\circ$ ,  $48.5^\circ$  corresponding to (220), (311), (222), (331) and (420) planes of Fe<sub>3</sub>O<sub>4</sub> (JCPDS card no.:01-079-0416 and 01-084-2782) in addition to NiB phase in Fe<sub>3</sub>O<sub>4</sub>-T/NiB-CP composite evidenced the successful deposition of Fe<sub>3</sub>O<sub>4</sub> over NiB-CP surface.

**5A-3.2 Electrochemical N<sub>2</sub> reduction reaction:** The potential application of as-fabricated electrode towards NRR under ambient conditions was studied in 0.1 M KOH by using a gas tight two compartment H-cell separated by a Nafion membrane (N-117). Firstly, linear sweep voltammetry (LSV) was executed under Ar and N<sub>2</sub> atmosphere [Figures 5A-7(a-b)] for NiB-CP as well as Fe<sub>3</sub>O<sub>4</sub>-70/NiB-CP electrodes within the potential range 0.3 to -0.6 V *vs.* RHE. A drastic increase in reduction current was witnessed for the Fe<sub>3</sub>O<sub>4</sub>-70/NiB-CP electrode at around -0.05 V in N<sub>2</sub>-atmosphere with comparatively positive onset potential of 0.15 V than that observed in Ar-atmosphere (-0.2 V *vs.* RHE), which was exclusively attributed to HER. The adsorption of dinitrogen could be observed at a relatively lower reduction potential owing to the good adsorption tendency of Fe<sub>3</sub>O<sub>4</sub> for nitrogen molecule which leads to the increase in cathodic current at -0.05 V (*vs.* RHE) itself.<sup>52</sup> The reason behind the increase in cathodic current density at high reduction potential in presence of Ar was attributed to HER since at a high reduction

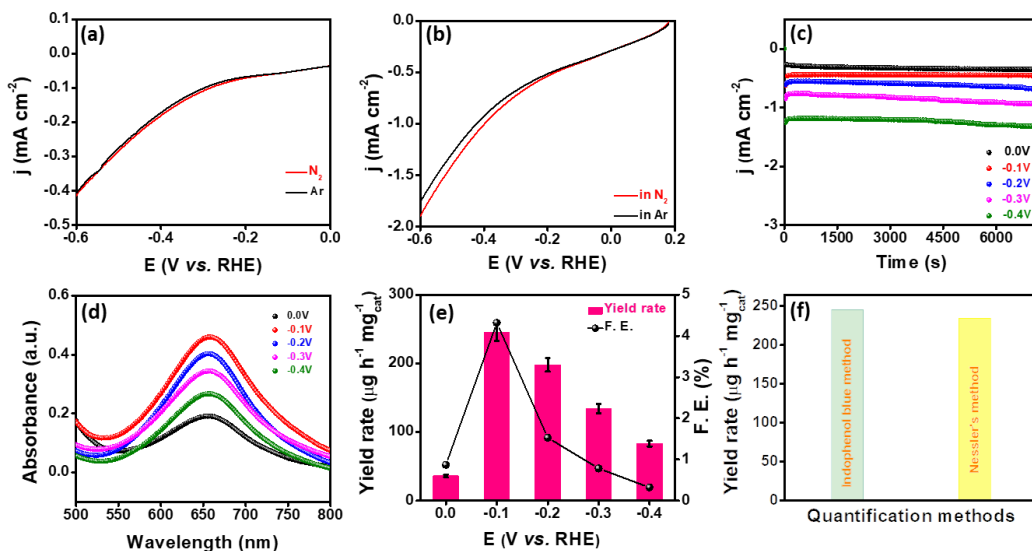


**Figure 5A-7.** LSV curves in Ar- and  $\text{N}_2$ -saturated electrolyte solution for (a) NiB-CP and (b)  $\text{Fe}_3\text{O}_4$ -70/NiB-CP, (c) chronoamperometric curves of  $\text{Fe}_3\text{O}_4$ -70/NiB-CP for different potentials, (d) corresponding UV-Vis spectrum for of the electrolyte samples after chronoamperometry (e) Faradaic efficiency and  $\text{NH}_3$  production yield rates at different potentials obtained by  $\text{Fe}_3\text{O}_4$ -70/NiB-CP. (f) bar graph comparison of  $\text{NH}_3$  yield after NRR by  $\text{Fe}_3\text{O}_4$ -70/NiB-CP at -0.1 V (vs. RHE) by different quantification methods.

potential, the low valance oxides can be formed at the surface of the electrode, so the adsorption of hydroxyl ion becomes more favourable as a result the HER becomes much more pronounced.<sup>53</sup> On the other hand, the NiB-CP showed comparatively lesser dinitrogen reduction. The observed net current density value of 0.024 mA  $\text{cm}^{-2}$  at -0.1 V vs. RHE for NRR ( $j_{\text{Ar}} - j_{\text{N}_2}$ ) imply the good electrocatalytic activity of  $\text{Fe}_3\text{O}_4$ -70/NiB-CP for effectual reduction of  $\text{N}_2$  under ambient conditions. Afterwards, the quantitative  $\text{NH}_3$  analysis was carried out by taking the electrolyte solution after performing chronoamperometry at different potentials (Figure 5A-7c), where  $\text{NH}_3$  and  $\text{N}_2\text{H}_4$  were examined as possible products. In this study,  $\text{NH}_3$  was found a selective product of the nitrogen reduction reaction without any traces of  $\text{N}_2\text{H}_4$  when quantified by indophenol blue (Figure 5A-7d) and Watt Chrisp method respectively.<sup>54</sup> The  $\text{NH}_3$  production yield rates and Faradaic efficiencies at different potentials are shown in Figure 5A-7e.

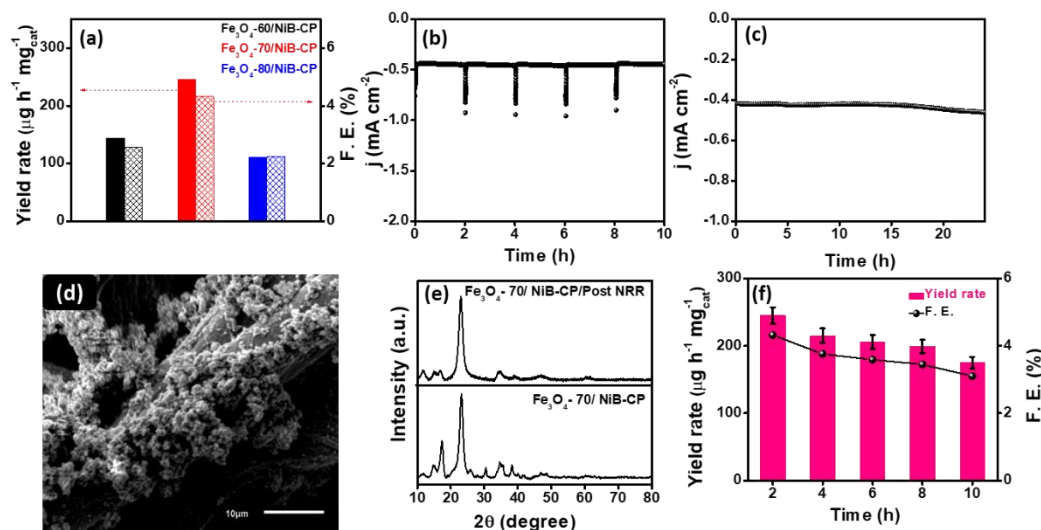


**Figure 5A-8.** (a) Comparison of NRR activity between  $\text{Fe}_3\text{O}_4\text{-T/NiB-CP}$  electrodes, (b) chronoamperometric curves for five different cycles, (c) chronoamperometric curves of  $\text{Fe}_3\text{O}_4\text{-70/NiB-CP}$  in  $\text{N}_2$  saturated electrolyte at -0.1 V vs. RHE, (d) SEM image of  $\text{Fe}_3\text{O}_4\text{-70/NiB-CP}$  electrode after stability study during NRR, (e) Diffraction pattern of  $\text{Fe}_3\text{O}_4\text{-70/NiB-CP}$  electrode before and after stability study during NRR and (f) corresponding F.E.,  $\text{NH}_3$  yield rates during cycling stability tests of 10 h for  $\text{Fe}_3\text{O}_4\text{-70/NiB-CP}$  electrodes.

Remarkably,  $\text{Fe}_3\text{O}_4\text{-70/NiB-CP}$  attained the maximum F.E. (4.32%) and yield rate ( $245 \mu\text{g h}^{-1} \text{mg}_{\text{cat}}^{-1}$ ) at -0.1 V vs. RHE, after which a decreasing pattern was observed. The obtained maximum yield rate by  $\text{Fe}_3\text{O}_4\text{-70/NiB-CP}$  was further supported by another quantitative method *viz.* Nessler's reagent method (Figure 5A-7f) i.e., the  $\text{NH}_3$  yield rate determined from Nessler's test ( $234 \mu\text{g h}^{-1} \text{mg}_{\text{cat}}^{-1}$ ) was in accordance with that obtained from Indophenol blue method, and pointing towards the reliability of  $\text{NH}_3$  yield rate. Remarkably, a high turnover frequency (TOF) value of  $0.83 \text{ h}^{-1}$  was perceived at a potential of -0.1 V for the nitrogen reduction by  $\text{Fe}_3\text{O}_4\text{-70/NiB-CP}$  electrode. In contrast, the catalytic activity of  $\text{Fe}_3\text{O}_4\text{-60/NiB-CP}$  and  $\text{Fe}_3\text{O}_4\text{-80/NiB-CP}$  electrodes towards  $\text{N}_2$  reduction was found to be inferior than  $\text{Fe}_3\text{O}_4\text{-70/NiB-CP}$  (Figure 5A-8a). The improved porous structure with the integration of active component became beneficial for the exposure of catalytic active sites in  $\text{Fe}_3\text{O}_4\text{-70/NiB-CP}$  and hence enhanced the mass transfer during NRR.<sup>55</sup> In addition to the high activity of  $\text{Fe}_3\text{O}_4\text{-70/NiB-CP}$

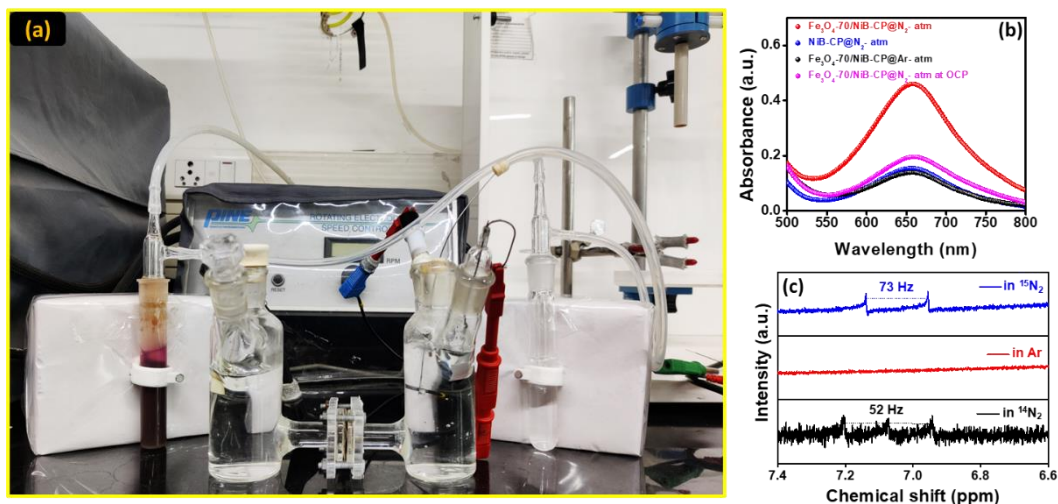


**Figure 5A-9.** (a) Image of H-cell setup prior to NRR measurements for purification of gas-streams passing through  $\text{KMnO}_4$  and acid trap, (b) UV-vis spectrum for the electrolytes collected after chronoamperometric measurement of  $\text{Fe}_3\text{O}_4$ -70/NiB-CP and NiB-CP at various conditions in 0.1 M KOH electrolyte, (c)  $^1\text{H}$  NMR spectra of electrolyte after electroreduction under  $^{14}\text{N}_2$ , Ar and  $^{15}\text{N}_2$  feeding.

electrode, it can retain the NRR activity even after 10 h of successive cycles (Figure 5A-8b). Moreover, a stable current response even after 24 h of NRR (Figure 5A-8c) was observed without any significant variation in the deposition and structural composition of  $\text{Fe}_3\text{O}_4$ -70/NiB-CP, pointing towards the robustness of the electrode [Figures 5A-8(d-e)]. The high stability of  $\text{Fe}_3\text{O}_4$ -70/NiB-CP during NRR in  $\text{N}_2$ -saturated 0.1 M KOH was confirmed by negligible change in the faradic efficiency as well as yield rate even after continuous cycling for 10 hours (Figure 5A-8f). It can be stated that the nitrogen molecule can easily adsorb over the surface of the  $\text{Fe}_3\text{O}_4$  and the electron deficient  $\text{BO}^{2-}$  species present in the NiB induces the strong electron effect which further benefit  $\text{N}_2$  binding and minimizing high energy barrier for  $\text{NH}_3$  formation and desorption.<sup>56, 57</sup>

Further, a series of control experiments were performed to confirm the thus obtained  $\text{NH}_3$  was completely from the electrochemical NRR process and not from any impurities which may be present in electrolyte as well as feeding gas. The feeding nitrogen gas was passed through the purification setup containing  $\text{KMnO}_4$

and  $\text{H}_2\text{SO}_4$  trap (Figure 5A-9a) to eliminate any trace N-containing impurities prior to NRR measurement.<sup>58</sup> The possible  $\text{NO}_3^-/\text{NO}_2^-$  contaminants in the electrolyte which might overestimate  $\text{NH}_3$  production were ruled out by following the spectrophotometric method where dissolved  $\text{NO}_3^-/\text{NO}_2^-$  species in the electrolyte were not observed. Moreover, when the electrolysis was performed in Ar-saturated electrolyte (Figure 5A-9b), no  $\text{NH}_3$  production was observed. These outcomes confirmed that the  $\text{NH}_3$  production during electrolysis was only due to NRR by the developed electrode and not by any N-containing impurities present in the system. Additionally, the isotopic labelling experiments were carried out by using  $^{14}\text{N}_2$  and  $^{15}\text{N}_2$  gas supply in 0.1 M KOH electrolyte to validate a reliable and true  $\text{NH}_3$  production. For this, the chronoamperometry measurements for two hours at -0.1 V (vs. RHE) were performed by taking  $\text{Fe}_3\text{O}_4$ -70/NiB-CP electrode in  $^{14}\text{N}_2$  and  $^{15}\text{N}_2$ -purged electrolyte and the electrolyte was analysed by  $^1\text{H}$ NMR spectroscopy. The  $^1\text{H}$ NMR spectra (Figure 5A-9c) demonstrated characteristic triplet and doublet for  $^{14}\text{NH}_4^+$  and  $^{15}\text{NH}_4^+$  respectively. These results lead to an inference that  $\text{Fe}_3\text{O}_4$ -70/NiB-CP exhibited an appreciable activity towards NRR for ammonia synthesis under ambient conditions

### 5A-3.3 Oxygen bifunctional activity

After assessing the ability of  $\text{Fe}_3\text{O}_4$ -70/NiB-CP towards NRR, we scrutinized the oxygen bifunctional activity of the same to be applied as an air cathode in Zn-air batteries. Firstly, the oxygen evolution reaction (OER) activity of  $\text{Fe}_3\text{O}_4$ -T/NiB-CP electrodes were studied in 1 M KOH by using Hg/HgO/1M NaOH as the reference electrode and Pt wire as the counter electrode. The LSV curves for the bare NiB-CP,  $\text{Fe}_3\text{O}_4$ -60/NiB-CP and  $\text{Fe}_3\text{O}_4$ -80/NiB-CP catalysts were shown in Figure 5A-10a. Amazingly, the  $\text{Fe}_3\text{O}_4$ -70/NiB-CP electrode exhibited the initialization of OER at around 1.41 V (overpotential 180 mV) to deliver  $10 \text{ mA cm}^{-2}$  which is lower than NiB-CP,  $\text{Fe}_3\text{O}_4$ -60/NiB-CP and  $\text{Fe}_3\text{O}_4$ -80/NiB-CP electrodes and even less than commercial  $\text{RuO}_2$  catalyst (1.52 V). Besides, a three-fold increase in current density value (at low potential i.e., 1.55 V vs. RHE) further described its

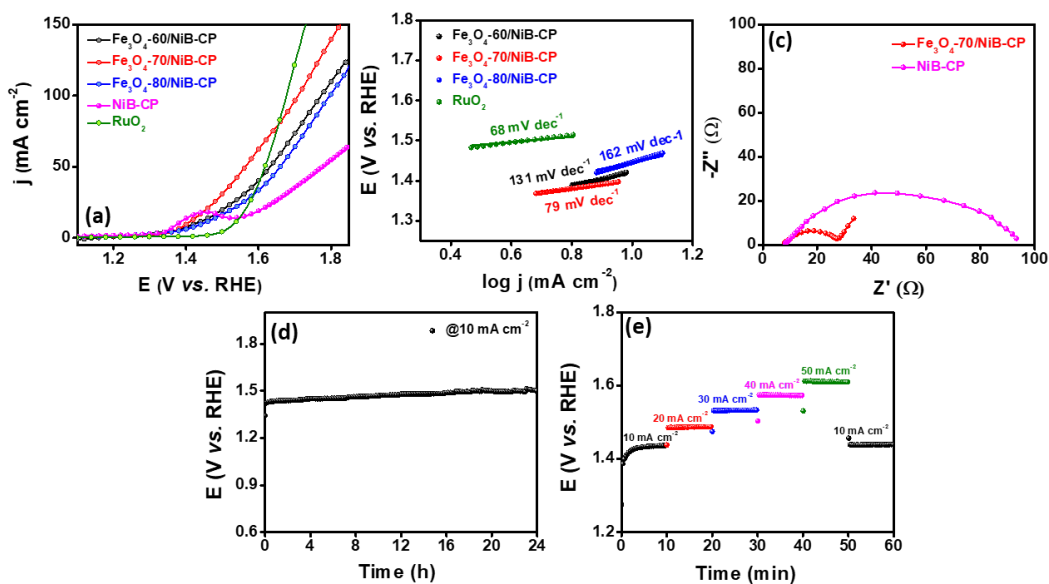


**Figure 5A-10.** (a) Linear sweep voltammograms ( $iR$ -corrected) for  $\text{Fe}_3\text{O}_4$ -T/NiB-CP, NiB-CP and  $\text{RuO}_2$  in 1M KOH electrolyte solution at  $10 \text{ mV s}^{-1}$ , (b) Tafel plots of different electrodes, (c) EIS spectra for different electrodes, (d) chronopotentiometric test for 24 h and (e) sequential chronopotentiometric measurement at different current densities for  $\text{Fe}_3\text{O}_4$ -70/NiB-CP electrode.

better activity surpassing the benchmark  $\text{RuO}_2$  catalyst and comparable to one of the most active NiFe-LDH catalyst for OER at similar potential value.<sup>57</sup> The superior activity of the  $\text{Fe}_3\text{O}_4$ -70/NiB-CP electrode was further supported by the Tafel slope analysis as it is often regarded as an indicator of reaction kinetics, where the lower slope values specifies a facilitated kinetics. As shown in Figure 5A-10b, the Tafel slope of  $\text{Fe}_3\text{O}_4$ -70/NiB-CP was found to be  $79 \text{ mV dec}^{-1}$  which was comparatively much lower than other electrodes such as: NiB-CP ( $283 \text{ mV dec}^{-1}$ ),  $\text{Fe}_3\text{O}_4$ -60/NiB-CP ( $131 \text{ mV dec}^{-1}$ ) and  $\text{Fe}_3\text{O}_4$ -80/NiB-CP ( $162 \text{ mV dec}^{-1}$ ) and it was even comparable to that of state-of-art  $\text{RuO}_2$  catalyst ( $68 \text{ mV dec}^{-1}$ ). These outcomes remark the excellent performance of  $\text{Fe}_3\text{O}_4$ -70/NiB-CP electrode towards OER, imitating it as one of the best flexible electrodes reported to date. In order to understand the roots of this high electrochemical activity towards OER, the charge-transfer resistance ( $R_{ct}$ ) and electrochemical surface area (ECSA) were



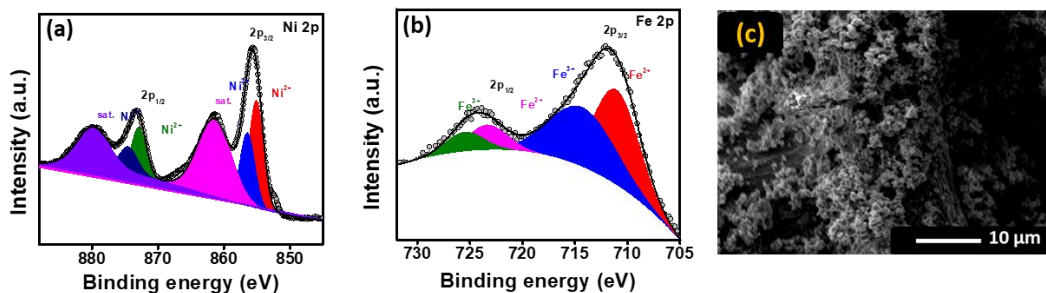


**Figure 5A-11.** Deconvoluted XPS spectra for (a) Ni 2p, (b) Fe 2p and (c) SEM image of Fe<sub>3</sub>O<sub>4</sub>-70/NiB-CP electrode after OER stability tests.

measured by means of electrochemical impedance spectroscopy (EIS) and a cyclic voltammetry (CV) method.<sup>59</sup> The ECSA value was determined to be 78.75 cm<sup>2</sup> for Fe<sub>3</sub>O<sub>4</sub>-70/NiB-CP electrode which was found higher than that of Fe<sub>3</sub>O<sub>4</sub>-60/NiB-CP (55.25 cm<sup>2</sup>) and Fe<sub>3</sub>O<sub>4</sub>-80/NiB-CP (34 cm<sup>2</sup>), as presented in Table 5A-2. This displayed the role of uniform deposition of Fe<sub>3</sub>O<sub>4</sub> over substrate surface, which consequences in plenty of active sites during electrochemical oxygen evolution reaction. The under-deposited nanoparticles in Fe<sub>3</sub>O<sub>4</sub>-60/NiB-CP led to less availability of active sites whilst the over-deposited aggregated nanoparticles in Fe<sub>3</sub>O<sub>4</sub>-80/NiB-CP caused blocking of the active sites and lowered the same and this was responsible for the inferior electrochemical performance as compared to the catalyst prepared at bath temperature of 70°C with uniform and optimal deposition. Similarly, the Nyquist plots demonstrated a typical semi-circle, with the highest charge transfer resistance ( $R_{ct}$ ) value of 85  $\Omega$  for NiB-CP. The decrease in  $R_{ct}$  value with the introduction of Fe<sub>3</sub>O<sub>4</sub> over the NiB-CP, signified that the Fe<sub>3</sub>O<sub>4</sub> nanoparticles promoted the transmission of electrons (Figure 5A-10c). The  $R_{ct}$  value among Fe<sub>3</sub>O<sub>4</sub>/NiB-CP electrodes followed the order Fe<sub>3</sub>O<sub>4</sub>-70/NiB-CP < Fe<sub>3</sub>O<sub>4</sub>-60/NiB-CP < Fe<sub>3</sub>O<sub>4</sub>-80/NiB-CP, which indicated the improved kinetics of Fe<sub>3</sub>O<sub>4</sub>-70/NiB-CP than other composite electrodes (Table 5A-2). Thus, the boosted performance could be attributed to the improved intrinsic activity via synergistic effect as well as the interfacial coupling between Fe<sub>3</sub>O<sub>4</sub> and NiB as evidenced by low overpotential, high current density, high ECSA and low  $R_{ct}$  values.<sup>60</sup> Besides



the remarkable OER activity the stability is another key parameter to evaluate the performance of electrodes. The long-term chronopotentiometric tests at  $10 \text{ mA cm}^{-2}$ , demonstrated that the stable potential response at almost identical value

**Table 5A-2. Electrochemical Impedance and ECSA analysis for various electrodes**

S.No.	Composites	$R_s (\Omega)$	$R_p (\Omega)$	$R_{ct} (\Omega)$	$C_{dl} (\text{mF}) @ 1.24 \text{ V vs. RHE}$	ECSA ( $\text{cm}^2$ )
1	$\text{Fe}_3\text{O}_4$ -60/NiB-CP	6	34	28	2.21	55.25
2	$\text{Fe}_3\text{O}_4$ -70/NiB-CP	7	27	20	3.15	78.75
3	$\text{Fe}_3\text{O}_4$ -80/NiB-CP	5	67	62	1.36	34

during continuous 24 hours measurement (Figure 5A-10d). Additionally, the sequential chronopotentiometric analysis was carried out at different current densities where a stable potential response for a designated time-period was observed as well as restoration of the potential was found when the applied current density was jumped back to initial value (Figure 5A-10e). Furthermore, the XPS analysis of electrode after long term electrolysis were shown in Figure 5A-11a & b. The diminishing of NiB peak and appearance of additional  $\text{Ni}^{3+}$  peak in the deconvoluted Ni 2p spectra with the positive shifting of binding energy value for  $2p_{3/2}$  and  $2p_{1/2}$  peaks indicated the formation of  $\text{NiOOH}$  and this was further supported by existence of  $\text{O}^{2-}$  peak in the deconvoluted O 1s spectra. Similarly, a positive shifting of binding energy value by  $\sim 0.5 \text{ eV}$  in comparison to as fabricated electrode was observed for  $2p_{3/2}$  and  $2p_{1/2}$  peaks in the high-resolution XP spectra of Fe 2p of  $\text{Fe}_3\text{O}_4$ -70/NiB-CP after OER analysis. These positive shifting of characteristic peaks corresponding to Fe  $2p_{3/2}$  and Ni  $2p_{3/2}$  demonstrated the formation of metal oxyhydroxide<sup>61, 62</sup> which was the indication of the probable electron/charge transfer<sup>63</sup> during the electrolysis. Moreover, the retention of uniform deposition over the NiB-CP was detected on the post electrolysis  $\text{Fe}_3\text{O}_4$ -70/NiB-CP electrode as evidenced by the SEM image (Figure 5A-11c), exhibiting the long-term durability of the electrode during OER in alkaline media.

In order to evaluate the inherent activity of paper electrode for practical applications, LSVs measurements under OER potential window were taken at

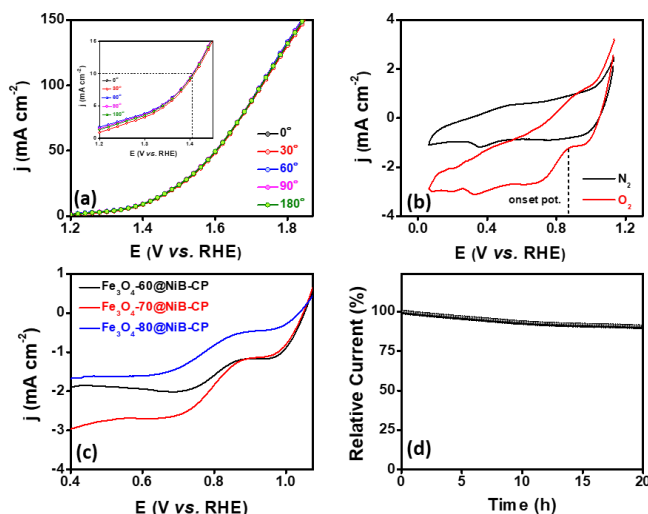


**Figure 5A-12.** (a) OER performance of Fe<sub>3</sub>O<sub>4</sub>-70/NiB-CP under various bending deformation states. (b) cyclic voltammogram for Fe<sub>3</sub>O<sub>4</sub>-70/NiB-CP, (c) LSV polarization curves for different electrodes towards ORR at 25 mV s<sup>-1</sup> of sweep rate at 0 rpm and (d) Stability test for 20 h during ORR by Fe<sub>3</sub>O<sub>4</sub>-70/NiB-CP electrode.

different bending angles. The Figure 5A-12a illustrated the almost similar current density as well as overpotential of Fe<sub>3</sub>O<sub>4</sub>-70/Ni-CP towards OER, affirming the actual practice of the same even under deformation states. To evaluate the bifunctional oxygen activity, we studied the potential ability of electrode towards oxygen reduction reaction (ORR) in 1 M KOH. The ORR activity of Fe<sub>3</sub>O<sub>4</sub>-70/NiB-CP was firstly compared with Fe<sub>3</sub>O<sub>4</sub>-60/NiB-CP and Fe<sub>3</sub>O<sub>4</sub>-80/NiB-CP by performing cyclic voltammetry and linear sweep voltammetry. Figures 5A-12(b-c) displayed a distinct reduction peak at 0.70 V vs. RHE for Fe<sub>3</sub>O<sub>4</sub>-70/NiB-CP with most positive potential, which highlighted the superior ORR activity over other Fe<sub>3</sub>O<sub>4</sub>-60/NiB-CP and Fe<sub>3</sub>O<sub>4</sub>-80/NiB-CP by showing a high value of onset potential (0.87 V vs. RHE). Similarly, the Fe<sub>3</sub>O<sub>4</sub>-70/NiB-CP also exhibited a good stability, as described by the retention of 90% of the current density even after prolonged chronoamperometry (20 h) in oxygen saturated electrolyte (Figure 5A-12d). Aforementioned outcomes demonstrated high activity and durability of Fe<sub>3</sub>O<sub>4</sub>-70/NiB-CP and its potential as an air electrode for rechargeable aqueous Zn-air batteries.

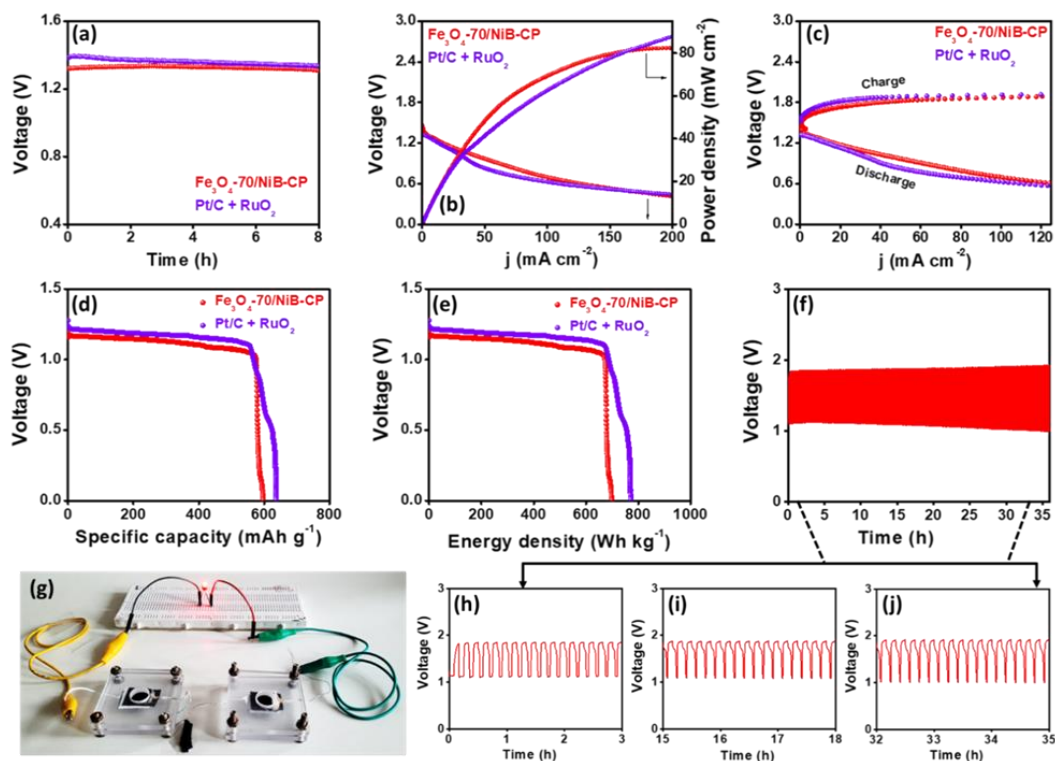


**Figure 5A-13.** (a) Open circuit potential, (b) peak power density curves, (c) charge-discharge polarization curves and, (d-e) corresponding specific capacity and energy density curves for as-assembled Zn-O<sub>2</sub> battery. (f) Cycling stability of Zn-air battery with  $\text{Fe}_3\text{O}_4$ -70/NiB-CP cathode during OER/ORR at  $5 \text{ mA cm}^{-2}$ . (g) Two Zn-air batteries connected in series lighting a red LED (2.0 V) and (h-j) zoomed cycling stability extracted from Figure 5A-13f at different time intervals

#### 5A-3.4 Application in Zn-air battery

By taking inspiration from this promising oxygen bifunctional activity, a homemade aqueous Zn-air battery was assembled by employing Zn metal as anode and  $\text{Fe}_3\text{O}_4$ -70/NiB-CP as an air-cathode which were separated by Whatman glass micro fibre separator where  $6 \text{ M KOH} + 0.2 \text{ M Zn (OAc)}_2$  was applied as an electrolyte. Thus assembled Zn-O<sub>2</sub> battery offered a high open circuit potential of 1.32 V and a peak power density of  $81 \text{ mW cm}^{-2}$  at 1.72 V which was comparable to commercial  $\text{RuO}_2$ +Pt/C [Figures 5A-13(a-b)]. The low potential gap between the overpotential during OER and onset potential during ORR are beneficial for

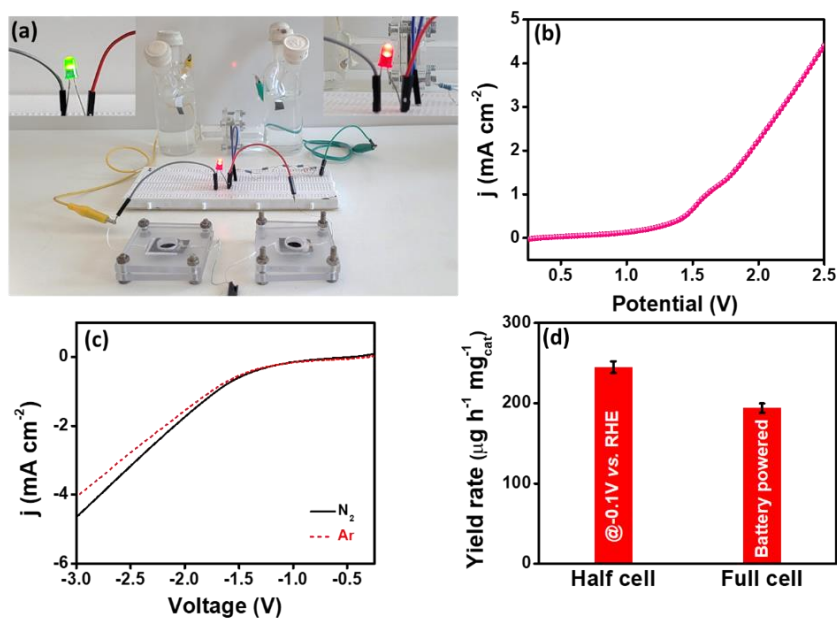


**Figure 5A-14.** (a) Photograph representing the battery powered NRR cell setup with two Zn-air batteries (equipped with Fe<sub>2</sub>O<sub>3</sub>-70/NiB-CP as air cathode) connected in series to power H-cell with Fe<sub>2</sub>O<sub>3</sub>-70/NiB-CP at both anode (OER) and cathode (NRR). Inset shows lighting up of red (2.0 V) and green (2.2 V) LED by the as-assembled setup. (b) & (c) LSV recorded under the full cell conditions during NH<sub>3</sub> synthesis, and (d) Bar graph comparison of NH<sub>3</sub> production yield rates obtained during half-cell and full-cell experiments.

better charge-discharge activity.<sup>64</sup> As a result, Fe<sub>3</sub>O<sub>4</sub>-70/NiB-CP reveal a small potential gap of 0.7 V for 5 mA cm<sup>-2</sup> during the charge- discharge (Figure 5A-13c). Furthermore, the Fe<sub>3</sub>O<sub>4</sub>-70/NiB-CP electrode was able to deliver a high specific capacity of 595 mA h g<sup>-1</sup> at 5 mA cm<sup>-2</sup> with a corresponding energy density of 698 W h kg<sup>-1</sup> (Figure 5A-13d-e). The as assembled battery further illustrated the excellent stability without any interrupted discharge at 5 mA cm<sup>-2</sup> for continuous 36 h (216 cycles with 5 minutes of charge and 5 minutes of discharge), with very small changes in potential gap [Figures 5A-13(f and h-j)]. In the end, the practical applicability of the Zn-air battery assembled with Fe<sub>3</sub>O<sub>4</sub>-70/NiB-CP air electrode was established by lighting up a red LED of 2.0 V (Figure 5A-13g) by taking this battery as a power source.

**5A-3.5 Application as trifunctional flexible electrode:** The main aim of this

study was to validate the applicability of as-designed electrode as a trifunctional flexible electrode. For this, two Fe<sub>3</sub>O<sub>4</sub>-70/NiB-CP equipped rechargeable Zn-air batteries, connected in series, were employed to power two-electrode NRR cell containing Fe<sub>3</sub>O<sub>4</sub>-70/NiB-CP flexible electrode at both anode and cathode for NH<sub>3</sub> synthesis (Figure 5A-14a). The bifunctional activity (i.e., OER at anode and NRR at cathode) was depicted by the steep increase of current density at 1.5 V during full-cell study (Figure 5A-14b). Similarly, the LSV curves recorded in Ar- and N<sub>2</sub>-saturated 0.1 M KOH clearly indicate the activity towards NRR (Figure 5A-14c). Finally, we carried out 2 h continuous electrolysis by using thus assembled battery as a power source to drive N<sub>2</sub> reduction and the produced NH<sub>3</sub> was quantified. Thus, developed Zinc-air battery powered two-electrode NRR cell was able to achieve ammonia yield rate of 194.25  $\mu\text{g h}^{-1} \text{mg}_{\text{cat}}^{-1}$  (Figure 5A-14d), which validated the ability of Fe<sub>3</sub>O<sub>4</sub>-70/NiB-CP to work as an efficient trifunctional flexible electrode.

#### **5A-4 Summary**

Here, we have developed Fe<sub>3</sub>O<sub>4</sub> deposited NiB-cellulose paper electrode *via* a two-step deposition method to achieve high activity towards OER, ORR and NRR. A straight forward approach of conversion of insulating cellulose paper into eco-friendly flexible electrode is presented. The conductivity is induced in the cellulose paper by electroless deposition of NiB, in which active electrocatalyst Fe<sub>3</sub>O<sub>4</sub> nanospheres is decorated by electrodeposition technique. This electrode was able to demonstrate electrocatalytic dinitrogen reduction with good yield rate (245  $\mu\text{g h}^{-1} \text{mg}_{\text{cat}}^{-1}$ ), promising Faradaic efficiency (4.32%) and a high TOF (0.83  $\text{h}^{-1}$ ) at a lower applied potential of -0.1 V *vs.* RHE. The observed inspiring oxygen bifunctional activity lead towards the development of eco-friendly, rechargeable Zn-O<sub>2</sub> battery. The as assembled battery demonstrated good power density, high specific capacity, and stable cyclability with small charge discharge overpotential. As an inspiration of the impressive trifunctional catalytic activity, this study is able to achieve paper electrode-based Zn-O<sub>2</sub> battery powered electrochemical nitrogen

reduction reaction with good  $\text{NH}_3$  yield of  $194.25 \mu\text{g h}^{-1} \text{mg}_{\text{cat}}^{-1}$ . Therefore, this work can encourage researchers for the development of cost effective, highly selective and efficient electrocatalyst decorated multifunctional eco-friendly paper electrodes towards energy storage and conversion and other electrochemical applications.

## 5A-5 References

1. Z. Wang, P. Tammela, M. Strømme and L. Nyholm, *Adv. Energy Mater.*, 2017, **7**, 1700130.
2. P. J. McHugh, A. D. Stergiou and M. D. Symes, *Adv. Energy Mater.*, 2020, **10**, 2002453.
3. Y. G. Guo, J. S. Hu and L. J. Wan, *Adv. Mater.*, 2008, **20**, 2878-2887.
4. R. Xu, L. Du, D. Adekoya, G. Zhang, S. Zhang, S. Sun and Y. Lei, *Adv. Energy Mater.*, 2021, **11**, 2001537.
5. H. Zhao and Y. Lei, *Adv. Energy Mater.*, 2020, **10**, 2001460.
6. H. Yang, X. Han, A. I. Douka, L. Huang, L. Gong, C. Xia, H. S. Park and B. Y. Xia, *Adv. Funct. Mater.*, 2021, **31**, 2007602.
7. X. Gao, X. Liu, W. Zang, H. Dong, Y. Pang, Z. Kou, P. Wang, Z. Pan, S. Wei and S. Mu, *Nano Energy*, 2020, **78**, 105355.
8. J. Ikäheimo, J. Kiviluoma, R. Weiss and H. Holttinen, *Int. J. Hydrog. Energy*, 2018, **43**, 17295-17308.
9. G. Soloveichik, *Nat. Catal.*, 2019, **2**, 377-380.
10. G. Qing, R. Ghazfar, S. T. Jackowski, F. Habibzadeh, M. M. Ashtiani, C.-P. Chen, M. R. Smith III and T. W. Hamann, *Chem. Rev.*, 2020, **120**, 5437-5516.
11. Q. Liu, Z. Pan, E. Wang, L. An and G. Sun, *Energy Storage Mater.*, 2020, **27**, 478-505.
12. M. Wang, C. Zhang, T. Meng, Z. Pu, H. Jin, D. He, J. Zhang and S. Mu, *J. Power Sources*, 2019, **413**, 367-375.
13. T. Jin, Q. Han and L. Jiao, *Adv. Mater.*, 2020, **32**, 1806304.
14. P. Wang and B. Wang, *ChemSusChem*, 2020, **13**, 4795-4811.
15. L. Dong, C. Xu, Y. Li, Z.-H. Huang, F. Kang, Q.-H. Yang and X. Zhao, *J. Mater. Chem. A*, 2016, **4**, 4659-4685.
16. A. Kaffle, M. Kumar, D. Gupta and T. C. Nagaiah, *J. Mater. Chem. A*, 2021, **9**, 24299-24307.
17. H. Liu, K.-s. Moon, J. Li, Y. Xie, J. Liu, Z. Sun, L. Lu, Y. Tang and C.-P. Wong, *Nano Energy*, 2020, **77**, 105058.
18. R. Q. Yao, H. Shi, W. B. Wan, Z. Wen, X. Y. Lang and Q. Jiang, *Adv. Mater.*, 2020, **32**, 1907214.
19. M.-S. Wu, Z.-B. Zheng, Y.-S. Lai and J.-J. Jow, *Electrochim. Acta*, 2015, **182**, 31-38.
20. X. Zhang, F. Yang, H. Chen, K. Wang, J. Chen, Y. Wang and S. Song, *Small*, 2020, **16**, 2004188.
21. H. Li, X. Zhang, Z. Zhao, Z. Hu, X. Liu and G. Yu, *Energy Storage Mater.*, 2020, **26**, 83-104.
22. F. Liu, X. Cao, L. Cui, L. Yue, D. Jia and J. Liu, *J. Power Sources*, 2019, **421**, 169-178.
23. P. Wang, R. Qin, P. Ji, Z. Pu, J. Zhu, C. Lin, Y. Zhao, H. Tang, W. Li and S. Mu, *Small*, 2020, **16**, 2001642.
24. H. G. Wang, W. Li, D. P. Liu, X. L. Feng, J. Wang, X. Y. Yang, X. b. Zhang, Y. Zhu and Y. Zhang, *Adv. Mater.*, 2017, **29**, 1703012.
25. C. Yu, J. An, Q. Chen, J. Zhou, W. Huang, Y. J. Kim and G. Sun, *Small Methods*, 2020, **4**, 1900824.

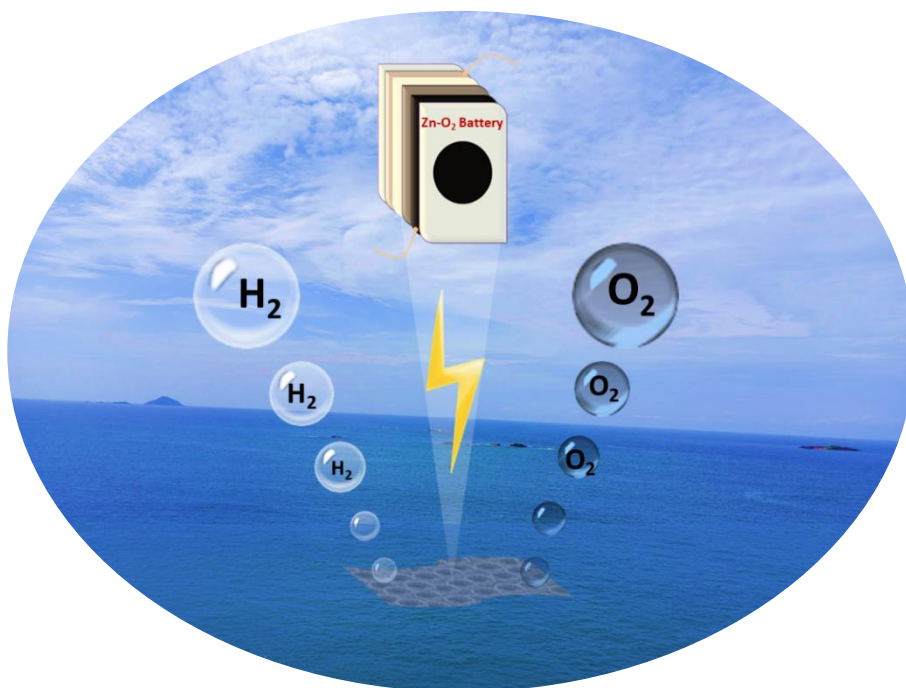
26. M. H. Lee, J. Lee, S. K. Jung, D. Kang, M. S. Park, G. D. Cha, K. W. Cho, J. H. Song, S. Moon and Y. S. Yun, *Adv. Mater.*, 2021, **33**, 2004902.
27. D. Zhao, Y. Zhu, W. Cheng, W. Chen, Y. Wu and H. Yu, *Adv. Mater.*, 2021, **33**, 2000619.
28. Y. Yang, Q. Huang, G. F. Payne, R. Sun and X. Wang, *Nanoscale*, 2019, **11**, 725-732.
29. Y.-Y. Li, P. Kang, S.-Q. Wang, Z.-G. Liu, Y.-X. Li and Z. Guo, *Sens. Actuators B Chem.*, 2021, **327**, 128878.
30. S. Jiang, J. Li, J. Fang and X. Wang, *Small*, 2021, **17**, 1903760.
31. S. Zhou, L. Nyholm, M. Strømme and Z. Wang, *Acc. Chem. Res.*, 2019, **52**, 2232-2243.
32. G. Zheng, L. Hu, H. Wu, X. Xie and Y. Cui, *Energy Environ. Sci.*, 2011, **4**, 3368-3373.
33. B. Anothumakkool, R. Soni, S. N. Bhange and S. Kurungot, *Energy Environ. Sci.*, 2015, **8**, 1339-1347.
34. P. Yáñez-Sedeño, S. Campuzano and J. M. Pingarrón, *Biosensors*, 2020, **10**, 76.
35. M. M. Hamed, A. Hajian, A. B. Fall, K. Hakansson, M. Salajkova, F. Lundell, L. Wagberg and L. A. Berglund, *ACS Nano*, 2014, **8**, 2467-2476.
36. L.-Q. Tao, K.-N. Zhang, H. Tian, Y. Liu, D.-Y. Wang, Y.-Q. Chen, Y. Yang and T.-L. Ren, *ACS Nano*, 2017, **11**, 8790-8795.
37. M.-C. Hsieh, C. Kim, M. Nogi and K. Suganuma, *Nanoscale*, 2013, **5**, 9289-9295.
38. D. Zabetakis and W. J. Dressick, *ACS Appl. Mater. Interfaces*, 2012, **4**, 2358-2368.
39. F. Muench, *ChemElectroChem*, 2021.
40. A. Sahasrabudhe, H. Dixit, R. Majee and S. Bhattacharyya, *Nat. Commun.*, 2018, **9**, 1-14.
41. W. Hao, R. Wu, H. Huang, X. Ou, L. Wang, D. Sun, X. Ma and Y. Guo, *Energy Environ. Sci.*, 2020, **13**, 102-110.
42. C. Li, Y. Fu, Z. Wu, J. Xia and X. Wang, *Nanoscale*, 2019, **11**, 12997-13006.
43. L. Hu, A. Khaniya, J. Wang, G. Chen, W. E. Kaden and X. Feng, *ACS Catal.*, 2018, **8**, 9312-9319.
44. P. Zhang, M. Wang, Y. Yang, T. Yao, H. Han and L. Sun, *Nano Energy*, 2016, **19**, 98-107.
45. D. K. Schroder, *Semiconductor material and device characterization*, John Wiley & Sons, 2015.
46. E. Liu, H. Yuan, Z. Kou, X. Wu, Q. Xu, Y. Zhai, Y. Sui, B. You, J. Du and H. Zhai, *Sci. Rep.*, 2015, **5**, 1-11.
47. J. Zhang, X. Li, Y. Liu, Z. Zeng, X. Cheng, Y. Wang, W. Tu and M. Pan, *Nanoscale*, 2018, **10**, 11997-12002.
48. C. Wu, H. Li, Z. Xia, X. Zhang, R. Deng, S. Wang and G. Sun, *ACS Catal.*, 2020, **10**, 11127-11135.
49. D. He, L. Zhang, D. He, G. Zhou, Y. Lin, Z. Deng, X. Hong, Y. Wu, C. Chen and Y. Li, *Nat. Commun.*, 2016, **7**, 1-8.
50. J. Schreifels, P. Maybury and W. Swartz Jr, *J. Catal.*, 1980, **65**, 195-206.
51. H. Ying, T. Chen, C. Zhang, J. Bi, Z. Li and J. Hao, *J. Colloid Interface Sci.*, 2021, **602**, 64-72.
52. H.-Q. Xie, X. Zheng, Q.-Y. Feng, X.-P. Chen, Z.-H. Zou, Q.-X. Wang, J. Tang, Y. Li and Y. Ling, *ChemSusChem*, 2022.
53. Z. Liang, H. S. Ahn and A. J. Bard, *J. Am. Chem. Soc.*, 2017, **139**, 4854-4858.
54. W. Liu, C. Li, Q. Xu, P. Yan, C. Niu, Y. Shen, P. Yuan and Y. Jia, *ChemCatChem*, 2019, **11**, 5412-5416.
55. H. Wang, W. Wang, Y. Y. Xu, S. Dong, J. Xiao, F. Wang, H. Liu and B. Y. Xia, *ACS Appl. Mater. Interfaces*, 2017, **9**, 10610-10617.
56. Z. Xu, Y. Ying, G. Zhang, K. Li, Y. Liu, N. Fu, X. Guo, F. Yu and H. Huang, *J. Mater. Chem. A*, 2020, **8**, 26130-26138.
57. Y. Li, H. Yu, Z. Wang, S. Liu, Y. Xu, X. Li, L. Wang and H. Wang, *Chem. Commun.*, 2019, **55**, 14745-14748.
58. U. B. Shahid, Y. Chen, S. Gu, W. Li and M. Shao, *Trends Chem.*, 2021.
59. N. Thakur, M. Kumar, D. Mandal and T. C. Nagaiah, *ACS Appl. Mater. Interfaces*, 2021.

60. W. Tian, D. Zheng, X. Sun, X. Guan, H. Feng, C. Li, M. Yan and Y. Yao, *Inorg. Chem.*, 2021, **60**, 14786-14792.
61. R. Tian, S. Zhao, J. Li, Z. Chen, W. Peng, Y. He, L. Zhang, S. Yan, L. Wu and R. Ahuja, *J. Mater. Chem. A*, 2021, **9**, 6469-6475.
62. B. Wei, C. Shang, X. Wang and G. Zhou, *Small*, 2020, **16**, 2002789.
63. J. Yang, Y. Xiao, Q. Zhao, G. Zhang, R. Wang, G. Teng, X. Chen, M. Weng, D. He and S. Mu, *Nano Energy*, 2019, **59**, 443-452.
64. Y. Niu, X. Teng, S. Gong, M. Xu, S.-G. Sun and Z. Chen, *Nanomicro Lett.*, 2021, **13**, 1-16.



## Chapter 5B

### NiFeP/NiB decorated cellulose paper based flexible electrode for self-powered alkaline water splitting



## 5B-1 Introduction

Hydrogen is considered as an ideal energy source due to its low weight and high energy density.<sup>1-3</sup> Till date, hydrogen production is dominated by steam reformation process consuming fossil fuels, which in turn lead to not only the depletion of fossil fuel reserves but also adverse effects on the environment and moreover, the as obtained hydrogen contains many impurities.<sup>4, 5</sup> Therefore, it is vital to produce high purity hydrogen avoiding the consumption fossil fuels.<sup>6</sup> Electrochemical water splitting is the utmost way to produce hydrogen in highly pure form which involves hydrogen evolution reaction (HER) at the cathode and oxygen evolution reaction (OER) at the anode of an electrolytic cell producing gaseous molecular hydrogen and oxygen, respectively.<sup>1, 7</sup> But the indolent kinetics of both HER and OER (especially OER) makes it an odorous task.<sup>8</sup> Unfortunately, most of the global electricity production relies on fossil fuel operated thermal plants. In addition to it, global crisis like frequent energy consumption and environment pollution due to heavy dependency on the energy extracted/supplied from fossil fuels have led to the development of alternatives integrated energy systems (IES) viz. combined solar cell and lithium storage unit, water splitting powered by solar cells/metal-air batteries to overcome the weather dependency associated with renewable energy such as solar power, hydropower and wind power etc.<sup>6, 9-12</sup> More importantly, integration of the energy storage and conversion devices will provide an advanced solution to the drawbacks in existing individual devices with a cumulative efficiency.<sup>13</sup> Inspired from this, self-powered water splitting could be a sustainable and viable choice for near future to meet the demands of green H<sub>2</sub> production by integrating with energy storage device like metal-air batteries, particularly Zn-air (O<sub>2</sub>) batteries. Zn-O<sub>2</sub> batteries have demonstrated their potential as the power source for high-density energy storage due to their high energy density (1218 Wh kg<sup>-1</sup>), efficiency and environment friendliness.<sup>14, 15</sup> Interestingly, a commercial water electrolyzer is operated at a cell voltage of 1.8–2.0 V (much higher than the theoretical minimum value of 1.23

V),<sup>16, 17</sup> which is the voltage that can be realized by Zn–air batteries.<sup>15</sup> The core of this integrated self-powered water splitting device lies in the designing of efficient and robust electrocatalysts with multifunctional activity which can be used for both water splitting and stable power supply by Zn-O<sub>2</sub> battery.<sup>14, 18, 19</sup> More precisely, the development of a trifunctional electrocatalyst with very high activity for complex and sluggish multielectron transfer processes such as the oxygen reduction reaction (ORR), OER and HER involved in water splitting and Zn-O<sub>2</sub> battery is of great interest. More importantly, pairing two different electrodes for OER and HER and applying different catalysts for OER and HER during water splitting and for ORR and OER at air cathode during Zn-O<sub>2</sub> battery operation increase reaction complexity, material and overall processing costs and further urges the development of a trifunctional catalyst.<sup>13, 20</sup> To date, precious IrO<sub>2</sub> and RuO<sub>2</sub> are considered as benchmarking catalysts for OER but not efficient for the ORR and HER. In contrast, Pt/C remains the state-of-the-art catalyst for the HER/ORR, but is unstable under oxidative conditions during OER.<sup>20, 21</sup> The high cost, scarcity and poor durability of these precious metal based catalysts hinder the practical scalability and thus necessitates the development of a cost-effective trifunctional catalyst based on non-precious elements.<sup>22</sup> Indeed, the designing of such a catalyst which possess ample number of active sites and robustness towards three different reactions with completely different fundamental mechanisms is yet complicated but the need of the hour.

In addition to all these above mentioned factors, the coherent design of electrode architecture also plays a vital role to further improve the electrochemical performance of any electrocatalyst.<sup>23, 24</sup> As the use of insulating binder in the conventional electrode fabrication techniques with the rigid current collector not only increase the overall fabrication cost but also hinders the electrocatalytic activity.<sup>25, 26</sup> In this context, binder free, self-standing three dimensional flexible electrode with an active catalyst grown over their surfaces can be a good strategy to enhance the electrochemical activity.<sup>27</sup> And moreover, these electrodes can be applicable for any type of reactors and devices so that it can also establish exciting

opportunities towards the advancement flexible electronics.<sup>23</sup> Thus, the development of durable, cost effective and eco-friendly flexible electrodes showing multifunctional activity is currently needed. At present, existing carbon and metal foam/foil-based substrates as flexible electrodes for catalyst hosting have many glitches including structural fragility, incompatibility for large scale fabrication and expensive procedures.<sup>27</sup> Besides these, disposals of used material is creating serious environmental issues. Therefore, development of eco-friendly, mechanically strong biodegradable substrate based flexible electrodes with overall high catalytic activity using cheap and easily available precursors adds up in initiation to overcome the aforementioned drawbacks. In this context, our group has established a fascinating approach for the development of bio-degradable material based highly flexible paper electrode via straightforward electroless-electrodeposition approach for sustainable eco-friendly energy storage and conversion applications.<sup>27</sup> Therefore, the strategy of combining electroless deposition and electrodeposition for the development of non-conductive substrate-based electrode can be explored with various type of active materials for different electrochemical applications.

With this view point, biodegradable and ubiquitous cellulose paper based self-standing three-dimensional flexible electrodes exhibiting trifunctional activity towards ORR, OER and HER for self-powered water splitting has been developed. Herein, laboratory Whatman filter paper was converted to conductive paper substrate by electroless deposition and well explored NiFeP composite as active electrocatalyst was decorated over it by electrodeposition method which was directly used as a working electrode for electrochemical applications. Thus, developed electrode demonstrated the good trifunctional activity towards ORR, OER and HER. A Zn-O<sub>2</sub> battery is assembled with the designed electrode as air-cathode which exhibited a good power density and high specific capacity, with stable cyclability. Additionally, this Zn-air battery is able to power an alkaline water electrolyser to perform overall electrochemical water splitting.

## **5B-2 Electrode fabrication**

**5B-2.1 Fabrication of NiB-CP:** The insulating cellulose paper (CP) was converted to conductive paper substrate by following the reported literature. Briefly, the clean laboratory Whatman filter paper (1cm x 1cm) was placed in an ice cold bath solution composed of 6 mmol  $\text{NiCl}_2$ , 13.5 mmol  $\text{NH}_4\text{Cl}$  and 6 mmol trisodium citrate in 15 mL of 1M NaOH solution in which ice cold  $\text{NaBH}_4$  solution (12 mmol  $\text{NaBH}_4$  dissolved in 10 mL of 1M NaOH) was added slowly from the wall of the vessel and left as such till the completion of the reaction. After that the NiB coated cellulose paper was cleaned by sonicating it in water followed by in ethanol: water (1:1) solution then dried in hot air oven at 60 °C and it is designated as NiB-CP.

**5B-2.2 Fabrication of NiFeP/NiB-CP:** The active electrocatalyst NiFeP was decorated over the NiB-CP surface by electrodeposition method for which the NiB-CP was taken as working electrode with Ag/AgCl/3M KCl and graphite rod reference and counter electrodes respectively. The electrodeposition was performed in a bath solution (composed of  $\text{NiSO}_4$ ,  $\text{FeSO}_4$ ,  $\text{Na(OAc)}$  and  $\text{NaH}_2\text{PO}_2$  in 40 mL water) by cyclic voltammetry at -1.0 to -0.3 V vs. Ag/AgCl and it was designated as NiFeP/NiB-CP. Similarly, the NiFeO/NiB-CP electrode was fabricated by following the same procedure in the absence of  $\text{NaH}_2\text{PO}_2$  in the bath solution. These electrodes were washed thoroughly with deionized water then finally dried in hot air oven at 60 °C.

## **5B-3 Results and discussion**

**5B-3.1 Physical characterization:** The NiFeP/NiB-CP and NiFeO/NiB-CP electrodes were prepared by a two-step deposition approach. Initially, NiB nanoparticle is coated over the CP to make it conductive by electroless deposition method by following reported literature and designated as NiB-CP. Thereafter, the active electrocatalyst NiFeP was coated over NiB-CP by electrodeposition method by performing cyclic voltammetry. The morphological features of these electrodes were obtained from SEM and TEM images. The SEM image of CP and NiB-CP

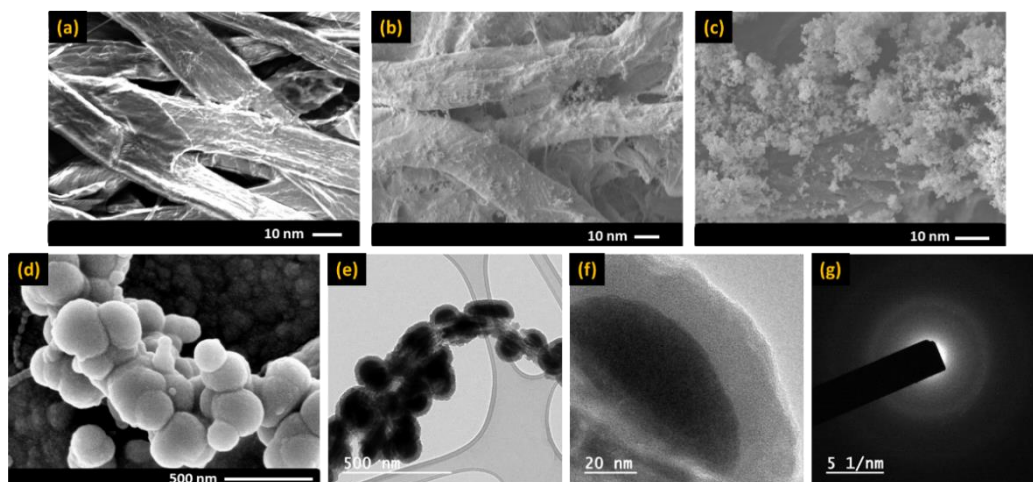


**Figure 5B-1.** SEM images of (a) bare cellulose paper (b) NiB-CP and (c) NiFeP/NiB-CP electrodes, (d) FE-SEM, (e) TEM and (f) HRTEM and (g) SAED pattern images of NiFeP/NiB-CP electrode.

(Figures 5B-1(a-b)) showed a uniform coating of NiB nanoparticles over cellulose paper. Similarly, the SEM image of NiFeP/NiB-CP electrode (Figure 5B-1c) demonstrated the granular particle deposition over the NiB-CP surface which was further analysed through the field-emission-scanning electron microscopy (FE-SEM) where a grape bunch like morphology was observed as shown in Figure 5B-1d which was further supported by TEM images (Figure 5B-1e). Additionally, the absence of lattice fringes in the HRTEM image (Figure 5B-1f) evidenced the amorphous nature of the deposit which was further supported by the SAED pattern (Figure 5B-1g). Similarly the EDS elemental dot mapping images evidenced the uniform distribution of respective elements over the scanned area (Figure 5B-2).

The microstructure of the prepared electrode was attributed by the PXRD analysis. As shown in Figure 5B-3, the NiFeP/NiB-CP displayed broad diffraction peak at  $2\theta$  value 38 to  $53^\circ$  closely matching with the  $\text{Fe}_2\text{NiP}$  phase (PDF no. 01-074-9000) along with the crystalline cellulose peaks at  $2\theta$  value  $16^\circ$ ,  $17.5^\circ$ ,  $23.7^\circ$  and  $35.3^\circ$  corresponding to planes (110) ( $1\bar{1}0$ ), (200) and (004) respectively.<sup>28</sup> The chemical composition of the NiFeP/NiB-CP electrode was investigated by X-ray photoelectron spectroscopy (XPS) analysis. The XP survey spectra of NiFeP/NiB-

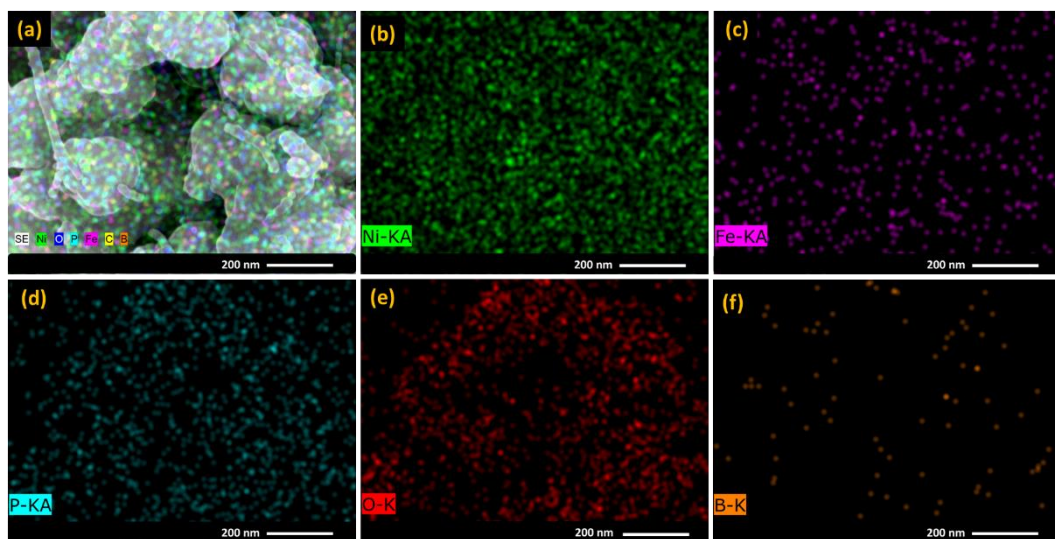


**Figure 5B-2.** Elemental dot mapping images for (a) all elements and separately for (b) Ni, (c) Fe, (d) P, (e) O and (f) B elements of NiFeP/NiB-CP electrode.

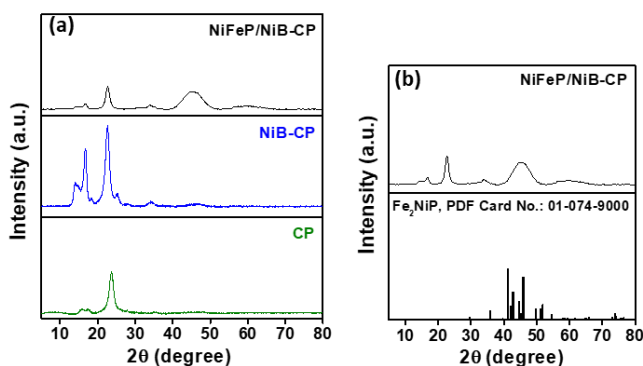


**Figure 5B-3.** The P-XRD pattern of (a) bare CP, NiB-CP, and NiFeB/NiB-CP and (b) comparison of NiFeB/NiB-CP with PDF card.

CP (Figure 5B-4a) confirmed the presence of Fe, Ni, O, P, and C elements. The high-resolution Ni 2p spectra upon deconvolution (Figure 5B-4b) demonstrated Ni 2p<sub>3/2</sub> and Ni 2p<sub>1/2</sub> peaks around 852.5 and 869.7 eV belonging to NiB as well as 855.4 and 873.1 eV corresponding to Ni<sup>2+</sup> respectively along with their satellite peaks.<sup>29</sup> Similarly, the peaks appeared around 710.1 and 723.8 eV belonging to Fe<sup>2+</sup> along with peaks at 713.8 and 726.8 corresponding to Fe<sup>3+</sup> in the deconvoluted Fe 2p spectra (Figure 5B-4c) confirmed the existence of iron in +2 and +3 oxidation states.<sup>30</sup> Furthermore, the peak at 133.1 and 134.1 eV in the high-resolution P 2p

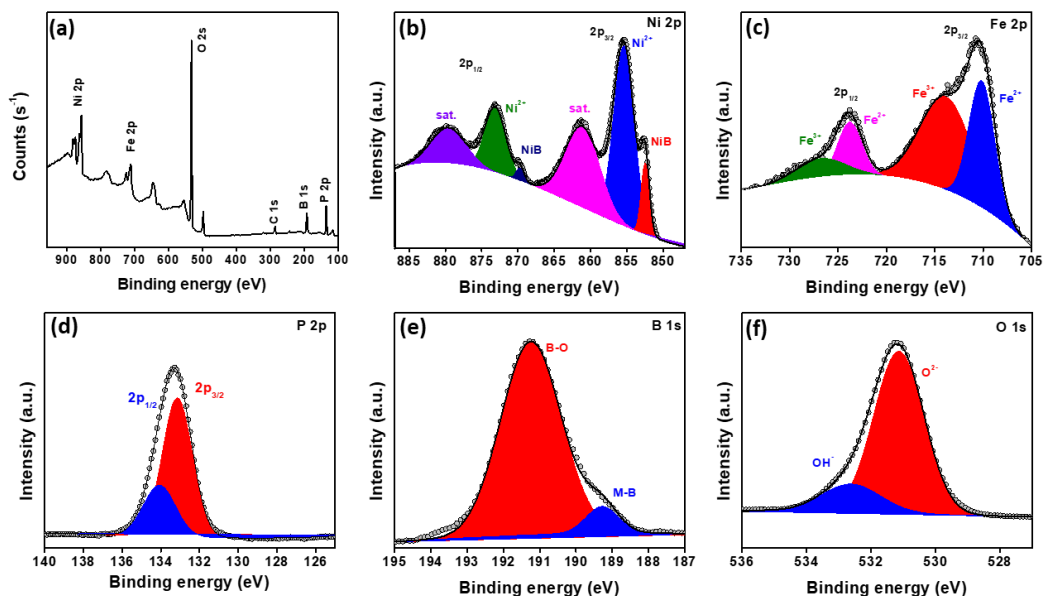


**Figure 5B-4.** The XPS spectra of NiFeP/NiB-CP (a) full survey scan and deconvoluted spectra of (b) Ni 2p (c) Fe 2p (d) P 2p (e) B 1s and (f) O 1s elements.

spectra attributes to the  $P2p_{3/2}$  and  $P2p_{1/2}$  peaks (Figure 5B-4d).<sup>31</sup> Also, the observed M- B and  $BO_x$  peaks around 189 and 192 eV in the deconvoluted B 1s spectra (Figure 5B-4e) confirmed the presence of NiB.<sup>32</sup> Additionally, the peaks located around 531.2 and 532.5 eV in the O 1s spectrum confirms the presence of  $O^{2-}$  and  $OH^-$  species (Figure 5B-4f). These results confirmed the successful incorporation of NiFeP over the surface of NiB-CP.

**5B-3.2 Electrochemical study:** To realize the applicability of the as-developed electrode towards Zn- $O_2$  battery powered water splitting, it is necessary to evaluate HER, OER and ORR performance. The electrochemical activities of these electrodes were investigated in 1.0 M KOH solution by taking the fabricated NiFeP/NiB-CP as a working electrode and Hg/HgO/1M NaOH) reference electrode along with Pt wire (during OER and ORR) and graphite rod (during HER) counter electrodes. The OER study was carried out by performing linear sweep voltammetry (LSV), chronopotentiometry (CP) and electrochemical impedance spectroscopy (EIS) studies. Initially the electrochemical activity towards OER was evaluated by performing LSV. The LSV curves of NiFeP/NiB-CP, NiFeO/NiB-CP



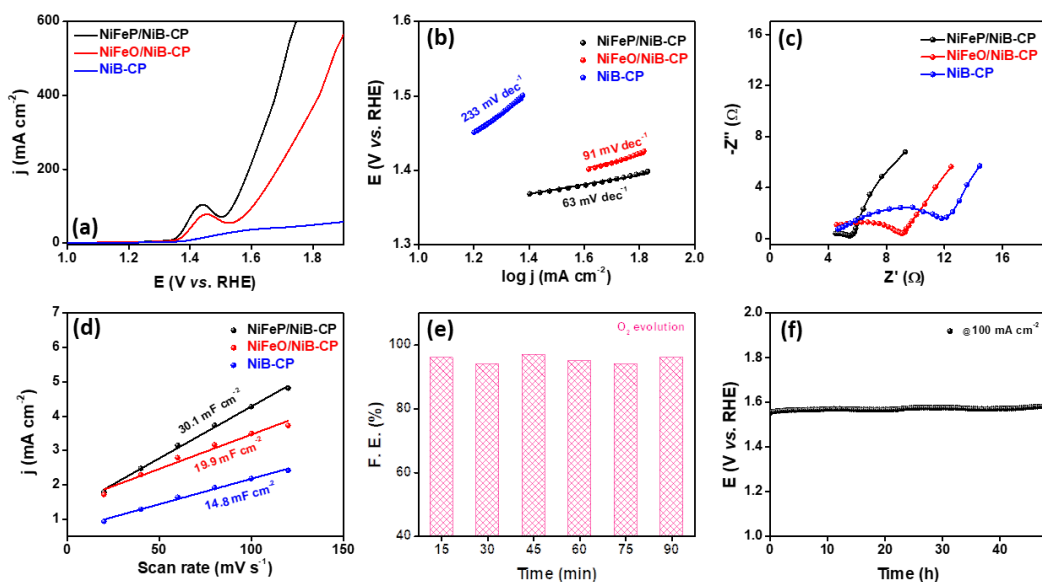


**Figure 5B-5.** (a) Linear sweep voltammograms ( $iR$ -corrected) for NiFeP/NiB-CP, NiFeO/NiB-CP and NiB-CP in 1M KOH electrolyte solution at  $10 \text{ mV s}^{-1}$ , (b) Tafel plots, (c) EIS spectra, (d)  $C_{dl}$  for various electrodes, (e) Faradic efficiency at different interval of time and (f) chronopotentiometric test for 48 h for NiFeP/NiB-CP electrode.

and NiB-CP are presented in Figure 5B-5a. The NiFeP/NiB-CP electrode displayed a smaller overpotential of 310 mV at a current density of  $100 \text{ mA cm}^{-2}$ , as compared to its oxide variant NiFeO/NiB-CP (372 mV), exhibiting better OER activity in comparison to recently reported catalysts. Additionally, OER kinetics was investigated from the Tafel plot, which was obtained from a graph of log of current density *vs.* potential plotted according to Tafel equation by taking corresponding LSV curves, (Figure 5B-5b). The NiFeP/NiB-CP electrode exhibited a smaller Tafel slope value of  $63 \text{ mV dec}^{-1}$  than NiFeO/NiB-CP ( $91 \text{ mV dec}^{-1}$ ). The observed LSV curves and Tafel slope results specify that the NiFeP/NiB-CP electrode catalyst possesses excellent activity and favourable kinetics towards OER. The significant variation in the electrocatalytic activity of the NiFeP/NiB-CP electrode than NiFeO/NiB-CP electrode could be due to the dissimilarity in the interfacial charge transfer kinetics, which can be analyzed by conducting electrochemical impedance spectroscopy (EIS). The NiFeP/NiB-CP electrode exhibited (Figure 5B-5c, Table 5B-1) a lower charge transfer resistance ( $R_{ct}$ ) of  $1.5 \Omega$  than that of the

NiFeO/NiB-CP ( $5.1 \Omega$ ), which demonstrates the higher conductivity and enhanced electron/ion transport dynamics of NiFeP/NiB-CP at the electrode and electrolyte interface resulting improved electrocatalytic activity. This higher activity was further supported by the electrochemical surface area (ECSA). The ECSA of the electrodes were determined via estimation of the electrical double-layer capacitance ( $C_{dl}$ ) by recording CVs with various scan rates at non-Faradaic region, as shown in Figure 5B-5d. The  $C_{dl}$  values of NiFeP/NiB-CP, NiFeO/NiB-CP and NiB-CP were found to be 30.1, 19.9 and 14.8 mF respectively. The higher ECSA of NiFeP/NiB-CP in comparison to other electrodes signifies the exposure of more active sites which are responsible for the high electrocatalytic activity. The Faradic efficiency (FE) is a vital parameter to know the selectivity of the electrochemical reaction. In order to estimate the FE, the evolved  $O_2$  gas was quantified by measuring the generated gas during 1.5 hours electrolysis by eudiometric method and compared with theoretical value. The FE value for NiFeP/NiB-CP was found to be 94 to 97% (Figure 5B-5e) which suggested that almost all the charge was consumed for the OER without any parasitic reactions.

**Table 5B-1. Electrochemical Impedance and ECSA analysis for various electrodes**

S.No.	Composites	$R_s (\Omega)$	$R_p (\Omega)$	$R_{ct} (\Omega)$	$C_{dl} (mF)$	ECSA ( $cm^2$ )
1	NiFeP/NiB-CP	4.2	5.7	1.5	30.1	752.5
2	NiFeO/NiB-CP	4.2	9.3	5.1	19.9	497.5
3	NiB-CP	4.5	12.1	7.6	14.8	370

In addition to good activity the durability of the electrode is also equally important. The long-term stability of the NiFeP/NiB-CP electrode was examined through chronopotentiometric analysis with an applied  $100 \text{ mA cm}^{-2}$  over 48 hours. The chronopotentiometry curve (Figure 5B-5f) indicated that there were no significant changes in the potential for 48 h, which demonstrated the outstanding electrochemical durability of the NiFeP/NiB-CP electrode towards OER. After the stability test, the post morphological properties of the NiFeP/NiB-CP electrode was investigated by SEM and TEM analysis. The SEM image (Figure 5B-6a)

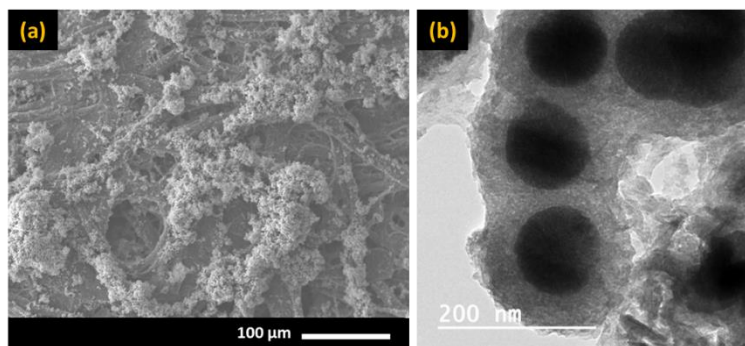


**Figure 5B-6.** (a) SEM and (b) TEM images of NiFeP/NiB-CP electrode after OER stability tests.

demonstrated retention of the active material coating over the substrate whereas similar type of morphology of the NiFeP deposited over the NiB-CP was observed in TEM image (Figure 5B-6b).

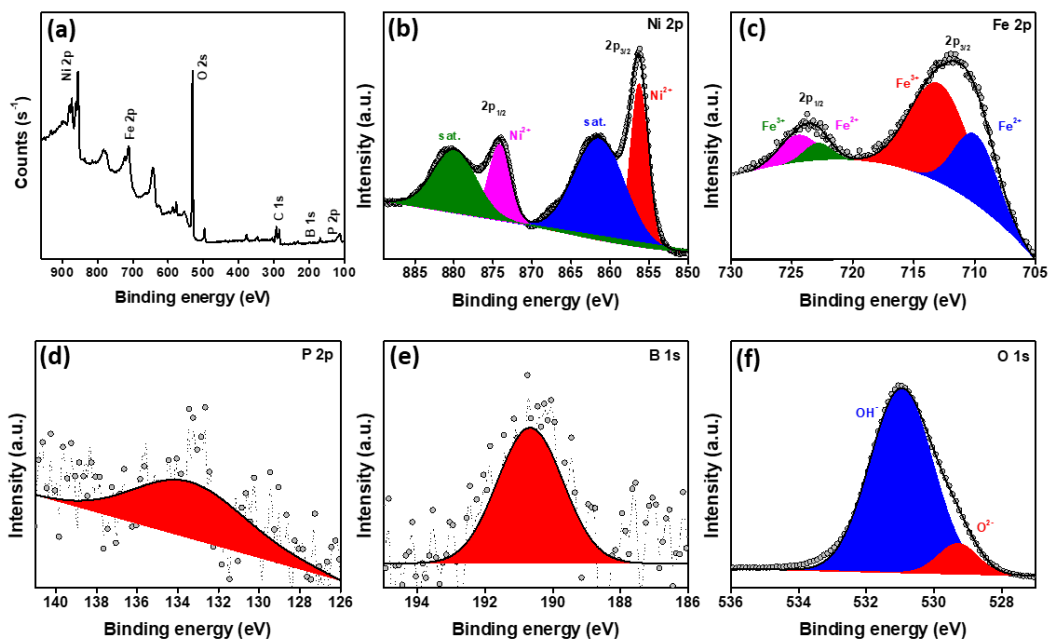


**Figure 5B-7.** (a) XPS survey spectra and deconvoluted XPS spectra for (b) Ni 2p, (c) Fe 2p, (d) P 2p, (e) B 1s and (f) O 1s elements of NiFeP/NiB-CP electrode after OER stability tests.

Additionally, the post electrolysis XPS analysis of the electrode demonstrated the existence of all the elements with their slight modification in chemical state (Figures 5B-7(a-f)). The disappearance of NiB peak in the deconvoluted Ni 2p

spectra (Figure 5B-7b) with the positive shifting of  $2p_{3/2}$  and  $2p_{1/2}$  peaks indicated the formation of NiOOH which was further supported by existence of  $O^{2-}$  peak in the deconvoluted O 1s spectra. All these points collectively validated the robustness of the NiFeP/NiB-CP electrode towards OER.

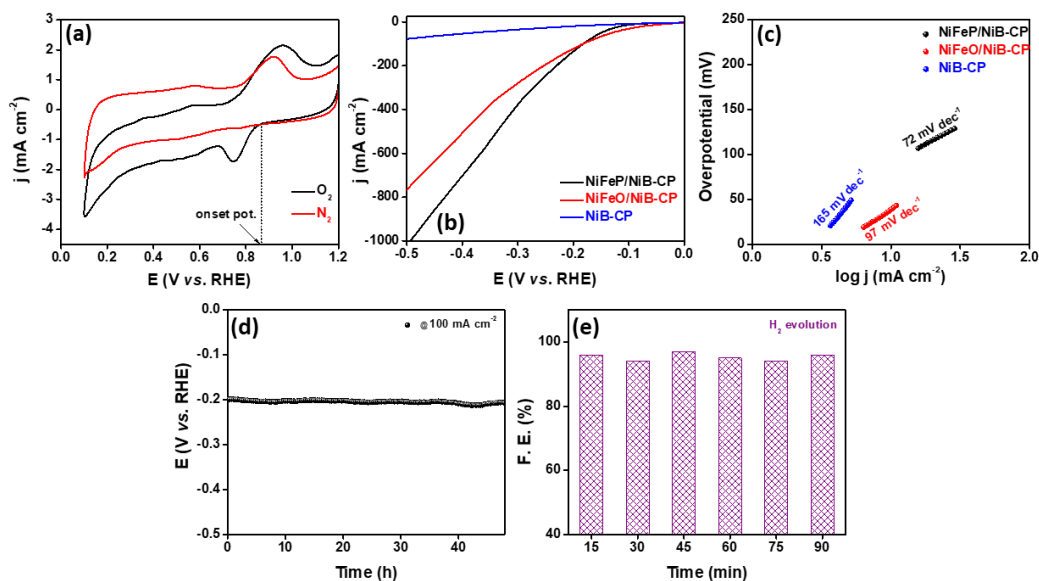


**Figure 5B-8.** (a) Cyclic voltammogram for NiFeP/NiB-CP electrodes towards ORR at 25 mV s<sup>-1</sup> of scan rate, (b) LSVs for NiFeP/NiB-CP with other control electrodes at 10 mV s<sup>-1</sup> of scan rate for HER, (b) corresponding Tafel slopes and (c) chronopotentiometric curve recorded at 100 mA cm<sup>-2</sup> in 1 M KOH for 48h and (e) Faradaic efficiency at various time interval.

Thereafter, the ORR activity of the prepared NiFeP/NiB-CP electrode was investigated by performing CV in N<sub>2</sub>- and O<sub>2</sub>-saturated 1.0 M KOH electrolyte. The CV demonstrated a clear reduction peak at 0.75 V vs. RHE for NiFeP/NiB-CP electrode in O<sub>2</sub>-saturated 1.0 M KOH electrolyte (Figure 5B-8a), which was not observed in N<sub>2</sub>-saturated electrolyte signifying that the NiFeP/NiB-CP electrode was active towards electrochemical oxygen reduction reaction.

Besides the outstanding OER activity of NiFeP/NiB-CP, the HER is also equally important half-cell reaction to evaluate the overall water splitting activity. Therefore, the HER performance of the prepared NiFeP/NiB-CP electrode was investigated by performing LSV in 1.0 M KOH. The LSV curves of the prepared

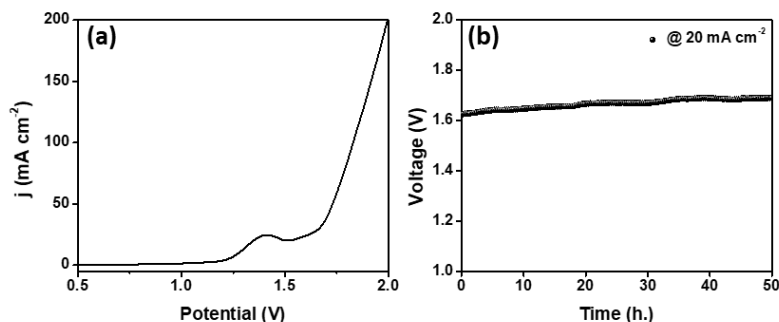


**Figure 5B-9.** (a) LSV and (b) chronopotentiometric curve at 20 mA cm<sup>-2</sup> for NiFeP/NiB-CP||NiFeP/NiB-CP full cell set up in 1 M KOH.

electrodes were shown in Figure 5B-8b, where NiFeP/NiB-CP exhibited a overpotential of 182 mV at 100 mA cm<sup>-2</sup> and achieved 377 mA cm<sup>-2</sup> current density at 300 mV overpotential which was found to be better than NiFeO/NiB-CP which required 190 mV overpotential to achieve the same current density and driven 280 mA cm<sup>-2</sup> current density at 300 mV overpotential. The better activity of the NiFeP/NiB-CP electrode was further supported by the lower Tafel slope of 72 mV dec<sup>-1</sup> (Figure 5B-8c) than that of NiFeO/NiB-CP (97 mV dec<sup>-1</sup>) following Volmer-Heyrovsky mechanism.<sup>33</sup> The lower overpotential and smaller Tafel slope value for NiFeP/NiB-CP electrode signifies the good inherent HER activity with faster reaction kinetics. Thereafter, the durability of the NiFeP/NiB-CP electrode during HER was investigated through chronopotentiometry measurements at 100 mA cm<sup>-2</sup> current density in 1.0 M KOH. The corresponding chronopotentiometry curve (Figure 5B-8d) exhibited the almost same potential for 48 h which signified that the improved durability of the electrode during HER. Furthermore, the selectivity of the HER was estimated by quantifying the amount of hydrogen gas produced during the electrolysis. The evolved hydrogen gas during the electrolysis (1.5 h) was quantified eudiometrically and compared with theoretical value from which the Faradic efficiency (FE) value for NiFeP/NiB-CP was found to be 95 to 98% (Figure 5B-8e) which confirmed that almost all the charge was consumed for the hydrogen evolution.

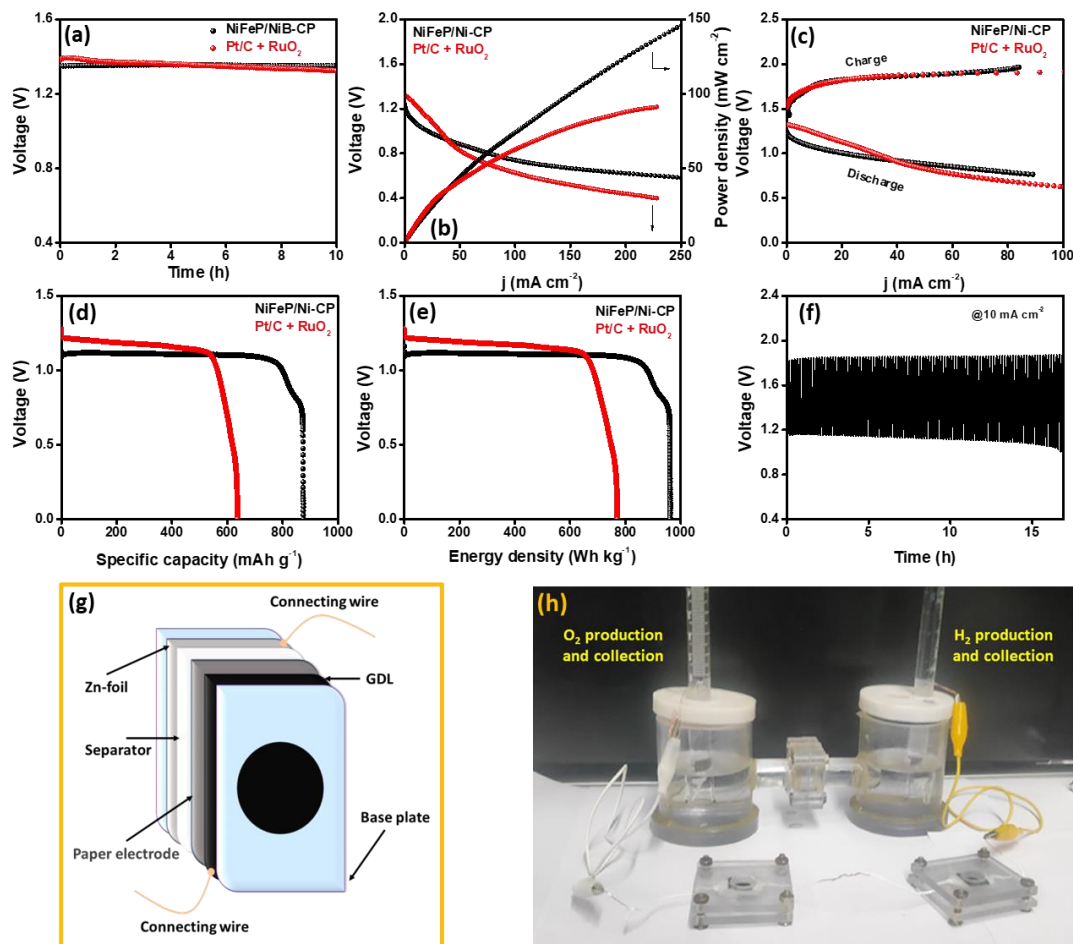


**Figure 5A-10.** (a) Open circuit potential, (b) peak power density curves, (c) charge-discharge polarization curves, (d) specific capacity curve, (e) energy density curve and (f) cycling stability of as-assembled Zn-O<sub>2</sub> battery with NiFeP/NiB-CP cathode during OER/ORR at 10 mA cm<sup>-2</sup>. (g) schematic representation of the Zn-O<sub>2</sub> battery assembly and (h) image of Zn-air battery powered water electrolyzer for overall water splitting.

By considering the good OER and HER activities, an alkaline water electrolyzer was established with the NiFeP/NiB-CP electrode both as anode and cathode electrodes. The performance of the water electrolyzer was evaluated by measuring the LSV and chronopotentiometry in 1.0 M KOH. As shown in Figure 5B-9a, the LSV curve of the NiFeP/NiB-CP||NiFeP/NiB-CP water electrolyzer demonstrated that the designed water electrolyser drove the current density of 20 mA cm<sup>-2</sup> at a cell voltage of 1.62 V only. Furthermore, the durability test of NiFeP/NiB-CP ||

NiFeP/NiB-CP towards overall water splitting was carried out by performing chronopotentiometry at  $20 \text{ mA cm}^{-2}$  (Figure 5B-9b), which demonstrated that the water electrolyser maintained a almost stable potential for 50 hours indicating its great potentiality to be a promising electrode towards overall water splitting. Based on the ORR and OER catalytic activities of the NiFeP/NiB-CP electrode, a homemade rechargeable zinc–air battery was assembled using NiFeP/NiB-CP electrode as the air cathode along with commercial zinc foil as anode.

The cathode and anodes are separated by a glass fibre cellulose paper separator and 6M KOH with 0.2 M Zn (OAc)<sub>2</sub> was used as electrolyte. In order to compare the activity of the Zn-O<sub>2</sub> battery, the state-of-the-art catalysts Pt/C and IrO<sub>2</sub> were mixed at a ratio of 1:1 and applied over NiB-CP by maintaining similar loading and used as an air cathode. The as assembled zinc–air battery achieved an open circuit voltage (OCV) of  $\sim 1.35 \text{ V}$  and it was found to be stable for 10 h as shown in Figure 5B-10a. The OCV of this electrode was found to be comparable with benchmark catalyst of Pt-C and IrO<sub>2</sub> ( $\sim 1.39 \text{ V}$ ). Further, the zinc–air battery based on the NiFeP/NiB-CP air cathode exhibited a power density of  $145 \text{ mW cm}^{-2}$  at  $1.95 \text{ V}$ , whereas the Pt/C + IrO<sub>2</sub> air cathode showed a power density of  $89 \text{ mW cm}^{-2}$  at  $1.21 \text{ V}$ . The specific capacity of the air cathode was studied at a discharge current density of  $10 \text{ mA cm}^{-2}$  based on consumed zinc mass at the anode, where the assembled zinc-air battery demonstrated the specific capacity and energy density  $877 \text{ mA h g}^{-1}$  and  $963 \text{ Wh Kg}^{-1}$  respectively (Figures 5B-10(d-e)). The NiFeP/NiB-CP air cathode displayed a initial round-trip overpotential of  $0.69 \text{ V}$  which was increased to  $0.88 \text{ V}$  after 18 h (Figure 5B-10f). The cycling stability test illustrated that the as assembled zinc–air battery has good stability at  $10 \text{ mA cm}^{-2}$  for continuous charge-discharge cycling up to 18 h. Therefore, it can be said that thus designed cellulose paper based flexible NiFeP/NiB-CP electrode is capable for enhanced electrochemical performance, storage capacity, and cycling stability.

By the inspiration of promising trifunctional electrocatalytic activity towards OER/ORR/HER and great potentiality for Zn-O<sub>2</sub> battery of the developed electrode, the above assembled water electrolyzer was powered by connecting two

Zn-O<sub>2</sub> batteries (as-assembled) in series as shown in Figure 5B-10h. The continuous bubble formation were observed in both the electrodes which witnessed the successful powering for overall water splitting by the as developed Zn-O<sub>2</sub> batteries.

#### 5B-4 Summary

In summary, a biodegradable substrate based three-dimensional flexible NiFeP/NiB-CP electrode was successfully developed via a facile electroless deposition followed by electrodeposition method. The fabricated NiFeP/NiB-CP electrode demonstrated excellent electrocatalytic activity towards OER ( $\eta_{100}$  = 310 mV), ORR (0.85 V *vs.* RHE), and HER ( $\eta_{100}$  = 182 mV) with excellent durability. Further, the water electrolyzer consisting of the designed electrode both as cathode and anode showed a good overall water splitting with a cell voltage of 1.62 V at 20 mA cm<sup>-2</sup>. Additionally, a rechargeable zinc–air battery was assembled by employing the NiFeP/NiB-CP air cathode which exhibited a power density of 145 mW cm<sup>-2</sup> at 1.95 V. Finally, a paper electrode-based Zn-O<sub>2</sub> battery powered water electrolyzer was exhibited for overall water splitting. Thus, the presented fabrication strategy provides a new route for the development and design of highly abundant eco-friendly substrate based flexible electrode for integrated energy conversion and storage applications.

#### 5B-5 References

1. J. Zhu, L. Hu, P. Zhao, L. Y. S. Lee and K.-Y. Wong, *Chem. Rev.*, 2019, **120**, 851-918.
2. M. Yue, H. Lambert, E. Pahon, R. Roche, S. Jemei and D. Hissel, *Renew. Sustain. Energy Rev.*, 2021, **146**, 111180.
3. J. O. Abe, A. Popoola, E. Ajenifuja and O. M. Popoola, *Int. J. Hydrog. Energy*, 2019, **44**, 15072-15086.
4. N. Dubouis and A. Grimaud, *Chemical Science*, 2019, **10**, 9165-9181.
5. W. Lubitz and W. Tumas, *Chem. Rev.*, 2007, **107**, 3900-3903.
6. Z. Sun, G. Wang, S. W. Koh, J. Ge, H. Zhao, W. Hong, J. Fei, Y. Zhao, P. Gao and H. Miao, *Adv. Funct. Mater.*, 2020, **30**, 2002138.
7. N.-T. Suen, S.-F. Hung, Q. Quan, N. Zhang, Y.-J. Xu and H. M. Chen, *Chem. Soc. Rev.*, 2017, **46**, 337-365.
8. A. Kafle, M. Kumar, D. Gupta and T. C. Nagaiah, *J. Mater. Chem. A*, 2021, **9**, 24299-24307.
9. C. Energy, 2002.
10. P.-H. Huang, J.-K. Kuo and Z.-D. Wu, *Int. J. Hydrog. Energy*, 2016, **41**, 8514-8524.

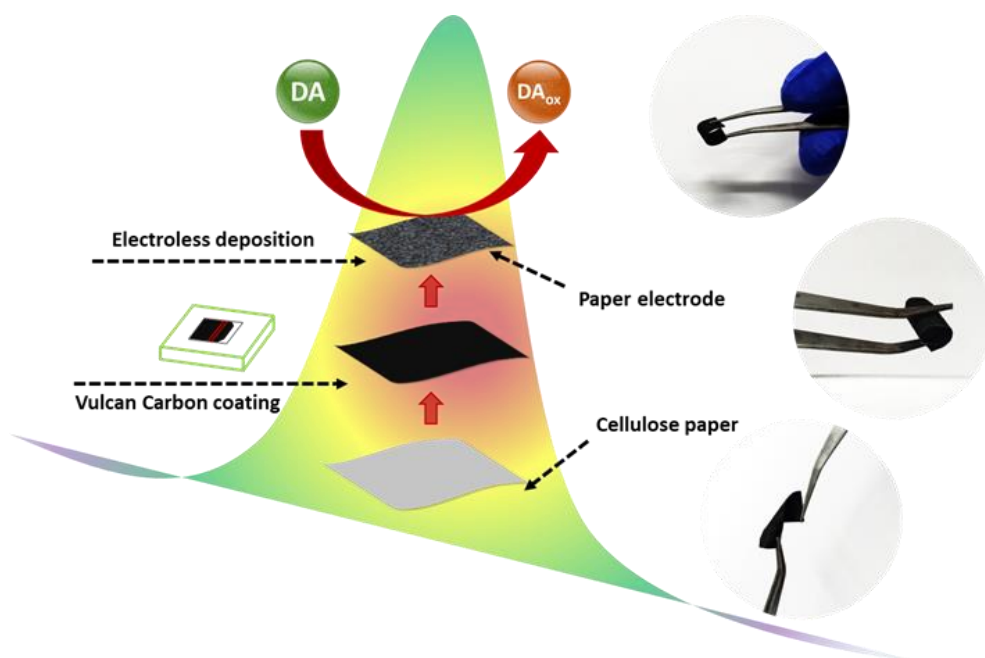


11. Z. Wang, C. Li and K. Domen, *Chem. Soc. Rev.*, 2019, **48**, 2109-2125.
12. M. R. Shaner, H. A. Atwater, N. S. Lewis and E. W. McFarland, *Energy Environ. Sci.*, 2016, **9**, 2354-2371.
13. M. Kumar and T. C. Nagaiah, *J. Mater. Chem. A*, 2022, **10**, 4720-4730.
14. Q. Jin, B. Ren, H. Cui and C. Wang, *Appl. Catal. B Environ.*, 2021, **283**, 119643.
15. J. Fu, Z. P. Cano, M. G. Park, A. Yu, M. Fowler and Z. Chen, *Adv. Mater.*, 2017, **29**, 1604685.
16. C. Xiang, K. M. Papadantonakis and N. S. Lewis, *Mater. Horiz.*, 2016, **3**, 169-173.
17. M. Wang, L. Zhang, Y. He and H. Zhu, *J. Mater. Chem. A*, 2021, **9**, 5320-5363.
18. H. J. Son, Y. R. Cho, Y.-E. Park and S. H. Ahn, *Appl. Catal. B Environ.*, 2022, **304**, 120977.
19. S. Ramakrishnan, D. B. Velusamy, S. Sengodan, G. Nagaraju, D. H. Kim, A. R. Kim and D. J. Yoo, *Appl. Catal. B Environ.*, 2022, **300**, 120752.
20. G. Janani, S. Surendran, H. Choi, M. K. Han and U. Sim, *Small*, 2021, **17**, 2103613.
21. A. Muthurasu, A. P. Tiwari, K. Chhetri, B. Dahal and H. Y. Kim, *Nano Energy*, 2021, **88**, 106238.
22. Q. Shi, Q. Liu, Y. Ma, Z. Fang, Z. Liang, G. Shao, B. Tang, W. Yang, L. Qin and X. Fang, *Adv. Energy Mater.*, 2020, **10**, 1903854.
23. A. Sahasrabudhe, H. Dixit, R. Majee and S. Bhattacharyya, *Nat. Commun.*, 2018, **9**, 1-14.
24. X. Lu, C. Wang, F. Favier and N. Pinna, *Adv. Energy Mater.*, 2017, **7**, 1601301.
25. T. Jin, Q. Han and L. Jiao, *Adv. Mater.*, 2020, **32**, 1806304.
26. P. Wang and B. Wang, *ChemSusChem*, 2020, **13**, 4795-4811.
27. A. Kafle, D. Gupta, A. Bordoloi and T. C. Nagaiah, *Nanoscale*, 2022, **14**, 16590-16601.
28. M. Costa, B. Veigas, J. Jacob, D. Santos, J. Gomes, P. Baptista, R. Martins, J. Inácio and E. Fortunato, *Nanotechnology*, 2014, **25**, 094006.
29. A. Kafle, D. Gupta and T. C. Nagaiah, *Electrochim. Acta*, 2023, **441**, 141779.
30. A. Kafle, N. Thakur and T. C. Nagaiah, *J. Mater. Chem. B*, 2022, **10**, 3681-3686.
31. D. Gupta, A. Kafle and T. C. Nagaiah, *Faraday Discuss.*, 2022.
32. D. He, L. Zhang, D. He, G. Zhou, Y. Lin, Z. Deng, X. Hong, Y. Wu, C. Chen and Y. Li, *Nat. Commun.*, 2016, **7**, 1-8.
33. H. Jin, C. Guo, X. Liu, J. Liu, A. Vasileff, Y. Jiao, Y. Zheng and S.-Z. Qiao, *Chem. Rev.*, 2018, **118**, 6337-6408.



## Chapter 6

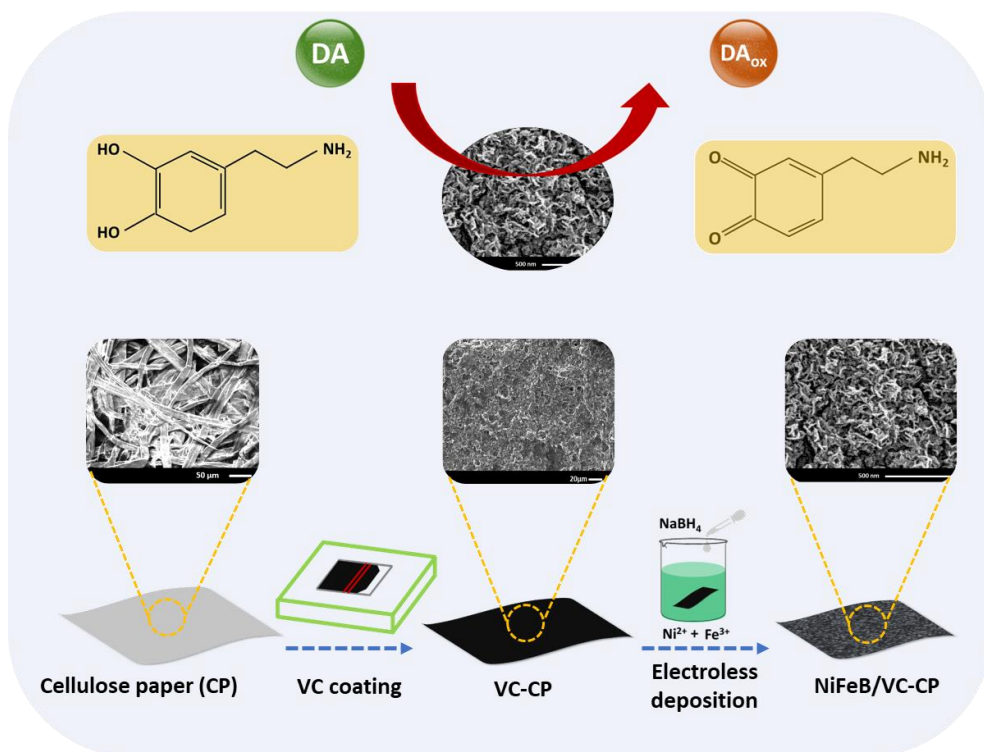
### Designing of the eco-friendly flexible electrodes for selective and sensitive detection of dopamine





# Chapter 6A

## Fabrication of NiFeB flexible electrode *via* electroless deposition towards selective and sensitive detection of dopamine



## 6A-1 Introduction

Dopamine (3,4-dihydroxyphenylamine, DA), a vital catecholamine neurotransmitter, is extensively found in body fluids like cerebrospinal fluid, urine, blood serum etc.<sup>1, 2</sup> DA plays an important role in the regulation of neuronal activities, hormonal balance and also involved in movement, cognition, motivation, and memory.<sup>3-5</sup> Dopamine level in the extra cellular fluid of the central nervous system lies in the range of 1-50 nM<sup>6</sup> while the caudate nucleus of the brain contains 50 nmole g<sup>-1</sup> of DA.<sup>7</sup> The abnormality of dopamine level in body fluids results into neurological as well as psychiatric disorders, which may cause several diseases, such as Parkinson's<sup>8</sup>, Alzheimer's<sup>9</sup>, anhedonia, HIV infection, and schizophrenia etc.<sup>10, 11</sup> Besides, dopamine hydrochloride used in cardioversion shock treatment may have huge impact on health such as kidney failure, heart attack, and numerous bacterial infections.<sup>12</sup> Therefore, accurate and sensitive detection of dopamine level is formost for the proper treatment of the neurological diseases. Several detection platforms like chemiluminescence, fluorometry, localized surface plasmon resonance (LSPR), photochemical analysis, high-performance liquid chromatography (HPLC) and mass spectrometry have been commonly used for the detection of dopamine.<sup>13, 14</sup> But, the major disadvantages of these techniques are expensive instrumentation, long time procedures, difficulties in realizing real-time high output, lack of portability, non-applicability for on-site monitoring. Additionally, poor limit of detection as well as presence of interfering species are the biggest hurdles to meet clinical demands for the detection of DA. Alternatively, because of the electroactive nature of dopamine its electrooxidation is more viable consequently, the electrochemical technique for dopamine detection has gained tremendous attention.<sup>14,15</sup> However, coexistence of ascorbic acid (AA) whose amount is 100–1000 times more than that of dopamine (0.01–1 mM), leads to regeneration of dopamine during the electrooxidation of dopamine making the detection unreliable.<sup>16</sup>

Previously, numerous efforts have been put forward to eliminate the interference

of ascorbic acid viz. use of functionalized nanomaterials, transition metal oxides/phosphides, carbon-based materials,<sup>17</sup> polymers, polyoxometalate etc.<sup>18, 19</sup> Besides the catalyst development, the fabrication of the electrode is equally important for the sensitive detection of dopamine. In conventional process, the electrodes preparation involves two steps i.e. electrocatalyst synthesis followed by catalyst coating over the conductive substrate such as graphite/metal foam/ITO/screen printed electrodes by using insulating binder.<sup>19,20,21</sup> Additionally, the structural fragility of the electrode substrate as well as environmental concerns related to the disposal of end-of-life products<sup>22</sup> are also serious issues. Furthermore, the catalyst synthesis involves multiple steps with complicated procedures and is time consuming which may require harsh conditions. In this regard a mechanically flexible and biodegradable electrode developed from cellulose paper can be a promising sustainable and cost effective alternative to the existing approaches.<sup>23-25</sup> Moreover, the excellent electronic conductivity and high surface area of carbon material is advantageous to achieve improved electrochemical activity.<sup>18, 26</sup> Furthermore, the electroless deposition is less hazardous to the environment, less time-consuming and a cost-effective technique, providing a uniform coating of active material over the substrate via controlled chemical reaction, which is fairly stable during a long-term electrochemical reaction and under various mechanical deformations.<sup>27</sup> Thus, in the present study NiFeB coated paper electrode has been explored as a free standing flexible electrode for the selective and sensitive detection of dopamine.

Herein, we have utilized the cellulose paper as flexible substrate and made it conductive by coating with Vulcan carbon (VC) over it, where in the active material NiFeB was decorated by electroless deposition method. We have explored a straightforward and cost-effective electroless deposition approach (dip coating) to fabricate a highly flexible and eco-friendly electrode by eliminating the conventional and expensive sensitizer and activator such as  $\text{SnCl}_2$  and  $\text{PdCl}_2$ .<sup>28</sup> Therefore, combining cellulose paper as a biodegradable eco-friendly substrate

with straight forward and cost-effective electroless deposition as a fabrication technique can be a revolutionary strategy.<sup>29</sup> The electrode fabricated by the electroless deposition of NiFeB nanoparticle over the Vulcan carbon coated cellulose paper substrate can be directly used as a three dimensional flexible electrode towards electrochemical dopamine sensing without any additional step for preparing sensor probe. Thus, the developed technique provides a uniform coating of active material over the substrate surface and the as prepared electrode shows a fair stability over 100 cycles and equally under various mechanical deformations, minimising the probable damage to the substrate. This flexible NiFeB/VC-CP electrode demonstrates a good sensitivity of  $35.35 \mu\text{A } \mu\text{M}^{-1} \text{ cm}^{-2}$  along with a wide detection range of 10 nM to 400  $\mu\text{M}$  even in the presence of high concentration of ascorbic acid, glucose and uric acid interferents.

## 6A-2 Electrode Fabrication

**6A-2.1 Fabrication of VC-CP:** Laboratory Whatman filter paper was cleaned by acetone with sonication followed by thoroughly washing with deionised water and was finally dried at 60 °C in hot air oven. The clean piece of cellulose paper (1cm × 1cm) was coated with the Vulcan carbon paste prepared by dispersing Vulcan carbon with PVDF binder (1:1) in N-Methylpyrrolidone (NMP) and finally dried at 60 °C in hot air oven for complete dryness.

**6A-2.2 Fabrication of NiFeB/VC-CP:** As fabricated VC-CP substrate was dipped in 1M NaOH solution (15 mL) containing 4.5 mmole  $\text{Fe}(\text{NO}_3)_3 \cdot 9\text{H}_2\text{O}$ , 1.5 mmole  $\text{NiCl}_2 \cdot 6\text{H}_2\text{O}$ , 6 mmole trisodium citrate and 13.5 mmole  $\text{NH}_4\text{Cl}$ . The aforementioned reaction mixture was kept in an ice bath to which sodium borohydride solution (12 mmole  $\text{NaBH}_4$  in 10 mL 1 M NaOH) was added slowly from the wall of the container and kept undisturbed until the effervescence siezed. After the completion of the reaction the paper was washed thoroughly with mixture of ethanol and water (1:1) then finally dried in hot air oven at 60 °C. The deposition of FeB and NiB were carried out by taking respective metal salt only in the similar experimental procedure as mentioned above. The metal ratio in the bath solution



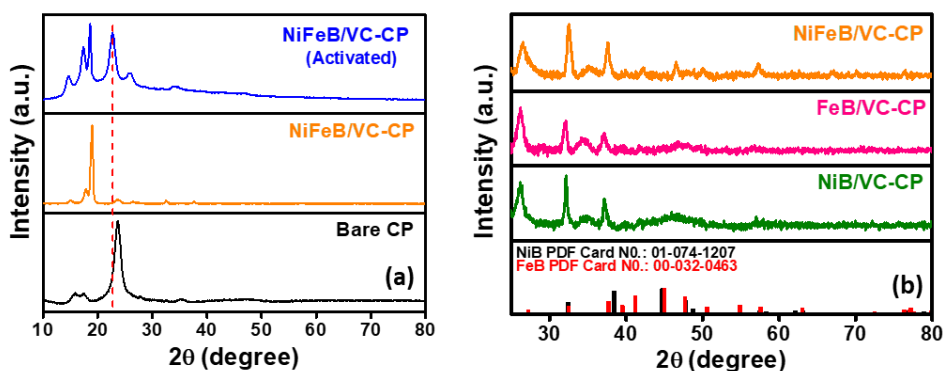


**Figure 6A-1.** PXRD pattern of (a) bare cellulose paper and NiFeB/VC-CP electrode and (b) various flexible electrodes.

was optimized by changing the molar ratio of Ni and Fe such as 1:1, 2:1, 3:1, 1:2 and 1:3 while maintaining the overall number of moles of metal precursor constant.

### 6A-3 Results and discussion

**6A-3.1 Physical characterization:** The NiFeB/VC-CP flexible electrode was fabricated by a straightforward electroless deposition technique. Firstly, the cleaned Whatman filter paper (CP) paper surface was modified with carbon coating by applying the Vulcan carbon (VC) paste over it followed by the electroless deposition in a bath solution composed of  $\text{Fe}(\text{NO}_3)_3 \cdot 9\text{H}_2\text{O}$ ,  $\text{NiCl}_2 \cdot 6\text{H}_2\text{O}$ ,  $\text{Na}_3\text{C}_6\text{H}_5\text{O}_7$ ,  $\text{NH}_4\text{Cl}$ ,  $\text{NaOH}$  and  $\text{NaBH}_4$ . The micro structure of the electrodes were analysed by powder X-ray diffraction (PXRD) analysis. The PXRD patterns of various electrodes viz., NiB/VC-CP, FeB/VC-CP, NiFeB/VC-CP and bare cellulose paper substrate were recorded using  $\text{CuK}\alpha$  radiation ( $\lambda=0.1542$  nm, 40kV, 40mA) within the  $2\theta$  range of  $5-80^\circ$  at a scan rate of  $5^\circ$  per minute and a proportional counter detector for structural investigation of catalysts. As observed in Figure 6A-1a the NiFeB/VC-CP showed characteristic peaks of planes (110), (121), (111) and (131) corresponding to NiB (PDF no. 01-074-1207), along with (020), (101), (210), (121), (211), (112), (041) corresponding to FeB (PDF no. 00-032-0463) and (002), (121) and (131) corresponding to  $\text{Fe}_2\text{B}$  (PDF no. 00-036-1332) respectively. Similarly, crystalline cellulose peaks at  $2\theta$  values of  $16^\circ$ ,  $17.5^\circ$ ,

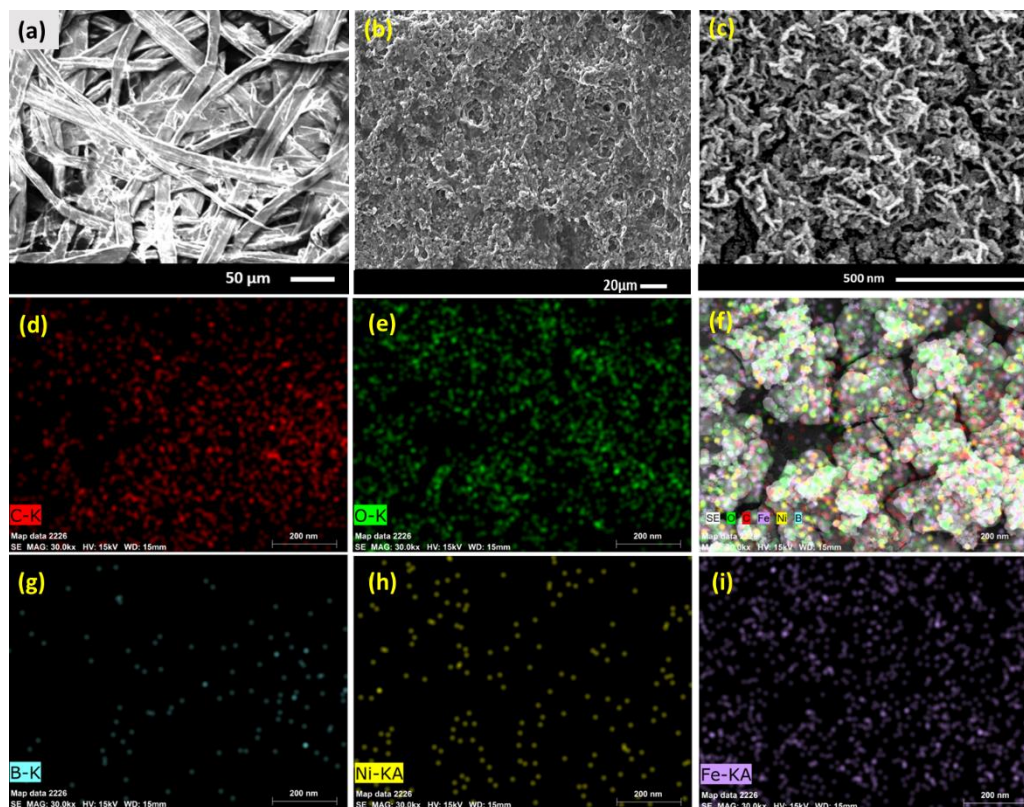


**Figure 6A-2.** SEM image of (a) bare cellulose paper and (b) VC-CP, (c) FESEM image of the NiFeB/VC-CP, and elemental dot mapping images (d) all elements, (e) Ni, (f) Fe, (g) B (h) C and (i) O for NiFeB/VC-CP electrode.

$23.7^\circ$  and  $35.3^\circ$  corresponding to (110) ( $1\bar{1}0$ ), (200) and (004) planes<sup>30</sup>, graphitic carbon peak at  $2\theta=26.4^\circ$ , and the high-intensity peak at  $2\theta=19^\circ$  were observed which is due to the oxides formation of Fe and Ni<sup>31, 32</sup> (Figure 6A-1b), which confirmed the deposition of NiFeB over VC-CP surface. The morphological features of as fabricated NiFeB/VC-CP electrode were analysed by scanning electron microscopy (SEM). SEM images in Figure 6A-2a & b confirms the deposition of Vulcan carbon over the surface of cellulose paper. The high-resolution field emission scanning electron microscopy (FE-SEM) image of NiFeB/VC-CP (Figure 6A-2c) demonstrated the granular morphology of NiFeB coating over the VC-CP where the uniform distribution of the respective elements were confirmed by the elemental dot mapping (Figure 6A-2d-i) of the NiFeB/VC-CP electrode. In order to evaluate the surface properties of NiFeB/VC-CP X-ray

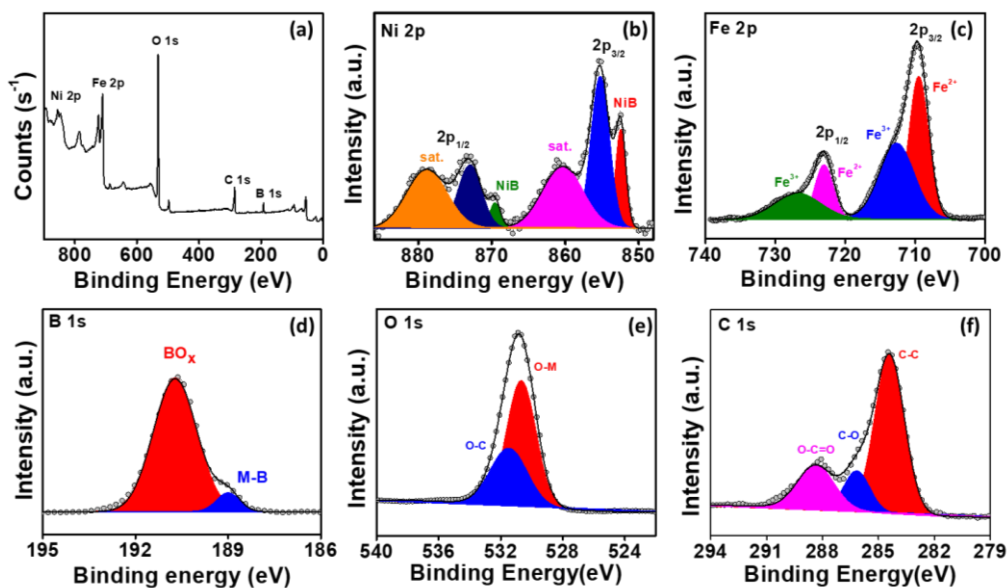


**Figure 6A-3.** (a) XPS survey spectra and and deconvoluted XP spectra of (b) Ni 2p, (c) Fe 2p, (d) B 1s, (e) O 1s and (f) C 1s of NiFeB/VC-CP electrode.

photoelectron spectroscopy (XPS) analysis was performed. The appearance of the peaks in the XP survey spectra of NiFeB/VC-CP at a binding energy (BE) of 192, 285, 531, 710 and 856 eV evidenced the co-existence of B 1s, C1s, O1s, Fe 2p and Ni 2p respectively (Figure 6A-3a). The high-resolution Ni 2p XP spectra upon deconvolution showed two major peaks at 855 eV and 873 eV along with two satellite peaks corresponding to Ni 2p<sub>3/2</sub> and Ni 2p<sub>1/2</sub> respectively (Figure 6A-3b) while the existence of the peaks at 852.5 and 869.5 eV confirmed the presence of NiB and oxide of nickel. Similarly, the deconvoluted XP spectrum of Fe 2p exhibited peaks at 709.5 & 712.8 eV and 723 & 727 eV corresponding to Fe 2p<sub>3/2</sub> and Fe 2p<sub>1/2</sub> (Figure 6A-3c) which evidenced the presence of Fe in +2 and +3 oxidation state respectively. Additionally, the presence of M-B peak around 188.5 eV and BO<sub>x</sub> peak at 191 eV in the deconvoluted B 1s spectra (Figure 6A-3d) as well as M-O & C-O peaks in deconvoluted O 1s spectra (Figure 6A-3e) further supported the existence of NiFeB in NiFeB/VC-CP.<sup>33,34</sup>

**6A-3.2 Electrochemical studies:** The applicability of as fabricated novel flexible NiFeB/VC-CP electrode for the electrochemical determination of dopamine was

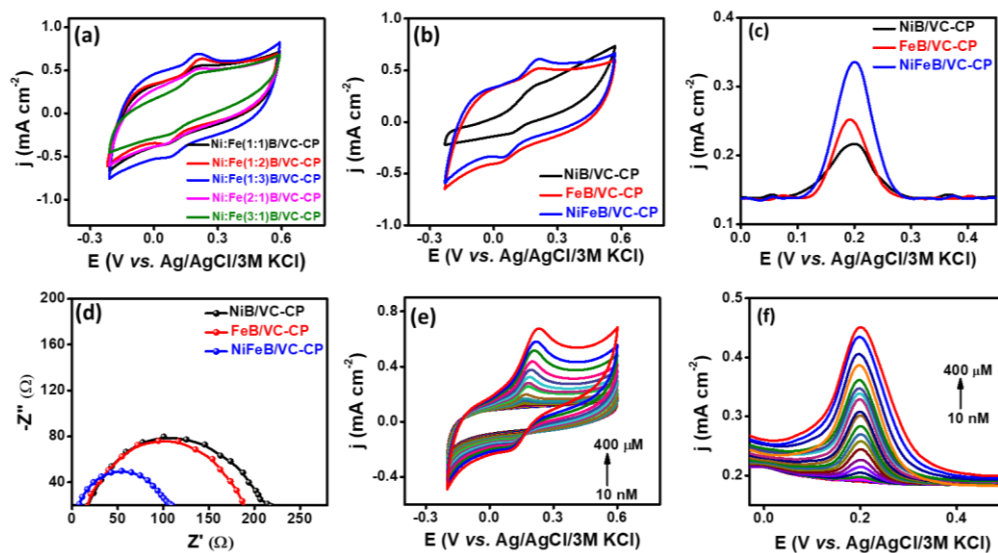


**Figure 6A-4.** (a) CV of various flexible NiFeB/VC-CP electrodes in 0.1 M PBS electrolyte containing 50 mM DA and 200 mM AA, (b) CV, (c) DPV and (d) EIS results for various catalysts in 0.1 M PBS electrolyte containing 50 mM DA and 200 mM AA at a frequency ranging from 2 Hz to 2.5 MHz, (e) CV and (f) DPV of flexible NiFeB/VC-CP electrodes in 0.1 M PBS electrolyte containing 200 mM AA and various concentrations of DA,

then examined by several electrochemical techniques. Firstly, the fabricated electrodes were conditioned by performing cyclic voltammetry in 1 M KOH in the potential range of 1.0 to 1.9 V vs. RHE. The cyclic voltammogram (CV) were recorded in 0.1 M phosphate buffer solution (PBS, pH 7.0) containing 50 μM dopamine and 200 μM ascorbic acid at a scan rate of 10 mV s<sup>-1</sup> using different flexible NiFeB/VC-CP electrodes fabricated in various bath composition by varying the metal precursor ratio. The cyclic voltammograms in Figure 6A-4a revealed that in all the electrodes, the appearance of redox peaks centred at 0.2 V and 0.08 V vs. Ag/AgCl/3M KCl were consistent with electrocatalytic oxidation of dopamine to dopaminoquinone and subsequent reduction of dopaminoquinone to dopamine, respectively. The NiFe(1:3)B/VC-CP electrode showed superior activity among all variants which was evidenced by the highest peak current density corresponding to dopamine oxidation observed in CV shown in Figure 6A-4a. Furthermore, similar experiments, including CV and differential pulse voltammetry (DPV) were carried out by using monometallic flexible electrodes i.e.

NiB/VC-CP and FeB/VC-CP electrodes (Figure 6A-4b & c), which showed inferior activity as evidenced by relatively less intense peaks while the NiFeB/VC-CP electrode displayed two times higher oxidation peak current density ( $0.33 \text{ mA cm}^{-2}$ ) than monometallic electrodes. The enhanced activity of flexible NiFeB/VC-CP electrode could be attributed to a change in the electronic properties after the incorporation of second metal to monometallic variants leading to improved electron transport at the electrode-electrolyte interface and subsequently the enhanced sensor performance towards the electrochemical oxidation of dopamine. Additionally, the  $\text{MOO}^-$  species formed as a result of conditioning of the electrode, inhibited the diffusion of negatively charged ascorbic acid over the electrode surface and facilitated the selective detection of dopamine.<sup>18, 35, 36</sup> These findings were further supported by electrochemical impedance spectroscopic (EIS) measurements, which were accomplished at 0.19 V vs. Ag/AgCl/3M KCl in the frequency range between 2 Hz to 2.5 MHz in 0.1 M PBS electrolyte containing 50  $\mu\text{M}$  dopamine and 200  $\mu\text{M}$  ascorbic acid. As shown in Figure 6A-4d, the monometallic NiB/VC-CP flexible electrode exhibited a maximum charge-transfer resistance ( $R_{\text{ct}}$ ) value while the NiFeB/VC-CP flexible electrode demonstrated the lowest  $R_{\text{ct}}$  amongst all, witnessed from its smaller diameter of semicircle. As a consequence of the higher  $R_{\text{ct}}$  value in NiB/VC-CP, the slower kinetics was resulted due to the resistance at the electrode electrolyte interface during electro-oxidation of dopamine. Whereas, lower  $R_{\text{ct}}$  in NiFeB/VC-CP specified the facile kinetics towards dopamine electrooxidation. The facile kinetics of the electrodes depend upon higher number of available electrochemical active sites, which was determined by using the double layer capacitance in the non-faradaic region. The NiFeB/VC-CP electrode exhibited higher electrochemical surface area (ECSA) than the monometallic variants (Table 6A-1). The sensitivity of the proposed flexible NiFeB/VC-CP electrode towards dopamine sensing was examined by performing CV and DPV experiments at various concentrations of dopamine from 10 nM to 400  $\mu\text{M}$  and keeping the constant concentration of ascorbic acid (200  $\mu\text{M}$ ). As shown in Figure 6A-4e, the oxidation current response increased with the

**Table 6A-1: Electrochemical surface area (ECSA) of various electrodes.**

S. No.	Composite	$C_{dl}$ (mF) @ 0.0 V vs. Ag/AgCl/3M KCl	ECSA (cm <sup>2</sup> )
1.	NiB/VC-CP	0.49	12.25
2.	FeB/VC-CP	0.82	20.5
3.	NiFeB/VC-CP	1.89	27.23

increment in the dopamine concentration, verified the effective catalysis towards the electrochemical oxidation of dopamine by the flexible NiFeB/VC-CP electrode. Also, DPV demonstrated a sharp increment in the oxidative-peak current response with increased concentration of dopamine (Figure 6A-4f). Furthermore, absence of oxidative peak corresponding to ascorbic acid even at a 200  $\mu$ M concentration, demonstrated the complete knockdown of ascorbic acid interference. The sensitivity of flexible NiFeB/VC-CP electrode was determined by the linear plot of

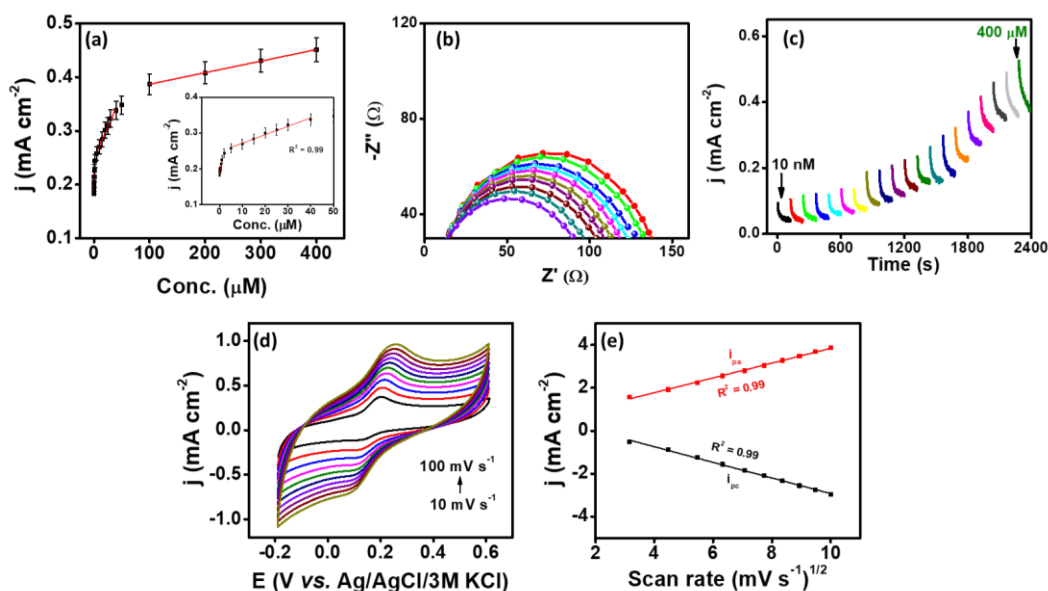


**Figure 6A-5.** (a) Plot of current density versus concentration of DA extracted from Figure 6A-4f (b) EIS, (c) chronoamperometric response in 0.1 M PBS electrolyte containing 200 mM AA and various concentrations of DA, (d) cyclic voltammograms in 0.1 M PBS electrolyte containing 200 mM DA and 200 mM AA at various scan rates ranging from 10 to 100  $\text{mV s}^{-1}$  and (e) corresponding peak current density versus square root of scan rate curve for NiFeB/VC-CP electrode.

dopamine concentrations vs. current response extracted from DPV (Figure 6A-5a) which was found to be  $35.35 \mu\text{A } \mu\text{M}^{-1} \text{ cm}^{-2}$ ,  $2.36 \mu\text{A } \mu\text{M}^{-1} \text{ cm}^{-2}$  and  $0.215 \mu\text{A } \mu\text{M}^{-1} \text{ cm}^{-2}$  for three linear ranges from 10 nM to 1  $\mu\text{M}$ , 5  $\mu\text{M}$  to 50  $\mu\text{M}$  and 100  $\mu\text{M}$  to 400  $\mu\text{M}$  respectively with a low detection limit of 2.1 nM, indicating the superior sensitivity towards dopamine detection. The resistance of the proposed flexible electrode was monitored simultaneously during the sensing measurements by electrochemical impedance spectroscopy to realize the conductivity of the flexible electrode (Figure 6A-5b). As expected, the resistance at the electrode-electrolyte interface under various concentrations of dopamine ranging from 10 nM to 400  $\mu\text{M}$  in presence of ascorbic acid concentration (200  $\mu\text{M}$ ) were decreased due to facilitated electron transport at the interface, validating its potential application. In the similar fashion, consecutive chronoamperometric study after every two minutes was performed with successive addition of dopamine and a subsequent change in current response was observed (Figure 6A-5c). A step-wise increase in current response with sequential addition of dopamine ranging from 10 nM to 400  $\mu\text{M}$  depicted the superior sensitivity of the as fabricated flexible NiFeB/VC-CP electrode for dopamine determination. Furthermore, cyclic voltammogram at various scan rates showed a linear relationship between the anodic as well as cathodic peak current while the square root of the scan rate validated that the oxidation of dopamine by flexible NiFeB/VC-CP electrode was a diffusion-controlled process (Figure 6A-5d & e). In addition to sensitivity, a selective determination is equally important to realize the practical application of the proposed flexible electrode for abolishing the interferences caused by endogenous species other than ascorbic acid. The selectivity towards dopamine was studied by performing CV and DPV in the presence of common co-existing interferents *viz.* uric acid (200  $\mu\text{M}$ ), ascorbic acid (1000  $\mu\text{M}$ ) and glucose (3000  $\mu\text{M}$ ) at various concentrations of DA under the same experimental conditions (Figure 6A-6a-c). The bar diagram in Figure 6A-6d demonstrated a negligible change in current response in presence of high concentration of AA and UA whereas a very minimal interference from glucose was observed, signifying



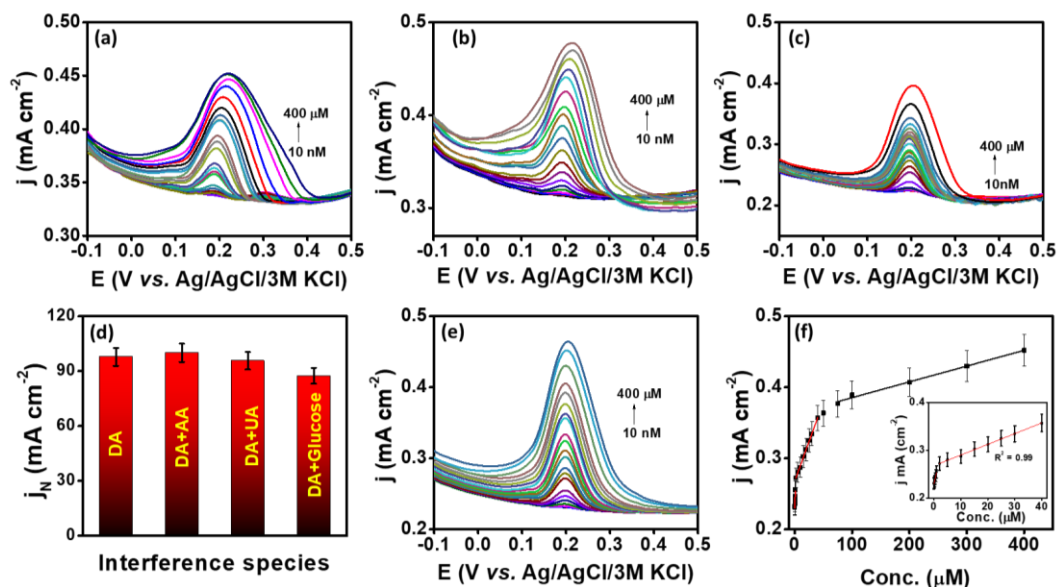


**Figure 6A-6.** Differential pulse voltammograms in presence of interferants (a) 200  $\mu\text{M}$  UA, (b) 1000  $\mu\text{M}$  AA and (c) 3000  $\mu\text{M}$  glucose at various concentrations of DA, (d) bar diagram representing the normalized current with respect to interferents at a 400  $\mu\text{M}$  concentration of DA, (e) DPV various concentrations of DA only and (f) plot of current density versus concentration of DA for NiFeB/VC-CP electrode extracted from DPV.

superior selectivity towards DA. Also, the similar current response was observed at various concentrations of dopamine (6A-6e-f). Besides, stability of flexible sensor is another crucial parameter to evaluate its practical application, for that cyclic voltammetry measurement was performed for 100 cycles, and a negligible decay in the current response was observed (Figure 6A-7a) which confirmed the excellent robustness of electrode. This was further supported by the post stability SEM image (Figure 6A-7b), and the similar response in DPV even after various mechanical deformations (Figure 6A-7c-i). The reproducibility of the flexible NiFeB/VC-CP electrode was evaluated by repetitive DPV measurements carried out by taking 50 and 100  $\mu\text{M}$  DA in presence of 200  $\mu\text{M}$  AA in PBS (pH=7.0) electrolyte where the relative standard deviations were found to be 1.41 and 4.93% for 50 and 100  $\mu\text{M}$  dopamine respectively validated the excellent reproducibility of the electrode (Figure 6A-8). Furthermore, the practical applicability of the flexible NiFeB/VC-CP electrode in clinical diagnosis was evaluated by carrying



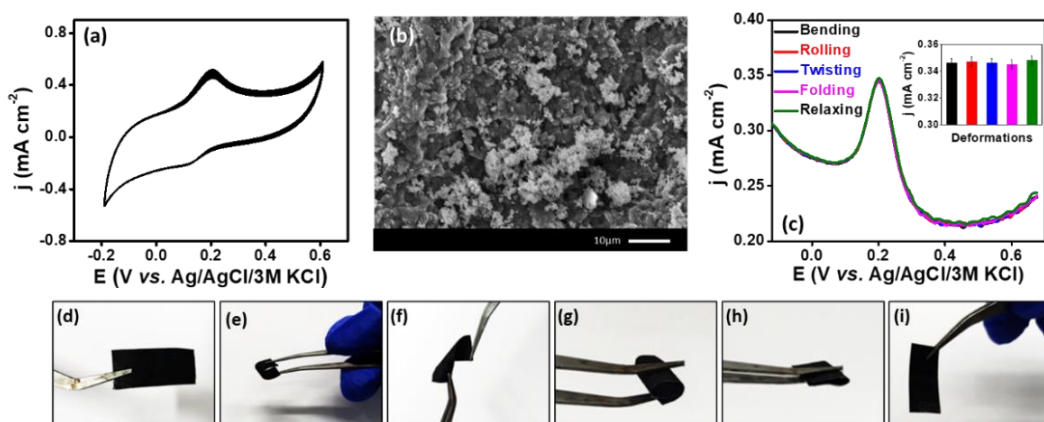


**Figure 6A-7.** (a) Cyclic voltammograms in 0.1 M PBS (pH 7.0) electrolyte containing 200 mM DA and 200 mM AA for 100 cycles at a scan rate of  $50 \text{ mV s}^{-1}$  and (b) SEM image of the electrode after stability study, (c) DPV curves at various deformation conditions in 0.1 M PBS electrolyte containing 200 mM AA and 50 mM DA and photographs of the electrode under (d) normal, (e) bending, (f) twisting, (g) rolling, (h) folding and (i) relaxing deformation conditions of the NiFeB/VC-CP electrode.

out detection of dopamine in a commercially available dopamine hydrochloride injections ( $40 \text{ mg mL}^{-1}$ ) as a certified reference material via standard addition method where 98 to 104% recovery of the spiked sample (Table 6A-2) confirmed the practical applicability of fabricated electrode for real-time application

**Table 6A-2. Analytical results of NiFeB/VC-CP electrode towards determination of dopamine from commercially available dopamine hydrochloride injection.**

S. No.	Conc. (taken)	Conc. (added)	Conc. (actual)	Conc. (found)	Recovery (%)
1.	5 $\mu\text{M}$	5 $\mu\text{M}$	10 $\mu\text{M}$	9.8 $\mu\text{M}$	98
2.	5 $\mu\text{M}$	10 $\mu\text{M}$	15 $\mu\text{M}$	15.6 $\mu\text{M}$	104
3.	5 $\mu\text{M}$	20 $\mu\text{M}$	25 $\mu\text{M}$	25.8 $\mu\text{M}$	103.2
4.	5 $\mu\text{M}$	30 $\mu\text{M}$	35 $\mu\text{M}$	34.5 $\mu\text{M}$	101.4
5.	5 $\mu\text{M}$	50 $\mu\text{M}$	55 $\mu\text{M}$	54.2 $\mu\text{M}$	98.5

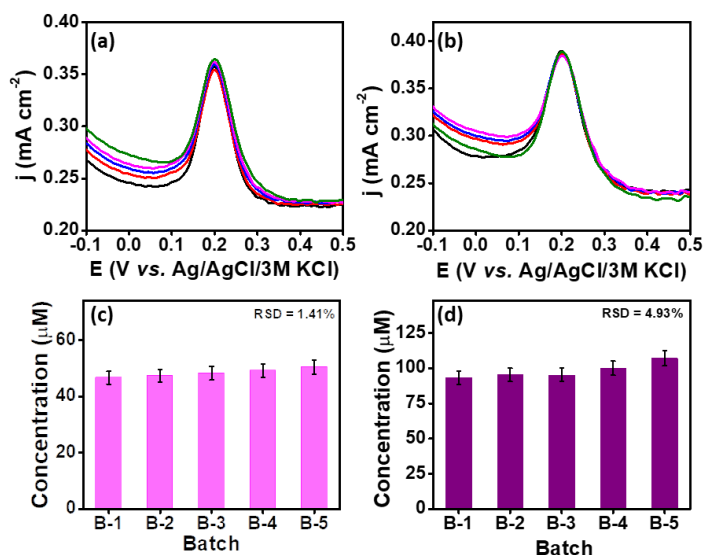


**Figure 6A-8.** Differential pulse voltammogram for the five successive measurements performed with five separately fabricated NiFeB/VC-CP electrodes at DA concentration (a) 50  $\mu\text{mol L}^{-1}$  and (b) 100  $\mu\text{M}$  and (c) & (d) corresponding bar diagram for the measured concentration performed in 0.1 M PBS electrolyte containing 200  $\mu\text{M}$  AA.

#### 6A-4 Summary

In summary, an eco-friendly cellulose paper based flexible NiFeB/VC-CP electrochemical sensor was developed by using laboratory Whatman filter paper (CP) as a substrate *via* a cost-effective electroless deposition method. The developed three dimensional flexible electrode can be directly applied for selective and sensitive detection of dopamine without any additional step for preparing sensor probe. This sensor establishes a high sensitivity of  $35.35 \mu\text{A } \mu\text{M}^{-1} \text{ cm}^{-2}$  with improved LOD of 2.1 nM, good selectivity even in presence of various co-existing interferents, excellent durability as well as it maintains the similar activity under the various mechanical deformations.

#### 6A-5 References

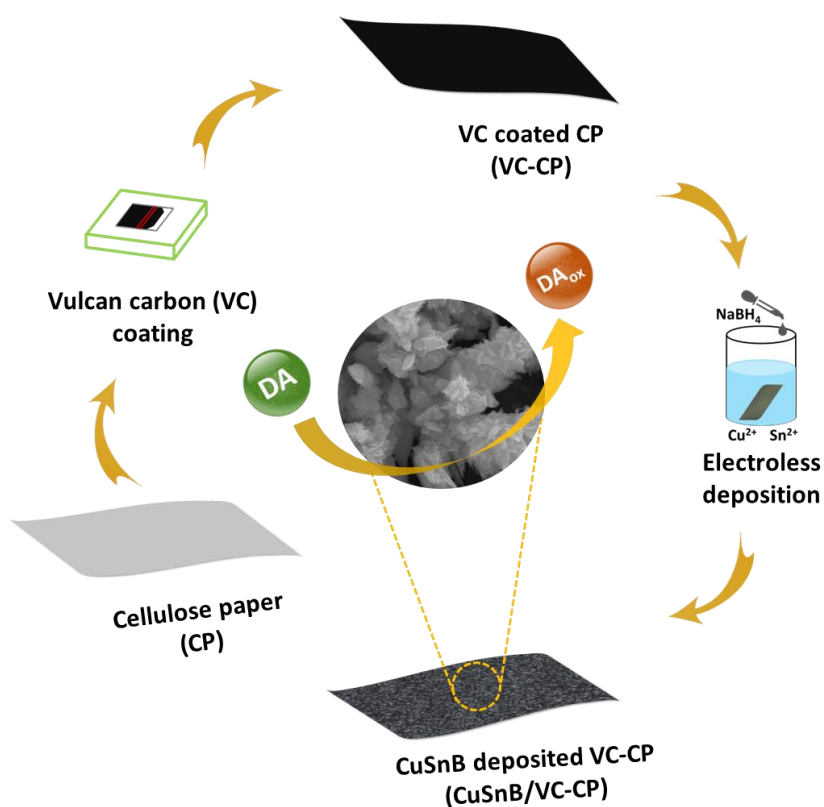
1. C. G. Swahn, B. Sandgärde, F. A. Wiesel and G. Sedvall, *Psychopharmacology*, 1976, **48**, 147-152.
2. A. Roy, D. Pickar, J. De Jong, F. Karoum and M. Linnoila, *Arch. Gen. Psychiatry*, 1988, **45**, 849-857.

3. M. A. Makos, Y. C. Kim, K. A. Han, M. L. Heien and A. G. Ewing, *Anal. Chem.*, 2009, **81**, 1848-1854.
4. J. Bergquist, A. Ściubisz, A. Kaczor and J. Silberring, *J. Neurosci. Methods*, 2002, **113**, 1-13.
5. T. Okumura, Y. Nakajima, M. Matsuoka and T. Takamatsu, *J. Chromatogr. B: Biomed. Sci. Appl.*, 1997, **694**, 305-316.
6. R. D. O'Neill, *Analyst*, 1994, **119**, 767-779.
7. R. M. Wightman, L. J. May and A. C. Michael, *Anal. Chem.*, 1988, **60**, 769A-793A.
8. W. Poewe, K. Seppi, C. M. Tanner, G. M. Halliday, P. Brundin, J. Volkmann, A. E. Schrag and A. E. Lang, *Nat. Rev. Dis. Primers*, 2017, **3**, 1-21.
9. D. A. Butterfield and B. Halliwell, *Nat. Rev. Neurosci.*, 2019, **20**, 148-160.
10. Y. Y. Li, P. Kang, S. Q. Wang, Z. G. Liu, Y.-X. Li and Z. Guo, *Sens. Actuators B Chem.*, 2021, **327**, 128878.
11. F. Zhu, Y. Ju, W. Wang, Q. Wang, R. Guo, Q. Ma, Q. Sun, Y. Fan, Y. Xie and Z. Yang, *Nat. Commun.*, 2020, **11**, 1-10.
12. A. K. Keyan, C. L. Yu, R. Rajakumaran, S. Sakthinathan, C.-F. Wu, S. Vinothini, S. M. Chen and T. W. Chiu, *Microchem. J.*, 2021, **160**, 105694.
13. S. Farajikhah, P. C. Innis, B. Paull, G. G. Wallace and A. R. Harris, *ACS Sens.*, 2019, **4**, 2599-2604.
14. Y. Ma, Z. Wei, Y. Wang, Y. Ding, L. Jiang, X. Fu, Y. Zhang, J. Sun, W. Zhu and J. Wang, *ACS Sustain. Chem. Eng.*, 2021.
15. K. Jackowska and P. Kryszynski, *Anal. Bioanal. Chem.*, 2013, **405**, 3753-3771.
16. N. Thakur, D. Gupta, D. Mandal and T. C. Nagaiah, *Chem. Commun.*, 2021, **57**, 13084-13113.
17. N. Thakur, A. Chaturvedi, D. Mandal and T. C. Nagaiah, *Chem. Commun.*, 2020, **56**, 8448-8451.
18. N. Thakur, S. Das Adhikary, M. Kumar, D. Mehta, A. K. Padhan, D. Mandal and T. C. Nagaiah, *ACS Omega*, 2018, **3**, 2966-2973.
19. Y. Shu, Q. Lu, F. Yuan, Q. Tao, D. Jin, H. Yao, Q. Xu and X. Hu, *ACS Appl. Mater. Interfaces*, 2020, **12**, 49480-49488.
20. W. Cai, T. Lai, H. Du and J. Ye, *Sens. Actuators B Chem.*, 2014, **193**, 492-500.
21. X. Li, X. Lu and X. Kan, *J. Electroanal. Chem.*, 2017, **799**, 451-458.
22. F. Gao, J. Song, Z. Xu, L. Xu, Y. Guo, L. Miao and X. Luo, *Sens. Actuators B Chem.*, 2021, **334**, 129675.
23. Z. Wang, Y. H. Lee, S. W. Kim, J. Y. Seo, S. Y. Lee and L. Nyholm, *Adv. Mater.*, 2021, **33**, 2000892.
24. D. Zhao, Y. Zhu, W. Cheng, W. Chen, Y. Wu and H. Yu, *Adv. Mater.*, 2021, **33**, 2000619.
25. M. Santhiago, M. Strauss, M. P. Pereira, A. S. Chagas and C. C. Bufon, *ACS Appl. Mater. Interfaces*, 2017, **9**, 11959-11966.

26. Y. R. Kim, S. Bong, Y. J. Kang, Y. Yang, R. K. Mahajan, J. S. Kim and H. Kim, *Biosens. Bioelectron.*, 2010, **25**, 2366-2369.
27. A. Kafle, M. Kumar, D. Gupta and T. C. Nagaiah, *J. Mater. Chem. A*, 2021, **9**, 24299-24307.
28. C. Tharamani, N. S. Begum and S. Mayanna, *Mater. Chem. Phys.*, 2004, **83**, 278-283.
29. W. Hao, R. Wu, H. Huang, X. Ou, L. Wang, D. Sun, X. Ma and Y. Guo, *Energy Environ. Sci.*, 2020, **13**, 102-110.
30. M. Costa, B. Veigas, J. Jacob, D. Santos, J. Gomes, P. Baptista, R. Martins, J. Inácio and E. Fortunato, *Nanotechnology*, 2014, **25**, 094006.
31. A. Glaria, M. L. Kahn, P. Lecante, B. Barbara and B. Chaudret, *ChemPhysChem*, 2008, **9**, 776-780.
32. S. Rakshit, S. Ghosh, S. Chall, S. S. Mati, S. Moulik and S. C. Bhattacharya, *RSC Adv.*, 2013, **3**, 19348-19356.
33. G. Liu, D. He, R. Yao, Y. Zhao and J. Li, *Nano Res.*, 2018, **11**, 1664-1675.
34. Y. W. Chen and N. Sasirekha, *Ind. Eng. Chem. Res.*, 2009, **48**, 6248-6255.
35. L. Wang, R. Yang, L. Qu and P. d. B. Harrington, *Talanta*, 2020, **210**, 120626.
36. L. Wu, L. Feng, J. Ren and X. Qu, *Biosens. Bioelectron.*, 2012, **34**, 57-62.

## Chapter 6B

### Modification of cellulose paper with CuSnB by electroless deposition for the selective and sensitive detection of dopamine



## 6B-1 Introduction

Dopamine (DA) is a principal neurotransmitter in the mammalian brain and is responsible for regulating the neurological functions like locomotion, emotion, cognition and reward.<sup>1, 2</sup> It is getting tremendous attention as abnormal level of dopamine is closely related to various psychiatric and neurological disorders including Parkinson's disease<sup>3</sup>, Alzheimer's<sup>4</sup>, schizophrenia<sup>5</sup> and attention-deficit hyperactivity disorder (ADHD).<sup>6</sup> Besides central nervous system processes, dopamine also influences various peripheral functions such as hormone release, gastrointestinal mobility, sodium balance and blood pressure etc.<sup>7</sup> Hence its pathophysiological importance demands selective and sensitive detection for the early stage diagnosis and treatment of associated diseases for the good human health.

Several dopamine detection techniques including fluorometry, chemiluminescence, photochemical analysis high-performance liquid chromatography (HPLC), surface plasmon resonance, spectrophotometry and electrochemical techniques are in practice. Although most of them are highly advantageous for neurobiological fundamental studies but not appropriate for point of care diagnosis. In this regard, electrochemical technique is getting tremendous attraction since it can overcome the limitations associated with aforementioned techniques such as lengthy procedure, expensive instruments, unsuitability for real time analysis. Furthermore, the electroactive nature of dopamine is advantageous for its quantification based on electrochemical response during its redox reactions at the electrode surface. As a result, development of a quick responding, highly reliable and easy assessable point of care diagnosis devices for dopamine sensing is upfront. However, the presence of coexisting electroactive metabolites in body fluids such as ascorbic acid (AA), uric acid (UA) and glucose interferents<sup>8, 9</sup> along with the drawbacks like surface passivation, poor stability of the electrode<sup>10</sup>, inefficient sensitivity leading to poor limit of detection (LOD) are the major challenges of electrochemical dopamine sensors.<sup>11</sup>

Besides the advancement in the material designing, researchers are developing various approaches to address and circumvent the aforementioned issues. Because of the structural similarities of DA, UA and AA, most of the conventional electrodes such as Au, Pt, and glassy carbon electrode (GCE) lacks selectivity towards their detection.<sup>12</sup> The incorporation of highly conductive carbonaceous material with active metallic nanoparticles is beneficial to achieve well-separated oxidation peaks and enhanced peak currents of AA, DA, and UA for selective and sensitive detection.<sup>13</sup> Further, the carbonaceous material can have high specific surface area, strong mechanical strength, excellent electronic conductivity, and high electrocatalytic activity. As a consequence of which, various carbon materials such as carbon nanotubes (CNTs), boron-doped diamond, carbon nanofibers, reduced graphene oxide (rGO) and graphite have been employed to elaborate the surface of the working electrodes leading towards betterment of LOD.<sup>14</sup> Formerly, various effort had been put to improve the LOD by eliminating the interaction with interferences by using transition metal phosphide/phosphate composites, functionalized nanomaterials polymers, polyoxometalates etc., among those transition metal hybrid nanocomposite with carbonaceous materials are considered as a highly promising candidate.<sup>9, 15-18</sup> In this scenario, the applicability of oxides of copper and tin towards selective detection of dopamine has been extensively studied where their promising activity is found to be encouraging towards the development of bimetallic composite for achieving good LOD.<sup>18-20</sup> Besides the development of catalyst material for electrode preparation, there are still many challenges to get a simple, quick responding, portable, affordable highly effective biosensors for point of care detection for which miniaturization of the sensor is mandatory.<sup>21</sup> The electrode architecture plays a crucial role to achieve miniaturized biosensors. In this context, development of flexible electrode capable of maintaining same activity under various mechanical deformations will be beneficial towards miniaturization as well as the development of wearable and foldable sensors.

Currently practicing carbon and metal foam/foil-based substrates for flexible electrode fabrication hold many pitfalls including structural fragility, incompatibility for large scale fabrication and expensive procedures.<sup>22</sup> Besides the disposal of the related end of life product is creating serious environmental issues. Therefore, to address the above stated issues, the development of eco-friendly, mechanically stable and biodegradable substrate based flexible electrodes using cost effective and easily available precursors by straight forward procedure will be a fruitful strategy. In this context, cellulose paper can be a good option as cellulose is the most abundant natural biopolymer with high surface area, mechanical flexibility, biocompatibility and thermal stability, due to which it is emerging as an ideal substrate for sustainable & eco-friendly energy storage and conversion applications.<sup>23</sup> The existing methods for fabrication of three-dimensional electrodes with cellulose paper substrate comprise of solvent free drawing,<sup>24</sup> thermal evaporation,<sup>25</sup> soak and drying,<sup>26</sup> spin coating,<sup>27</sup> electroless deposition,<sup>28</sup> etc. Amongst these, the electroless deposition is an effective technique because of its simplicity, rapidity, cost-effectiveness, minimal mechanical damage to the substrate and uniform coating and moreover it can be utilised for non-conductive substrates also.<sup>29, 30</sup>

By considering all aforesaid facts, herein we have chosen cellulose paper (CP) as a substrate, CuSnB over Vulcan carbon (VC) as an active electrode material and electroless deposition as a fabrication procedure to develop flexible electrode towards selective and sensitive detection of dopamine. With this view point, highly active metallic CuSnB nanoparticles were decorated over highly conductive Vulcan carbon coated cellulose paper by electroless deposition method. Thus, fabricated electrode was applied directly as flexible electrode for electrochemical sensing of dopamine without any additional step for sensor probe preparation. The as fabricated electrode achieved a uniform coating of active material over the substrate surface which is fairly stable over 500 cycles and even under various mechanical deformations. Thus fabricated CuSnB/VC-CP electrode demonstrates



a high sensitivity of  $3.92 \mu\text{A } \mu\text{M}^{-1} \text{cm}^{-2}$  with expanded detection range of 5 nM to 300  $\mu\text{M}$  even in the presence of interferents such as uric acid, ascorbic acid and glucose.

## **6B-2 Electrode fabrication**

**6B-2.1 Fabrication of VC-CP:** A piece of CP (Whatman filter paper) of size  $1\text{cm} \times 1\text{cm}$  was dipped in acetone and sonicated for five minutes then thoroughly washed with deionised water and dried in hot air oven at  $60^\circ\text{C}$ . The dried cellulose paper was coated with the VC paste (VC: PVDF, 3:1) dispersed in N-methylpyrrolidone (NMP) and dried at  $60^\circ\text{C}$  for complete dryness.

**6B-2.2 Fabrication of CuSnB/VC-CP:** The carbon coated cellulose paper (VC-CP) was dipped in 15 mL ice cold solution containing 3.75 mmole  $\text{SnCl}_2$ , 1.25 mmole  $\text{CuSO}_4$  and 2.5 mmole trisodium citrate and further kept in an ice bath in which sodium borohydride solution (12 mmole  $\text{NaBH}_4$  in 10 mL deionized water) was slowly added from the walls of the container and kept as such till the effervescence siezed. After the completion of the reaction the paper substrate was washed thoroughly with deionized water and finally with ethanol water (1:1) solution and dried at  $60^\circ\text{C}$  in hot air oven. Similarly, fabrication of control electrodes i.e. CuB/VC-CP and SnB/VC-CP were performed by taking respective metal salt only with the same procedure. The copper and tin ratio was optimized by varying the molar ratio of Cu and Sn from 1:1, 1:2, 1:3, 2:1 and 3:1 by keeping the total number of moles of metal salt to be similar.

## **6B-3 Results and discussion**

**6B-3.1 Physical characterization:** The cellulose paper based flexible CuSnB/VC-CP electrode was fabricated by a cost effective straightforward electroless deposition method. First of all, the cleaned cellulose paper (CP) paper was coated with a conductive carbon layer by applying the VC paste. The carbon coated paper was placed for electroless deposition in an ice-cold bath solution containing  $\text{CuSO}_4$

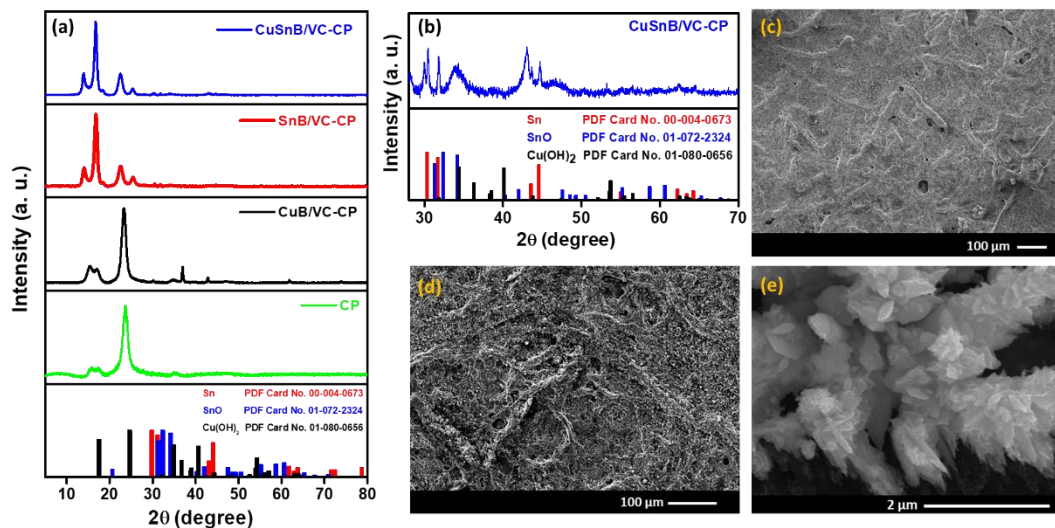


**Figure 6B-1.** PXRD pattern of (a) bare cellulose paper and various flexible electrodes, (b) CuSnB/VC-CP electrode, SEM images of (c) VC-CP, (d) CuSnB/VC-CP and (e) FE-SEM image of CuSnB/VC-CP electrode.

and  $\text{SnCl}_2$  where the addition of strong reducing agent  $\text{NaBH}_4$  resulted in the deposition of CuSnB over the surface of VC-CP. The structural pattern of the as fabricated flexible electrodes (CuB/VC-CP, SnB/VC-CP, CuSnB/VC-CP) and cellulose paper was investigated by powder X-ray diffraction (PXRD) analysis (Figure 6B-1a & b). The CuSnB/VC-CP demonstrated the characteristic peaks of planes (021), (002) at  $23.8^\circ$  and  $34.9^\circ$  corresponding to  $\text{Cu(OH)}_2$  (PDF no. 01-080-0656) and for (200), (101), (220), (211) at the angle of  $22\theta$  value  $30.6^\circ$ ,  $32.0^\circ$ ,  $43.8^\circ$  and  $44.9^\circ$  respectively corresponding to metallic Sn (PDF no. 00-004-0673). In addition to it the planes corresponding to SnO (PDF no. 01-072-2324) i.e. (101), (011) and (110) were also observed at  $2\theta$  value of  $31.3^\circ$ ,  $32.3^\circ$ ,  $34.2^\circ$  respectively. Similarly, it exhibited additional peaks at  $2\theta$  value of  $16^\circ$ ,  $17.5^\circ$ ,  $23.7^\circ$  and  $35.3^\circ$  corresponding to the crystalline cellulose planes (110) ( $1\bar{1}0$ ), (200) and (004) respectively<sup>31</sup> alongwith the graphitic carbon peak at an angle of  $26.4^\circ$ . These findings evidenced the successful modification of VC-CP surface with CuSnB. The morphological investigation of the as fabricated electrodes was then analysed by scanning electron

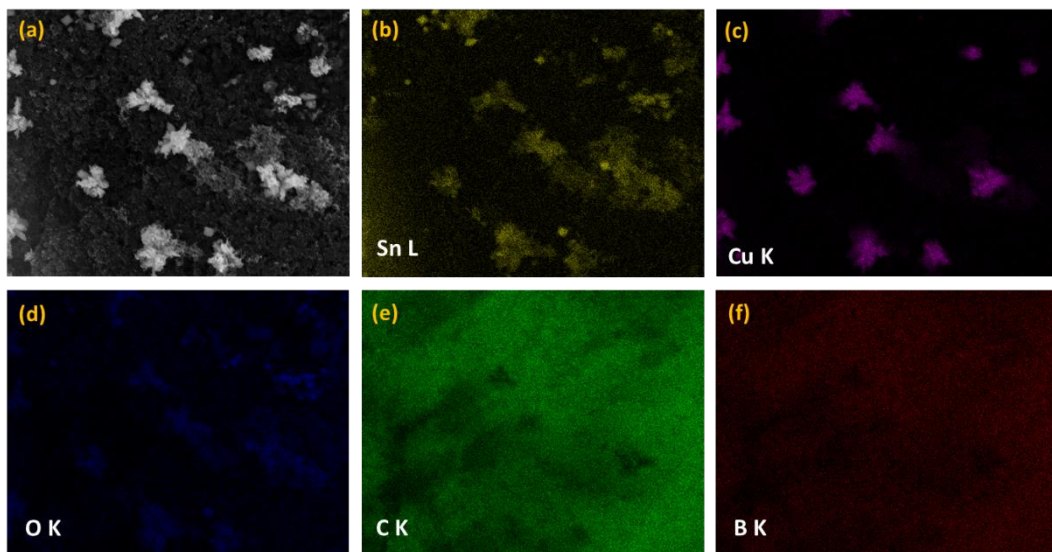


**Figure 6B-2.** Elemental dot mapping images for (a) selected area, (b) Sn, (c) Cu, (d) O (e) C and (f) B of CuSnB/VC-CP electrode.

microscopy (SEM) and field emission scanning electron microscopy (FE-SEM). The deposition of the Vulcan carbon over the cellulose paper surface was evidenced by SEM image in Figure 6B-1c whereas the deposition of CuSnB over VC-CP was verified by Figure 6B-1d. Similarly the FE-SEM image evidenced the leaf like morphology of the deposited CuSnB over the VC-CP Figure 6B-1e. Further the uniform distribution of these elements over the scan area was confirmed by the EDS elemental dot mapping images (Figure 6B-2). The elemental surface composition of the CuSnB/VC-CP was analysed by X-ray photoelectron spectroscopy (XPS). The existence of peaks at binding energy 932, 486, 532, 284.5 and 190 eV in XP survey spectra (Figure 6B-3a) affirmed the presence of Cu, Sn, O, C and B respectively. The high-resolution XP spectra of Cu 2p showed two major peaks at 933 and 953 eV corresponding to Cu 2p<sub>3/2</sub> and Cu 2p<sub>1/2</sub> evidencing the existence of Cu in +2 oxidation state (Figure 6B-3b).<sup>32</sup> Similarly, the peaks at binding energies of 484.5 & 493 eV and 486.5 & 495 eV upon deconvolution of high resolution XP spectra of Sn confirmed the presence of Sn in 0 and +2 oxidation state (Figure 6B-3c).<sup>33</sup> Furthermore, the existence of B<sup>0</sup> peak at 187 eV along with BO<sub>x</sub> peak at 192 eV in the deconvoluted B1s spectra (Figure 6B-3d) as well as C-O and M-O peaks in the O 1s spectra (Figure 6B-3f) supported the presence of

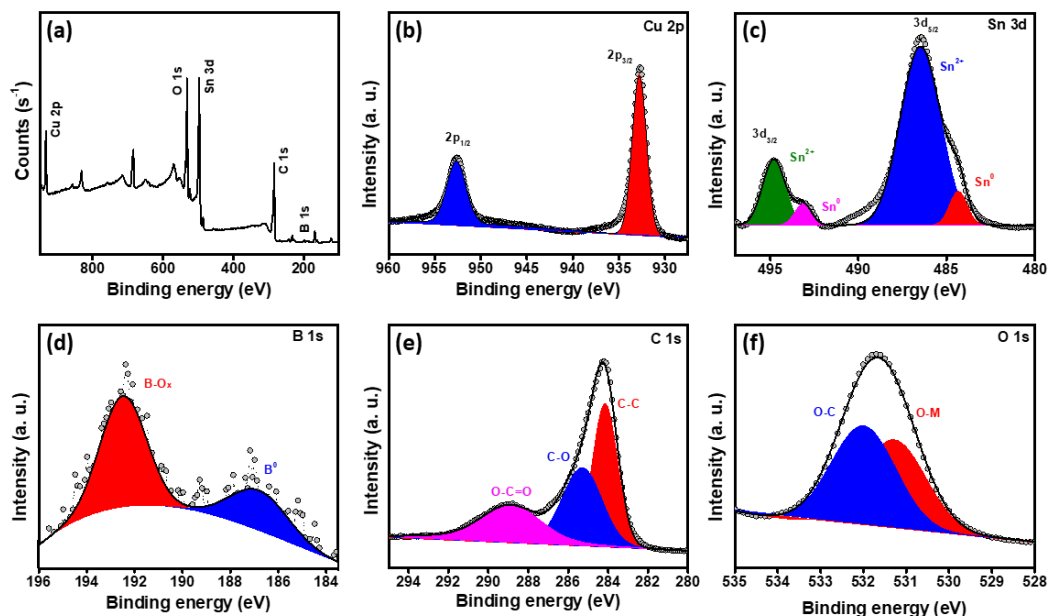


**Figure 6B-3.** (a) XP survey spectra and deconvoluted XPS spectra of (b) Cu 2p, (c) Sn 3d, (d) B 1s, (e) C 1s and (f) O 1s of CuSnB/VC-CP electrode.

CuSnB in the as fabricated electrode.<sup>29, 34</sup>

**6B-3.2 Electrochemical studies towards dopamine sensing:** In order to examine the electrochemical behaviour of the as fabricated CuSnB/VC-CP electrode towards dopamine detection cyclic voltammetry (CV), differential pulse voltammetry (DPV), chronoamperometry (CA) and electrochemical impedance spectroscopy (EIS) studies were performed by taking the paper electrode as a working electrode (WE), with Ag/AgCl/3M KCl and Pt-wire as a reference and counter electrode respectively in 0.1 M phosphate buffer solution (PBS) at pH=7.0. Initially, the CV studies were performed in 50  $\mu$ M DA and 200  $\mu$ M AA containing PBS electrolyte at a scan rate of 20 mV s<sup>-1</sup> for different CuSnB/VC-CP variant electrodes prepared with different metal precursor ratio. The obtained CV (Figure 6B-4a) demonstrated a well-defined redox behaviour with peaks centered around 0.20 and 0.10 V *vs.* Ag/AgCl/3M KCl for all variants which evidenced the formation of oxidised product of dopamine i.e. dopaminoquinone during oxidation and its subsequent reduced product dopamine during reduction respectively. Among the different variants, CuSn(1:3)B/VC-CP was found to be the best variant

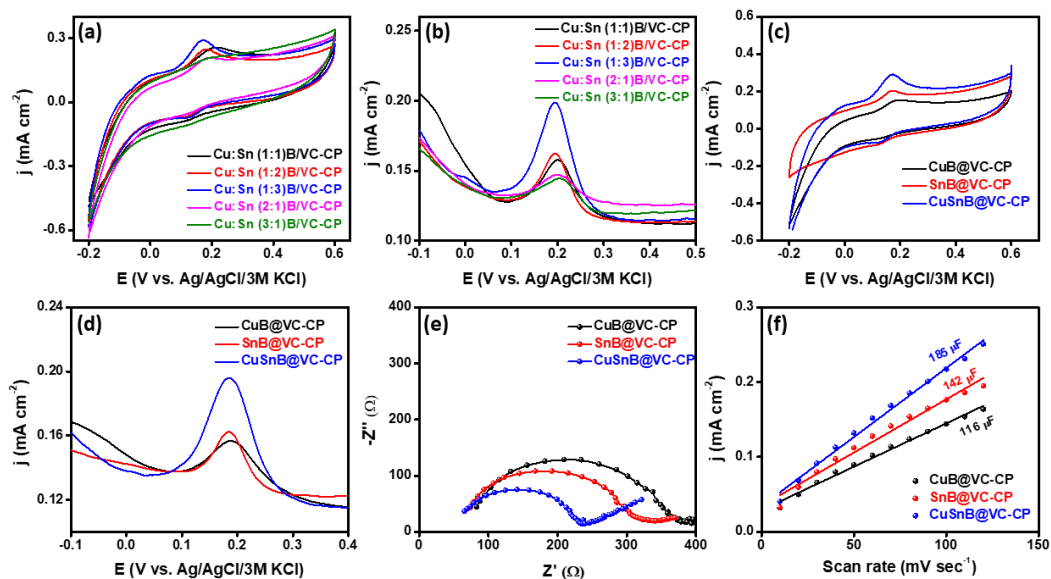


**Figure 6B-4.** (a) & (c) CV and (b) & (d) DPV, (e) EIS and (f)  $C_{dl}$  for various flexible CuSnB/VC-CP electrodes in 0.1 M PBS electrolyte containing 50 mM DA and 200 mM AA DPV: step height of 10 mV, pulse width of 900 ms, CE: Pt wire, RE: Ag/AgCl/3 M KCl.

as observed by maximum current density presumably due to oxidation of DA which was further supported by DPV (Figure 6B-4b). Similarly, CV and DPV experiments were performed for corresponding monometallic variants (CuB/VC-CP and SnB/VC-CP) to compare the activity with bimetallic variant (CuSnB/VC-CP). The monometallic variants CuB/VC-CP and SnB/VC-CP showed less intense peaks in comparison to bimetallic variant CuSnB/VC-CP (Figure 6B-4c & d). The superior activity of the CuSnB/VC-CP can be attributed to the improved electronic properties by the incorporation of an additional metal, which led to the enhanced electron transport at the electrode-electrolyte interface and ultimately boosted the overall performance of the sensor during the electrooxidation of the dopamine. The improvement in the electrochemical activity was further evidenced by the electrochemical impedance spectroscopic (EIS) spectra recorded at 0.20 V vs. Ag/AgCl/3M KCl with the frequency range 25 Hz to 2.5 MHz. The charge transfer resistance ( $R_{ct}$ ) is directly related to the kinetics of the electrode reaction as the higher  $R_{ct}$  indicates the slower kinetics whereas lower value specifies the facile

kinetics towards electrode reaction. Therefore, the lowest  $R_{ct}$  of CuSnB/VC-CP in comparison to their monometallic variants demonstrated the better activity towards electrooxidation of dopamine (Figure 6B-4e). Similarly, the electrochemical surface area (ECSA) is another key parameter for the determination of the kinetics of the electrode reaction. Higher the value of ECSA, greater is the number of electrochemical active sites and consequently the electrode reaction kinetics is more facile. Thus, the ECSA was determined by estimating the double layer capacitance ( $C_{dl}$ ) of the electrode since it is directly proportional to ECSA. The CuSnB/VC-CP electrode demonstrated the higher  $C_{dl}$  than their monometallic variant electrodes which further supported the improved kinetics of the CuSnB/VC-CP electrode over CuB/VC-CP and SnB/VC-CP electrodes (Figure 6B-4f and Table 6B-1).

**Table 6B-1: Electrochemical surface area (ECSA) of various electrodes.**

S. No.	Composite	$C_{dl}$ ( $\mu\text{F}$ ) @ 0.0 V vs. Ag/AgCl/3M KCl	ECSA ( $\text{cm}^2$ )
1.	CuB/VC-CP	116	2.9
2.	SnB/VC-CP	142	3.55
3.	CuSnB/VC-CP	185	4.62

The sensitivity of the fabricated CuSnB/VC-CP electrode towards dopamine sensing was evaluated qualitatively and quantitatively using various CV, DPV, chronoamperometry (CA) and EIS techniques at various concentrations of dopamine (from 5 nM to 300  $\mu\text{M}$ ) in presence of 200  $\mu\text{M}$  ascorbic acid. The CVs recorded for various concentration of dopamine (Figure 6B-5a) demonstrated the continuous increment in the oxidation current density with increase in dopamine concentration without any significant oxidation peak corresponding to ascorbic acid, which signified the ability of the fabricated CuSnB/VC-CP electrode for catalysing the electrooxidation of dopamine. In the similar fashion, the DPV (Figure 6B-5b) demonstrated the sharp increment in the oxidative peak current intensity with increasing concentration of the dopamine with no corresponding

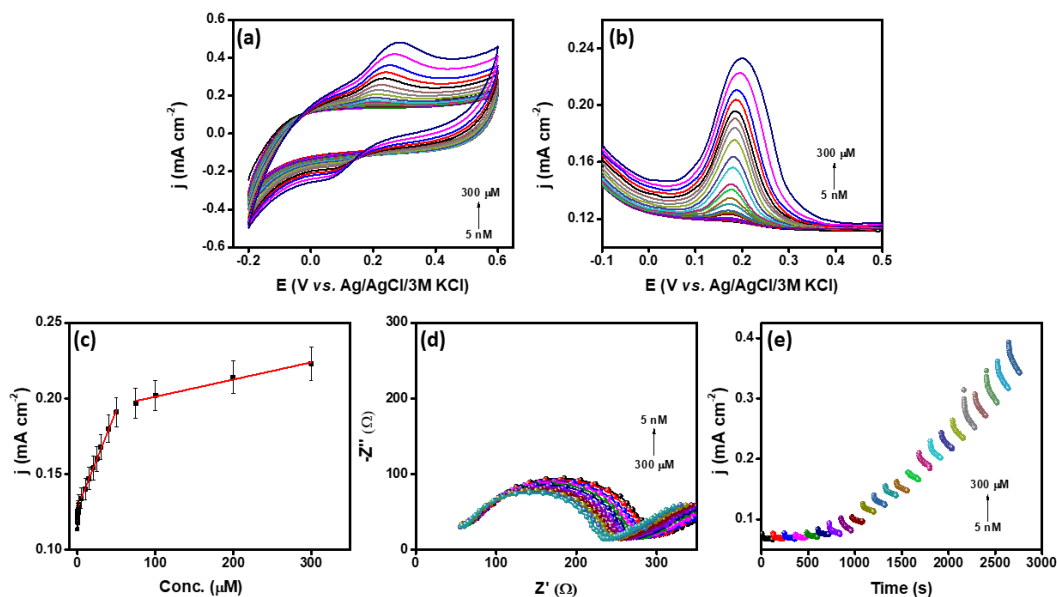


**Figure 6B-5.** (a) CV, (b) DPV, (c) plot of current density versus concentration of DA extracted from Figure 6B-5b (d) EIS, (e) chronoamperometric response of flexible CuSnB/VC-CP electrodes in 0.1 M PBS electrolyte containing 200 mM AA and various concentrations of DA

oxidation peak of ascorbic acid further evidenced the absence of ascorbic acid interference. The quantitative evaluation of the sensitivity of the as fabricated CuSnB/VC-CP electrode towards dopamine sensing was carried out from the linear plot between concentration of dopamine and current density extracted from DPV (Figure 6B-5b). As shown in Figure 6B-5c, three linear ranges from 5 nM to 2  $\mu$ M, and 5  $\mu$ M to 50  $\mu$ M and 75  $\mu$ M to 300 mM with LOD 0.5 nM were observed which demonstrated the admirable sensitivity and LOD towards dopamine sensing. Furthermore, the effect of concentration on the kinetics of electrooxidation of dopamine was analysed by EIS study (Figure 6B-5d). The continuous reduction in charge transfer resistance of the CuSnB/VC-CP upon the increment of the concentration of the dopamine signified the improved kinetics towards DA oxidation due to the facile electron transport at the electrode electrolyte interface. Similarly, sequential chronoamperometric study for two minutes was carried out with successive addition of dopamine concentration. The corresponding current



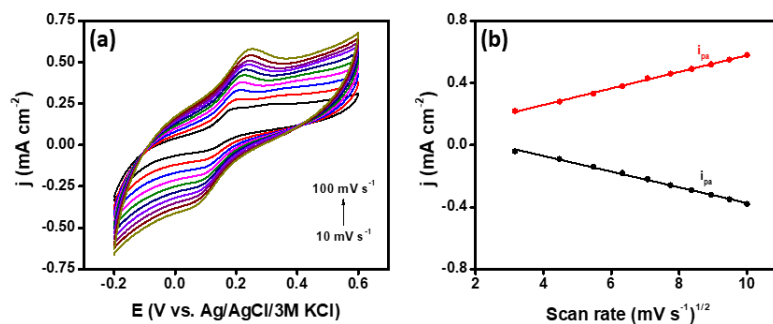


**Figure 6B-6.** (a) Cyclic voltammograms in 0.1 M PBS electrolyte containing 200 mM DA and 200 mM AA at various scan rates ranging from 10 to 100 mV s<sup>-1</sup> and (b) corresponding peak current density versus square root of scan rate curve for CuSnB/VC-CP electrode.

response for subsequent increment of dopamine concentration ranging from 5 nM to 300  $\mu$ M resulted a staircase like increment pattern of current density with time (Figure 6B-5e) evidenced the superior sensitivity of the CuSnB/VC-CP electrode towards dopamine detection. Additionally, the electrocatalytic response towards dopamine sensing behaviour at different scan rates was evaluated by performing CV at various scan rates 10 mV s<sup>-1</sup> to 100 mV s<sup>-1</sup> (Figure 6B-6a). The linearity between the peak current density and the square root of scan rate (Figure 6B-6b) evidenced the electrochemical oxidation/reduction process of dopamine by CuSnB/VC-CP to be a diffusion controlled process.

As the body fluid contains the other interfering electroactive endogenous chemicals like uric acid, glucose, ascorbic acid etc. along with DA, therefore the selective detection of dopamine along with sensitivity is equally important to realize the practical applicability of the prepared CuSnB/VC-CP flexible electrode. Thus, the selectivity of the as fabricated CuSnB/VC-CP flexible electrode towards dopamine sensing was evaluated by performing DPV with various concentration of dopamine in presence of ascorbic acid (1000  $\mu$ M), glucose (3000  $\mu$ M) and uric acid (200  $\mu$ M) under the similar conditions as shown in Figure 6B-7a-d. A negligible change in the overall current response was observed as shown in Figure 6B-7e even in the presence of high concentration interfering species and no variation in current



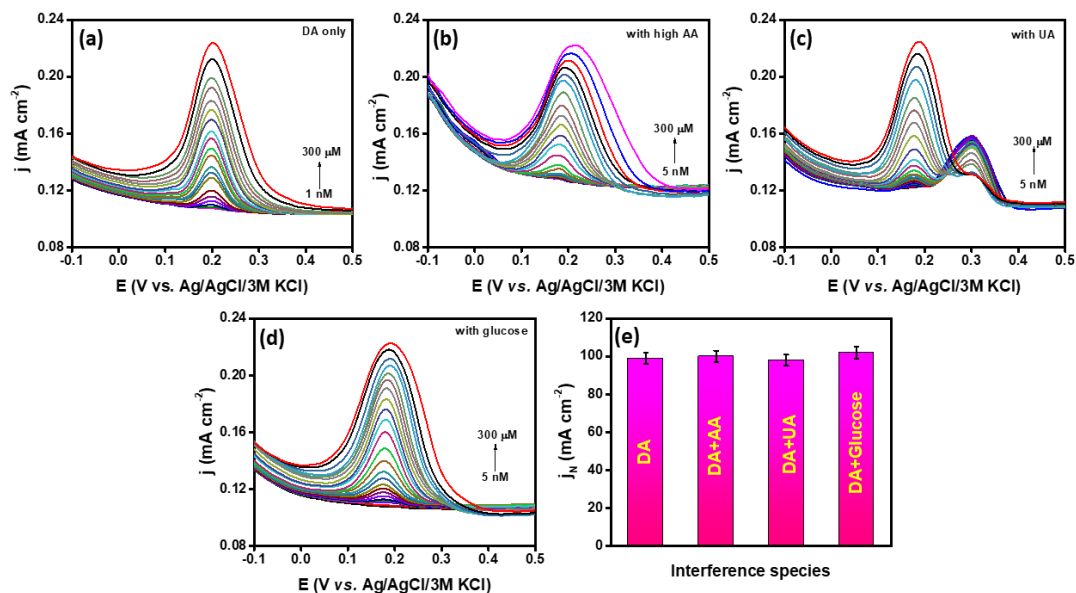


**Figure 6B-7.** Differential pulse voltammograms (a) various concentrations of DA only and in presence of interferants (b) 1000  $\mu$ M AA, (c) 200  $\mu$ M UA and (d) 3000  $\mu$ M glucose at various concentrations of DA and (e) bar diagram representing the normalized current with respect to interferents at a 300 mM concentration of DA for CuSnB/VC-CP electrode.

response was witnessed at different DA concentrations, signifying the virtuous selectivity towards dopamine sensing. Besides sensitivity and selectivity, the stability of the electrode also plays a vital role for the practical application of the as fabricated CuSnB/VC-CP electrode. The CV measurement was carried out for 500 cycles for the evaluation of the electrode behaviour during long term measurement, an insignificant decay in the current response (Figure 6B-8a) was observed which was further supported by the SEM image (Figure 6B-8b). Similarly, the DPV measurement during various deformation conditions including bending, rolling, twisting, folding and relaxing was carried out for the evaluation of the electrode performance under mechanical deformations. The negligible change in current response under various mechanical deformations (Figure 6B-8c) signified the robustness of the as fabricated flexible CuSnB/VC-CP electrode towards dopamine sensing. Moreover, the applicability of the electrode for clinical diagnosis was examined via standard addition method by taking commercial

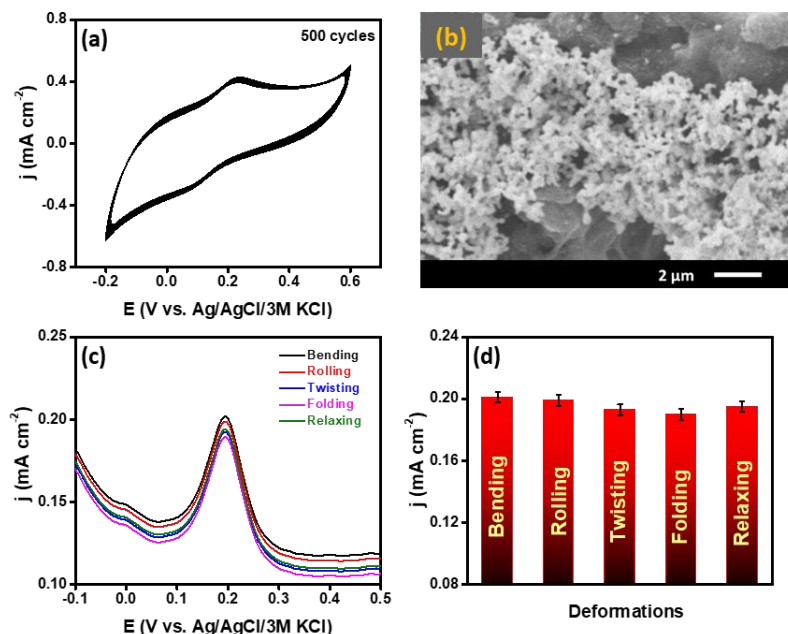


**Figure 6B-8.** (a) Cyclic voltammograms in 0.1 M PBS (pH 7.0) electrolyte containing 200 mM DA and 200 mM AA for 500 cycles at a scan rate of 50 mV s<sup>-1</sup> and (b) SEM image of the electrode after stability study, (c) DPV curves at various deformation conditions in 0.1 M PBS electrolyte containing 200 mM AA and 50 mM DA and (d) bar diagram comparing the current density response during various deformations.

**Table 6A-2. Analytical results of CuSnB/VC-CP electrode towards determination of dopamine from commercially available dopamine hydrochloride injection.**

S. No.	Conc. (taken)	Conc. (added)	Conc. (actual)	Conc. (found)	Recovery (%)
1.	5 μM	5 μM	10 μM	10.1 μM	101
2.	5 μM	10 μM	15 μM	14.6 μM	97
3.	5 μM	20 μM	25 μM	26.0 μM	104

dopaminehydrochloride injection (40 mg mL<sup>-1</sup>) as a certified reference material. The recovery range (98-104 %) as shown in table Table 6B-2 demonstrates the applicability of the flexible CuSnB/VC-CP electrode for practical clinical analysis as well.

## 6B-4 Summary

In this chapter, a novel eco-friendly flexible CuSnB/VC-CP electrode was developed by using biodegradable cellulose paper substrate via straight forward electroless deposition approach. This three dimensional electrode can be directly used for the electrochemical sensing applications which achieved a good sensitivity with excellent selectivity and durability towards dopamine detection. Moreover, the retention of the electrochemical activity under various mechanical deformations verified its potential application for flexible devices. In this way this work can be inspiring to the researchers for the development of wearale, foldable sensors for point of care sensing devices.

## 6B-5 References

1. C. Missale, S. R. Nash, S. W. Robinson, M. Jaber and M. G. Caron, *Physiol. Rev.*, 1998, **78**, 189-225.
2. N. R. Zahniser and A. Sorkin, *Neuropharmacology*, 2004, **47**, 80-91.
3. R. Franco, I. Reyes-Resina and G. Navarro, *Biomedicines*, 2021, **9**, 109.
4. X. Pan, A. C. Kaminga, S. W. Wen, X. Wu, K. Acheampong and A. Liu, *Front. Aging Neurosci.*, 2019, **11**, 175.
5. J. Kesby, D. Eyles, J. McGrath and J. Scott, *Transl. Psychiatry*, 2018, **8**, 1-12.
6. T. K. Lai, P. Su, H. Zhang and F. Liu, *Molecular brain*, 2018, **11**, 1-14.
7. W. He, X. Ye and T. Cui, *IEEE Sens. J.*, 2021, **21**, 26556-26565.
8. J.-W. Oh, Y. W. Yoon, J. Heo, J. Yu, H. Kim and T. H. Kim, *Talanta*, 2016, **147**, 453-459.
9. N. Thakur, A. Chaturvedi, D. Mandal and T. C. Nagaiah, *Chem. Commun.*, 2020, **56**, 8448-8451.
10. J. Liu, X. Jiang, R. Zhang, Y. Zhang, L. Wu, W. Lu, J. Li, Y. Li and H. Zhang, *Adv. Funct. Mater.*, 2019, **29**, 1807326.
11. M. Zhang, C. Liao, Y. Yao, Z. Liu, F. Gong and F. Yan, *Adv. Funct. Mater.*, 2014, **24**, 978-985.
12. M. M. Rahman and J.-J. Lee, *Electrochem. Commun.*, 2021, **125**, 107005.
13. J. Jiang and X. Du, *Nanoscale*, 2014, **6**, 11303-11309.
14. Y. Wang, Y. Li, L. Tang, J. Lu and J. Li, *Electrochem. Commun.*, 2009, **11**, 889-892.
15. N. Thakur, S. Das Adhikary, M. Kumar, D. Mehta, A. K. Padhan, D. Mandal and T. C. Nagaiah, *ACS omega*, 2018, **3**, 2966-2973.
16. Y. Shu, Q. Lu, F. Yuan, Q. Tao, D. Jin, H. Yao, Q. Xu and X. Hu, *ACS Appl. Mater. Interfaces*, 2020, **12**, 49480-49488.
17. Y. Zhao, J. Zhou, Z. Jia, D. Huo, Q. Liu, D. Zhong, Y. Hu, M. Yang, M. Bian and C. Hou, *Microchim. Acta*, 2019, **186**, 1-10.
18. S. Krishnan, L. Tong, S. Liu and R. Xing, *Microchim. Acta*, 2020, **187**, 1-9.
19. S. Reddy, B. K. Swamy and H. Jayadevappa, *Electrochim. Acta*, 2012, **61**, 78-86.
20. R. Nurzulaikha, H. Lim, I. Harrison, S. Lim, A. Pandikumar, N. Huang, S. Lim, G. Thien, N. Yusoff and I. Ibrahim, *Sens. Bio-Sens. Res.*, 2015, **5**, 42-49.
21. D. Liu, J. Wang, L. Wu, Y. Huang, Y. Zhang, M. Zhu, Y. Wang, Z. Zhu and C. Yang, *TrAC, Trends Anal. Chem.*, 2020, **122**, 115701.
22. A. Kafle, D. Gupta, A. Bordoloi and T. C. Nagaiah, *Nanoscale*, 2022, **14**, 16590-16601.

23. Z. Wang, Y. H. Lee, S. W. Kim, J. Y. Seo, S. Y. Lee and L. Nyholm, *Adv. Mater.*, 2021, **33**, 2000892.
24. G. Zheng, L. Hu, H. Wu, X. Xie and Y. Cui, *Energy Environ. Sci.*, 2011, **4**, 3368-3373.
25. Q. Zhong, J. Zhong, B. Hu, Q. Hu, J. Zhou and Z. L. Wang, *Energy Environ. Sci.*, 2013, **6**, 1779-1784.
26. L.-Q. Tao, K.-N. Zhang, H. Tian, Y. Liu, D.-Y. Wang, Y.-Q. Chen, Y. Yang and T.-L. Ren, *ACS Nano*, 2017, **11**, 8790-8795.
27. Y.-K. Yen, C.-H. Chao and Y.-S. Yeh, *Sensors*, 2020, **20**, 1372.
28. L. Zhang, P. Zhu, F. Zhou, W. Zeng, H. Su, G. Li, J. Gao, R. Sun and C.-p. Wong, *ACS Nano*, 2016, **10**, 1273-1282.
29. A. Kafle, N. Thakur and T. C. Nagaiah, *J. Mater. Chem. B*, 2022, **10**, 3681-3686.
30. F. Muench, *ChemElectroChem*, 2021, **8**, 2993-3012.
31. M. Costa, B. Veigas, J. Jacob, D. Santos, J. Gomes, P. Baptista, R. Martins, J. Inácio and E. Fortunato, *Nanotechnology*, 2014, **25**, 094006.
32. C.-K. Wu, M. Yin, S. O'Brien and J. T. Koberstein, *Chem. Mater.*, 2006, **18**, 6054-6058.
33. H. Zhu, D. C. Rosenfeld, M. Harb, D. H. Anjum, M. N. Hedhili, S. Ould-Chikh and J.-M. Basset, *ACS Catal.*, 2016, **6**, 2852-2866.
34. N. Xu, G. Cao, Z. Chen, Q. Kang, H. Dai and P. Wang, *J. Mater. Chem. A*, 2017, **5**, 12379-12384.

# Chapter 7

## Summary and future perspectives

### 7-1 Summary

Although the planetary energy reserve contains many folds renewable energy than the finite source of energy but around 80% of current global energy consumption is dependent on fossil fuel only. The energy extraction practice from fossil fuel not only depletes reserves but also creates serious environmental as well as health issues. Therefore, it is necessary to promote green energy production from clean and renewable sources. Among the various renewable energy resources, solar power, wind power, hydropower, and geothermal power are in current practice but all these systems involve continuous electricity generation which cannot be stored in current form for later use. So, one of the best ways to maximise utilization of the produced energy can be either conversion to value-added product or storing in an energy storage device. Among the energy conversion options, hydrogen ( $H_2$ ) production from water electrolysis is a sustainable option since  $H_2$  itself is a zero-emission energy as well as prime feeding gas for many industrial applications. Moreover, about 1% of global energy consumption is involved in  $H_2$  production only. Similarly, the zinc-air battery can be an attractive choice for the energy storage device owing to its high energy density, involvement of air as a feedstock and more importantly it works with aqueous electrolytes with very low hazardous risk. But, the performance of these devices highly relies on the activity of the electrode materials. Currently practising commercial electrolyzer contain a rigid electrode coated with electrocatalyst ink, where the involvement of an insulating binder for ink preparation hinders the electrocatalytic activity and moreover during the operation at high current density, the loss of catalyst materials is also problematic. In this context, the development of self-standing binder-free three-

dimensional flexible electrodes can be beneficial for efficient electrocatalytic performance. Additionally, the flexible electrodes can demonstrate device-friendly opportunity for any kind of reactor as well as portable and foldable electronics due to their stability under various mechanical deformations without alteration in the electrocatalytic activity.

Heading towards the development of flexible electrodes, contemporary researchers have explored common substrates like metallic wire, foam and foils (mainly nickel, titanium and iron), carbon paper etc. with satisfactory conductivity. However, their limitations such as poor flexibility, high cost, heaviness, fragility and the non-eco-friendly nature may adversely affect their flourishing. In this regard, carbon cloth and cellulose papers are promising substrates for electrode materials owing to their extensive availability, lightweight, low cost and mechanical flexibility. In addition to the choice of substrate, the electrode fabrication strategy is equally important. Currently practising fabrication techniques includes bar coating, screen printing, soak and drying, sputtering, chemical vapor deposition, electroless deposition, electroless plating methods etc. Amongst them, the electroless deposition method stands out as the economical way to achieve uniform coating along with its less hazardous nature and time efficiency. The biggest challenge of the electroless deposition is the use of the noble metal-based  $\text{PdCl}_2$  and  $\text{SnCl}_2$  reagents for sensitization-activation of the substrate which hikes the overall fabrication cost. So, the highlight of the present study involves the elimination of expensive  $\text{PdCl}_2$  and  $\text{SnCl}_2$ -based activators/sensitizers in the course of electroless deposition during the electrode fabrication.

Secondly, the sluggish kinetics of the electrochemical reactions that are involved in the energy conversion and storage devices significantly hinder their energy efficiency and practical application. Although Ir/Ru- and Pt-based electrocatalysts are well-established for OER and HER/ORR, the low natural abundance and high cost of these precious metals impede their wide application. More importantly, pairing two different electrodes for OER and HER increase, reaction complexity

and overall manufacturing cost. Therefore, it is highly attractive to design and develop efficient and low-cost water splitting catalysts made of earth-abundant elements. Among non-precious metal based electrocatalysts, transition metal-based catalysts especially Ni and Fe-based bimetallic sulfide, phosphide, boride etc. are known to exhibit the most promising activity towards overall water splitting owing to their high electrical conductivity, earth abundance, high activity and excellent stability in alkaline media. Therefore, the development of Ni and Fe-based electrocatalysts with good multifunctional activity towards various half reactions is more beneficial for practical applications of renewable energy conversion and device integration technologies. The strategy is advantageous on account of rationalizing the device fabrication and bringing down the overall cost. In this thesis, the aforementioned issues have been addressed by developing a single electrode as an alternative to the precious metal-based electrodes that can catalyze the three/two electrocatalytic processes (like OER, ORR, and HER or NRR) simultaneously.

First of all, Ni and Fe sulphide and phosphides decorated carbon cloth electrodes were explored as promising bifunctional electrocatalysts towards overall water splitting. Herein, the electroless deposition approach was explored for growing NiFeS and NiFeP over the highly flexible carbon cloth substrate. The carbon fiber-based substrates are of great research interest for various applications due to their high flexibility, low cost, corrosion resistance property and good biocompatibility as compared to metal foams or foils. Therefore, the development of carbon cloth (CC) based flexible electrodes with deposition of non-noble metal based electrocatalyst by just a simple dip-coating method adds up an initiation to develop a straightforward method towards flexible electrode fabrication. Conventionally, electroless deposition involves surface activation and sensitization using  $\text{SnCl}_2$  and  $\text{PdCl}_2$  followed by direct chemical reduction of the metal ion on the substrate. The present study eliminated the use of expensive  $\text{PdCl}_2$  and  $\text{SnCl}_2$  based activators/sensitizers to reduce the overall manufacturing cost by the introduction

of functional groups on the carbon cloth which provides strong adsorption of metal ions and simultaneously enhance the conductivity along with mass transport kinetics. The fabricated electrode was used directly as a flexible electrode which demonstrated a good bifunctional activity towards electrochemical water splitting in alkaline media and also showed good flexibility and electrochemical performance under various mechanical deformations (bending, twisting, folding etc.).

Despite being a clean and eco-friendly technology, the current commercial technologies for water electrolysis urge high-purity water which in turn hinders the broader implementation of the water electrolyzers, especially in those areas having a shortage of freshwater even for drinking purposes. The real scenario of the water distribution constitutes 96.5% of the total water on the earth is seawater whereas the availability of non-frozen freshwater is less than 1% only. In this aspect, the development of a water electrolyser, in which low-purity water or seawater can be directly employed as a feedstock may serve as an alternative for cost-effective and sustainable exploration of electrolyzers for green  $H_2$  production. Nevertheless, direct seawater splitting has significant drawbacks such as the presence of chloride ions in high concentration reduces the faradaic efficiency due to competition with chloride oxidation reaction, and the lifetime of electrolyser is limited due to the impurities present. Furthermore, the high concentration of chloride ions in the seawater feedstock may also result in toxic chlorine gas evolution at the anode in competition with the oxygen evolution reaction. Thus, the development of an alkaline water electrolyzer consisting of electrode material with good activity and high resistivity towards chloride ion corrosion could be a beneficial approach for sustainable seawater splitting. Herein, a facile and cost-effective fabrication strategy has been demonstrated for the fabrication of the binder-free three-dimensional carbon cloth flexible electrode incorporated with active electrocatalyst NiFeB over oxygen functionalized carbon cloth, OCC (i.e., NiFeB@OCC) by a simple electroless deposition method. The prepared electrode provided the three-



dimensional scaffold which could enable effective mass transport, facilitate the adsorption of reactant species and also inhibit the gas bubble accumulation over the electrode surface. Moreover, it demonstrated the remarkable performance towards OER, HER and overall water splitting in 1 M KOH as well as in 1 M KOH + 0.5 M NaCl electrolyte system with excellent stability. This study can act as a stepping stone towards green hydrogen production via saline water electrolysis.

After exploring carbon cloth based flexible electrodes, our research was focused towards the search for biodegradable substrate-based three-dimensional electrodes. For this, bio-based materials such as cellulose paper (CP) can be a good alternative as a cost-effective and biodegradable substrate. But the biggest hurdle for its exploration as an electrode material is the absence of a conductive pathway for the electric circuit because of its insulating nature. In this regard, the surface modification of cellulose paper with conductive metal composites is an effective route to induce conductivity. Herein, a cost-effective and straightforward approach has been developed to convert an insulating cellulose paper into a conductive substrate (designated as NiB-CP) via electroless deposition and this NiB-CP was employed as an eco-friendly substrate for flexible electrode development. Firstly, NiP/NiB-CP electrode was developed via two-step electroless deposition followed by an electrodeposition approach. This NiP/NiB-CP electrode possesses excellent bifunctional activity and long-term durability in both alkaline pure water and seawater electrolytes. This work opened an area for the development of cellulose paper based self-standing three-dimensional flexible electrodes for overall water/seawater splitting.

In addition to augmented energy demand, the incessantly increasing world's population also stresses high fertilizer production to provide the basis of nutrition. Therefore, the synthesis of  $\text{NH}_3$  is of huge significance, since it is a prime constituent of fertilizers as well as a novel green  $\text{H}_2$  storage material. But the commercial production of ammonia highly relies on the Haber-Bosch process which has several disadvantages *viz.* requirement of harsh operating conditions,

consumption of 2-3% of the world's energy and responsible for the more than 2% of global CO<sub>2</sub> emissions. Among various existing technologies, electrochemical nitrogen reduction has received a tremendous attraction for ammonia production with minimum energy consumption and reduced carbon footprint, as ammonia can be produced by using water as the hydrogen source under ambient conditions but requires a power source. On the other hand, rechargeable metal-air batteries are emerging as a potential candidate for energy storage systems owing to their high energy density and straightforward fabrication procedure. The potentiality of these above-mentioned technologies relies upon three important electrochemical reactions determining the overall efficiency of the system viz. nitrogen reduction reaction (NRR), oxygen evolution reaction (OER) and oxygen reduction reaction (ORR) which have sluggish kinetics. Therefore, the development of an electrode with trifunctional activity towards these electrochemical reactions is crucial. In order to address these issues an eco-friendly cellulose paper based three-dimensional flexible electrode was developed by taking NiB-CP as a substrate over which active catalyst Fe<sub>3</sub>O<sub>4</sub> nanospheres composed of thin nanosheets were decorated by electrodeposition. Since metal oxides having a porous structure with controlled morphology is beneficial to facilitate mass transport by exposure to a maximum number of active sites resulting in an improved activity. Thus, the fabricated electrode demonstrated promising NRR activity along with long-term stability. Additionally, the oxygen bifunctional activity for the designed electrode as an air-cathode for an aqueous Zn-O<sub>2</sub> battery was also studied. Remarkably, its practical applicability was confirmed by Zn-O<sub>2</sub> battery and electrochemical nitrogen reduction performance using the same battery as a power source. These exciting activities and the straightforward fabrication strategy may act as a milestone in the development of cost-effective and eco-friendly flexible electrodes towards electrochemical energy conversion and storage applications.

Thereafter, the same strategy was applied to develop eco-friendly cellulose paper based self-standing three-dimensional flexible electrodes exhibiting trifunctional

activity towards ORR, OER and HER for self-powered water splitting. Herein, NiFeP composite as an active electrocatalyst was decorated over NiB-CP by the electrodeposition method which was directly used as a working electrode for electrochemical applications. Thus, the developed electrode demonstrated good trifunctional activity towards ORR, OER and HER. A Zn-O<sub>2</sub> battery was established with the designed electrode as an air-cathode which exhibited a good power density and high specific capacity, with stable cyclability. Additionally, this Zn-O<sub>2</sub> battery was able to power an alkaline water electrolyser to perform overall electrochemical water splitting.

Besides the problems associated with energy, the consumption of fossil fuels also caused environmental pollution which may result in serious health issues. Polluted air may affect different body systems which can result in various hormonal imbalances, for instance, dopamine which is a major neurotransmitter has been reported to fluctuate with exposure to non-healthy living conditions mainly . Therefore, identification of dopamine levels is important for clinical diagnosis and treatment purposes. Herein, cellulose paper based three-dimensional flexible electrodes were explored towards selective and sensitive determination of dopamine. We have made the cellulose paper conductive by coating Vulcan carbon (VC) over it followed by electroless deposition of NiFeB as active material. The NiFeB/VC-CP and CuSnB/VC-CP electrodes were fabricated by the electroless deposition of NiFeB and CuSnB nanoparticles over the VC-CP substrate respectively and directly employed as a three-dimensional flexible electrode towards electrochemical dopamine sensing without any additional step for preparing sensor probe. As prepared electrodes demonstrated good sensitivity along with a wide detection range even in the presence of a high concentration of ascorbic acid, glucose and uric acid interferents. Moreover, fair stability during long-term electrolysis as well as under various mechanical deformations were achieved. The inspiring activities and the straightforward fabrication strategy may

act as a milestone in the development of conductive paper electrodes towards electrochemical dopamine sensing as well as in other electrochemical arenas.

## 7-2 Future Perspective

This thesis mainly highlighted the designing and fabrication of the self-standing three-dimensional flexible electrodes for electrochemical energy conversion/storage and biosensing applications especially water/sea water splitting, electrochemical dinitrogen reduction, Zn-O<sub>2</sub> battery and electrochemical dopamine sensing applications which are discussed in this report. Besides, this study has created some exciting future opportunities to explore the flexible electrodes for various electrochemical applications which are mentioned below.

1. Herein, transition metals NiFeS@OCC, NiFeP@OCC, NiFeB@OCC, NiP/NiB-CP, Fe<sub>3</sub>O<sub>4</sub>/NiB-CP, NiFeP/NiB-CP, NiFeB/VC-CP and CuSnB/VC-CP electrodes have been explored for bi/trifunctional systems and biosensing applications. These electrodes can be explored for other energy conversion/storage applications such as HCl electrolysis, CO<sub>2</sub> reduction, supercapacitors etc.
2. During this study, a biodegradable substrate-based NiB-CP three-dimensional conductive substrate compatible with Ni-foam has been developed which can be explored for the current collector as an alternative to Ni-foil/Ni-foam.
3. The present study explored carbon cloth and cellulose paper as a substrate for flexible electrode preparation so other eco-friendly substrates such as PET film, cotton cloth, and polymers can be explored as potential substrates for electrode development.
4. The developed NiB-CP can be used as a substrate for the deposition of various metals by means of electrodeposition and directly employed as an anode for the development of eco-friendly all paper-based metal-air batteries.
5. Herein, Vulcan carbon was employed as conductive support, other conductive carbon supports such as MNC, CNT, CNS etc. can be explored as a base materials over the biodegradable substrate to grow active electrocatalyst

towards the development of energy conversion and storage as well as biosensing applications. These flexible electrodes can be explored as a zinc air battery powered wearable sensor for biosensing applications.



## Alankar Kafle

Ph.D. Scholar

Department of Chemistry

Indian Institute of Technology Ropar

Rupnagar, Punjab-140001, India

Email ID: [2018cyz0014@iitrpr.ac.in](mailto:2018cyz0014@iitrpr.ac.in)

Contact No: +91-7347065560 (India), +977-9841531337 (Nepal)



### Research Interest

Designing three-dimensional flexible electrode for electrochemical energy conversion/storage and biosensing applications. Highly interested in mechanistic study of interfacial chemistry at electrode-electrolyte interphase with in-situ/operando analysis.

### Academic Profile

S.N.	Qualification	Board/ University	Passed Year
1.	S. L. C.	S. L. C. Board of Nepal	1993
2.	I. Sc.	Tribhuvan University, Nepal	1997
3.	B. Sc.	Tribhuvan University, Nepal	2001
4.	M. Sc.	Tribhuvan University, Nepal	2004
5.	Ph. D.	Indian Institute of Technology Ropar, India	2018-present

### Peer Reviewed Publications

1. **A. Kafle**, D. Gupta and T. C. Nagaiah\*, Facile fabrication of NiFeO<sub>4</sub> deposited flexible carbon cloth electrode towards overall water splitting in alkaline and saline solutions, *Electrochim. Acta*, 2022, 441, 141779
2. **A. Kafle**, D. Gupta, A. Bordoloi and T. C. Nagaiah\*, Self-standing Fe<sub>3</sub>O<sub>4</sub> decorated paper electrode as binder-free trifunctional electrode for

- electrochemical ammonia synthesis and Zn-O<sub>2</sub> batteries, *Nanoscale*, 2022, 14, 16590-16601.
3. **A. Kafle**, N. Thakur and T. C. Nagaiah\*, Fabrication of NiFeB flexible electrode via electroless deposition towards selective and sensitive detection of dopamine, *J. Mater. Chem. B*, 2022, 10, 3681-3686.
  4. **A. Kafle**, M. Kumar, D. Gupta and T. C. Nagaiah\*, The activation-free electroless deposition of NiFe over carbon cloth as a self-standing flexible electrode towards overall water splitting, *J. Mater. Chem. A*, 2021, 9, 4299-24307. (Highlighted as Back cover page)
  5. D. Gupta, **A. Kafle**, P. P. Mohanty, T. Das, S. Chakraborty, R. Ahuja and T. C. Nagaiah\*, Self-powered NH<sub>3</sub> synthesis by trifunctional Co<sub>2</sub>B-based high power density Zn-air batteries, *J. Mater. Chem. A*, 2023, **11**, 12223–12235
  6. D. Gupta, **A. Kafle**, T. C. Nagaiah\*, Dinitrogen Reduction Coupled with Methanol Oxidation for Low Overpotential Electrochemical NH<sub>3</sub> Synthesis Over Cobalt Pyrophosphate as Bifunctional Catalyst. *Small* 2023, 2208272.
  7. D. Gupta, **A. Kafle**, S. Kaur, T. S Thomas, D. Mandal and T. C. Nagaiah\*, Selective Electrochemical Conversion of N<sub>2</sub> to NH<sub>3</sub> in Neutral Media Using B, N-Containing Carbon with a Nanotubular Morphology, *ACS Appl. Mater. Interfaces*, 2023, 15, 4033–4043
  8. D. Gupta, **A. Kafle** and T. C. Nagaiah\*, Sustainable ammonia synthesis through electrochemical dinitrogen activation using Ag<sub>2</sub>VO<sub>2</sub>PO<sub>4</sub> catalyst, *Faraday Discuss.*, 2022, doi: 10.1039/D2FD00150K.
  9. D. Gupta, **A. Kafle**, S. Kaur, P. P. Mohanty, T. Das, S. Chakraborty, R. Ahuja and T. C. Nagaiah\*, High yield selective electrochemical conversion of N<sub>2</sub> to NH<sub>3</sub> via morphology controlled silver phosphate under ambient conditions, *J. Mater. Chem. A*, 2022, 10, 20616-20625.



10. D. Gupta, **A. Kafle**, A. Chaturvedi, T. C. Nagaiah\*, Recovery of High Purity Chlorine by Cu-Doped Fe<sub>2</sub>O<sub>3</sub> in Nitrogen Containing Carbon Matrix: A Bifunctional Electrocatalyst for HCl Electrolysis, *ChemElectroChem*, 2021, 8, 2858-2866. († Equal contribution)
11. T. C. Nagaiah\*, D. Gupta, S. Das Adhikary, **A. Kafle** and D. Mandal, Tuning polyoxometalate composites with carbonaceous materials towards oxygen bifunctional activity, *J. Mater. Chem. A*, 2021, 9, 9228-9237.

### Manuscript under progress

1. **A. Kafle**, D. Gupta, T. C. Nagaiah, NiP coated self-standing flexible paper electrode for alkaline saline water splitting.
2. **A. Kafle**, D. Gupta, T. C. Nagaiah, High performance NiFeP deposited flexible paper electrode for Zn-O<sub>2</sub> battery powered overall water splitting.
3. **A. Kafle**, D. Gupta, T. C. Nagaiah, Modification of cellulose paper with CuSnB by electroless deposition for the selective and sensitive detection of dopamine.

### Cover page

**Back cover:** **A. Kafle**, M. Kumar, D. Gupta and T. C. Nagaiah\*, The activation-free electroless deposition of NiFe over carbon cloth as a self-standing flexible electrode towards overall water splitting, *J. Mater. Chem. A*, 2021, 9, 4299-24307.

### Conference/Workshop

1. **Poster presentation** “International Conference on Nanotechnology for Better Living (NBL-2023)”, 25-29 May, 2023, NIT Srinagar, Kashmir.
2. **Oral presentation** “International Conference on Energy Conversion and Storage (IECS-2023) and Energy Hackathon Contest”, 18-20 Jan, 2023, IIT Madras, Chennai.
3. **Poster presentation** “Conference on Advances in Catalysis for Energy and Environment”, CACEE-2022, 31 Oct - 5 Nov, 2022, TIFR, Mumbai.

4. **Poster presentation** “Conference on Mechanistic investigation on heterogeneous processes”, ChemCatCon 2.0, 14-15 May, 2022 IIT Gandhinagar.
5. **Poster presentation** “International conference on Advanced Materials for Better Tomorrow”, AMBT-2021, 13-17 July 2021, IIT BHU, online.
6. **Oral presentation** “International Conference on recent trends in chemical science”, RTCS-2021, 21-24 Dec. 2021, Indian Chemical Society, Kolkata, online.
7. **Oral presentation** International Conference on recent trends in chemical science, (RTCS-2020)”, 26-29 Dec. 2020, Indian Chemical Society, Kolkata, online.
8. **Participated** in virtual conference on “Materials for Energy Harvesting and Catalysis” held from 1st- 3rd May 2020 via Zoom platform, TIFR, Mumbai and IISER Kolkata.
9. **Participated in** International Conference on “Advanced Nanomaterials Applications” (VCAN 2020), Centre for Nanotechnology Research (CNR), Vellore Institute of Technology, Vellore, India, 17th - 19th June 2020.

## Key Research Projects

- Development of three-dimensional flexible electrodes for electrochemical water splitting and Zn-O<sub>2</sub> batteries.
- Development of flexible electrodes active towards OER, NRR and ORR for Zn-air battery powered ammonia synthesis.
- Development of three-dimensional flexible electrodes for Dopamine, sensing.
- Designing of electrocatalysts for electrochemical HCl electrolysis.
- Designing of electrocatalysts for electrochemical dinitrogen reduction.

## Instruments Hands on Experience

- Electrochemical workstation.
- Scanning electrochemical microscopy (SECM)
- X-ray diffraction (XRD).
- Spectrophotometer including in-situ spectroelectrochemical analysis.
- Scanning electron microscopy (SEM), and energy disperse X-ray spectroscopy (EDAX).

## Teaching/Work Experience

- **Teaching Assistant**, Technology Museum laboratory, IIT Ropar (Instructor: Dr. Himanshu Palliwal and Dr. Vishwa Pal).
- **Teaching Assistant**, Practical for Masters, IIT Ropar (Instructor: Dr. Tharamani C.N. and Manoj Kumar Pandey)
- **Project Mentor**, Major M.Sc. Project entitled “Electrochemical Conversion of Benzyl Alcohol to Benzaldehyde Catalyzed by Vanadium Chromium Sulphide” by Ms. Helena Mech (2020), IIT Ropar (Supervisor: Dr. Tharamani C. N.).
- **Teaching Assistant**, Tribhuvan University, December, 2012- June, 2014.
- **Assistant Professor**, Tribhuvan University, June, 2014-date.
- **Lecturer**, College of Applied Sciences-Nepal, Kathmandu, September, 2005-December, 2012.
- **Environmental Chemist**, Nepal Environmental and Scientific Services (P) Ltd., Kathmandu, Nepal, August, 2008-December, 2012.

## Awards

Received “**Research Excellence Award**” at 57th Annual Convention of Chemists, 2020 & International Conference on “Recent Trends in Chemical Sciences (RTCS-2020)”, 26 - 29, 2020 Dec., Indian Chemical Society, Kolkata, India.